Transactions of the ASME, Journal of Heat Transfer (ISSN 0022-1481) is published monthly by The American Society of Mechanical Engineers, Three Park Avenue, New York, NY 10016. Periodicals postage paid at New York, NY and additional mailing offices. POSTMASTER: Send address changes to Transactions of the ASME, Journal of Heat Transfer, c/o THE AMERICAN SOCIETY OF MECHANICAL ENGINEERS, 22 Law Drive, Box 2300, Fairfield, NJ 07007-2300. **CHANGES OF ADDRESS** must be received at Society headquarters seven weeks before they are to be effective. Please send old label and new address.

Journal of Heat Transfer

Published Monthly by ASME

VOLUME 128 • NUMBER 8 • AUGUST 2006

FOREWORD

HEAT TRANSFER PHOTOGALLERY

RESEARCH PAPERS

(Contents continued on inside back cover)

This journal is printed on acid-free paper, which exceeds the ANSI Z39.48-1992 specification for permanence of paper and library materials. ♾™
♻ 85% recycled content, including 10% post-consumer fibers.

Journal of Heat Transfer Volume 128, Number 8 AUGUST 2006

TECHNICAL BRIEFS

DISCUSSION

ERRATUM

ANNOUNCEMENT

The ASME Journal of Heat Transfer is abstracted and indexed in the following:

Applied Science and Technology Index, Chemical Abstracts, Chemical Engineering and Biotechnology Abstracts (Electronic equivalent of Process and Chemical Engineering), Civil Engineering Abstracts, Compendex (The electronic equivalent of Engineering Index), Corrosion Abstracts, Current Contents, E & P Health, Safety, and Environment, Ei EncompassLit, Engineered Materials Abstracts, Engineering Index, Enviroline (The electronic equivalent of Environment Abstracts), Environment Abstracts, Environmental Engineering Abstracts, Environmental Science and Pollution Management, Fluidex, Fuel and Energy Abstracts, Index to Scientific Reviews, INSPEC, International Building Services Abstracts, Mechanical & Transportation Engineering Abstracts, Mechanical Engineering Abstracts, METADEX (The electronic equivalent of Metals Abstracts and Alloys Index), Petroleum Abstracts, Process and Chemical Engineering, Referativnyi Zhurnal, Science Citation Index, SciSearch (The electronic equivalent of Science Citation Index), Theoretical Chemical Engineering

Journal of Heat Transfer

Heat Transfer Photogallery

The Tenth Heat Transfer Photogallery was sponsored by the K-22 Heat Transfer Visualization Committee for the 2005 International Mechanical Engineering Congress and Exhibition (IMECE) held in Orlando, Florida, on November 5–11, 2005. The peer-reviewed evaluation process for the presented entries identified the six entrees for publication in the ASME *Journal of Heat Transfer* August issue of 2006.

The purpose of publishing these entries is to draw attention to the innovative features of optical diagnostic techniques and aesthetic qualities of thermal processes. To focus on visualization images and schematics, the text is kept to a minimum and further details should be found directly from the authors. My wish is that the readers enjoy viewing these collections, acquire knowledge of the state-of-the-art features, and also promote their participation in the 2006 IMECE Photogallery session.[1]

The **Call for Photogallery for 2006 IMECE** is also announced in this issue of *Journal of Heat Transfer*.

The Photogallery entries are listed with brief descriptions of their technical presentation contents:

1. "Nanosecond Imaging of Bubble Nucleation on a Microheater," by C. T. Avedisian, R. E. Cavicchi, and M. J. Tarlov of Cornell University.
2. "Evaporation and Dryout of Nanofluid Droplets on a Microheater Array," by C. H. Chon, S. W. Paik, J. B. Tipton, Jr., and K. D. Kihm of the University of Tennessee.
3. "Mili-Scale Visualization of Bubble Growth-Translation and Droplet Impact Dynamics," by R. M. Manglik, M. A. Jog, A. Subramani, and K. Gatne of the University of Cincinnati.
4. "Film Cooling Measurements for Novel Hole Configurations," by Y. Lu, H. Nasir, D. Faucheaux, and S. V. Ekkad of Louisiana State University.
5. "Jet Impingement Heat Transfer Visualization Using a Steady State Liquid Crystal Method," by E. Esposito and S. V. Ekkad of Louisiana State University.
6. "The Passing Behaviors of Vapor through Cloth," by A. Narumi, K. Uchida, and T. Konishi of Kanagawa Institute of Technology, Autech Japan, and Oita National College of Technology, Japan, respectively.

Kenneth D. Kihm
Department of Mechanical, Aerospace
and Biomedical Engineering,
University of Tennessee,
Knoxville, TN 37996-2210

[1]http://www.asmeconferences.org/congress06

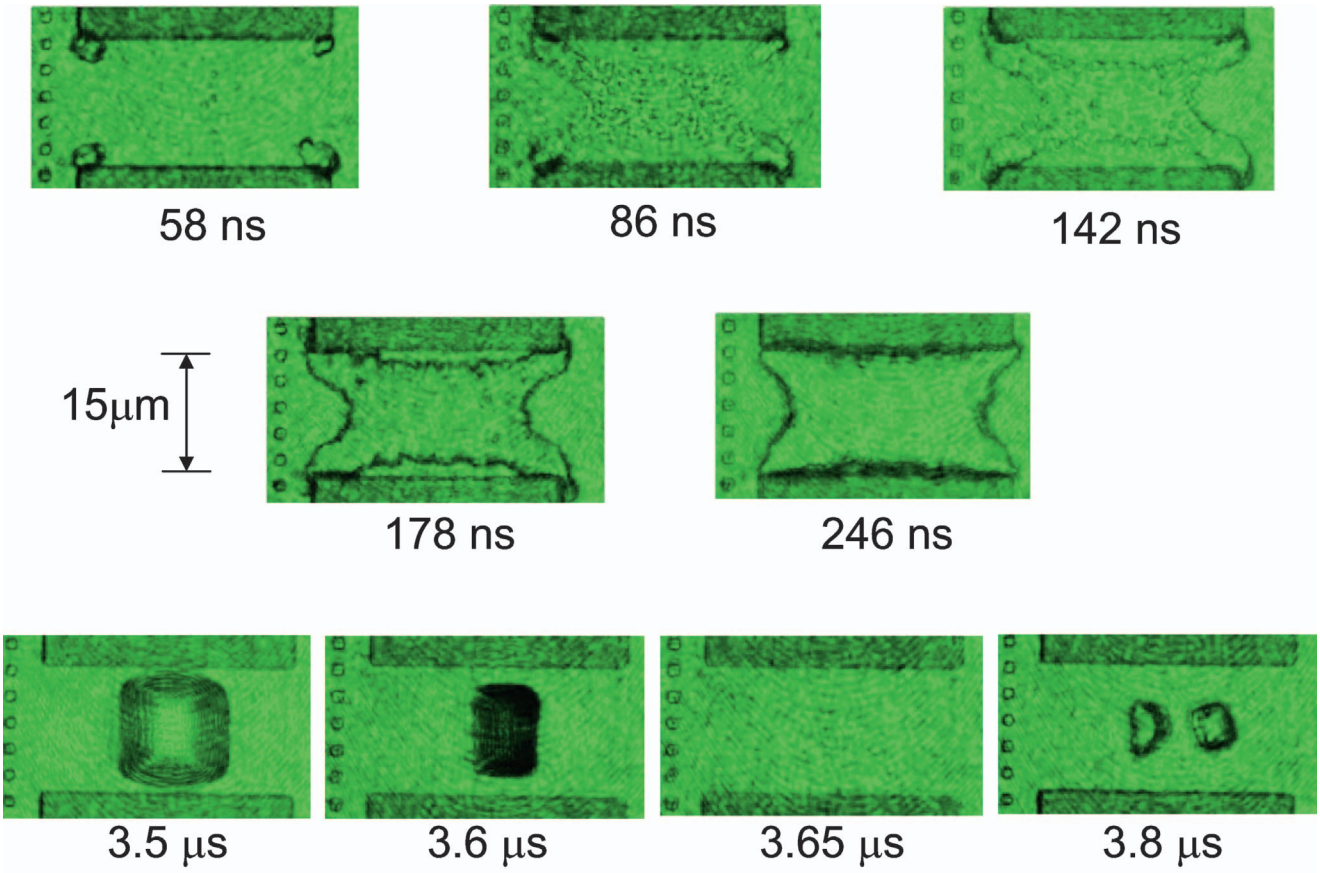

These images show bubble nucleation and growth of a thin film heater (a platinum film 15 μm wide, 30 μm long and 0.2 μm thick) that is heated by an 11.8 volt pulse of 0.50 μs duration in subcooled water. Imaging is by illumination from a Nd:Yag laser (hence the green colored photographs) that produces an effective frame rate of 1.3×10^8 frames/s (the method is described in Avedisian et al. (2006) and Balss et al. (2005)). Time is relative to the first appearance of bubbles. In the early phase, bubbles are visible at the four corners of the platinum surface (58 ns) which grow laterally into a vapor film (142 ns) that covers the surface by 178 ns after which the bubble thickens and grows into the bulk (246 ns and beyond). The collapse phase (e.g., 3.5 μs to 3.8 μs) continues well after the heater pulse is turned off. Vapor completely disappears (3.65 μs) but then bubbles reappear (3.8 μs) well after the power-off phase. Reappearance of bubbles is speculated to be the result of a stagnation-like flow induced by the rapid collapse and inward motion of liquid that jets upward to cause a local reduction of pressure to cavitate a bubble at 3.8μs.

Nanosecond Imaging of Bubble Nucleation on a Microheater

C. Thomas Avedisian, Richard E. Cavicchi and Michael J. Tarlov
Cornell University and National Institute of Standards and Technology

Avedisian, C.T., Cavicchi, R.E. Tarlov, M.J. *Rev. Sci. Intruments*, 2006, in press.
Balss, K.M., Avedisian, C.T., Cavicchi R.E., Tarlov, M.J. *Langmuir*, **21**, 10459-10467 (2005).

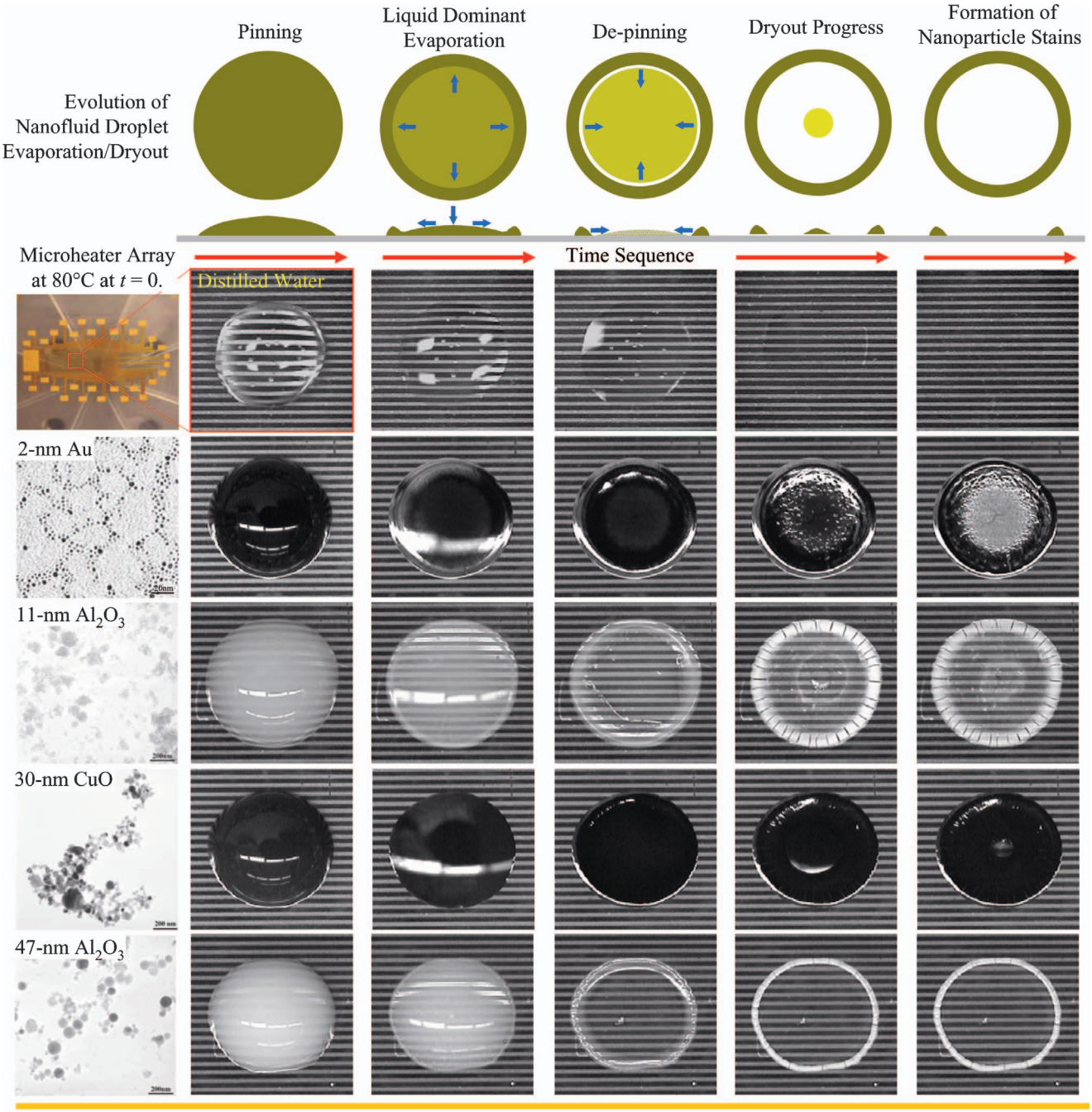

Evaporation and Dryout of Nanofluid Droplets on a Microheater Array

C. H. Chon, S. W. Paik, J. B. Tipton Jr., and K. D. Kihm
Micro/Nano Scale Fluidics and Energy Transport Laboratory [http://minsfet.utk.edu]
Department of Mechanical, Aerospace, and Biomedical Engineering
University of Tennessee, Knoxville, Tennessee

Nanofluid, a mixture of small concentration of metallic nanoparticles in a base fluid, is known to have substantial enhancement in thermal conductivity compared with that of the base fluid. The evaporation processes of different nanofluid droplets, all for 5-μl, 0.5 vol. % concentration and onto the micro-heater array at 80°C, are visualized to examine the effect of nanoparticle sizes on the dryout characteristics. While the distilled water droplet evaporates evenly in an axi-symmetric way, dryout patterns of the nanofluids containing nanoparticles (2-nm Au, 30-nm CuO, and 11-nm and 47-nm diameter Al_2O_3) are different in leaving concentric rims of dried nanoparticles near the initial wet-surface boundary. The formation of the rim is the most distinctive for the case of nanofluid containing 47-nm Al_2O_3, whereas the rims are less pronounced and more spreading for nanofluids containing smaller nanoparticles. For nanofluid containing 2-nm Au particles, the deposition is thicker and more uniform toward the droplet inner area in comparison with the other nanofluids containing larger nanoparticles. This is believed to be due to its slower flow and higher viscosity as a result of higher particle population, and high specific gravity.

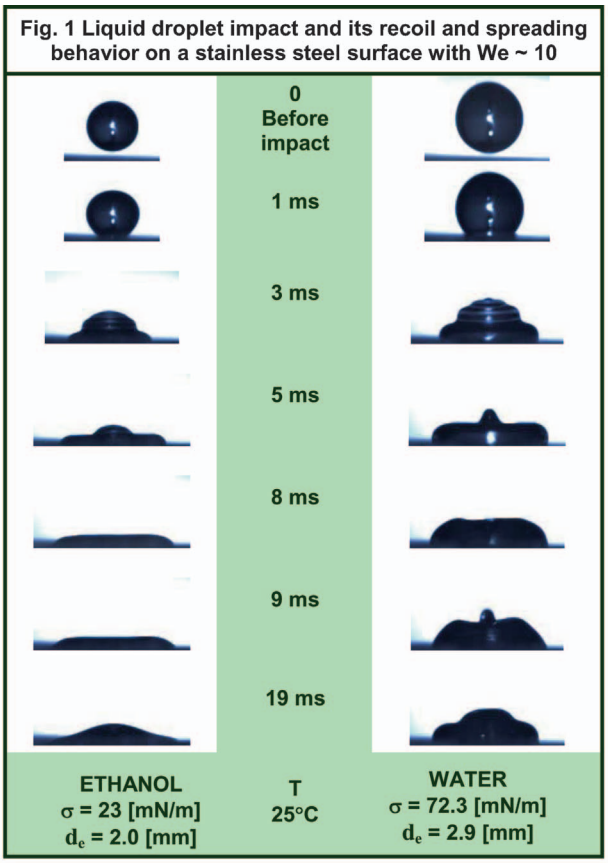

Fig. 1 Liquid droplet impact and its recoil and spreading behavior on a stainless steel surface with We ~ 10

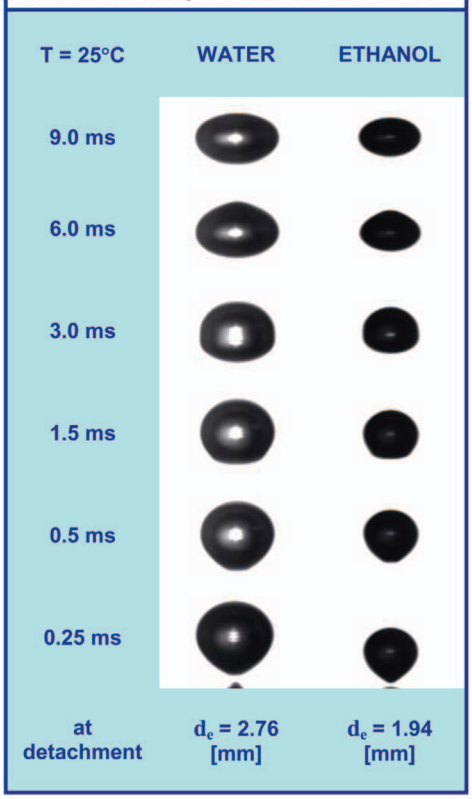

Fig. 3 Post-departure adiabatic air-bubble translation in a pool of water and ethanol

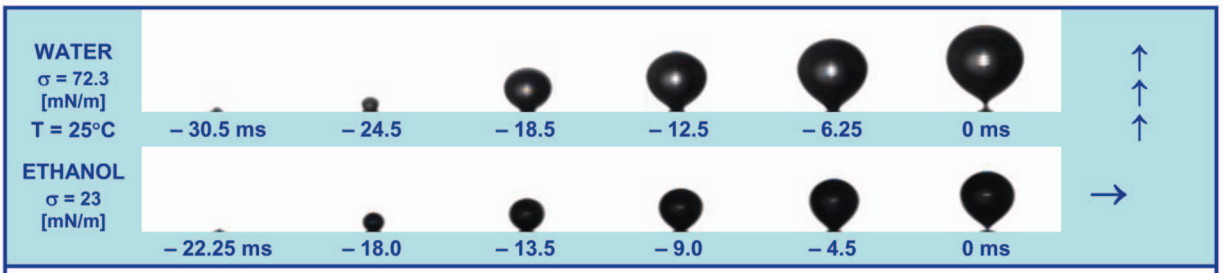

Fig. 2 Spatial-temporal evolution of an adiabatic air bubble in a pool of water and ethanol

MILI-SCALE VISUALIZATION OF BUBBLE GROWTH-TRANSLATION AND DROPLET IMPACT DYNAMICS

R.M. Manglik, **M.A. Jog**, **A. Subramani**, and **K. Gatne**
Thermal-Fluids & Thermal Processing Laboratory, University of Cincinnati, Cincinnati, OH 45221-0072

The dynamic behavior of an air bubble, emanating from a 0.32 mm i.d., 0.64 mm o.d., vertical capillary-tube orifice with a bubble interval of 0.22 – 0.28 s at constant pressure and adiabatic (T = 25°C) conditions, as well as droplet impact and spreading on a hydrophobic surface are characterized. Images of the mili-scale spatial-temporal evolution of bubbles (embryonic appearance at orifice tip → growth and detachment → translation) as well as droplets were acquired using a high-speed (5000 frames/s) digital video camera fitted with a 8× optical zoom lens. It was triggered through a computer interface to record continuous high-speed video from which any desired frame can be captured by digital-video-processing software; the equivalent departure diameter was estimated by area-averaging using image processing software.

The impact, spreading, and recoil behaviors of ethanol and water droplets on a horizontal stainless steel surface are depicted in Fig. 1. For constant Weber number (We ~ 10), the spreading and recoil dynamics in the two cases are significantly different. Higher wettability of ethanol promotes greater spreading and dampens recoil in comparison with that seen in water. Figure 2 depicts the growth of an air bubble in pools of ethanol and water. While displaying similar ebullience, a bubble of smaller size and surface age is produced in low-surface-tension ethanol. Dynamic shape variations of the air bubble as it translates upwards in the pool are seen in Fig. 3. From a nearly spherical, tear-drop bubble, the shape changes to an oblate ellipsoid during translation, and surface tension effects are manifest only in the size of respective bubbles.

Film Cooling Measurements For Novel Hole Configurations

Yiping Lu, Hasan Nasir, David Faucheaux and Srinath V. Ekkad

Mechanical Engineering Department, Louisiana State University
Baton Rouge, LA 70803

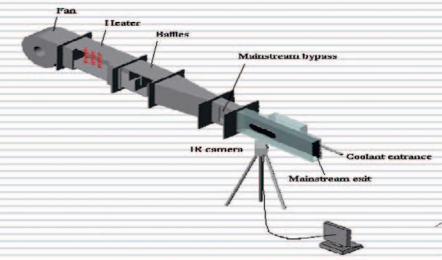

Schematic of experimental setup

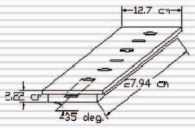

Test plate geometry without slot

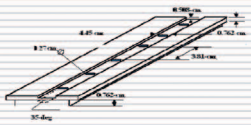

Test plate geometry with slot

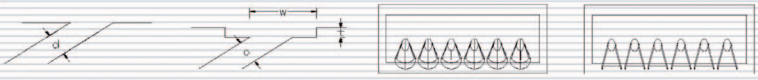

Flat Plate | Full Slot | Crescent Exit | Slot Exit

Pictures Taken During Experiment with Different Hole Configurations at Different Time Intervals

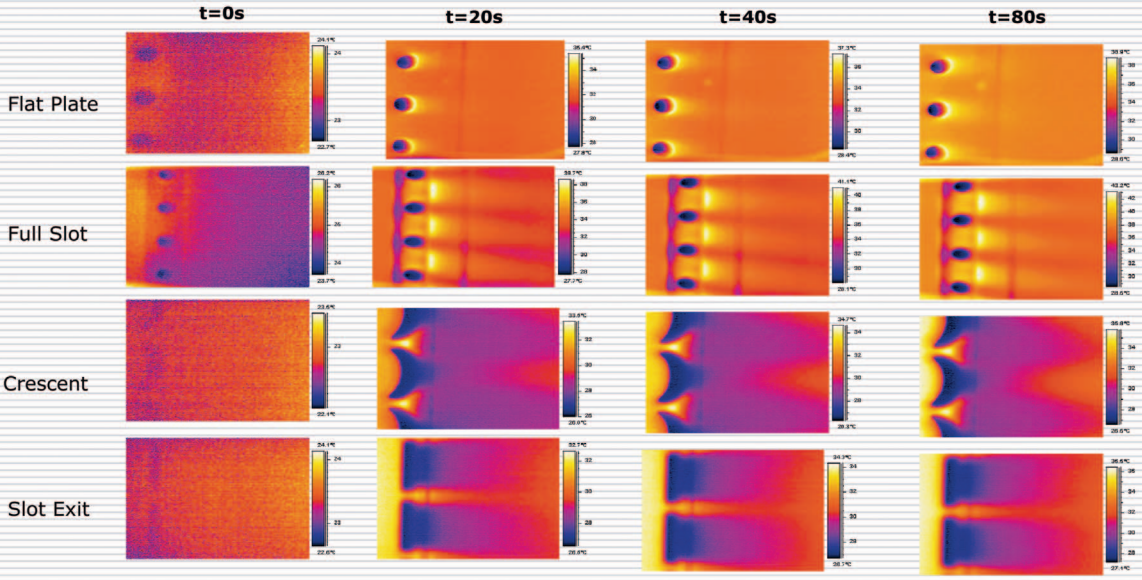

Experimental Procedure:

- Blower is set appropriately for required mainstream velocity
- Heater is turned on and allowed to heat the air to a desired mainstream temperature
- The coolant air is provided from separate compressed air supply and is metered for flow measurement
- The mainstream and coolant are triggered at the same instant when the IR system starts taking images and saving to hard drive at set intervals
- Images are saved then processed to calculate the heat transfer coefficients and film effectiveness using the theory

Results

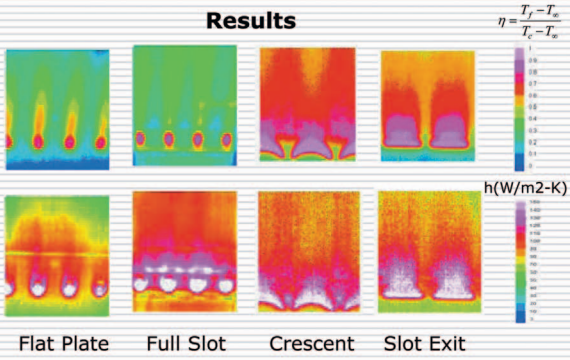

JET IMPINGEMENT HEAT TRANSFER VISUALIZATION

USING A STEADY STATE LIQUID CRYSTAL METHOD

Eric Esposito and Srinath V. Ekkad

Louisiana State University Department of Mechanical Engineering
Baton Rouge, LA 70803

Steady State Approach Using Heater Foil

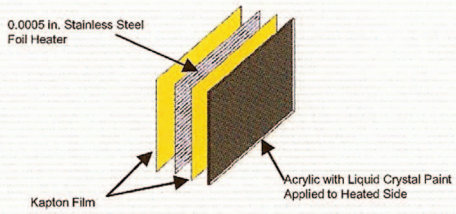

Experimental Test Rig

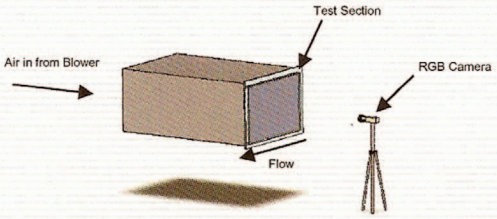

Pictures Taken During Experiment with Increasing Heater Flux

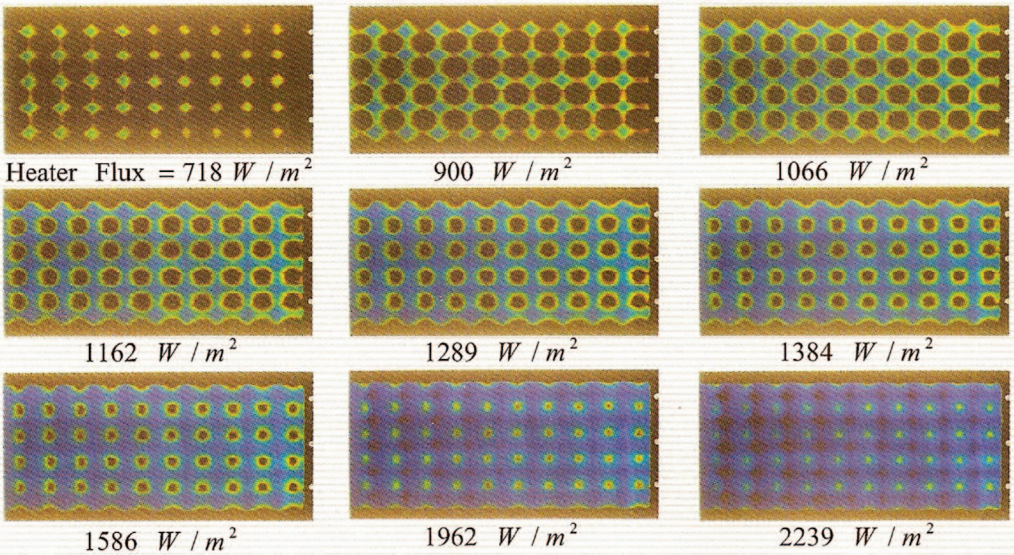

Liquid Crystal Range (SPN/R30C5W)

Experimental Procedure:

- Blower is set appropriately for required jet Reynolds number
- Heater is turned on and allowed to reach steady state
- A picture is taken of the liquid crystal coated test plate and heater amperage and voltage measured
- Heater power is incrementally increased and additional pictures taken to capture temperature and heater flux data at every point in the array
- Pictures are converted to Hue and liquid crystal calibration curve used to determine temperature at corresponding point

Results

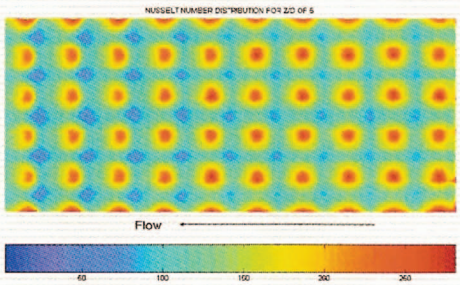

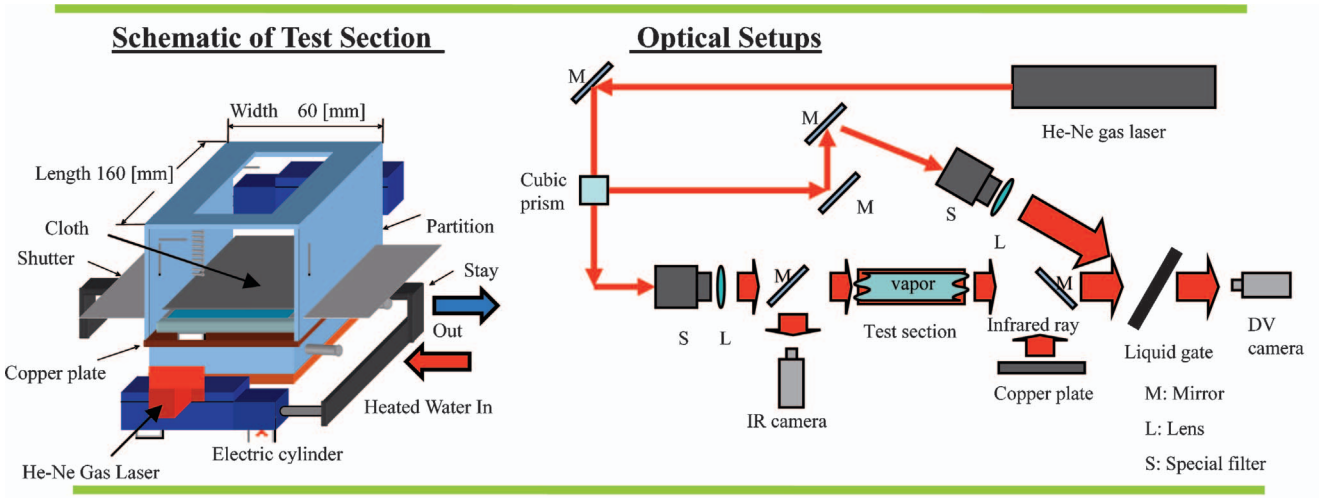

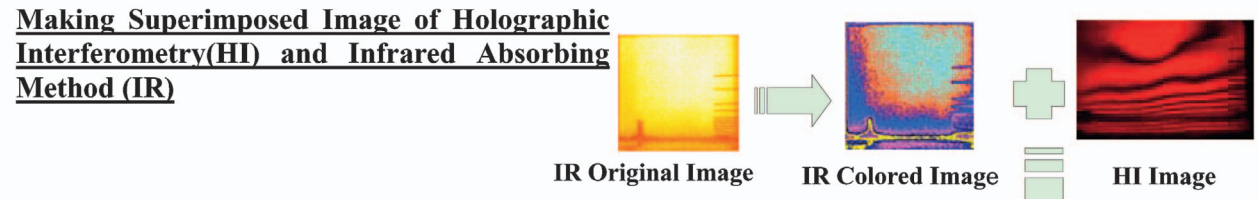

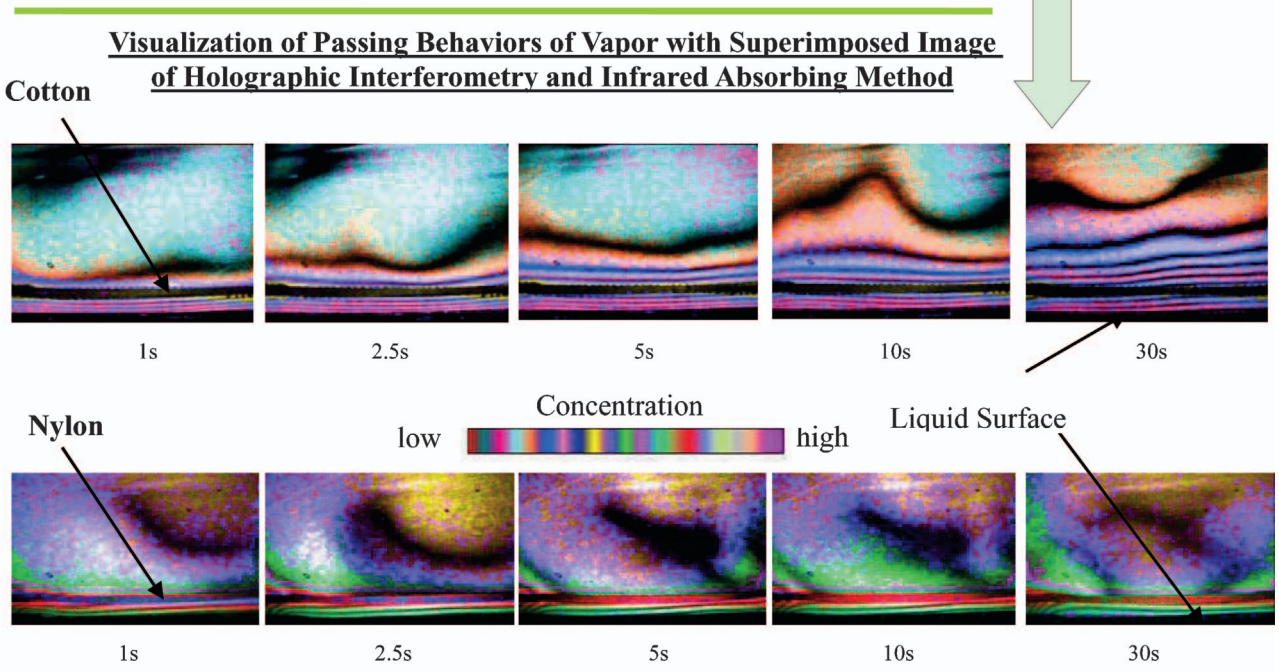

The Passing Behaviors of Vapor through Cloth

Akira NARUMI[1], Kenichi UCHIDA[2] and Tadashi KONISHI[3]

[1] Kanagawa Institute of Technology, Japan, [2] Autech Japan, Inc, Japan, [3] Oita National College of Technology, Japan

There occurs heat and mass transfer through cloth in the very small space from skin to the outside of cloth due to the release of heat and sweat evaporation from human body. The new simultaneous 2-D measurement technique of temperature and concentration distributions that combines infrared absorbing method (IR) with holographic interferometry (HI) was applied to this space. Cotton (porosity Φ=0.586, thickness t=324μm) and nylon (Φ=0.578, t=347μm) were used for the typical hydrophilic and hydrophobic clothes, respectively. N-propanol was used for liquid. The distance from liquid surface to cloth was 5mm. Liquid temperature was 40°C. The superimposed images of HI and IR show clearly that more vapor passes through cloth in the case of cotton than in the case of nylon. This fact demonstrates that this new technique is very useful for measuring the passing behaviors of vapor through cloth.

We appreciate that this research was partially supported by funds of Grant-in-Aid for Scientific Research in Japan.

Thermal and Flow Performance of a Microconvective Heat Sink With Three-Dimensional Constructal Channel Configuration

R. M. Moreno

Y.-X. Tao
e-mail: taoy@fiu.edu

Department of Mechanical and Materials Engineering,
Florida International University,
Miami, FL 33174

The design, performance, manufacturing, and experimental validation of two convective heat sinks with scalable dimensions are presented. The heat sinks consist of an array of elemental units arranged in parallel. Each elemental unit is designed as a network of branching channels whose dimensions follow a group of geometric relations that have been derived from physiological fluid transport systems and the constructal method. The goal of these relations is to optimize both the point-to-point temperature difference within the heat sink and the pressure drop across the device under imposed geometric constraints. The first branching network is a generic three-dimensional (3-D) structure that was analyzed to push the limit of the heat sinks capability. The second is a heat sink that was designed specifically with the tape-casting fabrication method in mind. The heat sink has a branching network embedded within low temperature cofire ceramic (LTCC) and the same network embedded within thick film silver, which has the ability of being cofired with low temperature cofired ceramic substrates. The performance is evaluated using both a channel-level lumped model and a CFD model. The performance for different heat sink materials (low-temperature cofired ceramic and silver) is presented. The key results are then compared with the experimental results of the two scaled models. The results show good agreement within the experimental uncertainty. This validation confirms that the thermal performance and pumping efficiency of the constructal heat sink is superior compared to porous metal and conventional microchannel heat sinks under the same operating conditions, and that the designs are only limited by manufacturing techniques.
[DOI: 10.1115/1.2211630]

1 Introduction

The power density of integrated circuits is increasing at a rapid pace. To keep up with this, the size and surface area of air-cooled heat sinks has also been increasing. The ability of these air-cooling systems to provide the low thermal resistances necessary to maintain electronics at safe operating temperatures has reached its limit [1]. Liquid, having about twenty times the thermal conductivity of air, has the capability of providing the high heat removal rates while maintaining the compact volumes necessary for cooling the next generation of microelectronic devices being developed [2,3]. Microchannel heat sinks, using liquid coolants, were first documented by Tuckerman and Pease in 1981 [4]. Since then they have been widely studied for being one of the promising technologies capable of providing high heat removal rates from compact volumes. However, these high heat removal rates require small long channels with high flow rates. High-pressure drops and limitations on available pumping power often restrict the implementation of microchannels in compact multichip modules and 3-D microelectronic packages [5]. This has created the need for alternative designs that can provide the effectiveness of microchannels without the cost of large pumping power. In this paper we present an alternative microconvective heat sink design that could potentially be integrated with microelectronic components. The target of this new approach seeks a design that (a) has high surface area-to-volume ratio geometry, (b) can achieve high heat removal rates (when compared with the traditional 2-D microchannel configuration), and (c) has an optimized overall flow resistance such that the ratio of total heat removed to the fluid pumping power required is maximized.

The previous goals can be achieved through the application of two methods. The first of these methods is the constructal method proposed by Bejan in [6]. The method developed a set of geometric relations that are used to design channel networks that reduce the overall thermal resistance by optimizing the shape of the heat generating volume surrounding each individual elemental channel or construct. Once the optimal shape of each elemental volume is found, a network of these volumes can be "constructed" or assembled together. When this is done, the channels form tree-like branching networks that maintain the heat generating material between them at a uniform temperature. The second method was developed by Murray in 1926 [7] and is known as Murray's Law. Murray theorized that the geometric patterns of physiological circulatory systems could be derived by minimizing the amount of energy required for the distribution of blood volume necessary to maintain a given metabolic rate. When he minimized the total work involved in the circulation of blood in a section of artery, he found that there is a relationship between the radii of the parent vessels and those of the daughter vessels. The law states that for a system of tubes containing a Newtonian fluid in laminar flow, the minimum volume for a given pressure drop occurs when the radii of the tubes at a branch point satisfies the relationship:

$$r_0^3 = r_1^3 + r_2^3 + r_3^3 + \cdots + r_n^3 \tag{1}$$

where r_0 is the radius of the incoming tube, and r_1, r_2, etc., are the radii of the outgoing tubes. The law was verified [8] through the measurement of a number of biological circulatory systems that link large arteries and veins via smaller vessels and ultimately

Contributed by the Heat Transfer Division of ASME for publication in the JOURNAL OF HEAT TRANSFER. Manuscript received April 27, 2004; final manuscript received March 6, 2006. Review conducted by Y. Jularia.

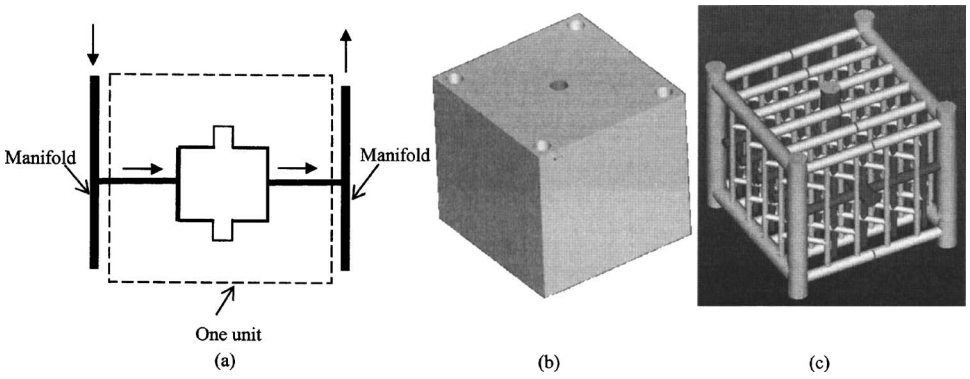

Fig. 1 A 3-D microconstructal flow system: (*a*) Schematic of four-level construction of one path in a unit connected to the manifold: (*b*) the outer view of the unit with one inlet port and four outlet ports; and (*c*) inner channel network (solid rendering where the dark ones are similar to the artery and the light ones are to the vein)

linked by capillary beds, a slight deviation within zoological systems from the law was also reported.

One of the challenges of applying the previous methods is that the designs have to conform to limits imposed by fabrication technologies. In this paper, we first present a scalable microheat sink design that is compatible with the EFAB micromanufacturing method [9]. A scaled-up model was tested to demonstrate the performance characteristics predicted analytically, and to illustrate the ultrahigh performance potential of such a design. Two types of heat transfer fluids are considered: one is a single phase fluid such as water and the other is a fluid containing nanosize phase change materials (NPCM). The NPCM flow mixture can be used to further enhance the heat transfer performance and reduce the flow resistance of constructal channel networks.

A slight variation of the scalable design is then presented that is compatible with a method developed at Florida International University using tape casting and co-fired technology. The method, the techniques developed to design the heat sink, and a CFD analysis of the proposed design are discussed. A scaled prototype is then experimentally tested to verify the performance against the prediction.

2 General Design Methodology

The design of the heat sink is described in two parts. The first is of a unit element design, and the second is the heat sink assembly that consists of an N number of elements. The unit element is constructed with a four-level branching system similar to [2], in which the internal connections follow a capillary structure resembling the connection between arteries and veins of cardiovascular systems. Murray's Law is followed at each branch level and the dimensions of the unit element are scalable. This allows one to obtain a desired flow channel volume fraction for a specified thermal constraint by varying the inlet channel diameter. In this way the heat sink design is very flexible and can easily accommodate the designer's specific needs.

The schematic of the fluid flow path through the four-level unit element construction is illustrated in two dimensions in Fig. 1(*a*), and the exterior appearance of the unit heat sink without the manifold is shown in Fig. 1(*b*). The complete channel structure in solid rendering is shown in Fig. 1(*c*). A demonstration of the performance analysis is presented in the following section for a heat sink with an overall size of 10 by 10 by 1 mm and consisting of 100 unit elements, each having the dimensions: 1 by 1 by 1 mm cube. The geometrical constraint of the cubic shape and the complexity of the fabrication lead to some localized deviation of branching from Murray's Law. We also considered a number of alternative designs with six to eight-levels of channel system construction and found that the four-level configuration is more compatible with the available manufacturing technologies such as EFAB.

The complete heat sink is shown in Fig. 2, which consists of 100 units and an overall size of 10 by 10 by 1 mm. Each element will have an independent flow path connected to a manifold, which has a traditional microchannel configuration.

2.1 Performance Analysis. To estimate the performance of the benchmark heat sink shown in Fig. 2, we formulate the following analysis.

Assumptions. The analysis is focused on the heat sink itself, excluding the manifold. The flow in the heat sink is incompressible and laminar. A steady state is imposed, and the fluid is Newtonian. When the encapsulated nanophase change particles (NPCM) are considered in the flow, it is assumed that the capsule material is neglected such that it does not participate in the mass and heat transfer balance, and the two-phase medium is homogeneous; therefore a constant liquid volume fraction is imposed. We also assume that phase change occurs locally in a thermodynamic equilibrium fashion such that the temperature difference within the particles is neglected. The entire network flow system is divided into an N number of segments with each segment corresponding to a constant length and diameter.

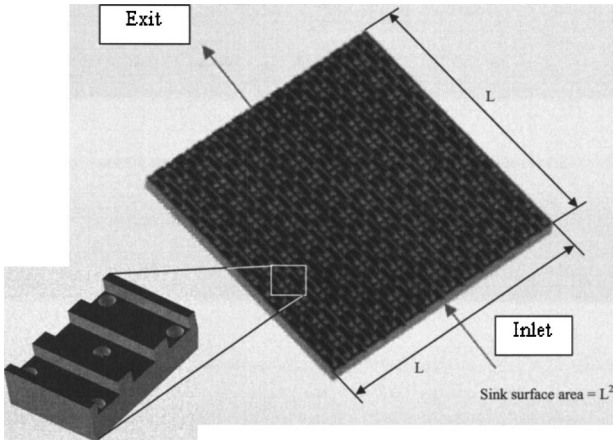

Fig. 2 Illustrating how multiple unit elements are connected in parallel by a manifold to cover the area requiring thermal management. The top layer of the manifold has been omitted so that the manifold channels, inlet, and exit holes are visible.

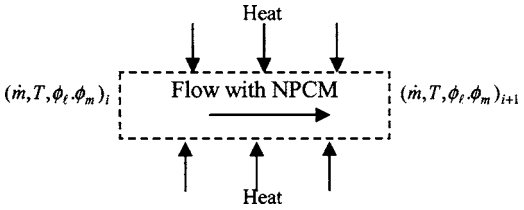

Fig. 3 Control volume for a piping segment where T_i represents the inlet temperature for the segment *i*

Computational Method. The modified Bernoulli equation yields the following:

$$\frac{p_i - p_{i+1}}{\rho g} = H_{L,i} \tag{2}$$

where i represents the ith segment of the piping and $h_{L,i}$ is the head loss found using the well-known Darcy friction factor for the major loss and loss factor for minor loss.

The energy equation yields the following:

$$q_i = \dot{m}_i c_p (T_{i+1} - T_i) \tag{3}$$

For the constant temperature wall boundary condition without NPCM, we have

$$\frac{T_{i+1} - T_w}{T_i - T_w} = \exp\left(-\frac{hPL}{\dot{m}_i c_p}\right)_i \tag{4}$$

For the constant heat flux boundary condition, the following equations is used to find T_{i+1} and T_w, respectively,

$$T_{i+1} = \frac{q''PL}{\dot{m}_i c_{pi}} + T_i, \quad T_{w,i+1} = \frac{q''}{h} + T_{i+1} \tag{5}$$

If NPCM is included, the following iterative computation is conducted (see also Fig. 3):

(a) Assume phase change occurs and calculate the melting mass fraction of solid in the capsule:

$$\phi_{m,i+1} = \frac{hPL(T_w - \overline{T_i})}{(1-\phi_{m,i})(1-\phi_l)\dot{m}_i h_{ls}} \tag{6}$$

(where $\overline{T_i}$ is the average fluid temperature of the segment$=((T_{i+1}+T_i)/2)$) and assign $T_{i+1}=T_i$. We also have

$$\phi_{m,i} = \phi_{m,k} + \phi_{m,k+1}(1-\phi_{m,k}) \tag{7}$$

where the subscript k denotes the index of the upstream segment whose outlet connects to the inlet of the present segment i.

(b) If $\phi_{m,i+1} \geqslant 1$ (the $>$ sign has no physical meaning), it indicates that the latent heat carried by NPCM is not sufficient to balance the heat transferred from the wall in the segment i; therefore, the outlet temperature T_{i+1} is adjusted according to Eq. (7),

$$T_{i+1} = \frac{q_i'' PL - (1-\phi_{m,i-1})(1-\phi_l)\dot{m}_i h_{ls}}{\phi_l \dot{m} c_p} + T_i \tag{8}$$

(c) If $\phi_{m,i} \geqslant 1$, there is no phase change taking place in the ith segment; Eq. (5) will be used.

(d) Since q_i'' depends on T_{i+1} for the constant temperature boundary condition, the iterative computation is carried until the converged results are obtained.

(e) The total heat transfer rate for the heat sink (the constant wall temperature condition) is calculated by summarizing the individual segment as follows:

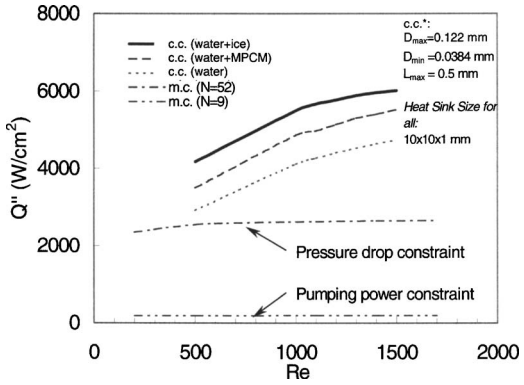

Fig. 4 A comparison of cooling capacity between a micro constructal heat sink and a 2-D microchannel: the benchmark condition: T_w=120°C; $T_{c,in}$=6°C, heat sink size=10×10×1 mm. Note: m.c.—2-D microchannel; c.c.—constructal channels.

$$q = \sum [\phi_l \dot{m}_i c_p (T_{i+1} - T_i) + (1-\phi_{m,i-1})(1-\phi_l)\phi_{m,i}\dot{m}_i h_{ls}] \tag{9}$$

The deviation between the total heat transfer calculated from Eq. (8), i.e., the segmented local energy balance, and the result obtained from the global energy balance is within 2.5%.

Due to the lack of experimental data for the heat transfer coefficient of NPCM suspension flow in a microchannel, we conduct a numerical study [10] for NPCM suspension flow in a L/D=100 microchannel for a range of Reynolds numbers and slurry concentrations comparable to those in this study. The conclusion is that if within the flow channel the two-phase flow is undergoing a melting process, the resulting heat transfer coefficient is higher than that of single-phase flow under the same thermal and flow boundary conditions. The heat transfer coefficient would be lower than that of single phase if the slurry flow does not experience a phase change. To simplify the previous analysis, we assume in this paper that the heat transfer coefficient of the slurry flow has the same functional dependency on Reynolds and Prandtl numbers as the single-phase flow.

2.2 Results. The computational results indicate that the heat sink has an overall thermal resistance about 0.02°C/(W/cm^2), which is defined as the maximum temperature difference across the heat sink divided by the total heat transfer rate by fluid and multiplied by the flat surface area of the sink (see Fig. 2). Under the constraint of $T_{s,max}$=120°C, the heat sink can transfer about 4000 W/cm^2 using pure water, or 6800 W/cm^2 if the fluid contains 50% nanophase change ice particles (Fig. 4). For this case, the Reynolds number based on the maximum tube diameter (=122 μm for both inlet and outlet diameters) is 1500, which results in a pressure drop of about 250 kPa and pumping power of about 0.051 W.

Micronetworking Piping versus Parallel Microchannels. Assuming flow is laminar and incompressible, we apply the classic energy balance principles to find out both temperature distribution and pressure drop in the network piping systems. The entrance flow model is used for estimate the local heat transfer coefficient for the first segment of the flow path. A fully developed flow model is used for the remaining segments of the flow path. This is a very conservative way of estimating the overall cooling performance of the heat sink. A separate numerical analysis [10] reveals that all the piping segments are under the developing thermal condition, which would lead to at least another 80–90% increase in the total cooling capacity. Even though we temporarily neglect the thermal resistance of the heat sink material, which may result in a 50–60% reduction in cooling capacity, we should be able to

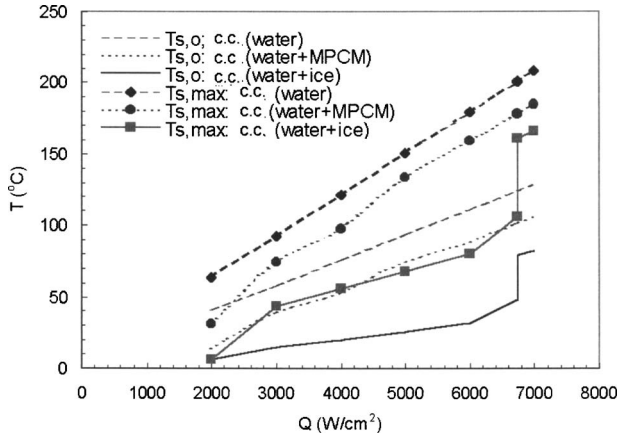

Fig. 5 Outlet surface temperature and maximum tube surface temperature as a function of heat flux: Constant heat flux boundary condition: $T_{c,in}=6°C$, and constructal heat sink size $=10\times10\times1$ mm

obtain a reasonable confidence level from the analysis. Both constant wall temperature and constant wall heat flux boundary conditions are applied during the analysis. For comparison, we also analyze a microchannel heat sink of the same overall size with the number of channels as the variable. The analysis is conducted for both water, water with micro encapsulated phase change material (octadecane), and water with encapsulated ice particles. Another conservative approach we adopted for the analysis with phase change particles assumes the same Nusselt number as the single phase (Nu=3.66(T_w=const) or 4.63(q''=const)). Although it lacks the specific correlations for the conditions we are studying, it has been shown that flow with suspended PCM tends to increase the local Nusselt number under laminar flow conditions (two to four times higher) [11,12].

The typical results are shown in Figs. 4 and 5. For the same Reynolds number, Re, we can compare the proposed heat sink with the microchannel heat sink in two ways: first, by specifying that both heat sinks must maintain the same pressure drop and, second, by specifying that both maintain the same pumping power (the pressure drop times the flow rate). Under the constant wall temperature boundary condition and a Re=1500, the proposed heat sink transfers about 6000 W/cm^2 with much less flow rate (water/ice mixture) compared to the possible 2600 W/cm^2 from the microchannel heat sink at the same pressure drop of 250 kPa (the number of channels N=52, and requiring 15 W pumping power). If we impose the constraint for the same pumping power (0.025 W with a flow rate of Q=899 ml/min, and Re=1500), the microchannel can only deliver 186 W/cm^2 (the number of channels must be N=9 to meet the constraint). The reason for such a big difference stems from the difference in geometry. Table 1 summarizes the main geometric differences between the proposed piping system and microchannels. They are the specific surface area, maximum diameter (or hydraulic diameter), thermal resistance, and void fraction. It should be noted that the proposed heat sink only has 20% in its void fraction. This means that with the proper selection of materials the new heat sink could be integrated with multiple microelectronic elements and circuit configurations.

Table 1 Geometric comparison of micro construal heat sink and microchannel (m.c.) heat sink

	Geometric comparison[a]		
	m.c.[b] (N=9)	m.c.[c] (N=52)	This study
D_{max}, mm	1.0000	0.1658	0.1220
A_s/V_f, 1/mm	2.0111	12.0851	49.0616
R_o, cm^2 K/W	1.5200	0.1060	0.0208
ϕ	0.7426	0.3878	0.2012

[a]All have the same heat sink size of $10\times10\times1$ mm.
[b]With approximately the same pumping power as this study.
[c]With approximately the same pressure drop as this study.

Single Phase versus PCM Slurry. Figures 4 and 5 also demonstrate the benefits of using nanoscale phase change materials (NPCM). It will reduce the maximum temperature significantly. Using encapsulated NPCM ensures the controllability and reliability of the phase change process unlike the boiling process. Although liquid and particle mixture (slurry) will increase the effective viscosity, it has a minor effect on the total pressure drop as long as the diameter to particle ratio is maintained at a reasonably large value. This is because slurry flow tends to create a particle-free boundary layer near the wall [10].

2.3 Experimental Validation. A scaled-up prototype for one unit element is tested. The overall size of the unit, made of aluminum, is 75 by 75 by 75 mm. The channels are machined in ten aluminum plates and assembled together to form a complete unit element. Figure 6 shows the photos of the typical layered patterns that are combined to form the scaled-up model assembly. *T*-type thermocouples with an accuracy of 0.5°C are mounted at the inlet and exit locations of the internal flow. The pressure difference between the flow inlet and exit is measured using a U-tube manometer that has an uncertainty of 10%. The prototype is immersed in a thermal bath and is tested under two controlled ambient temperature conditions simulating a constant temperature boundary condition. Results for the overall heat transfer rate and pressure drop are presented in Fig. 7 as a function of the Reynolds number. As expected the analytical prediction results under predict the heat transfer rate (Fig. 7(*a*)), which demonstrates that the proposed design indeed delivers a very promising, high cooling capability. The pressure drop data comparison reveals that reasonable agreement exists for the low and high Reynolds number range (Fig. 7(*b*)). The predicted value is significantly lower than the measured value for the Reynolds numbers between 800 and 1400. This may be partly due to the influence of developing flow experienced within the heat sink.

3 Design Based on Tape-Casting and Cofiring Fabrication Method

To further validate the performance of the proposed heat sink, another design is created that is similar to that presented in Sec. 2, except that the material and the minimum feature sizes of the tape-casting and cofiring fabrication method are used as constraints in the design process. The design of the unit element is broken down into three main steps. The initial step uses the constructal method to optimize the geometry of the smallest feature; i.e., the elemental volume [6]. For this design the elemental volume has a fixed width and length, (W_0 and L_0) that has been fixed by constraints in the manufacturing technique to be 254 and 398 μm, respectively (Fig. 8). The last dimension (H_0) is left as a degree of freedom and is used to determine the optimal amount of material that can be placed around the channel so that all the heat conducted by the material is swept away by the fluid stream. The optimization performed by [6] on the elemental area $A_0=H_0\times L_0$ found that the optimal external shape of the elemental volume is directly proportional to the dimensionless flow rate:

$$\left(\frac{H_0}{L_0}\right)_{opt}=\left(\frac{4}{M}\right)^{2/3} \tag{10}$$

where

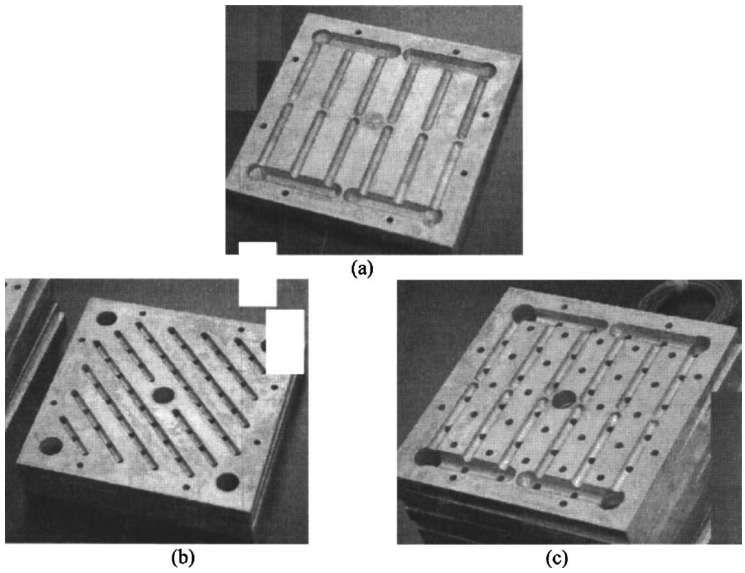

Fig. 6 Scaled-up unit-model prototype: (*a*)–(*c*) channel features of three inner layers

$$M = \frac{\dot{m}_0'' \cdot Cp \cdot A_0^{1/2}}{k} \tag{11}$$

and the mass flow rate per unit area of the elemental volume is determined by

$$\dot{m}_0'' = \frac{\dot{m}_0}{W_0 \cdot H_0} \tag{12}$$

These equations can be used to determine the optimal shape of the elemental volume with the restrictions that $M > 4$ and $(H_0/L_0)_{opt} < 1$ [6]. Also, the flow of coolant through the elemental volume is assumed to be laminar and fully developed. A schematic of the elemental volume is shown in Fig. 8.

The dimension of the fluid channel that penetrates the elemental volume is chosen by Murray's Law. Each of these elemental fluid channels is fed by a channel perpendicular to the elemental fluid channel, named the first construct [6]. In the second step, the length of this first construct is determined by the number of elemental volumes that are used. To keep the overall shape of the final unit element compact only three elemental volumes are used in this design. This makes the length of the first construct equal to $L_1 = 3H_{0\ opt}$. The elemental volumes and their corresponding first constructs are arranged in such a way that a rectangular layer is created, as shown in Fig. 9(*a*). The final step in the design of the unit element is to determine the dimensions of the inlet, exit, first construct and elemental volume channels. This can be done by either fixing the minimum channel size that can be created or by fixing the diameter of the vertical inlet hole. For the design considered in this paper, the vertical inlet hole is constrained by the minimum diameter vertical channel that could be created by the manufacturing technique. In our case this is 152 μm. Murray's Law [7] in the form of equation (1) is used to determine the dimensions of the remaining channels. This law is used to ensure that the pumping power required by each unit element is minimized.

Following the method discussed in Sec. 2, a number of unit elements sufficient to cover the area of heat removal are connected in parallel by a manifold, as shown in Fig. 2. When the flow rate, or Reynolds number for the fluid is chosen and the low thermal conductivity material that the channel structure is removing heat from is known, the design should ensure that increasing the flow rate above the specified amount does not significantly increase the heat sink performance.

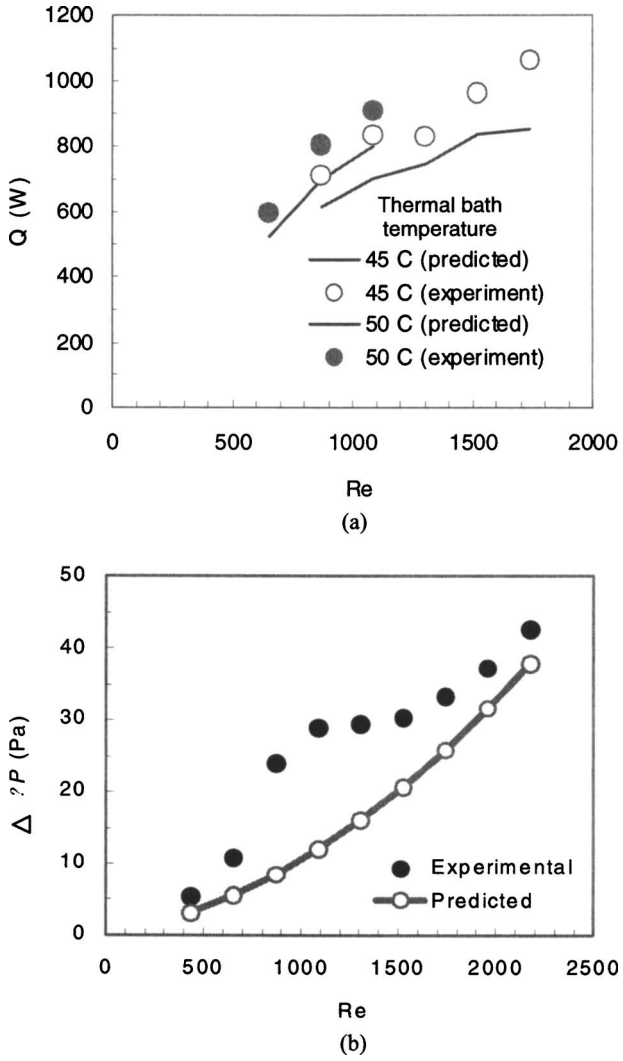

Fig. 7 Measurement results for the scaled-up unit prototype under two controlled ambient temperatures (Fluid: water, single phase): (*a*) Heat transfer rate compared with the prediction. (*b*) Pressure drop comparison.

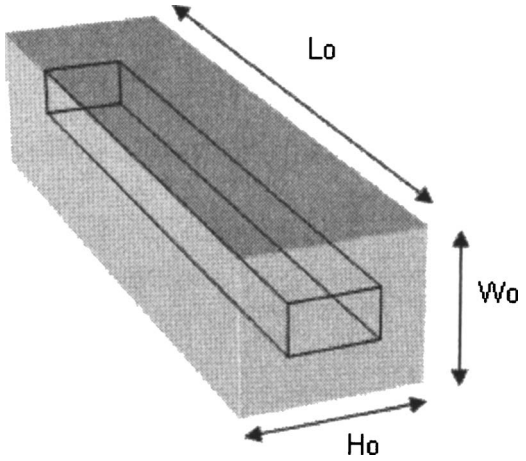

Fig. 8 Schematic of the elemental volume with the critical dimensions (H_0=202 μm and the hydraulic diameter=152 μm). The channel of fluid is shown as the outline through the center of the elemental volume.

3.1 Manufacturing Method. The development of microscale 3-D structures is a critical step in the realization of the proposed heat sink. The complex channel network and three-dimensional nature of the design creates some significant manufacturing challenges. A technique being developed at Florida International University uses machined Kapton® inserts embedded into thick film tapes that when cofired form enclosed channels within the final substrate. This method works for both a thick film low temperature cofired ceramic (LTCC), which is used as a substrate material for microelectronic packages, or thick film silver tapes, which can be used as a standalone substrate or cofired with LTCC as a heat spreader. Embedding channels within these materials allows for the capability of heat sinks that are integrated within the substrates. This eliminates, or reduces, contact resistances and provides the capability of relocating coolant hook up points away from areas that contain critical electronic components.

Thick film tape casting has been an established technique used for the fabrication of ceramic substrates for multilayer ceramic packages. The tape casting process begins with a slurry that is created by mixing together fine particles, a solvent, a dispersant, binders, and a plasticizer. This slurry is then cast into thin sheets with typical thicknesses in the range of 25 to 500 μm. The tape is then dried, cut to shape, stacked, and fired to the sintering temperature of the particles to form a solid structure. Thick film silver tape was originally developed to be cofired with ceramic tape for the purpose of decreasing the overall thermal resistance of the substrate and aiding in the spread of heat generated from embedded electronics. The silver was placed in thermal contact with the heat generating region through the use of thermal vias [13].

The fabrication technique used to fabricate the channel networks consists of embedding machined Kapton® inserts in between layers of the LTCC or silver tape prior to firing. During the firing process, the Kapton® breaks down and leaves a gap in the finished substrate. The shape of the gap is controlled by the shape of the Kapton® and forms complex microscale channel structures embedded in the solid substrate. An illustration of this is demonstrated in Fig. 10.

3.2 CFD Analysis for Single Phase Flow and Heat Transfer. To analyze the thermal and pressure drop performance of the heat sink, a three-dimensional CFD numerical model was used. For this analysis, the heat transfer fluid is liquid water. The analysis of the heat sink was broken into two parts. In the first part the design method described in Sec. 3, was implemented to create a unit element design that is optimized for use within a LTCC substrate and having a coolant inlet Reynolds number of 500. This

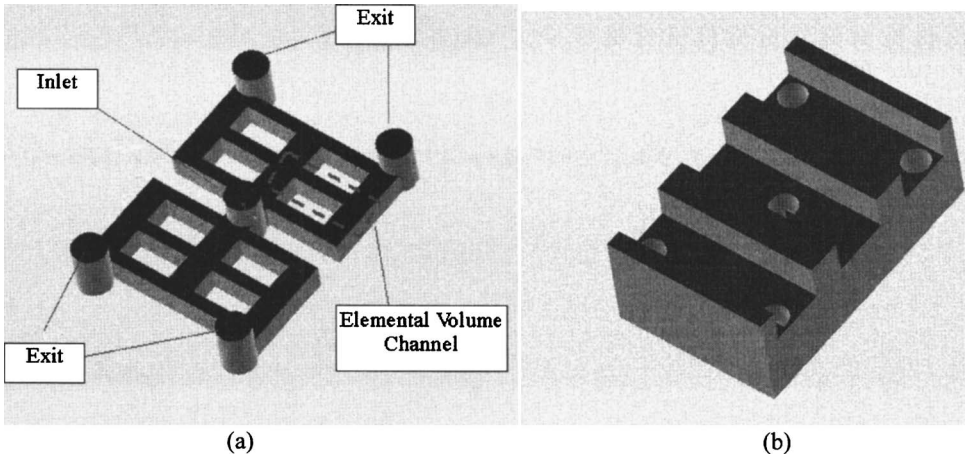

Fig. 9 (*a*) One layer of the heat sink channel structure that contains a total of 12 elemental volumes connected together by two first constructs, and (*b*) the solid unit element of the heat sink with the channel structure shown in (*a*) and the manifold on top. The top layer of the manifold has been omitted so that the manifold channels, inlet, and exit holes are visible.

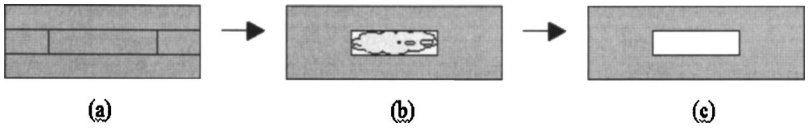

Fig. 10 Schematic of the process of firing tape with kapton inserts to form embedded channels: (*a*) the layered structure during the stacking and lamination of the tape/kapton substrate; (*b*) the vaporization of the insert material during the firing and sintering stage; and (*c*) the finished substrate with an embedded channel structure

Table 2 Properties assigned to substrate and coolant elements

Substrate	Thermal conductivity W/(m K)	Cp J/(kg K)	ρ kg/m^3
LTCC	3	989	3100
Silver	429	235	10,500
Coolant			
Water	0.6	4182	998

one layer unit element was analyzed in the CFD model. The element has an inlet channel hydraulic diameter of 152 μm that branches off to feed two first constructs that in turn distribute coolant to the elemental volumes. Using Eqs. (10)–(12) for a coolant inlet Reynolds number of 500 and thermal conductivity of LTCC (3 W/m K), the value for H_0 is approximately 202 μm. This translates to a unit element with a length of 1.4 mm a width of 1 mm and a thickness of 398 μm, shown in Fig. 9. In the second part, the channel network dimensions were maintained but the material properties were changed to that of silver.

The 3-D composite solid fluid model was created and a tetrahedral grid was generated using GAMBIT 2.0. The model was analyzed using the Fluent 6.0 CFD software. Multiple grid models were analyzed, each with different mesh interval sizes. For this particular model, a grid independent solution was obtained with an average volume mesh interval size of 0.15. This value generated a model with 551320 substrate elements, and 135516 coolant elements. Water was assumed to be the coolant and the properties of the solid block were those of LTCC for the first case and later those of silver. These properties are presented in Table 2.

The two independent cases of the design for LTCC and silver were performed using the above model. The first case focused on the LTCC model and the results were analyzed to study two main areas. The first area focused on determining if the 2-D design optimization procedure was successful in predicting that the point where both pressure drop and thermal resistance are at a minimum within the heat sink would occur when the coolant inlet Reynolds number has a value of 500. The second analysis focused on determining the overall performance of the LTCC heat sink. LTCC is a highly insulating material with an extremely low thermal conductivity, as can be seen in Table 2. Current electronic packaging with LTCC substrates make use of thermal vias, columns of high conductivity material, to spread the heat created by the electronics embedded within the LTCC to areas where the heat can be removed by a heat sink or other means. Embedding the microheat sink within the LTCC substrate would allow the heat sink to be in close proximity to the embedded electronic components and create a more efficient compact heat spreading/removal technique.

The second part of the analysis focused on the performance enhancement due to the use of thick film silver tapes in place of LTCC as the heat sink material. For this case the properties of the substrate were changed from those of LTCC to those of silver.

3.3 Results for Tape Casting and Cofiring Constructal Heat Sinks. The Fluent 6.0 coupled solver was used in each case. The program solves the governing equations of continuity, momentum, and energy simultaneously and uses an implicit scheme to linearize the nonlinear governing equations and produce a system of equations for the dependent variables in every computational cell. The resultant linear system is then solved to yield an updated flow-field solution. The results are considered to be converged once the scaled residual values given by the Fluent software for velocity are less than 10^{-3}% and when the energy residual is less than 0.1%.

The inlet fluid temperature was assumed to be 11°C and a constant heat flux of 100 W/cm^2 was imposed on the bottom surface to simulate the heat input from the chip. The velocity of the coolant at the inlet was varied to create a variation in the Reynolds number. For all of the analysis, the thermal resistance of the heat sink was determined by Eq. (13).

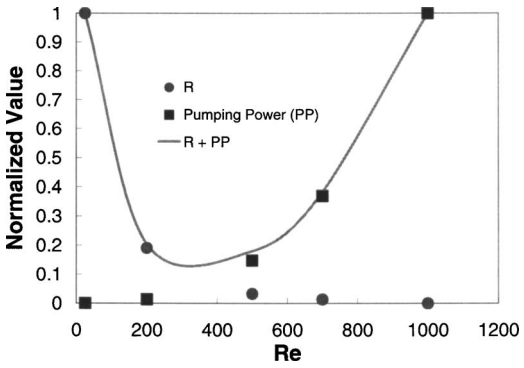

Fig. 11 Thermal resistance (*R*) and pressure drop values (implied in the pumping power PP) normalized by Eq. (14) for the LTCC heat sink. The minimum pressure drop and thermal resistance occurs between Re=300–400.

$$R = \frac{T_{surf} - T_{in}}{q''} \tag{13}$$

For the analysis of the LTCC heat sink the inlet temperature of the fluid was maintained at 11°C and the coolant inlet velocity was varied to produce inlet Reynolds numbers ranging from 25 to 1000. To determine the point where the minimum pressure drop and the minimum thermal resistance of the heat sink would occur the values obtained for pressure drop and thermal resistance obtained by the CFD model were normalized to produce values between 0 and 1:

$$\text{Value}_{norm} = \frac{\text{Value} - \text{Value}_{\min}}{\text{Value}_{\max} - \text{Value}_{\min}} \tag{14}$$

The results of this analysis can be seen in Fig. 11. The results show that a minimum occurs where the gain in thermal resistance at the cost of increased pumping power is optimum. Although the calculated optimum operating coolant inlet Reynolds number value by the CFD analysis is less than 500 (in the range of 300–400), the results show that the optimization method for the heat sink elemental volume by the constructal theory (Eqs. (10)–(13)) was successful in designing the heat sink to operate optimally at a specified Reynolds number. The difference between the constructal theory result and CFD result is believed to be the result of only considering a 2-D elemental volume in the design (i.e., the cross section of the channel) and not taking into account the three-dimensional nature of the heat transfer problem simulated by the CFD analysis. In general, the design method presented in this paper could be easily extended to any Reynolds number and material constraint to generate different elemental volume geometries.

Another goal of the optimization was to determine whether or not the heat sink would maintain a uniform temperature when exposed to the constant surface of heat input. The ability to maintain a uniform surface temperature over the entire unit element surface of the heat sink ensures that when the larger area is covered by multiple unit elements a uniform temperature throughout the chip surface can be maintained. Figure 12 shows that the temperature is reasonably uniform for a heat flux of 100 W/cm^2 at the specified cross section. From the results shown in Fig. 13, it can be seen that for Re$>$200, the temperature variation on the bottom surface is approximately ±20 K. Furthermore, Figs. 12 and 13 also show that increasing the Reynolds number above the optimized value of Re=500 has little to no effect on the surface temperature. This is a further proof that the designed Reynolds

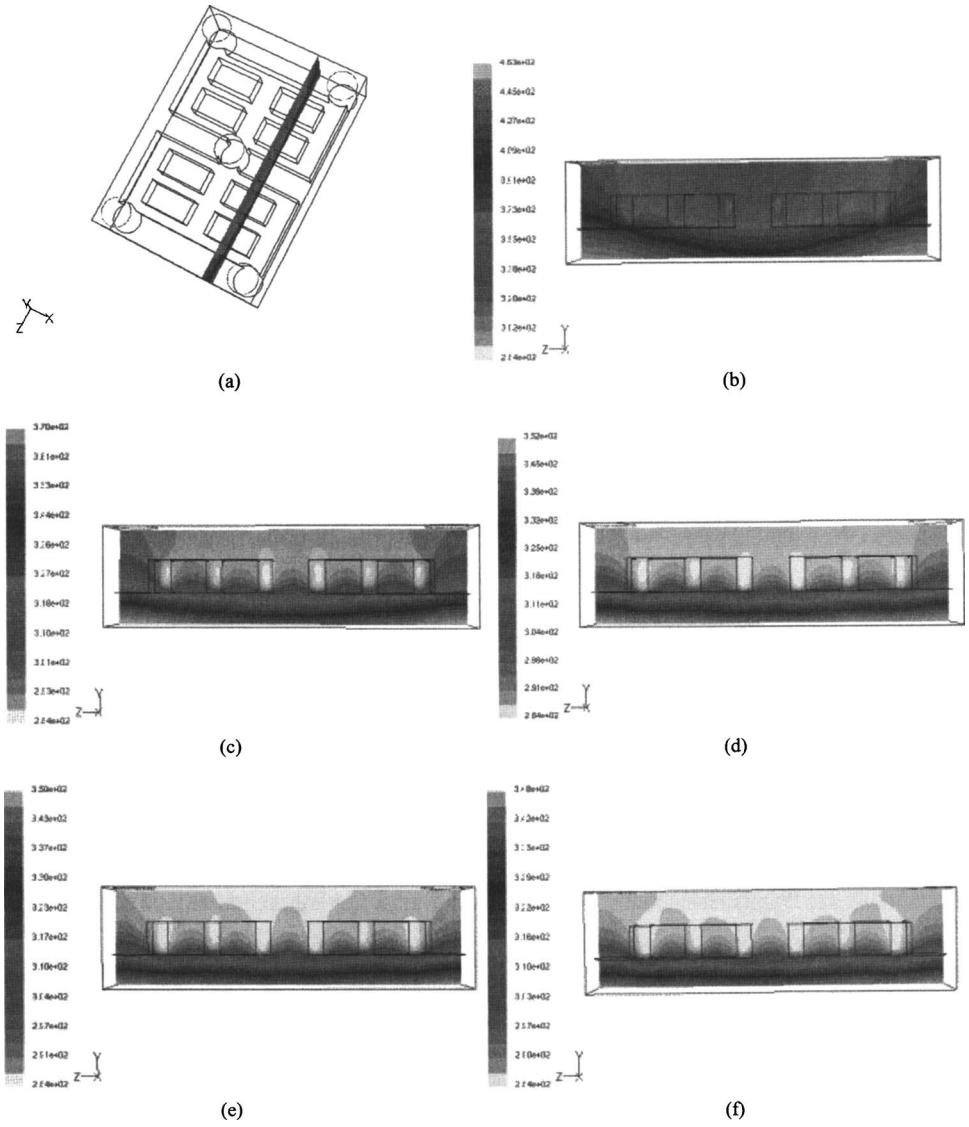

Fig. 12 Temperature contours at the cross section in (*a*) of one unit element of the LTCC heat sink in degrees Kelvin at (*b*) Re=25, (*c*) Re=200 (*d*) Re=500, (*e*) Re=700, and (*f*) Re=1000

number of 500 is optimal and any attempt to decrease temperature by increasing pumping power (or flow rate) is not justified for this channel network configuration.

Given a heat flux of 100 W/cm^2 and a coolant inlet temperature of 11°C, the heat sink is able to maintain an average surface temperature of 74°C. This corresponds to the minimum thermal resistance of one unit element of the LTCC heat sink being 0.63°C cm^2/W. This thermal resistance was achieved at a flow rate of 0.0072 L/min and a pressure drop of only 28.4 kPa. The coolant to average surface temperature difference for this heat sink was only 63°C, using a material with a thermal conductivity of 3 W/m K. This means that under the same heat flux conditions if the inlet fluid temperature was raised to ambient temperature, approximately 25°C, the average surface temperature of the embedded electronic component could be maintained at 88°C while maintaining a pressure drop of 28.4 kPa. The heat sink design would allow the electronic component to be completely embedded within the substrate and still maintain a safe operating temperature. At the designed coolant inlet Reynolds number of 500, the heat sink still has a thermal resistance of 0.67°C cm^2/W with a pressure drop of only 8.38 kPa and a flow rate of 0.0036 L/min. The variation of thermal resistance with the flow rate is shown in Fig. 14. The figure also shows the system curve for the proposed network. Pumping curves can be superimposed on this figure to determine the thermal resistance that one element can obtain at the operating point of the system.

The ability of thick film silver tape to be cofired with LTCC makes the tape a higher performance alternative for the heat sink material. To study this performance increase the substrate properties of the CFD model were changed to those of silver and cases were run similar to those for LTCC substrate cases. The performance enhancement can be seen from Fig. 15. For the same heat flux of 100 W/cm^2 and the same coolant inlet temperature of 11°C, the silver tape heat sink can reduce the surface temperature to only 19.4°C with the same pressure drop and flow rate requirements as the LTCC heat sink operating at a Re=500. Therefore, using silver tape instead of LTCC as the heat sink material under the same operating conditions we can reduce the overall thermal resistance of the heat sink to only 0.084°C cm^2/W.

It should be pointed out that the prior discussion is based on the assumption of constant thermophysical properties of the fluid. It is assumed that no significant variation of the coolant properties is experienced within the stated temperature ranges.

The performance of the heat sink using silver tape is further

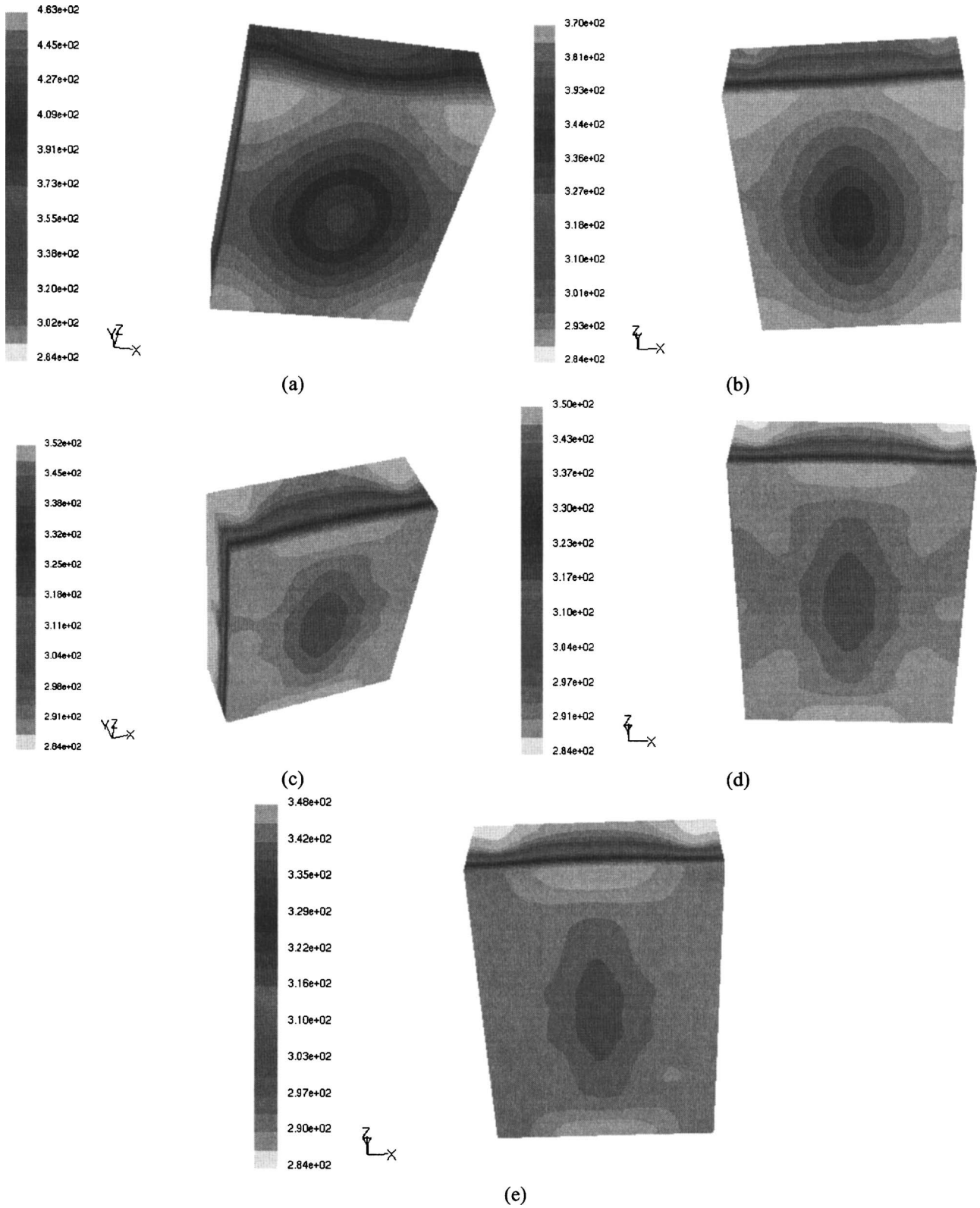

Fig. 13 Temperature contours at the bottom surface of one unit element of the LTCC heat sink in degrees Kelvin at (*a*) Re =25, (*b*) Re=200 (*c*) Re=500, (*d*) Re=700, and (*e*) Re=1000

evaluated by comparing the results with the performance of both porous metal heat sinks [14] and microchannel heat sinks [15] in Table 3. This comparison is based on the fact that both types of sinks have been reported to have high heat removal rates. Both the porous metal and silver tape heat sinks had an internal surface area of approximately 220 cm^2 and were exposed to a surface heat flux of 100 W/cm^2. For the silver tape heat sink this would correspond to approximately 154 elements connected in parallel similar to Fig. 2. It can be seen that the proposed heat sink has the lowest overall thermal resistance (more than 10% less than that of porous metal heat sink and conventional microchannel heat sink) and requires much less fluid pumping power (=flow rate × pres-

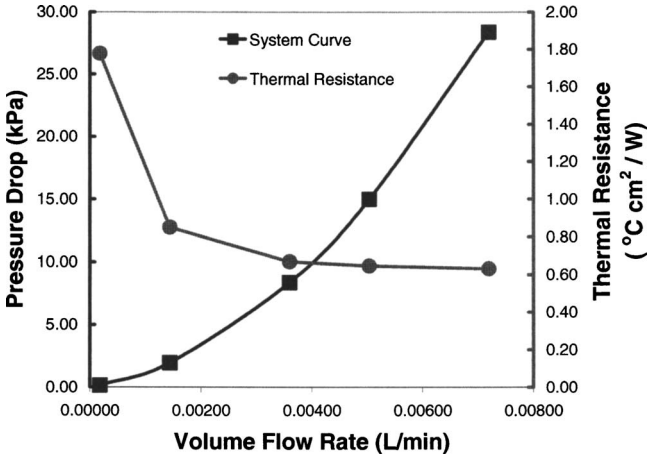

Fig. 14 The thermal resistance and pressure drop as a function of flow rate for the LTCC heat sink

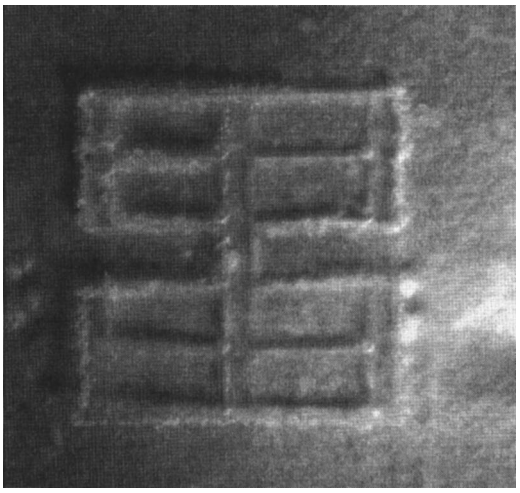

Fig. 16 Microscope picture showing the channel structure of one unit element stacked on a layer of silver magnified 100X

sure drop with one to two orders of magnitude less). The high heat removal to pumping power ratio shows the value of the proposed heat sink in compact high heat-flux cooling applications.

3.4 Experiments for a Silver Heat Sink. To test the performance of the heat sink, an experimental prototype was created. The fluid was feed to the heat sink inlet by an acrylic manifold that also served to direct the flow from the exit ports away from the test section. For pressure measurement, a pressure transducer was used at the inlet to the device. An electric heater was used as the heat source and was placed in direct contact with a copper slab, which acted as a heat spreader. A heat flux meter was placed between the spreader and the bottom surface of the heat sink to take measurements of the heat entering the test section. T-type thermocouples with an uncertainty of 0.5°C were used to record the inlet and exit temperatures of the coolant. A thermocouple was also used to record the bottom surface temperature of the heat sink. This thermocouple was placed between the heat flux meter and the bottom surface embedded in a layer of Omegatherm OT-201 thermal paste from Omega Engineering Inc. to try and reduce the contact resistance. Figure 16 shows a microscopic photo of the test piece channel structure, a one-layer silver heat sink.

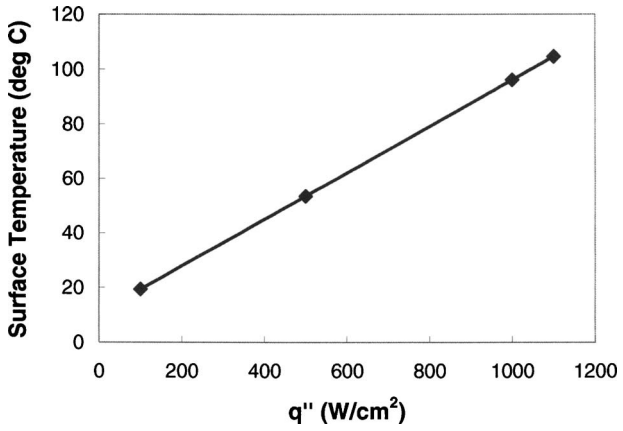

Fig. 15 Variation of the average bottom surface temperature with the heat flux into the surface of the silver tape heat sink: Re=500

The heat flux measurements obtained during the experiments were used as the uniform heat flux for the calculations. The average heat flux imposed on the bottom surface during the experiments was 0.8227 W/cm^2 or 8.227 W/m^2. For the calculation the effect of conduction through the 625 μm layer of silver tape was determined by using the calculated wall temperature and assuming that the thermal conductivity of the silver tape was equal to that of silver (k_s=429 W/(m K)) [16]. These results are compared to the experimental results graphically in Figs. 17 and 18. The figures show both the pressure drop and thermal resistance as a function of the flow rate. The results for thermal resistance were obtained by using Eq.(13).

It can be seen from Fig. 17 that the experimental values obtained for the pressure drop across the heat sink agree well with calculation. However, the experimental results for the thermal resistance are in poor agreement with the calculated results. This large difference in thermal resistance is due to the high surface temperatures measured during the experiments. The large difference between the measured surface temperatures and those calculated is believed to be caused by the difference between the assumed thermal conductivity of the silver tape and its actual value. This heat sink is, to the knowledge of the authors, the first device that has been created by the combination of these two materials and testing to determine the thermal properties of the device still needs to be done.

Table 3 Performance characteristics of different heat sinks

Performance: For a Heat flux of 100 W/cm^2	Pressure drop (kPa)	Volume flow rate (L/min)	Thermal resistance (°C cm^2/W)	Surface area to volume ratio (m^2/m^3)
Silver tape heat sink	8.379	0.554	0.084	6219.140
Porous metal heat sink	115.000	2.000	0.094	12,000.000
Microchannel heat sink	1029.000	4.956	0.100	34.560

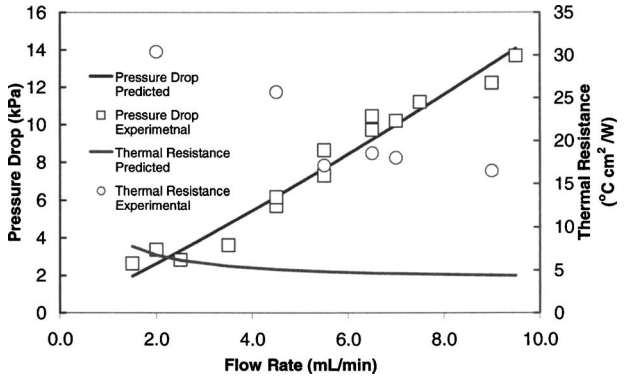

Fig. 17 Thermal resistance and pressure drop as a function of flow rate for the silver heat sink

During the manufacturing process, Kapton® is used as the sacrificial material, which is an amorphous polymer undergoing a second order transition at temperatures ranging from 360°C to 410°C. This transition is assumed to be the glass transition temperature by DuPont Inc. [17]. Because firing temperatures for the silver tape substrate reach over 700°C it was assumed that that complete breakdown of the Kapton® occurs during the firing process. This may not be the case. What may actually occur is that at these high temperatures the Kapton® may be absorbed into the walls of the silver forming an insulating coating decreasing the effective thermal conductivity of the resulting substrate. If we assume that the resulting substrate contains a series combination of Kapton® and silver, the effective thermal conductivity of this type of substrate can be estimated by finding the porosity of the resulting substrate. We find this using the volume of Kapton® in the channel and the volume of silver below the channel assuming the majority of the Kapton® is absorbed into the bottom of the channel and using the following equations

$$\varepsilon = \frac{V_k}{V_S + V_k} \tag{15}$$

$$\frac{1}{k_{eff}} = \frac{\varepsilon}{k_k} + \frac{(1-\varepsilon)}{k_s} \tag{16}$$

we can determine a theoretical value for the effective thermal conductivity of the substrate [16]. Finding that the thermal conductivity of Kapton® is 0.12 W/(m K) [17], and $\varepsilon = 0.1689$, then the effective thermal conductivity assuming a series arrangement is $k_{eff} = 0.7096$ W/(m K). If we then use this in our calculation as the conductivity of the substrate and recalculate the thermal resistance, we see from Fig. 18 that the calculated value is a much better representation of the experimental results. Further more if we take into account that there is a layer of Omegatherm OT-201 thermal paste $k_{tp} = 2.3$ W/(m K) [18] between the thermocouple measurement and the surface of the heat sink we obtain an almost exact representation for the higher flow rate experiments.

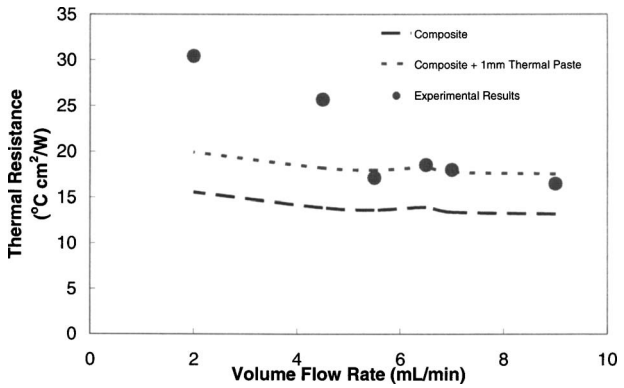

Fig. 18 Thermal resistance curves using the effective thermal conductivity assumption with series arrangement of Kapton® and silver

4 Conclusions

In this paper we presented the design, performance analysis, manufacturing, and experimental validation of two active microconvective heat sinks having geometry that provides high surface area to volume ratios while requiring minimal pumping power. These geometries are produced using the constructal method to minimize the point-to-point temperature difference within the heat sink and Murray's Law to minimize pressure drop across the device. The results of the performance analysis on the benchmark heat sink indicates an overall thermal resistance of $0.02°C/(W/cm^2)$. Under the constraint of $T_{s,max} = 120°C$, the heat sink can transfer about 4000 W/cm^2 using pure water, or 6800 W/cm^2 if the fluid contains 50% nanophase change ice particles. For this case, the Reynolds number based on the maximum tube diameter (=122 μm for both inlet and outlet diameters) is 1500, which results in a pressure drop of about 250 kPa and pumping power of about 0.051 W.

The results of the tape-cast heat sink showed that the minimum thermal resistance of one unit element of the LTCC heat sink being $0.63°C\,cm^2/W$ and was achieved at a flow rate of 0.0072 L/min and a pressure drop of only 28.4 kPa at an inlet Re of 1000. The results also show that at the designed value of Re =500 the LTCC heat sink has a thermal resistance of $0.67°C\,cm^2/W$ with a pressure drop of only 8.38 kPa and a flow rate of 0.0036 L/min. This performance can further be increased by the use of thick film silver tape to produce an overall thermal resistance of $0.084°C\,cm^2/W$.

Although the experimental validation of the performance analysis is limited to two slightly different scaled models, the results show that the superior high performance of the 3-D constructal heat sinks is valid within the constraints of the experiments: One model confirms the high thermal performance and the other confirms the low pumping power. Their potentials to achieve an even higher thermal performance (low thermal resistance) and efficient operation (low pumping power) are only limited by the manufacturability. Overall, the analysis in this paper proves that the 3-D constructal heat sinks have a superior performance over both porous metal and conventional microchannel heat sinks, and projects a promising potential for the full realization and development of a complete, advanced microcooling device.

Acknowledgment

Support from the FIU Foundation and NSF (Award No. 0206028) are acknowledged. The authors would also like to acknowledge their great appreciation for assistance received from Mario Sanchez of the Manufacturing Research Center, Dr. Kinzy Jones, Dr. Liu, Randy, and Jane of the Hybrid Microelectronics Laboratory at Florida International University during prototype manufacturing.

Nomenclature

A_0 = elemental area (m^2)
c_p = specific heat at constant pressure (J/(kg K))
D = tube hydraulic diameter (μm)
H_0 = elemental volume height (μm)
h = heat transfer coefficient $W/m^2\,K$
H_L = head loss, m
h_{ls} = heat of fusion, J/kg
K = number of unit elements
k = thermal conductivity (W/(m K))

L_o = elemental volume length (μm)
$\dot{m}$ = mass flow rate (kg/s)
$\dot{m}'$ = mass flow rate per unit length (kg/s m)
$\dot{m}''$ = mass flow rate per unit area (kg/sm^2)
M = dimensionless mass flow rate, defined in Eq. (11)
P = perimeter, m
p = pressure (Pa)
q'' = heat flux (W/cm^2)
q = heat transferred (W)
R = thermal resistance (°C cm^2/W)
Re = Reynolds number, $\rho VD/\mu$
r = radius (m)
T = temperature (K)
V = velocity (m/s)
W_0 = elemental volume width (μm)

Greek Symbols

μ = viscosity (Pa s)
ρ = density (kg/m^3)
ϕ_m = mass fraction of melting
ϕ_l = mass fraction of liquid

Subscripts

0 = parent branch
1, 2, 3 = daughter branch number
i = ith segment of the piping system
in = inlet
k = upstream pipe segment
l = liquid
m = melting
min = minimum
max = maximum
n = number of branches (−)
norm = normalized
opt = optimum
s = solid
surf = surface
w = wall

Other

– = (overbar) average

References

[1] Ortega, A., 2002, "What are the Heat Flux Limits of Air Cooling?" *2002 International Mechanical Congress and Exposition, Panel: Challenges in Cooling High Heat Flux Electronics Systems*, New Orleans, LA, November 17–22.
[2] Drexler, E. K., 1992, *Nanosystems, Molecular Machinery, Manufacturing and Computation*, Wiley, New York, Chap. 11.
[3] Frank, M. P., and Knight, F. T., Jr., 1998, "Ultimate Theoretical Models of Nanocomputers," Nanotechnology, **9**, pp. 162–176.
[4] Tuckerman, D. B., and Pease, R. F. W., 1981, "High-Performance Heat Sinking for VLSI," IEEE Electron Device Lett., **EDL-2**, pp. 126–129.
[5] Singhal, V., Liu, D., and Garimella, S. V., 2003, "Analysis of Pumping Requirements for Microchannel Cooling Systems," *Proc. of IPACK03 the ASME International Electronic Packaging Technical Conference and Exhibition*, July 6–11, Maui, Hawaii.
[6] Bejan, A., and Errera, M. R., 2000, "Convective Trees of Fluid Channels for Volumetric Cooling," Int. J. Heat Mass Transfer, **43**, pp. 3105–3118.
[7] Murray, C. D., 1926, "The Physiological Principle of Minimum Work I. The Vascular System and the Cost of Blood Volume," Proc. Natl. Acad. Sci. U.S.A., **12**, pp. 207–214.
[8] LaBarbera, M., 1990, "Principles of Design of Fluid Transport Systems in Zoology," Science, **249**, pp. 992–1000.
[9] Cohen, A. L., 2002, "Electrochemical Fabrication (EFAB™)," in *The MEMS Handbook*, M. G.ad-el-Hak, ed., CRC Press, Boca Raton, FL, Chap. 19.
[10] Hao, Y., and Tao, Y.-X., 2004, "A Numerical Model for Phase Change Suspension Flow in Microchannels," Numer. Heat Transfer, Part A, **46**, pp. 55–77.
[11] Yamagishi, Y., Takeuchi, H., Pyatenko, A. T., and Kayukama, N., 1999, "Characteristics of Microencapsulated PCM Slurry as a Heat-Transfer Fluid," AIChE J., **45**, pp. 696–797.
[12] Charunyakorn, P., Sengupta, S., and Roy, S. K., 1991, "Forced Convection Heat Transfer in Microencapsulated Phase Change Material Slurries: Flow in Circular Flow," Int. J. Heat Mass Transfer, **34**, pp. 819–833.
[13] Wang, P., 2002, "Tape Casting of Thick Silver Film and Co-Firing Behaviors With Low Temperature Co-Fired Ceramic Substrate," Masters thesis, Department of Mechanical Engineering, Florida International University, Miami, Florida.
[14] North, M. T., and Cho, W., 2003, "High Heat Flux Liquid-Cooled Porous Metal Heat Sink," *Proc. of IPACK03, The ASME International Electronic Packaging Technical Conference and Exhibition*, July 6–11, Maui, Hawaii.
[15] Lee, P. S., Ho, J. C., and Xue, H., 2002, "Experimental Study on Laminar Heat Transfer in Microchannel Heat Sink," *IEEE Inter Society Conference on Thermal and Thermalmechanical Phenomena in Electronic Systems ITHERM 2002*, May 30–June 1, pp. 379–386.
[16] Kaviany, M., 2002, *Principles of Heat Transfer in Porous Media*, Wiley, New York.
[17] www.dupont.com/kapton
[18] www.omega.com

High Pressure Spray Cooling of a Moving Surface

G. G. Nasr
Head of Spray Research Group (SRG),
Institute of Materials Research (IMR),
School of Computing, Science and Engineering,
University of Salford,
Manchester M5 4WT, UK
e-mail: g.g.nasr@salford.ac.uk

R. A. Sharief

A. J. Yule

Department of Mechanical,
Aerospace and Manufacturing Engineering,
UMIST,
P.O. Box 88,
Manchester M60 1QD, UK

A novel technique is described for investigating spray cooling of moving hot surfaces. An experimental investigation is described for vertically downwards water sprays impinging on a horizontal steel annulus of 250 mm *diameter with a surface temperature up to* 600 °C, *and rotating at up to* 120 rpm, *giving a tangential velocity of* 1.35 ms^{-1}. *The central homogeneous zones of sprays from full-cone atomizers are used at pressures up to* 2.07 MPa *and the ranges of impacting spray parameters are* 0.98 to 12.5 $kg\,m^{-2}\,s^{-1}$ *for mass flux,* 49–230 μm *for volume median drop diameter, and* 9.8–32.3 ms^{-1} *for impinging velocity (Yule, A. J., Sharief, R. A., and Nasr, G. G., 2000, "The Performance Characteristics of Solid Cone Spray Pressure Swirl Atomizers," Ann. Tokyo Astron. Obs.,* ***10****(6), pp. 627–646). Time histories of the steel temperature, at positions within the annulus, are presented and analyzed to deduce the transient cooling as the instrumented section of the annulus was swept repeatedly under the spray. Discussion is provided on the physical processes occurring on the basis of the observations. Correlation equations derived to find relationships of surface heat flux with the spray and surface parameters provide further insight into these processes. The results confirm results for static surfaces, that droplet size is a relatively weak parameter, while droplet momentum flux and surface velocity are important. As the surface velocity is increased, peak heat transfer rate at the surface reduces, and its position moves downstream with respect to the spray centerline.* [DOI: 10.1115/1.2217747]

Keywords: heat transfer, cooling, film cooling, high temperature, droplet, sprays and atomization

1 Introduction

Sprays are used to cool hot objects in many industrial processes because of their convenience of use and high heat dissipating ability. For example, one of the major secondary processes carried out in the metallurgical industries is that of cooling for products and other objects moving through stationary sprays. The heat transfer rates achievable, and the hydrodynamic and thermodynamic behavior of spray-surface interaction in these conditions, are poorly documented and understood. Steel manufacturing processes, for example, continuous casting, descaling, and hot rolling, require knowledge of transient heat flux to impacting water sprays. Under most conditions droplets or water films at the surface are isolated by the vapor layers that occur above the Leidenfrost temperature, and the process is then particularly complex, chaotic, and lacking in experimental data. Such data are important in order to control overall production costs and, at the same time, maintain the final product quality [2]

Common water-cooling methods in the steel industry include: (a) relatively dilute sprays, used in the downstream, continues casting processes, (b) higher pressure, denser sprays to cool mill rollers, (c) laminar water "curtains" or coarse sprays, positioned between rolling stands to cool metal sheets in the hot strip mill: so-called inter-stand cooling [3]. Trial and error selection of the atomization methods and operating conditions is used and this can provide a non-ideal heat transfer process, giving inconsistent material properties, overheating of rollers, and distortion of rollers and excessive water consumption. In the inter-stand cooling process, although the strip is most commonly cooled by nearly laminar streams of water (water curtain), this can sometimes provide inconsistent cooling due to a lack of controllability so that the use of water sprays is of interest. Here the strip speed and temperature may reach over 10 ms^{-1} and 900 °C. The angle of the steel strip in the hot rolling mill may be changed up to 45 deg with respect to the horizontal (and thus 45 deg with respect to vertical sprays or water curtains), by a "looper" which is installed between stands in order to maintain an appropriate strip tension. However, there are many combinations of conditions of interest including, at the lower limits, surface velocities less than 1 ms^{-1} and temperatures in the transitional boiling regime, i.e., typically between 150 and 250 °C.

Experimental work has been published for dilute sprays, rather than dense sprays, cooling stationary flat plates. This has used individual droplet generators or two-fluid atomization, and results have restricted industrial applications. Quantitative information is required with regard to the spray parameters at high water pressure, typically in excess of 1 MPa, and their effects on the heat transfer characteristics of hot surfaces in the film boiling regime. The situation of a high velocity dense spray impacting on a hot surface has a number of other applications, including combustion chambers of diesel engines and gas turbines, and in metal powder production [6]. For the latter case previous studies for stationary objects have used both steady state and transient conditions, for example, Choi and Kang [4] and Sharief et al. [5]. In the steady state case a controlled heat input is used to maintain a steady state surface temperature. In the transient case the surface is allowed to cool during spraying. These investigations found that the different boiling regimes of pool boiling existed, but the divisions between the regimes were less clear cut in the spray cooling situation. Thus the highest heat transfer rates, and the critical point (temperature for maximum heat transfer) occurred in the nucleate boiling (or "wetted") regime, below the Leidenfrost temperature for the surface. At higher temperatures the film boiling (or "non wetted") regime gave stable heat transfer beyond around 100 K above the Leidenfrost temperature, however, an unstable "transitional regime" occurs between CHP and stable film boiling, in which heat transfer rates are difficult to measure [9].

Some work on cooling of moving surfaces has been conducted

Contributed by the Heat Transfer Division of ASME for publication in the JOURNAL OF HEAT TRANSFER. Manuscript received May 13, 2003; final manuscript received June 24, 2005. Assoc. Editor: R. M. Manglik.

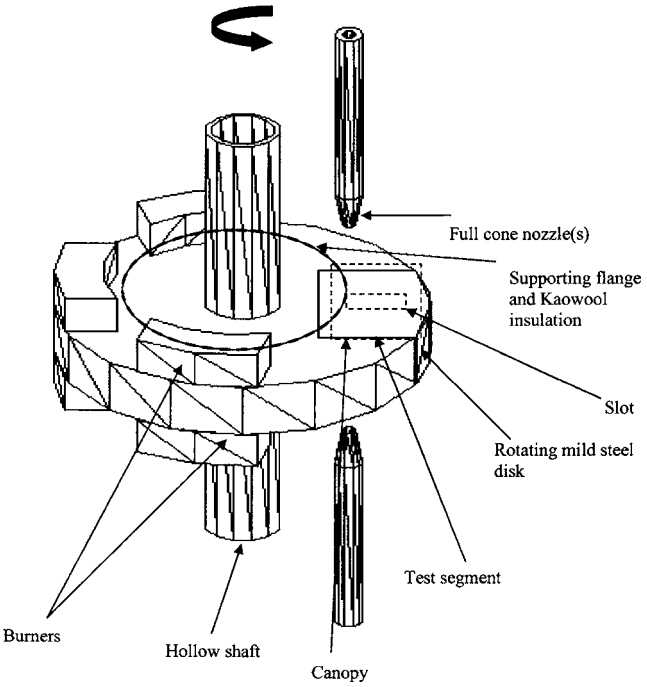

Fig. 1 Schematic of test apparatus

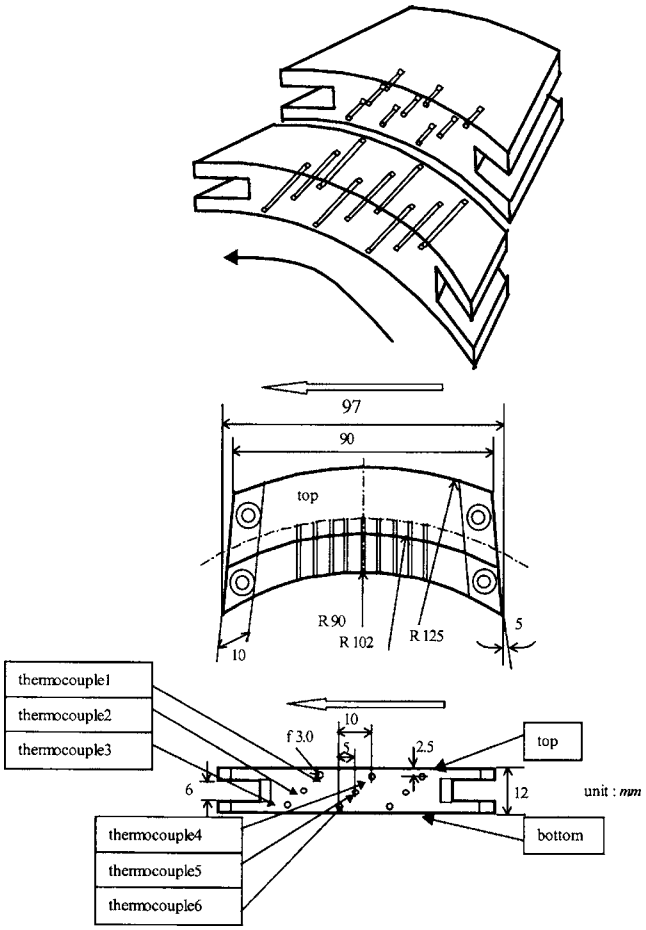

Fig. 2 Detail of test segment

using instrumented hot rolls or steel slabs moving under stationary sprays, Raudensky et al. [10]. However, due to commercial confidentiality, the results of these tests have not been fully reported. The experimental investigation described here is novel in that it uses a rotating disk to provide the moving surface. Although differing from the configurations found in the steel industry, basic similarities between linearly moving and rotating surfaces are expected near the impaction zone. The spray nozzles utilized are of the full-cone pressure jet types that are common in steelmaking, Yule et al. [1].

2 Experimental Apparatus and Procedure

2.1 Test Apparatus. Ideally, to meet the various conditions found in steelmaking, a test apparatus should be able to meet the specifications of providing a test surface with a uniform initial temperature, in the range 100–900°C, with a surface velocity $0.1-10\ \mathrm{ms}^{-1}$, and with spray angles up to 45 deg with respect to the surface. In addition, simultaneous spraying of bottom and top surfaces and adjustment of the moving surface to have an angle up to 45 deg to the horizontal, would cover most applications. The apparatus should provide measurement of the temperature drop at the surfaces, and within the metal, as the surfaces pass through the spray, such that heat flux can be calculated. The rotating disk apparatus described here was developed to fulfil these conditions in a laboratory environment. The apparatus consists of a main frame constructed of tubular steel box section, and, as shown schematically in Fig. 1, a heating system, a spray system, and a rotating test disk. The main frame supported the hollow shaft on which the disk was mounted, and a slip ring commutator. The shaft was driven by variable speed electric motor. The design allowed the possibility of the shaft and disk being tilted without significant deformation occurring. The atomizers are mounted on a separate frame so that their orientation could be changed independently of the disk. The "disk" is actually an annular mild steel ring, shown in Fig. 2, which, as shown in Fig. 1, is heated by gas burners and which contains an instrumented test segment. Mild steel was chosen for this research because it is directly related to the product in the hot rolling process. The present tests sprayed vertically downwards onto the top surface of the horizontal rotating surface, i.e., simultaneous top and bottom surface spraying was not used. As indicated in Fig. 2, the mild steel test segment was tapered 10 deg so that it would not come loose due to centrifugal force when the disk was rotated. The test segment consists of two pieces, for convenience, when welding thermocouples to the bottoms of their respective holes. The inverse heat conduction technique would, it was considered, lead to too many thermocouple "drillings" which would cause unacceptable temperature field distortion. Specially developed data processing methods were used here, as described in Sec. 3. There are nine holes on three planes, which provide temperature differences in order to derive heat fluxes in the metal. Six of the positions were used in the tests described here, labeled as thermocouple 1 to thermocouple 6 in Fig. 2. Each set of holes was staggered at 45 deg to avoid significant temperature distortion which may be caused if all three ceramic insulators were in a vertical line. The bare *K*-type thermocouple wires are 80 μm/in diameter and they are spot welded directly to the steel, giving a time response of the order of 50 ms (measured in separate tests) which is more than sufficient for the present purposes. Ceramic insulating beads protect the bare wires from contact with the metal and are not a factor in determining response. As shown in Fig. 1, the top surface of the test segment was directly exposed to the spray through a rectangular 40 mm × 10 mm slot in a protective canopy made from a thin stainless steel sheet. The slot was 20 mm above the cooled surface. The characteristics of full cone sprays, such as the radial distributions of the droplet mass flux, volume median diameter, and average drop velocity, are relatively homogeneous at the centerline of the spray, Yule et al. [1]. Thus the slot was adopted to select this homogeneous central spray zone for impact on the sur-

face. Homogeneous cooling of the surface was required, ideally, so that the temperature was uniform across any radius of the test segment, thus simplifying data processing.

To heat the rotating disk, six specially designed propane-oxygen "surface mix surface tube" burners manufactured by Nordsea Gas Technology Ltd. are used. Three burners are mounted on top of the disk and three underneath it, as shown in Fig. 1. The maximum heat output from the burners is 34 kW. The heat to the disk can be controlled by adjusting the propane and air flow rates or by adjusting the distance of the burners from the surface (10–50 mm).

Water was supplied to the full cone atomizers by a high-pressure plunger pump (type: NP25/50-120, manufactured by Speck Triplex). The atomizers were manufactured by Spraying Systems Co and they are referred to as TG0.5, TG1.0, and TG3.5, which are manufacturer codes which relate to tip type and nominal capacity (gallons/min). The maximum possible injection pressure was 12.0 MPa. Details of the performance of the atomizers are given in Sharief et al. [5] and Yule et al. [1].

To measure the rapid temperature drop as a function of time under rotating conditions, thermocouples were connected to a slip ring commutator manufactured by I.D.M. Electronics Ltd. A timer disk with a hole and 126 slots was used to measure the speed of the disk, to synchronize measurements and to measure the position of the instrumented segment of the disk relative to the spray. This was attached to the top of the hollow shaft and two optical detectors were connected to a tachometer, for measuring the disk speed, and for providing synchronization pulses to a PC. The speed of the rotating disk was displayed digitally with an accuracy ±2.0 rpm. The synchronizing pulse of +10 V was sent when the leading edge of the instrumented segment passed through the vertical centerline of the atomizer nozzle. The data acquisition system consisted of a Pentium PC and an analog-to-digital converter, fed by eight preamplifiers (manufactured by Bell & Howell) six of which were connected to the thermocouples in the test segment. The maximum sampling data rate was 16 kHz per channel. The outputs of the thermocouples were amplified up to a maximum ±10 V and were converted to temperatures by a calibration data file in the computer. A Temperature Reference Unit manufactured by CP Instruments was used, with an accuracy ±0.05°C. Overall, individual temperatures samples were measured to an accuracy ±1°C.

2.2 Test Procedure. Tests were performed with vertically downward sprays impinging on the horizontal rotating disk. At rotational speeds much higher than 120 rpm, heat transfer rate for higher temperatures became difficult to measure due to low signal/noise ratio. Thus two rotational speeds were used, 60 and 120 rpm. Measurements were made at vertical distances of 140 and 240 mm from the atomizer tip to the disk, using water pressures 0.69, 1.39, and 2.07 MPa. The segment and the whole disk were heated first, rotating at either 60 or 120 rpm without the spray, until all thermocouples registered the required initial temperature (to within ±2°C). When the temperature was achieved, the burners were switched off and the spray was turned on, but it was not allowed to impact on the disk until it had achieved a stable spraying condition which took at least 5 s and a sliding cover was used to cover the slot orifice for this period. Approximately 1.0 s before this cover was rapidly removed, the data acquisition system was started. The test segment was polished before starting a test in order to minimize the effects on heat transfer of roughness of the surface as described by Choi and Kang [4] and Sabry et al. [11]. As the specimen cooled the time histories of the temperatures were recorded, as well as the synchronizing pulses from the optical trigger. Tests were carried out using different data rates and total sampling times, to enable both detailed measurements for the first pass of the instrumented segment through the spray, and also to measure longer term temperature decay due to multiple passes. The method of calculating heat flux from the surface is described in a subsequent section, following a description of the temperature data.

Although temperatures up to 1000°C were possible, temperatures were restricted to 600°C in these experiments, to ensure that there was no failure of equipment. It is intended that an extension of the project may move to a higher temperature. The rotational speeds of the disk (60 and 120 rpm) provided tangential velocities of 0.7 and 1.4 ms^{-1}, for the center of the test segment. These velocities, although relatively low, are commonly found in steel making. The experiments were carried out at five initial temperatures 200, 300, 400, 500 and 600°C. As will be seen from the results, there is random scatter produced by electrical noise introduced by the slip ring and, as described below, this, together with an estimated ±1°C error in instantaneous temperature measurements, gives an estimated maximum expected error in heat flux, which is $\pm 1 \times 10^5$ W m^{-2}, Rho [7]. Although this error appears high, it should be noted that maximum heat fluxes above 2×10^6 W m^{-2} were found in the spray cooling tests.

3 Results and Discussion

3.1 Temperature-Time Characteristics. The performances of the high-pressure solid cone atomizers used in the experiments were described by Yule et al. [1]. These atomizers were characterized by phase Doppler anemometry and other techniques. For the central spray zones, which were allowed through the canopy slot, the ranges of spray parameters considered is 0.98–12.50 kg m^{-2} s^{-1} for mass flux, 49.0–230.4 μm for volume median drop diameter, and 9.8–32.3 ms^{-1} for mean droplet impinging velocity. The test conditions are given in Table 1. An ideal experimental approach would be to select combinations of nozzles, operating pressures, and atomizer-surface distance such that, say, two tests could be carried out at the same values of mass flux and impinging velocity, but with different values of volume mean diameter. This parametric approach is not possible in practice, as Table 1 shows. Thus, in order to deduce the effects of independent parameters as part of the data analysis, correlations between heat transfer and the spray parameters must be developed, as described in Sec. 4.

Temperature-time histories were generally recorded at 143 samples per channel/s for 60 rpm, and 286 samples/s for 120 rpm. The temperatures were obtained from the six thermocouples at positions 1–6 (Fig. 2) and time histories were recorded during 4 s, for 60 rpm, and 2 s, for 120 rpm. These were stored as Microsoft Excel files for further processing. The temperature-time histories had random noise due mainly to the slip rings in the communtator, but also due to amplifier noise. The noise consisted mainly of high frequency random noise, combined with "spikes" in the signals. A numerical smoothing process was developed in which, in the first stage, each data point at time t was replaced by an average of the value measured at that time, and the two data points before and after that time. Further smoothing to remove evidence of the spikes was applied using the following equation: $F_{t+1}=F_t+\alpha(A_{t+1}-F_t)$, where A_{t+1} is the measured value at time $t+1$ and F_{t+1} and F_t are the smoothed values at times $t+1$ and t. Here $t+1$ refers to the next sampled data point after time t. This procedure limits the amplitude of changes from one data point to the next and the smoothing constant α was chosen by trial and error to have the value of 0.2. The high frequency noise and spikes were successfully removed by the smoothing process. However, noise below approximately 20 Hz could not be removed as it was at a similar frequency to the real signal. Comparison of smoothed signals for repeat tests indicated that, after smoothing, the residual noise produced a maximum scatter of approximately, ±1.0°C. All data presented below have been passed through the smoothing process.

Table 1 Properties of central regions of water sprays

Manufacturer's code for atomizer (Spraying Systems Co.)	distance x(mm)	Supply pressure P(MPa)	Mass flux G(kg m^{-2} s^{-1})	Impinging velocity U(m s^{-1})	Volume median drop diameter $D_{v0.5}$(μm)
TG1	140	0.69	1.86	9.81	118.9
	240		0.98	9.77	101.7
	140	1.38	2.79	16.77	80.6
	240		1.37	16.70	59.5
	140	2.07	3.68	23.87	65.9
	240		1.93	21.48	49.0
TG2	140	0.69	3.82	13.06	176.5
	240		1.48	12.20	145.8
	140	1.38	5.59	19.11	122.1
	240		2.35	17.66	88.0
	140	2.07	7.30	27.19	91.0
	240		3.32	23.10	75.3
	140	0.69	7.11	14.49	230.4
TG3.5	240		3.26	12.83	215.5
	140	1.38	9.89	23.18	174.6
	240		4.71	20.55	145.9
	140	2.07	12.50	32.32	107.4
	240		5.03	25.21	102.4

4 Results

In the examples in Fig. 3, the temperature-time curves consist of four periods: a "non-spray" period, followed by three transits under the spray. The non-spray period was useful for confirming that thermocouples were operating satisfactorily and that temperature was homogeneous in the test piece to within ±1°C. The temperature at the end of the non-spray period specifies the initial conditions prior to spray cooling. When the forepart of the test piece passed the vertical centerline of the nozzle, the synchronizing pulse was used to define "zero time," as shown in Fig. 3. There is a further time interval of 0.05 s at 60 rpm, and 0.025 at 120 rpm, before the center thermocouple, number 5, is under the spray centerline. Thermocouples 4, 5, and 6 are used in all data that are presented below and they are spaced across the thickness of the test piece segment and are, as shown in Fig. 2, nearly in line through its center. The signals from the other thermocouples were used to check that the temperature field in the test piece varied significantly in the circumferential and vertical directions only, i.e., two dimensionality could be assumed as a reasonable approximation (to within ±1°C). Thermocouple 1, near the cooled surface and near the leading edge of the test piece, tended to give inconsistent readings, caused by leakage of water into the small gap between the test piece and the main annular steel ring. As seen in Fig. 3(*a*), after the relatively constant values in the non-spray zone, the temperature dropped rapidly during and after impaction of the water spray. After the test piece leaves the main cooling area, temperature recovers to some extent (due to heat redistribution in the metal), until entering the next cooling region. The repeated cooling and heat recovering signals are very similar in their patterns, which is an additional check on experimental accuracy.

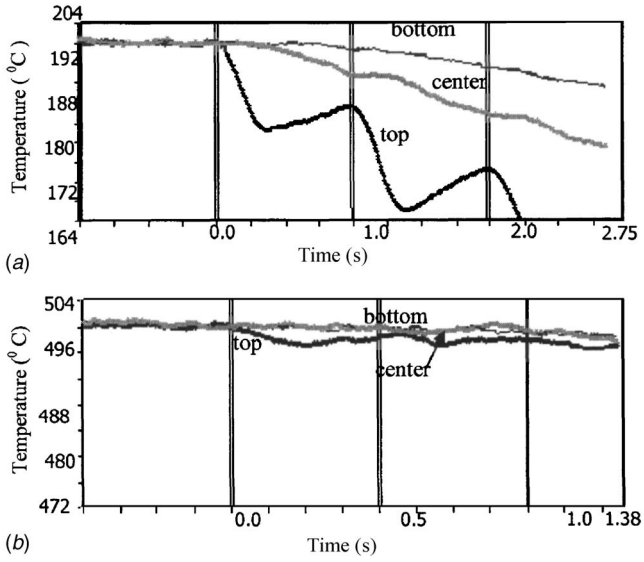

Fig. 3 Temperature-time histories using 1.70 mm nozzle at 2.07 MPa, (*a*) initial temperature 200°C, 60 rpm, x=140 mm, (*b*) 500°C, 120 rpm, x=240 mm

Figure 3 shows the representative temperature-time histories in the "top," "center" and "bottom" (thermocouples 4, 5, and 6) for two cases near the extremes of cooling rate. These both use a water pressure 2.07 MPa, and nozzle diameter, 1.70 mm. Figures 3(*a*) and 3(*b*) show, respectively, cases with rotating speeds, 60 and 120 rpm, surface-nozzle distances, x, 140 and 240 mm, and initial temperatures 200 and 500°C. The impacting water mass flux for case (*b*) is less than half that for case (*a*), as shown in Table 1. The effect of different surface-nozzle distances, on the cooling rate of a test piece, has been studied by Fry [8], for stationary surfaces. Case (*a*) is near the expected critical (peak) cooling rate, Sharief et al. [5], on the boundary of the nucleate and mixed cooling regimes, while case (*b*) is in the film regime. Naruhito et al. [12] concluded that, what they called, the "quenching point" (the Leidenfrost point) occurred in the temperature range between 230 and 240°C, in their experimental results. The temperatures from 300 to 600°C in the present experiments can be regarded as being in the film boiling regime. Visually, as in all previous experimental work using cooling by high density sprays, visual observation to provide definitive assessment of the structure near the surface was not possible. In all cooling cases, combinations of droplet bouncing, shattering, and a chaotic near-surface liquid film, occurred.

It is clear that in the case in Fig. 3(*b*), the temperature drop per revolution is comparable with temperature fluctuation occurring within one revolution. However, fluctuations of this magnitude are not observed in the case shown in Fig. 3(*a*). Thus their occurrence in case (*b*) is likely to show real variations in cooling rate with time that are occurring in the film regime. The lower temperature drop at thermocouple position 4, at the higher rotational speed 120 rpm, is also attributed to the reduced residence time of the spray at any part of the surface. Naruhito et al. [12] and Chen and Tang [13] experienced the adverse effect on cooling of the speed of a cooled object.

Considering Fig. 3(*a*), the temperature at position 4, which lies near the surface, drops rapidly after impaction of the first water

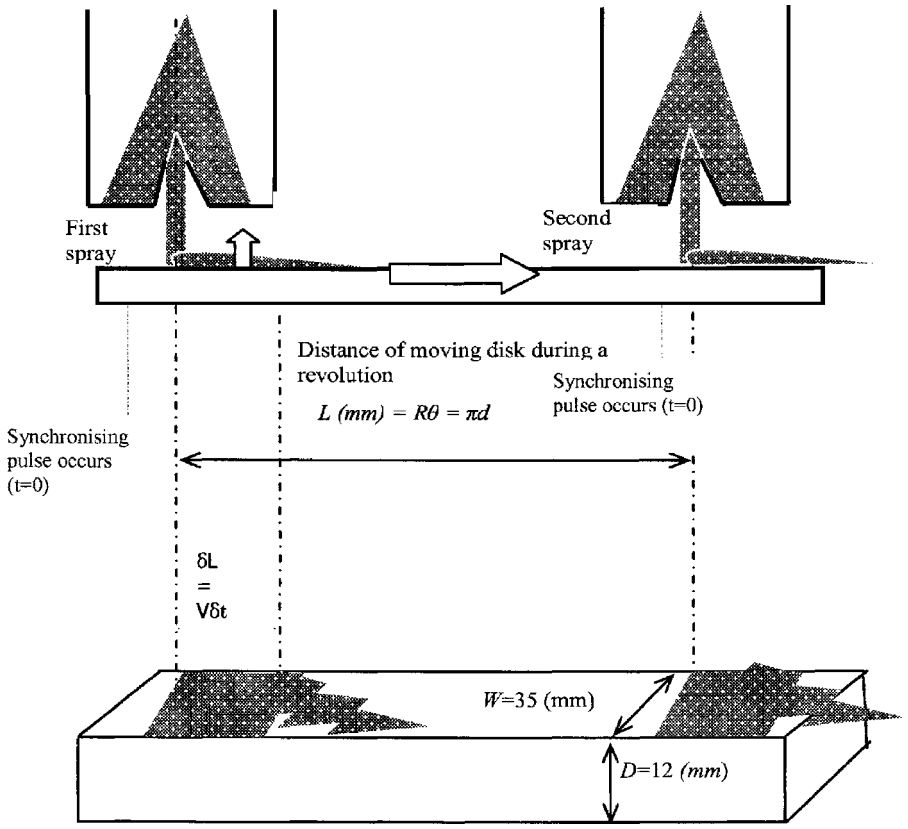

Fig. 4 Surface temperature-time histories at four different mass fluxes, G ($kg\,m^{-2}\,S^{-1}$), at (*a*) 200°C with rotating disk at 60 rpm, and (*b*) at 500°C at 120 rpm

spray, and reaches a minimum before it recovers relatively slowly, by means of heat redistribution from the lower part of the test piece, until the segment enters the next cooling stage, giving repeated cooling and heat recovering. Temperatures in the central part of the test piece (i.e., thermocouple 5) generally maintain mid-range temperatures between top and bottom thermocouple positions, without rapid temperature drops. For the case in Fig. 3(*b*) there are occasional crossovers of measurements at the central and bottom positions (thermocouples 5 and 6). Temperatures in the bottom part of the test piece (thermocouple 6) are observed to decay nearly monotonically, with no sign of transient cooling as the top surface passes through the spray.

It is recalled that to minimize temperature distortion within the test piece, the thermocouples were staggered in their positions. The phase differences at 60 rpm due to stagger were 0.007 s, both between thermocouples 4 and 5, also between thermocouples 5 and 6, and half this time at 120 rpm. The data files have not been corrected for these phase differences because they are small relative to the time scales of temperature variations.

From the general results obtained, for which Fig. 3 represents just two examples, temperature-time curves display relatively repetitive curves of the cooling and restoring process in and after the spray zones. The present study focused on the first spray zone for which the spray impacted upon a dry, vapor-free surface with uniform temperature across the test piece. Figure 4 shows typical temperature time histories at the top position (thermocouple 4) during this "first spray," with mass flux, G, values 1.86, 5.59, 9.89, and 12.50 $kg\,m^{-2}\,s^{-1}$. These are, for Fig. 4(*a*), 200°C temperature at 60 rpm, and for Fig. 4(*b*), 500°C at 120 rpm. The spray cases used here may be deduced from Table 1 where it can be seen that droplet velocity and diameter are also changing from case to case. Thus care must be taken when interpreting results, such as those in Fig. 4, in terms of the effect of any one parameter. Deconvolution of the effects of the different parameters requires correlation procedures, as discussed below.

It is noted that the actual surface temperature in the region of direct contact with the water spray should be lower than that measured at the top thermocouple position of the test piece, because the active junction of thermocouple 4 was welded 2.5 mm under the surface. A correction could be made, if required, by extrapolating the measurements at positions 4 and 5, to the surface. However, it is not necessary for present purposes where only the initial surface temperature is specified as a parameter and this does not suffer from this error source. In all cases the temperature reductions increase with increasing mass flux, confirming that the mass flux is one of the main parameters determining heat transfer in both transition and film regimes. The temperature-time curves without a spray, obtained with the disk speeds 60 and 120 rpm, are also shown in Fig. 4. These temperature reduction rates are due to radiation, air convection, and conduction to the supports. The temperature reductions for one disk revolution without spraying, are shown in Table 2. These reductions are small compared with those due to the spray cooling, particularly at the lower initial

Table 2 Temperature reductions for one disk revolution without water spray: (Units: °C)

Initial disk temperature	200°C	300°C	400°C	500°C	600°C
60 rpm	negligible	0.1	0.3	0.8	1.0
120 rpm	negligible	0.4	0.5	0.9	Not used

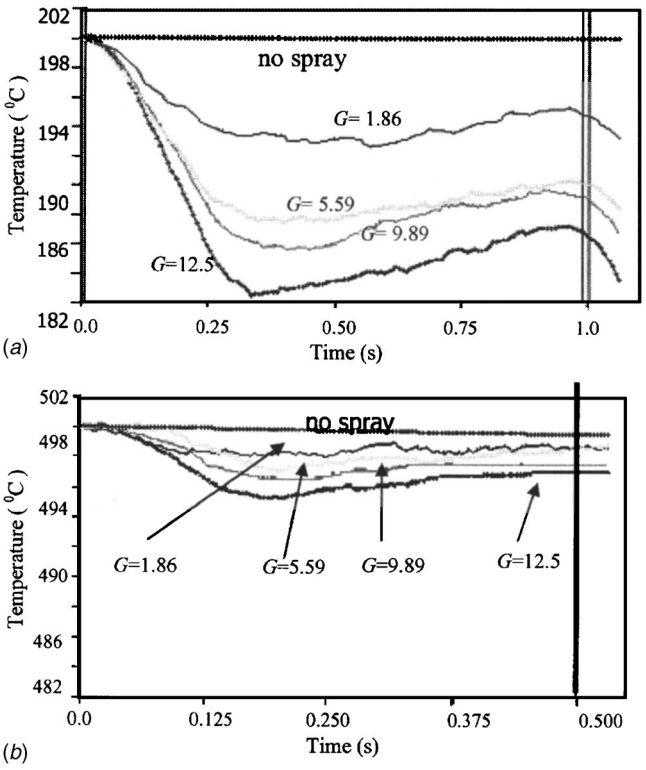

Fig. 5 Schematic diagram for heat flux calculation

disk temperatures. However, they are taken into account in the spray cooling heat flux calculations, as described later.

In summary, after the higher frequency noise had been filtered out, the temperature signals obtained for different spraying conditions were deemed to be repetitive and self-consistent and their use for heat transfer calculations is justified.

4.1 Local Heat Flux. A one-dimensional heat flux calculation procedure was used to obtain the local heat flux from the surface. The heat flux due to the spray, after that expected due to radiation is accounted for, is usually referred to as the "evaporative heat flux." In practice, of course, heat transfer to the water goes (i) to raise temperature in the liquid phase, (ii) to produce a phase change for some of the water, and (iii) to superheat some vapor. In spray cooling the situation is too complex to estimate the relative proportions for these heat sinks by use of analysis, hence the need for empirical information.

As sketched in Fig. 5, to use the temperature data to calculate the local evaporative heat flux at the surface of the rotating test piece, the test piece is represented by an infinite plate, which moves with a velocity which is that of the tangential velocity of the center of the test segment. This velocity is $V=2\pi\omega R$, where the radial position of the center of the test segment is at $R=0.1075$ m and ω is the rotational speed (revolutions per second). The local evaporative heat flux due to the spray is calculated from $q_s=\rho DC_p d/\mathrm{d}t(T_{\text{no spray}}T_{av})(\mathrm{W/m^2})$. Here, ρ is the density of the metal and C_p is the specific heat of the metal. The average temperature, T_{av}, for the thickness of the test segment, D, was calculated, using a quadratic fit to the three measured temperature values. The equation assumes that temperature does not vary radially across the test segment. Subtracting the segment temperature measured without spraying, $T_{\text{no spray}}$, is a means of correcting for radiative heat transfer, although it is also removing heat transfer that occurs to the air for the non-spraying case.

Results are shown in Fig. 6 for the three full cone atomizers at different conditions, where the spray properties near impact are given in Table 1. Note that the synchronization pulses shown in

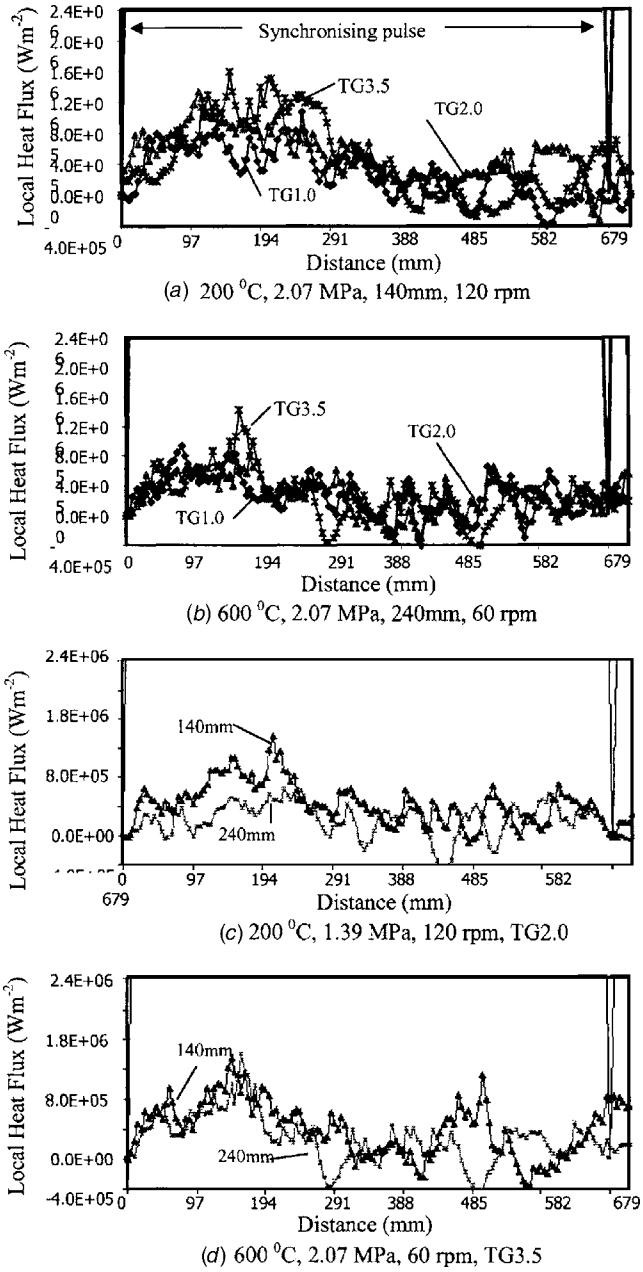

Fig. 6 Surface heat flux at temperatures of 200 and 600°C for different conditions

the graphs represent where the forepart of the test segment passed under the spray centerline. In these figures the position of the spray centerline is at $L=21.5$ mm, for both 60 and 120 rpm. Figure 6(*a*) shows the heat flux distribution for 200°C initial surface temperature, for the three atomizers operating at 2.07 MPa, for nozzle-surface distance 140 mm, at 120 rpm. Due to the differentiation of the temperature-time histories required to obtain heat flux, there is more scatter in the curves than for the temperature-time histories shown in Fig. 4. The levels of heat flux are seen to increase as the atomizer size is increased with its consequent increase in spray mass flux (Table 1), and peak heat fluxes around 1.5 $\mathrm{kW/m^{-2}}$ are shown. Because the relatively low heat flux at 600°C at the higher rotational speed was found to be "drowned" by the scatter in the results, the 600°C cases were recorded and processed for rotation at 60 rpm only, as shown in Fig. 6(*b*). Figure 6(*b*) shows similar trends for the cases in Fig. 6(*a*), but with

lower heat flux, as expected in the film boiling regime.

Figure 6(*c*) shows cases for one atomizer with a lower water pressure than the cases in (*a*) and (*b*), and with two atomizer-surface distances. This shows the increasing problems due to scatter in the data as mass flux is reduced, which occurs both when pressure is reduced and also when the distance between the atomizer and the surface is increased (Table 1). Situations and regions where scatter, due to signal noise, is unacceptable are indicated by regions of unrealistic, negative excursions of heat flux. Figure 6(*d*) shows that increasing atomizer-surface separation at 600°C also introduces significantly poorer signal to noise ratio, at distances beyond the region of peak heat flux. In general, local heat flux initially increases, moving downstream from the centerline of the impacting spray. For the 60 rpm case, peak heat flux occurs in the region 80±20 mm downstream of the spray centerline. This increases to 150±20 mm downstream for the 120 rpm case. Fry [8] and Raudensky et al. [10] found that heat flux, from stationary plates, is highest in the stagnation zone at the spray centerline. It is thus tempting to assume a near linear increase in distance downstream to peak heat flux, as the velocity of the surface is increased. However, this may be too simplistic an assumption to be made, because of the restricted velocities and spray types that could be used.

Although the scatter in the results becomes important at lower heat fluxes and, in particular, this results in unrealistic negative values in places, the trends of heat flux are qualitatively as expected. This is particularly true for the first 90 deg of rotation, i.e., up to a distance 165 mm. Of course, with increasing angle the situation deviates increasingly from the case of a spray impacting on a flat rectangular plate with linear motion. Generally, within the first 90 deg of rotation, heat flux increases with increasing nozzle orifice size, increasing supply pressure, and decreasing nozzle-surface separation. In addition, heat flux decreases significantly with increased rotational speed. Perhaps the most surprising characteristic is both the delay in the occurrence of the peak heat flux, beyond the main impaction zone of the spray, and, for some cases, the persistence of significant heat transfer to the spray beyond 300 mm, that is, when the surface has moved 180 deg away from the impaction zone. To some extent this is expected from the observations of Raudensky et al. [10] who showed the persistence of cooling to surface vapor and water far from the impaction zone.

As shown in Table 1, spray characteristics of the central zones of full cone nozzles are functions of supply pressure (P), exit orifice diameter of atomizer (d_o) and atomizer-surface distance (x). When the distance from the atomizer exit to the heated surface is increased, all of the three parameters, mass flux (G), impinging velocity (U), and drop median diameter ($D_{v0.5}$), are decreased. It is observed in Fig. 6 that when the surface-nozzle distance is 140 mm, heat fluxes are relatively higher than those for the surface distance, 240 mm. The difference is clear for all nozzle pressures, at 200°C, but is more pronounced for the higher pressure (2.07 MPa) for 300, 400 and 500°C. The differences are less clear for 600°C, but this is possibly because they are hidden by the greater relative importance of scatter in the data. Most authors agree that mass flux is the main parameter affecting heat flux, at least for the case of a stationary surface. Fry [8] mentioned that the heat transfer coefficient increased linearly with increasing surface temperature, decreasing nozzle "stand-off" distance and increasing flow rate. Although the results of the present research confirm that the heat fluxes are decreasing with increasing nozzle-surface distance, a linear increase of heat transfer coefficient (as opposed to heat flux) with temperature is not apparent from inspection of the data.

Ideally, dimensionally consistent correlations should be derived by using dimensionless parameters that should have physical significance, such as Weber, Reynolds, Jacobs and other related numbers. However, the authors were not able to derive such a dimensionally consistent correlation that gave good fit to the data, and future work will be required, which will be using a larger volume of data, to achieve this. The effects of mass flux, G, median droplet diameter, $D_{v0.5}$, and mean droplet velocity U, cannot be easily discriminated by visual inspection of the data. This requires applying correlation methods and maximum values of heat flux, which are chosen to elucidate relationships. Figure 7 shows the maximum heat flux plotted against individual spray characteristics for the 200°C case, however, as has been described, great care must be taken when examining Fig. 7, because it was impossible to vary one parameter at a time. The clearest correlation (i.e., with least scatter) is that between maximum heat flux and mass flux. This confirms the importance of mass flux in determining heat transfer. The polynomial trend lines also demonstrate the important effect of the rotating speed of the surface. Otherwise, nothing conclusive emerges from the data presented in this way. The ranges of maximum heat flux are from 4.0×10^5 to 2.6×10^6 W m^{-2} for the speed of rotating disk 60 rpm, and from 4.8×10^5 to 1.6×10^6 W m^{-2} for 120 rpm. Maximum heat fluxes in the film boiling regime, in the range of temperature 300–600°C, are significantly lower in comparison with the transition regime. The ranges of maximum heat flux in the film boiling regime are from 4.0×10^5 to 1.4×10^6 W m^{-2} with the speed of rotating disk 60 rpm and from 4.8×10^5 to 1.1×10^6 W m^{-2} with 120 rpm. These various ranges are all within the range of values found in previous work on spray cooling of stationary surfaces [5].

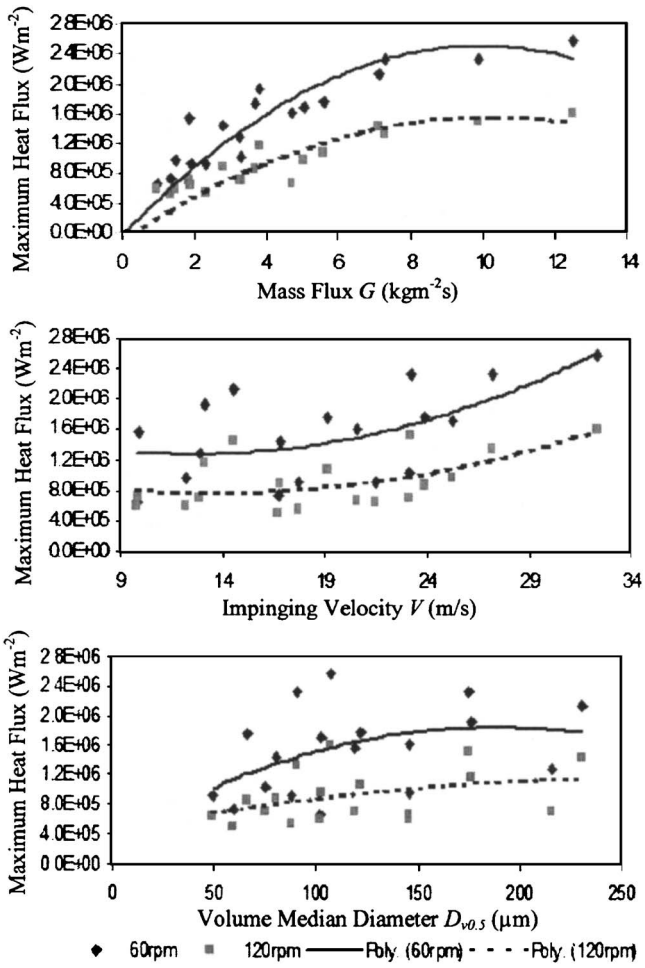

Fig. 7 Effect of spray characteristics on maximum heat flux at temperature 200°C (G, U, and $D_{v,0.5}$ were not varied independently of each other)

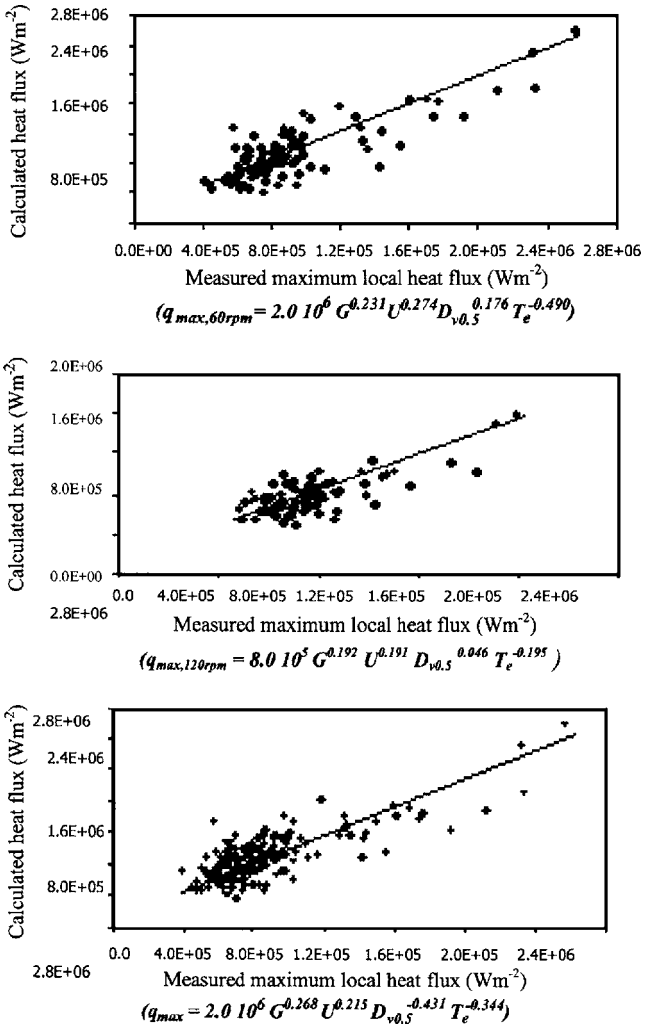

Fig. 8 Comparison of the measured maximum local heat flux with the heat flux from the correlation equations (1)–(3)

Empirical correlations for maximum local heat flux, $q_{\max}$(W m^{-2}), were obtained using Microsoft Excel software and by using experimental data covering ranges of spray parameters, 0.98–12.50 kg m^{-2} s^{-1} for mass flux G, 49.0–230.4(μm) for volume median drop diameter $D_{v0.5}$, and 9.8–32.3 m s^{-1} for average drop impinging velocity U.

The optimum curve fit was obtained for the maximum heat flux, equated to products of G, $D_{v0.5}$, U, and surface superheat ΔT_e, raised to different powers. For the 60 rpm cases the best fit was, in SI units for G, U and ΔT_e, but using μm for $D_{v0.5}$:

$$\dot{q}_{w\ \max,60\ \mathrm{rpm}} = 2.0 \times 10^6 G^{0.231} U^{0.274} D_{v0.5}^{0176} \Delta T_e^{-0.490} \quad (1)$$

For the 120 rpm cases the best fit was:

$$\dot{q}_{w\ \max,120\ \mathrm{rpm}} = 8.0 \times 10^5 G^{0.192} U^{0.191} D_{v0.5}^{0.046} \Delta T_e^{-0.195} \quad (2)$$

While recognizing that such equations are not dimensionally correct, they are very useful in revealing features of the physics of the flows, as is described below.

The top two scatter diagrams in Fig. 8 compare the measured values of $q_{\max,60\ \mathrm{rpm}}$ and $q_{\max,120\ \mathrm{rpm}}$, with values calculated from Eqs. (1) and (2). It is noted that the full temperature range of results is used for calculating the correlations, i.e., $100\,^\circ\mathrm{C} \leqslant \Delta T_e \leqslant 500\,^\circ\mathrm{C}$, and thus the use of a single power for T_e is a simplification in view of the different cooling regimes that are covered by the data. This is a reason for the relatively high scatter in Fig. 8. For both cases maximum heat flux increases with increasing mass flux, G and impinging velocity, U, each raised to similar powers. This is interesting because the product GU is the droplet momentum flux at the surface. Thus the results are indicative of relationships between Nusselt and Reynolds number, both suitably defined using spray parameters. Retrospectively this may appear to be unsurprising, yet it is not a concept that has been raised in previous published work. The powers in Eqs. (1) and (2) show that the values of spray parameters and superheat have less influence on maximum heat flux for the lower speed of the test piece. This was not obvious from examining the "raw data" results, thus showing the usefulness of such correlations. An explanation is that as the surface speed is increased, the relative velocity between the wall spray and the surface reduces, and it is likely that a thicker water layer at the surface results so that there is less dependency of heat transfer on the spray properties.

From Eqs. (1) and (2), the drop size has the smallest effect on heat transfer, in agreement with previous work with stationary surfaces. Thus the maximum heat flux was again correlated, but dropping $D_{v0.5}$ from the equation and adding the tangential speed of the test piece V. It is noted that V could not be used with all of the other four parameters to obtain a single correlation, due to lack of convergence of the iterative procedure. For the 60 and 120 rpm data combined, the best fit was:

$$\dot{q}_{w\ \max} = 2.0 \times 10^6 G^{0.268} U^{0.215} V^{-0.431} \Delta T_e^{-0.344} \quad (3)$$

The bottom scatter diagram in Fig. 8 shows the fit of this correlation. From Eq. (3) the main result is the confirmation that the speed of the surface very significantly affects the maximum spray cooling heat flux. An obvious drawback of Eq. (3) is that it is inapplicable when $V \rightarrow 0$. It is interesting to compare the effects of spray characteristics with those for steady state cooling of a stationary test piece. Sharief et al. [5] derived a correlation equation, showing that the total heat flux had 0.363 and 0.304 power dependency on the liquid mass flux and drop impinging velocity, respectively, in the surface superheat temperature range between 152 and 630°C, using the range of spray parameters: 0.23–3.32 kg m^{-2} s^{-1}, 34.71–127.99 μm, and 7.05–23.10 m s^{-1}.

Thus comparison with the results from the present equations confirms that the effect of mass flux and impinging velocity can be combined as a spray momentum flux and that this parameter tends to be more important for reduction in surface velocity. However, the heat fluxes measured by Sharief, although in agreement with previous experiments on the cooling stationary surfaces, are lower than the peak heat fluxes that are reported here. This can be seen by the curve included in Fig. 7. This difference is probably due to the heat transfer for the stationary case, being measured at a stagnation zone, while the present results show that peak heat transfer occurs downstream of the main impaction zone.

5 Conclusions

A novel rotating disk technique has been shown to be a convenient method for determining moving surface heat transfer. The data are consistent, however care is required in interpreting the rotating surface results in terms of linearly moving plates, especially beyond 90 deg of rotation. Local heat flux increases moving downstream from the zone of impaction of the spray, and reaches a maximum at a position downstream that increases as the surface speed is increased. The heat fluxes at a temperature 200°C, in the transition regime, are higher than at temperatures (300–600°C) in the film boiling regime for the moving surfaces. Heat flux generally increases with increasing nozzle orifice size, increasing supply pressure, and decreasing nozzle-surface separation. Correlation shows that maximum heat flux increases with increasing mass flux, G and impinging velocity, U raised to similar powers, indicating the importance of droplet momentum flux. The effects of mass flux, impinging velocity droplet size, and temperature are more significant for reduction of surface velocity.

Increasing the surface velocity V significantly reduces peak heat flux, possibly due to the changes in residence time on the surface of the wall spray, and the different spray angle relative to the surface.

Acknowledgment

The authors wish to acknowledge the contributions that S. Rho (POSCO Ltd.) made to this publication during his MPhil program of study.

Nomenclature

A = area of impacting spray on the test piece
$D_{v0.5}$ = volume median diameter
G = drop mass flux
m = mass of the test piece corresponded to the total steel annulus (ρV)
q_s = evaporative heat flux
$T_{\text{no spray}}$ = disk temperature with no spray
T_{avi} = average disk temperature
ΔT_e = surface superheat temperature drop ($T_s - 100$)
U = drop impinging velocity

References

[1] Yule, A. J., Sharief, R. A., and Nasr, G. G., 2000, "The Performance Characteristics of Solid Cone Spray Pressure Swirl Atomizers," Ann. Tokyo Astron. Obs., **10**(6), pp. 627–646.

[2] Nasr, G. G., Sharief, R. A., Yule, A. J., James, D. D., Widger, I. R., and Jeong, J. R., 1999, "Transient High Pressure Spray Cooling of a Rotating Steel Plate at High Temperature," *Proceedings of 15th ILASS Europe*, Toulouse, France.

[3] Nasr, G. G., Yule, A. J., and Bendig, L., 2002, *Industrial Sprays and Atomization: Design, Analysis and Applications*, Springer-Verlag, New York.

[4] Choi, K. J., and Kang, B. S., 1993, "Parametric Studies of Droplet Wall Direct Heat Transfer in Spray Cooling Process," ASME FED 178/HDT-270, Proc. ASME Heat Transfer Div., pp. 161–165.

[5] Sharief, R. A., Nasr, G. G., Yule, A. J., James, D. D., Widger, I. R., and Jeong, J. R., 2000, "Steady State High Pressure Spray Cooling of High Temperature Steel Surfaces," *Proceedings of 8th ICLASS Conference*, Jet Propulsion Lab., Pasadena, CA, pp. 392–399.

[6] Yule, A. J., and Dunkley, J. J., 1994, *Atomization of Melts*, Oxford University Press, Oxford.

[7] Rho, S., 2001, "Water Spray Cooling of Moving Heated Steel Surfaces," Masters thesis, UMIST, Manchester, UK.

[8] Fry, J. C., 1998, "A Study of the Cooling Effect of Water Sprays on Steel Strip at High Temperatures," Ph.D. thesis, University of Wales, Swansea.

[9] Yao, S. C., and Cai, K. J., 1988, "The Dynamics and Leidenfrost Temperature of Drops Impacting on a Hot Surface at Small Angles," Exp. Therm. Fluid Sci., **1**, pp. 363–371.

[10] Raudensky, M., Druckmuller, M., and Horsky, J., 1998, "Inverse Heat Conduction Problems and Generalization of Experimental Results," 361–5, *Proceedings of the ASME Heat Transfer Division* 5, HSME pp. 65–71.

[11] Sabry, T. I., Mousa, M., and Yoshida, H., 1994, *Studies on the Spray Cooling of Hot Surfaces*, ICLASS-'94 Rouen, France, Begell House, New York, pp. 891–898.

[12] Naruhito, S., Hariki, M., Haraguchi, Y., and Morita, M., 2000, "Mechanism of Uneven Thermal Distribution Formation During Water Cooling at Low Temperature for a Moving Plate," ISIJ Int., **86**(6), pp. 381–387.

[13] Chen, S. J., and Tseng, A. A., 1992, "Spray Cooling and Jet Cooling in Steel Rolling," Int. J. Heat Fluid Flow, **13**(4), pp. 358–369.

A. Jain
Department of Applied Mechanics,
M.N.R. Engineering College,
Allahabad, India-211004

B. Mohanty
Department of Chemical Engineering,
Indian Institute of Technology,
Roorkee, India-247667

B. Pitchumani
Department of Chemical Engineering,
Indian Institute of Technology,
Delhi, India-110016

K. S. Rajan
School of Chemical and Biotechnology,
Shanmugha Arts, Science,
Technology and Research Academy,
Thanjavur, India-613402
e-mail: rajan_sekar@yahoo.com

Studies on Gas-Solid Heat Transfer in Cyclone Heat Exchanger

Cyclones can be used for heating solid particles where the direct contact with the gas is permitted. Since cyclones have potential applications as heat exchangers in fertilizer, polymer powder, pharmaceutical and other industries, study of cyclone as heat exchanger is deemed important. Experiments on air-solid heat transfer were carried out in a cyclone heat exchanger of 100 mm *inside diameter, using sand. The effects of solid feed rate* (0.5–7.5 g/s), *cyclone inlet air velocity* (9–22 m/s), *and four average particle sizes* (163–460 μm) *on the heat transfer rate, exit solid temperature, and heat transfer coefficient have been studied. An empirical correlation has been proposed for the prediction of heat transfer coefficients based on the present experimental data. The proposed correlation predicts the heat transfer coefficients with an error of* +10% to −15% *for the present data and within an error of* +25% to −15% *for the data of other investigators.*
[DOI: 10.1115/1.2217748]

Keywords: cyclone heat exchanger, heat transfer coefficient, correlation

Introduction

Though cyclones are well known for their efficiency to separate particles, their use as heat exchangers is gaining popularity. Cyclone as heat transfer equipment may be used for drying, solidification, sublimation, reactions, etc. Series of reverse flow cyclones have already been in used as raw meal preheater in the cement industries. Very little information related to design on cyclone as heat exchanger is available in the open literature, due to its high patent value. Ramanan et al. [1] reported heat transfer studies in the industrial cyclone heat exchanger while Pitchumani et al. [2] reported the cyclone performance at high temperatures. Yen et al. [3] and Raju et al. [4] reported experimental investigations on air-solid heat transfer in reverse flow cyclones and proposed correlations for gas-solid heat transfer in cyclone. This paper presents the study of cyclone as gas-solid heat exchanger and proposes correlations that can be easily and reliably used for design of cyclone for commercial applications. This work is a part of the research project on the gas-solid heat transfer, with the experiments conducted in a specially designed cyclone heat exchanger test rig and fabricated in house at the Heat Transfer Research Laboratory of Chemical Engineering Department of the Indian Institute of Technology, Roorkee.

The knowledge of flow profiles of gas and solid in the cyclone is of paramount importance to the understanding of functions of cyclone as heat exchanger. The gas entering the cyclone takes a tangential path and starts moving along the circumference. Gas inside the cyclone has positive velocities in three directions: axial, radial, and tangential. The tangential velocity is of the order of inlet velocity. Radial velocity is high at low solid loadings resulting in bypass of the gas from the outer vortex into the inner vortex without reaching the bottom. The axial velocity is responsible for the movement of gas from the top to the bottom of the cyclone and then into the inner vortex. The axial velocity is high and is independent of gravity. With increase in solid feed rate, the radial velocity decreases and more gas reaches the bottom of the cyclone without much bypassing.

Contributed by the Heat Transfer Division of ASME for publication in the JOURNAL OF HEAT TRANSFER. Manuscript received December 15, 2004; final manuscript received January 5, 2006. Review conducted by Phillip M. Ligrani.

Experiment

Description. A schematic diagram of the experimental setup is shown in Fig. 1. The experimental setup consists of an air inlet duct fitted with heaters, solid feeding system, cyclone separator, bag filter, and a blower operating under suction. Coiled heaters (six in number) are used in series to supply the necessary heat to increase the temperature of air to approximately 200°C. The duct is circular in cross section with 50 mm inside diameter. The cyclone is a standard one as given in Perry, et al. [5] with 100 mm diameter. The solid feeding system consists of a hopper provided with an opening at the bottom, and U-channel feeder with an electromagnetic vibrator wherein a constant head of solid is maintained using a scrapper at the solid discharge point. Powder is discharged into a conical funnel, leading to the throat of the venturi in the gas duct. Solid is collected in the bin attached to the bottom of the cyclone at solid exit. Hot air leaving the cyclone is cooled by constantly dripping water on the jute lining covering the portion of duct between the cyclone outlet and the bag filter. A 2 hp induction motor, connected to 440 V, three-phase supply, runs the blower at 2880 rpm with a capacity of 132 l/s at a suction of 500 mm of water. Bypass valves V1 and V2 are used to control the velocity of air through the duct. The hold up of the particles is measured by simultaneously closing the airflow, solid flow, and the heater. The solid left inside the cyclone at that moment is collected in the bin and is weighed to determine the hold up. The body of the cyclone and the pipeline are insulated using two layers of asbestos rope wound around them and covered with a mixture of plaster of Paris, magnesia, and asbestos powder to prevent the heat loss.

Cyclone. Earlier studies by Yen et al. [3] and Raju et al. [4] used cyclones with short cylindrical section, compared to the conical section. However, as higher cylindrical height of the cyclone aids heat transfer, cyclone with equal height of cylindrical and conical section, as used by Lapple [6] and detailed in Perry, Chilton, and Cecil [5], is used in the present investigation. Though generally the size of solid opening is less than the air outlet diameter, a small solid discharge opening could affect the flow of solid. Hence, a solid outlet of 30 mm diameter is used instead of 25 mm as obtained by geometric ratio. The width of inlet is kept equal to 20 mm instead of 25 mm to increase the efficiency. Gradual tran-

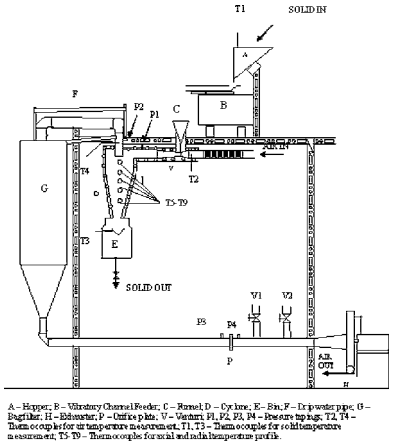

A – Hopper; B – Vibratory Channel Feeder; C – Funnel; D – Cyclone; E – Bin; F – Dripwater pipe; G – Baghfilter; H – Blowster; P – Orifice plate; V – Venturi; P1, P2, P3, P4 – Pressure tapings; T2, T4 – Thermocouple for air temperature measurement, T1, T3 – Thermocouple for cold temperature measurement; T5-T9 – Thermocouples for axial and radial temperature profile.

Fig. 1 Schematic diagram of the experimental setup

sition of the inlet from circular to rectangular has been done to avoid excessive pressure drop. Moreover, to achieve uniform distribution of particles in the air at the inlet, the inlet section has been kept straight with gradual transition. The cyclone inlet is tangential to the top plate of the cyclone to eliminate eddy flow and turbulence to reduce top-plate erosion. Sideways transition of inlet is kept at an included angle of 15 deg. This requires an entry length of about 110 mm. Since the outer vortex can extend beyond the solid outlet into the solid receiver bin, entrainment of the solid into the inner vortex will take place leading to further reduction in separation efficiency. Hence, it is important to keep the solid level in the receiver at a level such that it is not carried into the inner vortex at any point of time. Therefore, size of the solid receiver has considerable influence on the performance of cyclone as a separator. Hence, the solid receiver is provided with 200 mm height and 150 mm diameter. The receiver is transparent to allow visual inspection of the level of solid inside it. For regular withdrawal of collected particles from the solid receiver bin, a collapsible rubber tube is provided at the bottom of the receiver for ease of operation. Another bin with a conical cup arrangement inside is also provided to collect the solid required for the hold-up measurement. Figure 2 shows the sketch of cyclone with dimensions.

Instrumentation. The experimental setup is fully equipped with instruments to measure airflow rate, solid feed rate, solid and air temperature, etc. Flow rate of air is controlled by monitoring differential pressure across an orifice, indicated by a pressure indicator connected to a differential pressure transducer. The temperature of hot incoming air is measured using a resonant tunneling device indicator and is maintained at a constant value using a silicon controlled rectifier. A thermocouple placed in the hopper is used to measure the solid inlet temperature. Eight pairs of thermocouples (one shielded and the other bare) are placed at various distances in the cylindrical and conical part of the cyclone to measure the axial variation in temperature of air and the air-solid mixture. The shielded thermocouples are expected to indicate the temperature of air, while the bare thermocouples indicate the temperature of air-solid mixture. They can also be traversed in the radial direction to measure the radial profiles of temperature in the cyclone. To measure the exit temperature of the solid, a thermocouple is placed in a spoon. The spoon and the sensing part of the thermocouple are placed inside the solid receiver below the cyclone outlet. All the thermocouples are made of copper-constantan wires and are connected to a 24-point selector switch, in turn connected to a Keithley Digital Multimeter model 177 to record the electromotive force (emf) generated. Melting ice in a thermos flask is used as the cold junction. The emf generated is converted to temperature using the power series as given in the National Bureau of Standards.

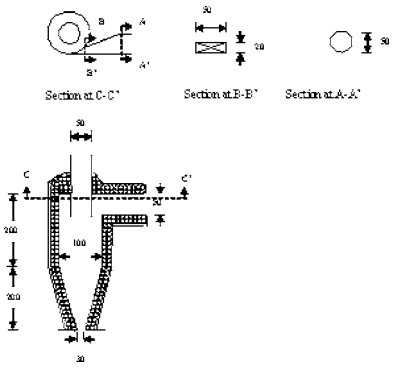

Fig. 2 Sketch of cyclone with dimensions (mm)

Table 1 Range of variables used in the present study

Variable	Range
Cyclone inlet velocity	9–22 m/s
Mass flow rate of solid	0.5–7.5 g/s
Inlet air temperature	200°C
Hold up	0.89–14.38 g
Reynolds number based on inlet velocity	46.72–307.91

Introduction of thermocouples at various locations is expected to create a local disturbance in temperature at those points. Hence, the thermocouples are bent to a small distance inside cyclone in such a way that the effect of local disturbance is not reflected in measurements. Uncertainties in the measurement of exit air and solid temperatures are ±0.1 and ±1°C respectively. Hold up of particles is measured by simultaneously shutting down the blower, heater, and feed of solid and, at the same time, the conical cup inside solid receiver is turned up with the help of a handle so that the conical cup matches with cyclone bottom opening. Solids collected in the bin are the ones, which were present at that instant and hence used to determine the hold up. The collected solids are weighed on digital precision balance having model number 205ASCS manufactured by Precisa, Switzerland, with a least count of 0.001 g. Ranges of variables studied are given in the Table 1.

Experimental Procedure. A typical experimental procedure consists of adjusting airflow rate using the bypass valves to achieve the desired inlet velocity and then switching the heater on. Once the steady state temperature of air is attained, particles of a particular average size, carefully screened and stored in the hopper, are fed into the system with the help of an electromagnetic arm imparting vibrations to channel feeder. A steady solid feed rate is achieved for a particular combination of particle size, gas velocity, and the funnel opening. The emf generated are noted and then converted to temperatures. The holdup of the particles is measured by simultaneously closing the airflow, solid flow, and the heater. The solid left inside the cyclone is collected in the bin, which is unscrewed and weighed to measure solid holdup.

Results and Discussions

Earlier investigations reported by Yen et al. [3] and Raju et al. [4] have considered plug flow in the cyclone. Yen et al. [3] confirmed it experimentally by observing the flow patterns in a transparent cyclone and measured the particle residence time distribution in the cyclone. Szekely and Carr [7] also confirmed the plug flow of iron particles in the cyclone.

Heat transfer from gas to solid involves two steps: Transfer of heat from bulk of the gas to the surface of the solid across the gas film surrounding the solid (external process) and the propagation of heat through conduction within the particle to reach isothermal

Table 2 Particle size distribution

S. No	ASTM screen (Mesh)	Sieve opening (μm)	Average particle size (μm)
1	−80+100	149 to 177	163
2	−50+60	250 to 297	274
3	−40+50	297 to 420	359
4	−35+40	420 to 500	460

condition within the particle (internal process). Internal geometry and conduction controls the heat transfer if Biot number, *Bi*, is greater than 2.

Biot number is defined as

$$Bi = \frac{Rh_p}{k_s} \tag{1}$$

For the particle sizes under study, the high thermal conductivity of solids results in $Bi < 2$, leading to a gas-film controlled process. Hence, the resistance to heat transfer can be assumed to rest solely with the gas-film surrounding the particle. The gas-solid heat transfer coefficient is defined as

$$h_p = \frac{q}{A\Delta T} \tag{2}$$

Since the gas and solids (plug flow) move parallel in same direction, the cyclone can be considered as co-current heat exchanger. Accordingly, ΔT in Eq. (2) is the log-mean temperature difference defined as

$$\Delta T = \frac{(T_{\text{Gin}} - T_{\text{Sin}}) - (T_{\text{Gout}} - T_{\text{Sout}})}{\ln\left(\frac{T_{\text{Gin}} - T_{\text{Sin}}}{T_{\text{Gout}} - T_{\text{Sout}}}\right)} \tag{3}$$

The heat transfer area A is the total surface area of the particles in the cyclone at any instant of time. It is related to hold up, (the total weight of the particles in the cyclone at any instant of time) density and size of the particles as given by Eq. (4).

$$A = \frac{6M_h}{\rho_s d_p} \tag{4}$$

The heat transfer rate "q" is defined as

$$q = m_s c_{ps}(T_{\text{Sout}} - T_{\text{Sin}}) \tag{5}$$

In conventional heat exchangers, the heat transfer area is fixed from the dimensions and the geometry of the heat exchanger. In cyclone heat exchangers, the particles' total heat transfer area varies from position to position due to the variation of concentration of particles with position. The heat transfer coefficient is a convenient and a simple measure of the performance of cyclone as a heat exchanger and is determined using Eq. (2) after measuring solid hold up, inlet and exit temperatures of air and solid, and heat transfer rate.

Effect of Solid Feed Rate on Heat Transfer Rate, Solid Exit Temperature, and Heat Transfer Coefficient. Experiments were conducted with uniform size particles at different feed rates for nearly constant inlet air velocity. The sizes studied are given in Table 2. Figure 3 shows the effect of solid feed rate on heat transfer rate at different air velocities for particles of size 359 μm.

It can be seen from the Fig. 3 that the heat transfer rate increases rapidly with the solid feed rate up to a certain feed rate, after which the increase in heat transfer rate is slower. This can be explained from the flow profiles in cyclones as follows:

Increase in solid feed rate at a constant inlet air velocity results in the reduced radial velocity of the air. As a result, bypass of air decreases and more air reaches the bottom of the cyclone. Since more gas at high temperature is available at the bottom of the cyclone, the driving force is large resulting in higher heat transfer rate. This is predominant till the solid feed rate is equal to critical solid feed rate. Also, the presence of more solid extracts more heat from the gas and hence the heat transfer rate increases.

Hence, it can be concluded that the increase in solid feed rate increases heat transfer rate for particles of 359 μm average size at most inlet air velocities. In Fig. 3, for solid feed rates less than 2 g/s, the data suggest that increasing air velocity does not increase heat transfer rates.

Figure 4 shows the variation of exit solid temperature with solid feed rate at different air velocities for particles of size 359 μm. It is clear from Fig. 4 that the exit solid temperature increases with solid feed rate up to a certain solid feed rate, after which the solid exit temperature decreases. This can be explained as follows:

The quantity of bypass air from outer to inner vortex governs

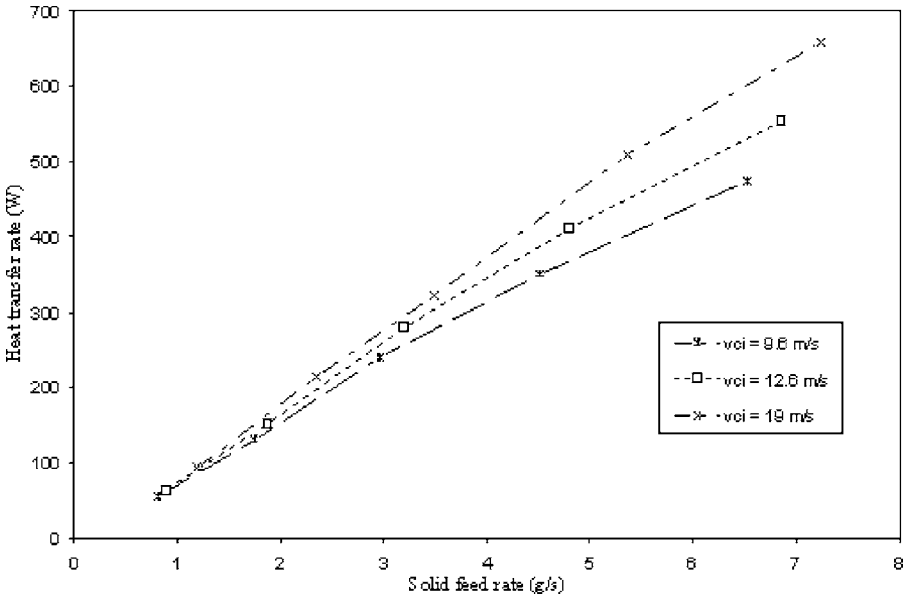

Fig. 3 Effect of solid feed rate on heat transfer rate at different inlet air velocities for average particle's size of 359 μm

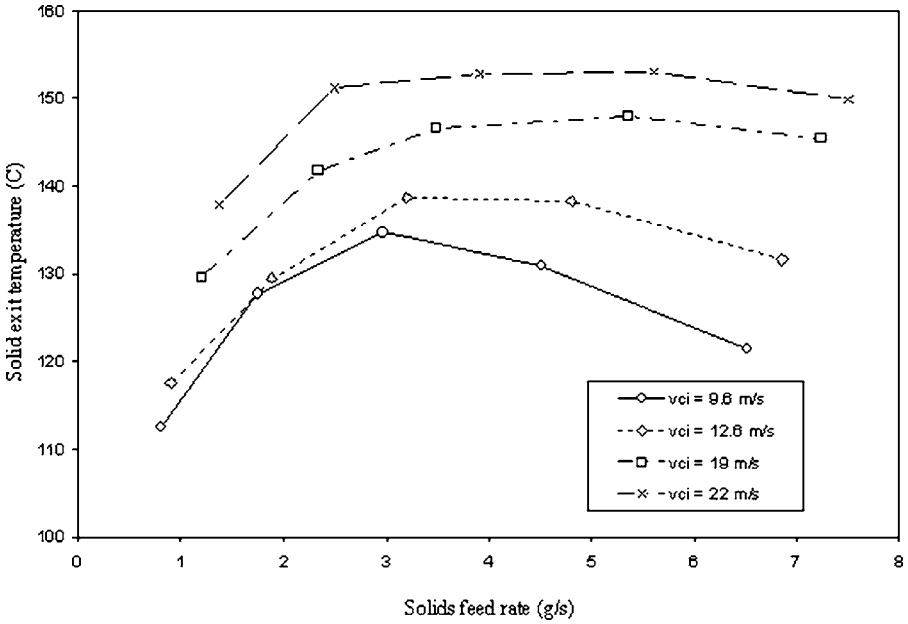

Fig. 4 Effect of solid feed rate on solid exit temperature at different inlet air velocities for average particle's size of 359 μm

the air available for heat transfer to solids in the outer vortex and the rise in solid temperature. With reduced bypass at higher solid feed rate, more gas at high temperature is available at the bottom, resulting in increased solid temperature. This occurs till the increase in solid feed rate exceeds the reduction in air bypass, after which the exit solid temperature decreases. Also with the increasing solid feed rate, the laminar boundary layer breaks down due to the increased number of particles approaching the wall. At low solid feed rate, when the particles are moving together, the access of air to the particles is less and therefore exit solid temperature is low. As the solid feed rate increases, particles spread over the cyclone wall and access of air to particle increases giving rise to higher solid temperature at exit. When the particle's flow pattern is stabilized, at the exit solid temperature is solely governed by heat balance leading to reduced exit solid temperature with rising solid feed rate. The same phenomenon is observed with the other average particle sizes investigated and is shown in Fig. 7 for air inlet velocity of 9.5 m/s.

Figure 5 shows the variation of heat transfer coefficient with the solid feed rate at different air inlet velocities for particles of size 359 μm. It is clear from Fig. 5 that the heat transfer coefficient increases with solid feed rate. Since the heat transfer rate and heat transfer area increase and ΔT decreases with increase in solid feed rate, the heat transfer coefficient increases. At lower solid feed rates, the increase in heat transfer coefficient is rapid, while at

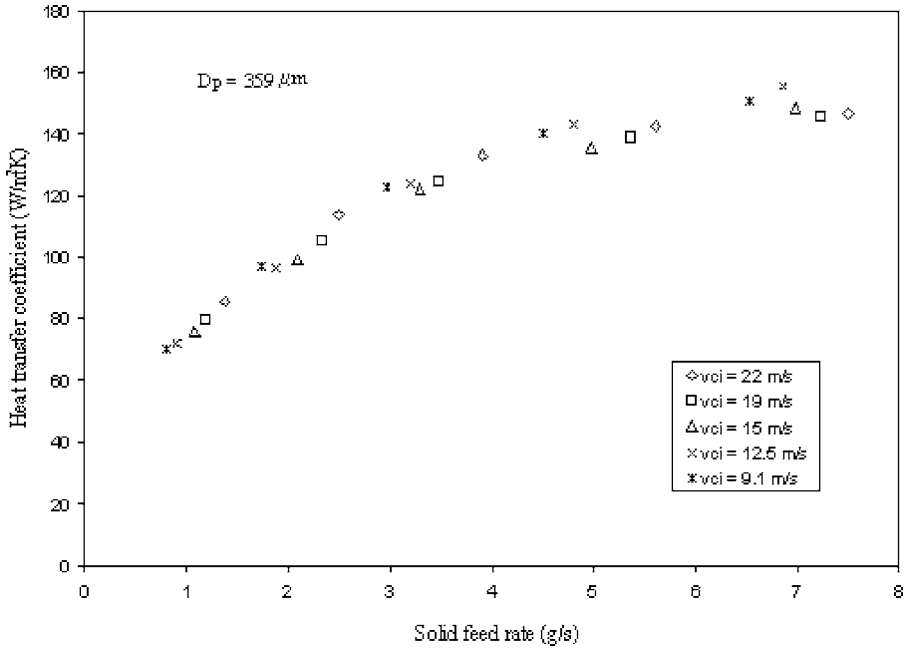

Fig. 5 Effect of solid feed rate on heat transfer coefficient for average particle's size of 359 μm at different air inlet velocities

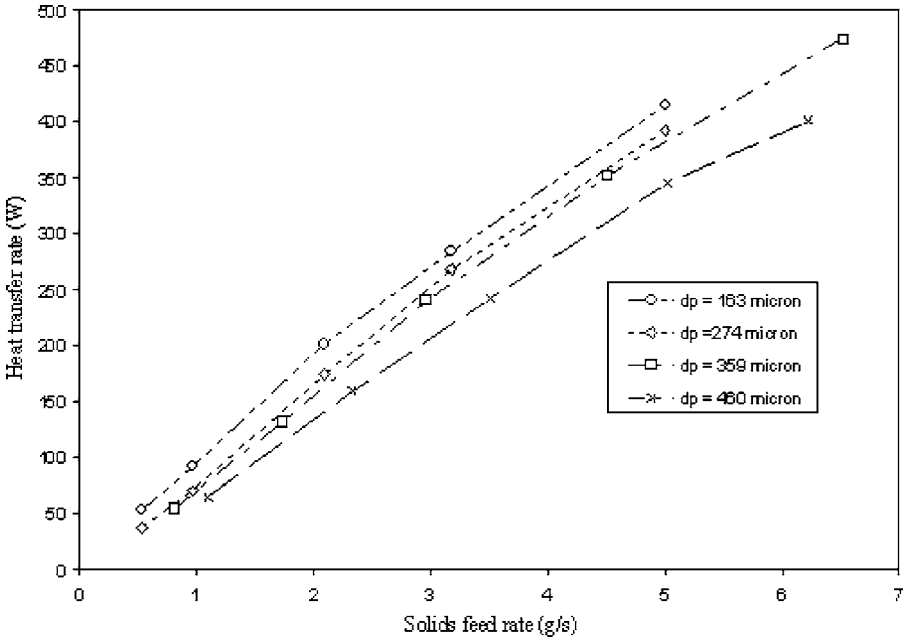

Fig. 6 Effect of average particle size on heat transfer rate at different solid feed rates for air inlet velocity of 9.5 m/s

higher feed rates, the rate of increase of heat transfer coefficient is low. Raju et al. [4] and Pawar and Bhaskara Rao [8] observed that the heat transfer coefficient increases with increasing solid to air mass flow rate ratio up to a certain value, after which heat transfer coefficient attains almost a constant value. Trends of those findings support the present data.

Effect of Inlet Velocity on Exit Solid Temperature, Heat Transfer Rate, and Heat Transfer Coefficient. To study the effect of inlet air velocity on gas-solid heat transfer in cyclone, airflow was varied with the help of valves V1 and V2. Solids of a particular size were fed at uniform rate and the exit air and solid temperatures were measured to determine the heat transfer rate. The results are plotted as shown in Fig. 3 for the particle of size 359 μm.

Figure 3 indicates that the heat transfer rate increases with the increase in inlet air velocity at constant solid feed rate. The rate of increase is predominant at higher solid feed rates, when compared with that at lower solid feed rates.

As the inlet air velocity increases at constant solid feed rate, mass flow rate of air increases. Therefore, with the increase in heat capacity of air, decrease in temperature of air is less. Subsequently, gas is available at high temperature at the bottom resulting in increased driving force. Hence, the heat transfer rate also increases. At lower solid feed rates, despite increasing the air inlet velocity, increase in heat transfer rate is less due to large bypass of the air. It can be concluded that increasing gas inlet velocity at higher solid feed rate results in appreciable increase in the heat transfer rate.

The effect of inlet air velocity on the solid exit temperature can be easily seen from Fig. 4, plotted for the particles of 359 μm average size. It can be seen from Fig. 4 that the exit solid temperature increases with the increase in inlet gas velocity at constant solid feed rate. This is observed for particles of all sizes and at all solid feed rates.

Due to the increase in heat capacity of air at higher inlet velocities, more gas at high temperature is available for the heat transfer. As a result of this, solids extract more heat from the gas, resulting in increase in the solid exit temperature due to the thermal balance between gas and the solid. Hence, it can be inferred that the increase in inlet air velocity results in higher exit solid temperature indicating rapid heat transfer.

Figure 5 shows that the heat transfer coefficient is essentially independent of inlet air velocity for a given solid feed rate for particles of size 359 μm. This behavior is observed for all sizes of particles at all solid feed rates investigated. In the range of air inlet velocities studied, the flow is turbulent. There is very little change in the flow profiles of velocity, pressure, and turbulence properties for the same cyclone geometry, despite the increase of over 300% in air flow rate. Hence, the effect of air velocity may not be pronounced in the cyclone, resulting in near uniform heat transfer coefficient at all velocities. Moreover, increase in heat transfer rate, heat transfer area, and log-mean temperature difference with increasing air velocity are such that net effect on heat transfer coefficient is nullified.

Yen et al. [3], Wamseley and Johanson [9] and Chang and Wen [10] made a similar observation. Hence, it can be concluded that the heat transfer coefficient is essentially independent of inlet air velocity.

Effect of Particle Size on the Exit Solid Temperature, Heat Transfer Rate, and Heat Transfer Coefficient. The effect of particle size on the heat transfer rate was studied by using solids of different sizes at nearly uniform air inlet velocity. Both the air velocity and solid feed rate could not be maintained constant for different particle sizes, as the combination of velocity with different size particles produces different solid feed rates. Hence, the effect of particle size on the heat transfer rate is plotted as a function of solid feed rate shown in Fig. 6 for an air inlet velocity of 9.5 m/s.

It can be seen from Fig. 6 that the heat transfer rate decreases with increasing particle size at all solid feed rates for an inlet air velocity of 9.5 m/s. This is also observed for other inlet velocities. The decrease is heat transfer rate is more predominant at higher solid feed rates.

Moreover, the change in heat transfer rate with particle size is small compared to that due to solid feed rate.

Figure 7 shows the variation of solid exit temperature with the particle size at different solid feed rates for an air inlet velocity of 9.5 m/s. It is clear from Fig. 7 that the exit solid temperature decreases with increasing particle size indicating lower heat transfer rate and heat recovery. This is attributed to the following:

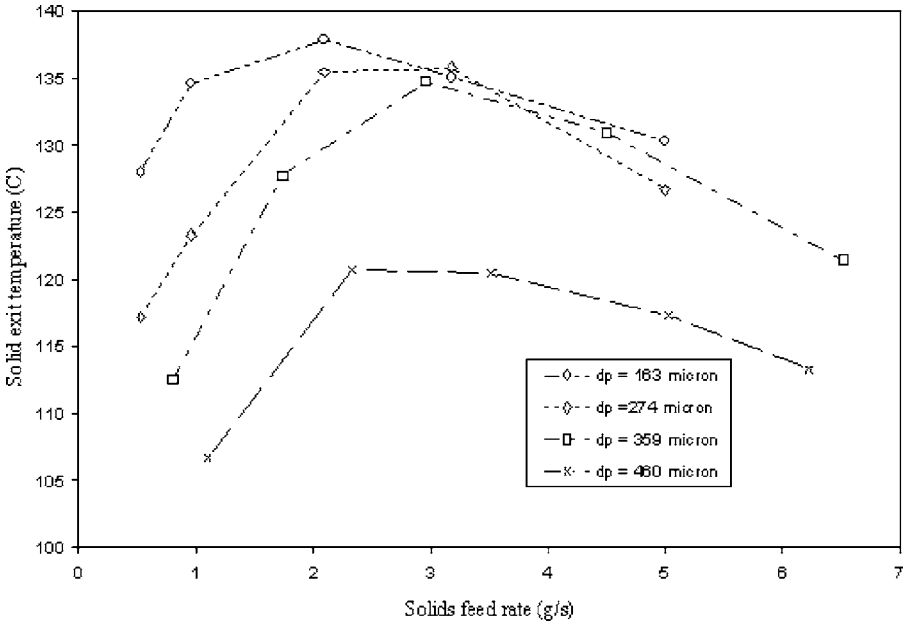

Fig. 7 Effect of average particle size on exit solid temperature at different solid feed rates for air inlet velocity of 9.5 m/s

Total heat transfer area is higher for smaller size particles for the same solid feed rate. As heat picked up by a particle is directly proportional to the area of the particle, more smaller particles at the same feed rate are in a position of advantage than the bigger particles. Hence, the bigger particles pick up less heat and the exit temperature of solid decreases for larger size particles.

Hence, with increase in particle size, the heat recovery, heat transfer rate as shown in Fig. 6 and the exit temperature of solids (Fig. 7) both decrease at constant solid feed rates.

Also, it can be observed from Fig. 8 that the heat transfer coefficient increases with increasing particle size at all solid feed rates for an inlet air velocity of 9.5 m/s. This is observed at all the inlet air velocities under study. With the increase in particle size, the rate of heat transfer decreases (Fig. 6) as a result of which the exit solid temperature also decreases (Fig. 7). Also, with the larger particles, hold up decreases due to increased drag. The total heat transfer area, as expressed in Eq. (4), is proportional to hold up. Hence the total heat transfer area decreases with increase in the particle size.

The larger particle sizes decrease the heat transfer rate, log-mean temperature difference, and the heat transfer area, in such a way that the heat transfer coefficient is increased. Hence, with higher particle size, higher heat transfer coefficients are achieved.

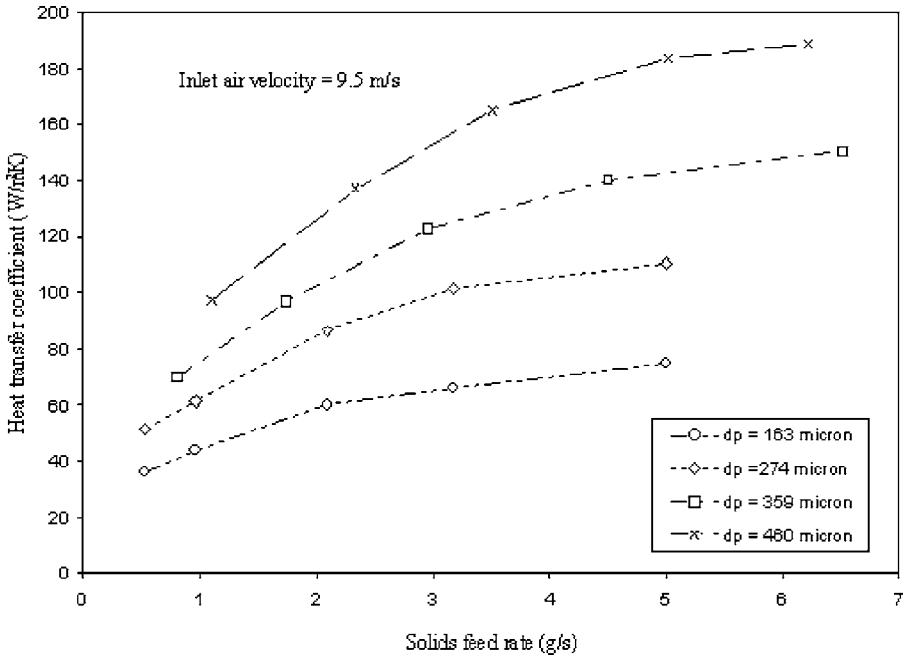

Fig. 8 Effect of particle size on heat transfer coefficient at different solid feed rates for air inlet velocity of 9.5 m/s

Prediction of Heat Transfer Coefficient Data With the Correlations in the Literature. Yen et al. [3] carried out experiments on air-sand heat transfer and air-cement raw meal heat transfer in a reverse flow cyclone of 120 mm diameter. Similarly, Raju et al. [4] conducted heat transfer studies in a reverse flow cyclone of 130 mm diameter for air-sand system. Correlations for heat transfer coefficient in terms of Nusselt number, Reynolds number, solid-gas mass flow ratio, and Prandtl number were proposed by Yen et al. [3] and Raju et al. [4]. Since these correlations were developed for nearly the same cyclone diameter, they are tested for their suitability to predict the current experimental results. The correlations are as follows:

Yen et al. [3] correlation:

$$\mathrm{Nu}_c = 1300\mathrm{Re}_c^{0.41}F_m^{0.47}\left(\frac{2d_p}{D_c}\right)\mathrm{Pr}^{1/3} \tag{6}$$

Raju et al. [4] correlation:

$$\mathrm{Nu}_p = 0.001217\mathrm{Re}_p^{1.41}F_m^{0.501}\mathrm{Pr}^{2/3} \tag{7}$$

where Nu_p, Re_p, Pr, and F_m are defined as

$$\mathrm{Nu}_c = \frac{h_p D_c}{k_a} \tag{8}$$

$$\mathrm{Re}_c = \frac{D_c v_{ci}\rho_a}{\mu_a} \tag{9}$$

$$\mathrm{Pr} = \frac{c_{pa}\mu_a}{k_a} \tag{10}$$

$$F_m = m_s/m_a \tag{11}$$

The correlation of Yen et al. [3] consistently over predicts the present data within an error band of 100%–20%. The trend of the predicted heat transfer coefficient matches with the present experimental data. However, all the predicted values are higher by a factor of about 1.67. The correlation of Raju et al. [4] predicts the present data within 10% to −70% and in general the correlation under predicts the data. Scatter in data points suggests that the correlation lacks in terms of some pertinent group.

Development of a New Correlation for Heat Transfer Coefficient. Nusselt number, particle Reynolds number, and Prandtl number have been widely used to correlate gas-particle heat transfer coefficient. The particle Reynolds number is computed based on cyclone inlet air velocity as widely done by Yen et al. [3] and Raju et al. [4]. The flow inside a cyclone is very complicated because of its three-dimensional nature and presence of tangential, radial, and axial velocity components. The tangential velocity component is about ten times higher than the radial or vertical components. The tangential velocity in the outer vortex is minimum near the cyclone wall and increases towards the axis. In the vicinity of the wall, where most of the particles are present, the tangential velocity is approximately equal to the gas velocity on entry. Hence, the inlet velocity is used as the characteristic velocity in the particle Reynolds number.

Nusselt number is considered as a function of Fedorov number as proposed by Ludera [11]. Fedorov number is a function of particle size and physical properties of air and solid particles as given below:

$$\mathrm{Fe} = d_p\left[\frac{4g\rho_a^2}{3\mu_a^2}\left(\frac{\rho_s}{\rho_a} - 1\right)\right]^{1/3} \tag{12}$$

Gnielinski [12] defined mean Nusselt number for flow through a packed bed and a fluidized bed as a function of Nusselt number for single sphere as

$$\mathrm{Nu}_p = f_\varphi \mathrm{Nu}_{\text{single sphere}} \tag{13}$$

Gnielinski expressed f_φ as a function of porosity. In general, f_φ may be a function of all relevant parameters other than Reynolds number and Prandtl number, which influence the particle and gas flow and their mutual interaction.

For developing a correlation in the present study, Gnielinski's approach has been adopted, giving a form to the proposed correlation as:

$$\frac{\mathrm{Nu}_p}{\mathrm{Nu}_{\text{single sphere}}} = b_1\mathrm{Fe}^{b2}F_m^{b3} = f(\phi) \tag{14}$$

Nusselt number for single sphere is defined as (Jain [13])

$$\mathrm{Nu}_{\text{single sphere}} = 2 + 0.664\mathrm{Re}_p^{0.5}\mathrm{Pr}^{0.33} \tag{15}$$

Incorporating Eq. (15) in Eq. (14),

$$\mathrm{Nu}_p = b_1\mathrm{Fe}^{b2}F_m^{b3}(2 + 0.664\mathrm{Re}_p^{0.5}\mathrm{Pr}^{0.33}) \tag{16}$$

The coefficient b_1 and exponents b_2 and b_3 have been evaluated by regression analysis as described in Kafarov [14] for the present experimental data having solid-to-air mass flow ratio range from 0.05 to 0.87 and Fedorov number range from 5.63 to 17.3, particle Reynolds number range from 46.8 to 308, Prandtl number range from 0.68 to 0.69 and Nusselt number range from 0.15 to 2.45. The resulting correlation is

$$\mathrm{Nu}_p = 0.0047\mathrm{Fe}^{1.45}F_m^{0.375}(2 + 0.664\mathrm{Re}_p^{0.5}\mathrm{Pr}^{0.33}) \tag{17}$$

The heat transfer coefficients predicted by Eq. (17) are compared with the present experimental data in Fig. 9. It shows the plot of predicted value of heat transfer coefficients for the present experimental conditions and the experimental data.

It is clear from the figure that the proposed correlation predicts the present experimental data very well within an error of +10% to −15% with a correlation coefficient (R^2) of 0.986.

To validate further, the proposed correlation has been used to predict the heat transfer coefficients for the data of Yen et al. [3] and Raju et al. [4]. The proposed correlation predicts their data within an error band of −15% to 25% The proposed correlation may be further improved by incorporating the effect of cyclone dimensions, which requires experiments to be carried out using cyclones of different dimensions.

Conclusions

The following conclusions can be drawn from the present study of air-to-solid heat transfer in a cyclone:

1. The air-solid heat transfer rate increases with increasing solid feed rate, inlet air velocity, and decreasing particle size.
2. The average heat transfer coefficient between air and the solid particles in the cyclone is found to be essentially independent of air velocity investigated, increases with increasing particle size, and increases with increasing solid feed rate with progressively reducing rate.
3. The proposed correlation predicts heat transfer coefficients of the present investigation within an error band of 10% to −15% and that of earlier investigators' data within an error band of +25% to −15%. This appears to be an improvement over the correlations proposed by Yen et al. [6] and Raju et al. [4].

Nomenclature

English Symbols

A = total particles heat transfer area, m^2
Bi = biot number
b_1, b_2, b_3 = constants
c_{pa} = specific heat of air, J/kg K
c_{ps} = specific heat of solid, J/kg K
D_c = diameter of cylindrical section of cyclone, m
d_p = particle diameter, m
Fe "Eq. (12)" = Fedorov number

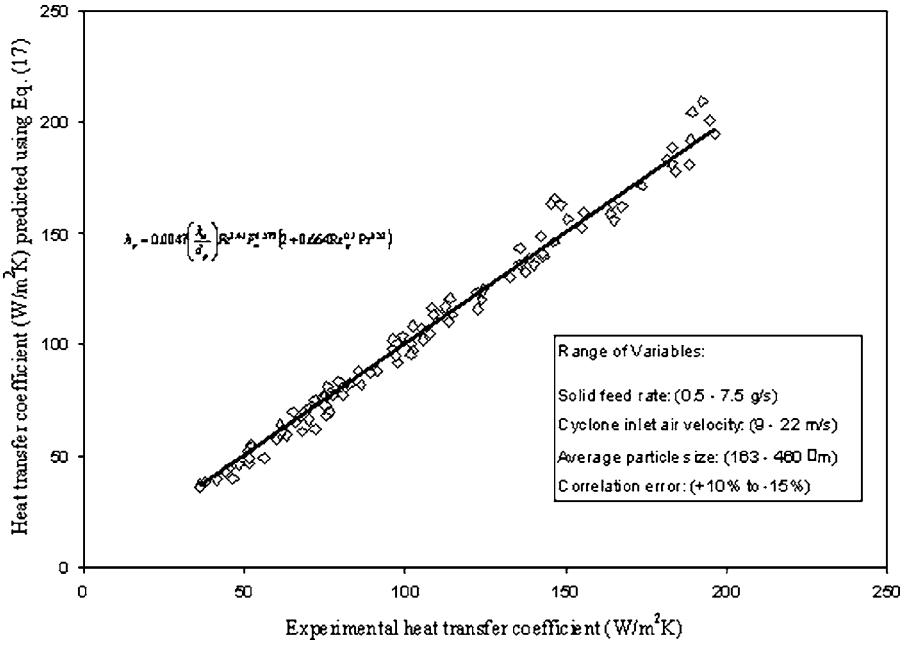

Fig. 9 Comparison between heat transfer coefficients predicted using Eq. (17) and experimental heat transfer coefficients

F_m "Eq. (11)" = solid loading ratio
f_ϕ "Eq. (14)" = a function of porosity
g = gravitational acceleration, m/s^2
h_p = gas-particle heat transfer coefficient, $W/m^2\,K$
k_a = thermal conductivity of air, W/m K
k_s = thermal conductivity of solid, W/m K
m_a = mass flow rate of air, kg/s
M_h = holdup of solid, kg
m_s = mass flow rate of solid, kg/s
Nu_p = particle Nusselt number
$Nu_{single\ sphere}$ = single particle Nusselt number
Pr = Prandtl number
q = heat transfer rate, W
R = Particle radius, m
Re_p = particle Reynolds number
T_{Gin}, T_{Gout} = inlet and exit air temperatures, C
T_{Sin}, T_{Sout} = inlet and exit solid temperatures, C
v_{ci} = cyclone inlet air velocity, m/s

Greek Symbols

ε = volume fraction of hold-up of solid
ρ_s = density of solid, kg/m^3
μ_a = viscosity of air, Ns/m^2
ρ_a = density of air, kg/m^3
ΔT = log-mean temperature difference, K

References

[1] Ramanan, P., Rao, T. R., and Pitchumani, B., 1997, "Studies in Industrial Cyclone Heat Exchanger," *Proc. International Conf. on Heat and Mass Transfer*, Kanpur, India.
[2] Pitchumani, B., Andries, J., and Scarlett, B., 1991, "Cyclone Performance at High Temperature and Pressure," Industries minerals, Mines et carrieres les-technique, pp. 171–176.
[3] Yen, S. C., Lu, W.-M., and Shung, S. C., 1990, "Gas-Solid Heat Transfer in a Gas Cyclone," J. Chin. Inst. Eng., **21**(4), pp. 197–206.
[4] Raju, A. V., Sita, R., Subrahamanyam, J. P., Rao, T. R., and Pitchumani, B., 1994, "Gas-Solid Heat Transfer in Cyclone Heat Exchanger," Indian Chem. Eng., Sect. A, **36**(1–2), pp. 58–62.
[5] Perry, R. H., Chilton, H., and Cecil, H., 1976, *Chemical Engineers' Handbook*, 5th edition, McGraw-Hill, Kogakusha, Tokyo.
[6] Lapple, C. E., 1951, "Process Uses Many Collector Types," Chem. Eng. J., **58**(5), pp. 144–151.
[7] Szekely, J., and Carr, R., 1966, "Heat Transfer in a Cyclone," Chem. Eng. Sci., **21**(12), pp. 1119–1132.
[8] Pawar, K., and Bhaskara, R., 1988, "Cyclone Heat Exchanger," M.Tech thesis, Indian Institute of Technology, Delhi, India.
[9] Wamseley, W. W., and Johanson, L. N., 1954, Chem. Eng. Prog., **50**, pp. 347.
[10] Chang, T. M., and Wen, C. Y., 1966, "Fluid-to-Particle Heat Transfer in Air-Fluidized Beds," Chem. Eng. Prog., Symp. Ser., **62**(67), pp. 111–117.
[11] Ludera, L. M., 1988, "Design Methods for Cyclone Preheaters of Rotary Kilns," Zem.-Kalk-Gips, **41**(11), pp. 551–558; 1989, translation in Zem.-Kalk-Gips, **42**(1), pp. 10–12.
[12] Gnielinski, V., 1981, "Equations for the Calculation of Heat and Mass Transfer During Flow Through Stationary Spherical Packings at Moderate and High Peclet Numbers," Int. Chem. Eng., **21**, pp. 378–383.
[13] Jain, A., 2003, "Studies on Gas-Solid Heat Transfer in Cyclone," Ph.D. thesis, Indian Institute of Technology, Roorkee, India.
[14] Kafarov, V., 1976, *Cybernetic Methods in Chemistry and Chemical Engineering*, Mir, Moscow.

Numerical Study of the Heat Transfer Rate in a Helical Static Mixer

Ramin K. Rahmani
Research Assistant
e-mail: rkhrahmani@yahoo.com

Theo G. Keith
Distinguished University Professor
ASME Fellow
e-mail: tkeith@eng.utoledo.edu

Anahita Ayasoufi
Research Assistant
e-mail: aayasoufi@yahoo.com

Department of Mechanical, Industrial and Manufacturing Engineering,
The University of Toledo,
Toledo, OH 43606

In chemical processing industries, heating, cooling, and other thermal processing of viscous fluids are an integral part of the unit operations. Static mixers are often used in continuous mixing, heat transfer, and chemical reactions applications. In spite of widespread usage, the flow physics of static mixers is not fully understood. For a given application, besides experimentation, the modern approach to resolve this is to use powerful computational fluid dynamics tools to study static mixer performance. This paper extends a previous study by the authors on an industrial helical static mixer and investigates heat transfer and mixing mechanisms within a helical static mixer. A three-dimensional finite volume simulation is used to study the performance of the mixer under both laminar and turbulent flow conditions. The turbulent flow cases were solved using $k-\omega$ model. The effects of different flow conditions on the performance of the mixer are studied. Also, the effects of different thermal boundary conditions on the heat transfer rate in static mixer are studied. Heat transfer rates for a flow in a pipe containing no mixer are compared to that with a helical static mixer. [DOI: 10.1115/1.2217749]

Keywords: static mixer, heat transfer rate, thermal conductivity, turbulent flow, residence time distribution

Introduction

In chemical processing industries, heating, cooling, and other thermal processing of viscous fluids are an integral part of the unit operations. In these processes, mechanical heat transfer predominantly occurs by screws or scraping vanes. But, thermal processing by conventional equipment with mechanically moving parts has several shortcomings, including abrasion, contamination, fluid leakage, and abnormal stagnation of fluid. Furthermore, revolving scrapers may consume more energy and contaminate the product being processed with metallic tailings from the scrapings. Static mixers can be employed for those applications. The range of practical flow Reynolds numbers for helical static mixers in industry is usually from very small ($\mathrm{Re} \approx 0$) to moderate values (e.g., $\mathrm{Re} = 5000$).

Static mixers have been utilized over a wide range of applications such as continuous mixing, blending, heat transfer processes, chemical reactions, etc. The device relies on a systematic splitting, reorientation, and recombination of two fluids using a series of mixing elements. Static mixers offer several advantages. For example, they have low maintenance, low space requirements, and no moving parts. Moreover, because of the increased internal film coefficients and heat transfer rates provided by motionless mixer elements, heat exchanger designs utilizing static mixers can be smaller than conventional shell-tube heat exchangers.

One typical static mixer, the helical static mixer, consists of left- and right-twisting helical elements placed at right angles to each other (Fig. 1). The helical insert causes a secondary flow in plane perpendicular to the predominant axial flow. Compared to a tube of the same length and same diameter with no mixer, the helical static mixer is able to provide a substantial enhancement of heat and mass transfer from the surface of the tube to the fluid. Static mixer elements can reduce film buildup and improve heat transfer, allowing the reduction of heat exchanger size and space requirements. Static mixers can provide a more uniform temperature distribution in flow field, and prevent the occurrence of local heating or cooling.

Due to the industrial importance of static mixers, many studies have been undertaken in an attempt to characterize their performance. Pressure drop across a static mixer was measured experimentally [1–5], since this information is essential in order to correctly size the pump feeding the static mixer. Mass transfer [6] and also drop size distribution [7] in static mixers have also been studied experimentally.

A number of studies have considered heat transfer in different static mixers [8–13]. Joshi et al. studied wall to tube heat and mass transfer in a Kenics static mixer and recommended that a more compact mixing element [9] can improve the rate of heat transfer. Li et al. [10] studied pressure drop, heat transfer, and mixing mechanism in a Sulzer SMX static mixer. Based on their experimental results, a general heat transfer coefficient correlation in a Sulzer SMX mixer shows an enhancement of up to a factor of 5 compared to a tube with no mixing element [10].

For a given application, besides experimentation, the modern approach to study the performance of a helical static mixer is to use powerful computational fluid dynamics (CFD) tools. In recent years, significant progress has been made in the characterization of fluid-mechanical mixing using Lagrangian tracking techniques [14–19]. The majority of the previous work on static mixers has focused on model flows that are two dimensional in space and periodic in time. A smaller set of studies has considered simple, three-dimensional, spatially periodic flows, e.g., [14,15] where a simplified, two-dimensional analytical approximation to the velocity field was obtained.

The static mixer studied here is an industrial helical static mixer: the TAH static mixer (Robbinsville, NJ). The mixer geometrical parameters are shown in Table 1. Each mixing element twists through an angle of 180 deg. The solid material thickness of the mixer is about 22% of each segment length, which makes the zero thickness assumption of the mixer, as has been used in previous studies, questionable. Also, the ratio of the each segment

Contributed by the Heat Transfer Division of ASME for publication in the JOURNAL OF HEAT TRANSFER. Manuscript received February 13, 2005; final manuscript received February 13, 2006. Review conducted by Karen Thole. Paper presented at the 2004 ASME International Mechanical Engineering Congress (IMECE2004), November 13–19, 2004, Anaheim, CA.

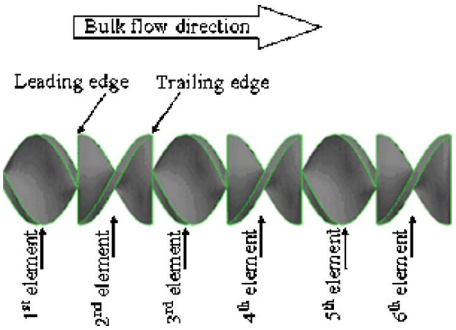

Fig. 1 A six-element static mixer

length to the mixer diameter is about 0.846. In a standard Kenics mixer, the segment length is 1.5–2.5 times the mixer diameter.

Generally, the heat transfer rate in a static mixer is a function of the physical properties of the working fluid and the solid surface, the flow conditions, and the geometrical parameters of the mixer. Since in this study, the working fluid and the geometrical parameters are not changed, the heat transfer rate can only be related to the flow conditions and the thermal boundary conditions. The effects of different flow conditions and different thermal boundary conditions on the performance of the mixer are studied. Heat transfer rates for a flow in a pipe containing no mixer are compared to those with a helical static mixer.

Analysis

For steady incompressible flow, the mass conservation and the momentum equations can be written as

$$\frac{\partial u_i}{\partial x_i} = 0 \tag{1}$$

$$\rho \frac{\partial (u_i u_j)}{\partial x_j} + \frac{\partial p}{\partial x_i} = \frac{\partial \tau_{ij}}{\partial x_j} + \rho g_i + F_i \tag{2}$$

In the absence of a gravitational body force and any external body force, the two last terms on the right side of Eq. (2) are zero.

The energy equation for steady incompressible flow is

$$\frac{\partial (\rho u_i E + p)}{\partial x_i} = \frac{\partial}{\partial x_i}\left(K \frac{\partial T}{\partial x_i} + u_j \tau_{ij} \right) \tag{3}$$

The stress tensor, τ_{ij}, in Eq. (2) and Eq. (3) is given by

$$\tau_{ij} = \mu \left(\frac{\partial u_i}{\partial x_j} + \frac{\partial u_j}{\partial x_i} \right) - \frac{2}{3} \mu \frac{\partial u_k}{\partial x_k} \delta_{ij} \tag{4}$$

where μ is the molecular viscosity. It is mentioned that for an incompressible steady flow the last term of Eq. (4) is zero.

The first term on the right hand side of Eq. (3) is heat conduction term. The second term on the right hand side is the viscous dissipation term. The importance of viscous dissipation is well known in flow in capillary tubes and flow of very viscous fluids [20,21]. The effect of viscous dissipation on the flow is also significant in micro-fluidic devices [22,23]. For thermally developing laminar forced convection in a pipe, significant viscous dissipation effects have been observed for large Brinkman numbers [21]. This effect is more pronounced when the fluid is cooling by the surface of the solid wall, which has a temperature lower than the temperature of the flow [21]. The total energy in Eq. (3) is

$$E = h - \frac{p}{\rho} + \frac{u_i u_i}{2} \tag{5}$$

For a pure material with no phase change the enthalpy is given by

$$h = \int_0^T c_p dT \tag{6}$$

For the material used in this study, water, value of density is 998.2 kg/m^3. Although the specific heat is a function of temperature, for the temperature range used in this study its changes can be neglected; hence, specific heat is set at 4182 J/kg K. However, for the thermal conductivity and the viscosity, the change of their values based on the temperature is significant and has an impact on the results of the numerical simulation. Therefore, the thermal conductivity and the viscosity are assumed piecewise linear functions of the temperature using the values from [24].

Table 1 Static mixer geometry

Diameter (d)	4.80 mm
Segment (element) length	4.06 mm
Thickness	0.89 mm
Entrance length	9.60 mm
Exit length	9.60 mm

Numerical Simulation

Mesh Generation. Effective numerical processes for CFD problems depend on the geometric modeling as well as the grid generation and grid quality. An unstructured mesh was generated to model the static mixer inside a pipe; the geometry was modeled completely, with no simplifications. To achieve the most accurate results from the solver all efforts have been made to maximize the quality of the mesh using the technique described in detail in [25]. For the laminar cases, a uniform computational grid containing 1,333,173 cells was used to compute the flow fields. For the turbulent case, a non-uniform grid with 2,345,777 cells was used. The distance of the computational cell centroid from the solid wall measured in viscous length, $y^+ = y\sqrt{\rho \tau_w}/\mu$, was monitored in order to measure the fineness of the mesh in near wall region. For the mesh used in this study it was observed that y+ is equal or less than 2.97.

Heat and Mass Flow Computation. The solver used in this study for the flow computation is a commercial code (FLUENT[1]). This code uses the Eulerian approach to solve the equations on a computational mesh, based on a cell-centered finite volume discretization. The selected solver is a segregated, implicit, second-order upwind [26], double precision, finite volume solver.[2] Using the segregated approach, the governing equations are solved sequentially. To obtain second-order accuracy, quantities at the cell faces are computed using a multidimensional linear reconstruction approach [26,27]. Pressure-velocity coupling is achieved by using the SIMPLEC (SIMPLE-Consistent) algorithm [28].

Turbulence Model. Turbulent flows are characterized by fluctuating velocity fields. These fluctuations mix transported quantities of mass, momentum, and energy and in turn cause the transported quantities to fluctuate as well. These fluctuations can be of small scale and high frequency, therefore they are too expensive to simulate directly. Different turbulence modeling techniques can be found in the literature, e.g., [29–32]. In this study, for turbulent case (Re=3000), the three-dimensional, steady Reynolds-averaged, Navier-Stokes equations are solved. The momentum equation can be written as

$$\rho \frac{\partial (u_i u_j)}{\partial x_j} = \frac{\partial}{\partial x_j}\left[\mu \left(\frac{\partial u_i}{\partial x_j} + \frac{\partial u_j}{\partial x_i} \right) - \frac{2}{3} \mu \frac{\partial u_k}{\partial x_k} \delta_{ij} \right] - \frac{\partial p}{\partial x_i} + \frac{\partial}{\partial x_j}(-\rho \overline{u_i' u_j'}) \tag{7}$$

[1] FLUENT is a registered trademark of Fluent Inc., Lebanon, NH.

[2] Other choices are available in FLUENT; the set of solver here is the appropriate one for this study.

For the incompressible flow Eq. (7) is reduced to the following

$$\rho\frac{\partial(u_i u_j)}{\partial x_j} = \frac{\partial}{\partial x_j}\left[\mu\left(\frac{\partial u_i}{\partial x_j} + \frac{\partial u_j}{\partial x_i}\right)\right] - \frac{\partial p}{\partial x_i} + \frac{\partial}{\partial x_j}(-\rho\overline{u_i' u_j'}) \quad (8)$$

The Reynolds stresses, $-\rho\overline{u_i' u_j'}$, must be modeled in order to close the set of equations. A common method employs the Boussinesq hypothesis to relate the Reynolds stresses to the mean velocity gradients. In this study the $k-\omega$, as a Boussinesq approach model, is employed to solve the turbulent flow. The $k-\omega$ model, which was introduced by Kolmogorov [33] in 1942, was selected for two reasons. First, the $k-\omega$ model is valid all the way to the wall boundary, and so, the wall-function approach that bridges the gap between the fully turbulent region and the viscous sublayer is not needed. Turbulence models that rely on the wall-function approach, although expedient from a computational standpoint, are not suitable for quantitatively accurate predictions of complex, three-dimensional flows with strong vortices [34]. Second, the $k-\omega$ model has been validated extensively in complex, three-dimensional shear flows and has been shown to be superior to $k-\varepsilon$-type models [35,36]. Also, comparisons between the results obtained by $k-\omega$ and Reynolds stress model (RSM) turbulent models show that the $k-\omega$ has enough accuracy to capture the main aspects of mixing flows, while it is computationally much less expensive than the RSM model [25]. The $k-\omega$ model used in this study has been introduced by Menter in 1994 [37], referred to as shear-stress transport (SST) model or the SST $k-\omega$ model, which is a modified version of the original $k-\omega$ model of Wilcox [38].

Boundary Conditions. The fluid temperature at the inlet is set to 298.15 K (25°C) for all cases but one, which is set to 278.15 K. The pipe surface in the entrance and exit regions where there are no mixing elements is adiabatic. Heat conduction flux in a material depends upon the material thermal conductivity and temperature gradient in the material. Two extreme limits for the value of thermal conductivity are zero and infinity; the thermal conductivity of a real material lays somewhere between these to limits. Zero thermal conductivity can be modeled by adiabatic conditions and infinite thermal conductivity can be modeled by constant temperature distribution in the material. Two different boundary conditions are applied to the mixer surface: as the first boundary condition the mixer surface is considered adiabatic; and as the second boundary condition, the mixer surface temperature is considered constant. These two boundary conditions on the mixer surface model two extreme limits for the mixer performance based on the thermal properties of a material that can be used to manufacture a helical static mixer: a material with no conductivity and a super conductive material. The pipe surface temperature in the region including the static mixer is set at various constants (318.15, 348.15, and 368.15 K). No-slip boundary conditions are applied to the solid surface of the static mixer and also at the wall of the pipe. A constant mass flow rate is applied at the inlet and outlet boundaries. Different Reynolds numbers for the flow inside the pipe are obtained by varying the mass flow rate at the inlet boundary. The velocity profile for fully developed flow in a pipe (parabolic distribution for laminar flow and one seventh-root law for turbulent flow) is used at the flow field inlet. The turbulence intensity is used to specify the turbulent boundary conditions at the flow inlet. Moreover, low-Reynolds-number correction is applied at the near wall region.

Residence Time Distribution. The residence time distribution (RTD) is used to characterize the uniformity of the history of fluid elements in the static mixer. A similar history for all fluid elements in the flow is a desirable feature in order to provide the uniformity of the product quality. This can be achieved by a narrow distribution of the residence times for chemical reactors. RTD for flows in a static mixer has been studied experimentally [39] and numerically [40–43]. Here, the RTD for flow in a helical static mixer was calculated by tracking about 55,000 uniformly spaced, zero-mass, zero-volume, particles initially located on a plane at the inlet in the top half of the flow field inlet. For a steady flow, the particle trajectories correspond to streamlines. Therefore, trajectories are tracked by integrating the vector equation of motion, using the numerically computed velocity field as input.

$$\frac{dx_i}{dt} = u_i \quad (9)$$

Some care must be taken in integrating the equation that describes particle motion in order to retain a sufficient degree of accuracy [25]. The number of lost particles (particles that have trajectories cause them to be trapped near a solid wall, where the local velocity is zero, or leave the computational domain) is maximum for the case of turbulent flow (Re=3000), which is 6.89% of particles entered the flow field inlet.

The residence time of each particle was measured from the point when the particle passed the cross sectional plane of the leading edge of the first mixing element to the point when the particle crossed the cross sectional of trailing edge of the last mixing element. The measured residence time is nondimensionalized by the residence time of a fluid particle traveling at the bulk flow velocity in a pipe with no mixer. Given the value of the non-dimensionalized residence time (t^*) for all fluid particles which have passed the cross-sectional plane, the fraction of the volumetric flow which has a residence time between t^* and $t^* + dt^*$ can be calculated. This parameter is known as the distribution function, $f(t^*)$.

For the turbulent flow case, some considerations are needed. In turbulent flows scalar transport and stirring are the result of both the large-scale coherent vortices and the broad range of turbulent eddies. Reynolds averaged navier-stokes (RANS) modeling procedure smoothes the flow field and, therefore, particle tracking, using the statistically stationary mean flow as the advecting velocity field, does not take into account the effect of small scale turbulence on transport. In order to overcome this shortcoming, turbulent Reynolds stresses can be used to generate instantaneous velocity [25]. In this study, a random flow generation technique presented by Smirnov et al. [44] is employed, which is able to generate a realistic instantaneous flow field efficiently. This velocity domain, then, is used in order to compute the trajectories of fluid elements and determine the residence time distribution.

Temperature Difference Ratio. To decrease the temperature gradient of two fluids entering into a pipe, helical static mixers can be employed. Effectiveness of static mixers can be estimated using a non-dimensional ratio of the temperature difference in fluid at a specific flow cross section in a pipe containing a static mixer to that in an empty pipe of the same diameter. If this ratio is greater than one, the static mixer is not effective; however, this situation does not actually occur in practice. The smaller this ratio is, the more efficient the static mixer becomes. When this ratio is zero at a flow cross section, it means that in there is no temperature difference in that cross section of the pipe which contains a static mixer. When this ratio is one, it means that the static mixer has no impact on temperature blending of fluid elements in the flow. Temperature difference ratio (TDR), in a given flow cross section, can be defined as

$$\mathrm{TDR} = 1 - \frac{(T_{\max} - T_{\min})_{\text{pipe with mixer}}}{(T_{\max} - T_{\min})_{\text{pipe without mixer}}} \quad (10)$$

TDR is between zero and one. The higher TDR generally means that the static mixer is more efficient. However, when TDR=1, it cannot determine the mixer efficiency. It is possible that the temperature gradient of fluid inside an empty pipe of the same diameter is also very small, or the temperature gradient might be significant. In this situation, other parameters rather than TDR should be considered in order to evaluate the performance of mixer.

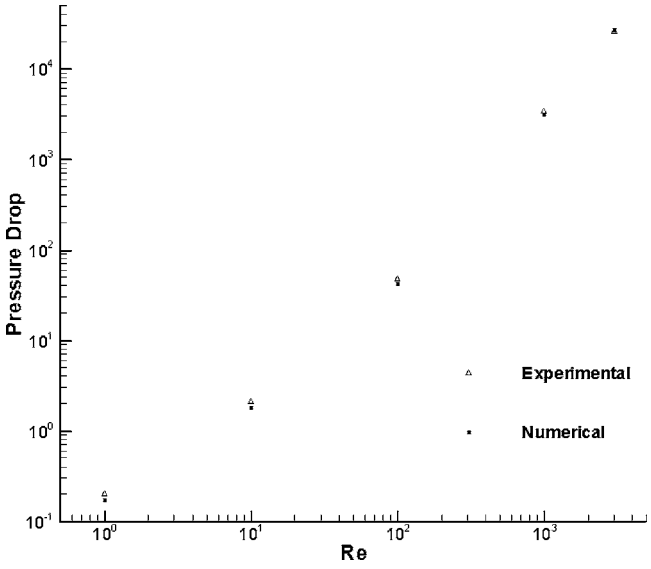

Fig. 2 Comparison between the predicted pressure drop and the experimental data (Pa)

Heat Flux Ratio. The ratio of heat flux from the solid wall into the fluid in a pipe containing a static mixer to the heat flux in a pipe with no mixer is the heat flux ratio. In practice, helical static mixers, which are used in heat exchangers, are made of thermally conductive materials such as copper. Therefore, static mixers are able to increase the heat flux significantly. For cases in which the static mixer is made from a non-conductive material, the heat flux ratio can be close to one or slightly less than one, depending on the flow conditions.

Numerical Solution Accuracy. The accuracy of the numerical solutions should be analyzed before confidence in the predictive ability of the numerical techniques can be justified. For the present study of mixing under non-creeping flow conditions, there is unfortunately an absence of sufficiently detailed and accurate experimental data to undertake a complete validation of the numerical results. Accordingly, a detailed mesh convergence study was performed and indicated that the computational mesh employed in the present study is sufficiently refined to provide good numerical resolution. It is noted that 1,333,173 mesh cells were used to compute the flow fields. The value of heat flux from the solid surfaces to the fluid, predicted by a computational grid containing 2,211,841 cells, is only 0.447% more than the value of heat flux predicted by the grid with 1,333,173 cells, when Re $=100$.

Figure 2 compares the predicted values for pressure drop across the mixer to the experimentally measured values from flow Reynolds number that ranged from 1 to 3000. Here, the pressure drop is defined as the absolute difference between the area-weighted average pressure at the computational flow field upstream and the area-weighted average pressure at the flow field downstream. The values of pressure drop across the mixer, obtained numerically, are found to be in good agreement with the experimental data. The computed values of Nusselt number for a fully developed flow in a long tube with no mixer shows good agreement with the experimental equation given by Seider and Tate [45,46]. The maximum error occurs for Re $=10$, at which the computed Nusselt number is 0.885 of the Nusselt number given by the Seider-Tate equation. The predicted values for Nusselt numbers for a pipe with static mixer shows agreement with the experimental data; the maximum error occurs when Re $=1$, using the constant temperature boundary condition, which is about 19%.

Results and Discussion

The heat transfer and flow in a six-element static mixer has been analyzed for a number of different conditions. The residual, less than 10^{-9} for temperature and less than 10^{-6} for other variables, defined as the $L2$ norm, is used as convergence criteria.

The temperature distribution and its gradient in a flow cross section can have a critical role in the processing of materials. For flow Reynolds numbers of 1, 10, 100, 1000 and different values of pipe wall temperature, contours of fluid temperature are obtained. For the case of Re $=1$, the fluid temperature reaches the wall temperature shortly after entering the heated region of the pipe, applying either adiabatic boundary condition or constant temperature boundary condition.

For the adiabatic boundary condition, the left columns of Figs. 3–5 show contours of temperature at the end of the second, the fourth, and the sixth mixing element, from top to bottom, respectively, for laminar flows in a pipe that contains a six-element static mixer. The right columns show the temperature contours at the same axial cross sections in a pipe with no mixer. The pipe wall temperature is 318.15 K. The fluid temperature at inlet is 298.15 K.

For higher Reynolds numbers, the core flow remains at a low temperature in a pipe with no mixer; however, inserting a static mixer in the pipe breaks up the thermal boundary layer, leading to high temperature fluid particles. For Re $=10$, after the fourth mixing element, the entire flow cross section reaches the wall temperature. For the case of Re $=100$, the area of the low temperature region is decreased after the second element. This area continues to decrease as the flow passes through the helical static mixer. At the end of the sixth mixing element the area of the low temperature fluid is noticeably smaller when compared to the same flow cross section for the case of a tube with no mixer in it. By increasing the Reynolds number, the difference of fluid temperature distribution in a cross section between a tube with a static mixer and a tube with no mixer is more pronounced.

The area-weighted averaged and the minimum fluid temperatures at different flow cross sections for the adiabatic boundary condition and different flow Reynolds numbers are shown in Tables 2 and 3, respectively, for laminar flows in a pipe containing a six-element helical static mixer and for a pipe with no mixer. For the case of Re $=1$, the averaged temperature and the minimum temperature are almost the same for both cases of a pipe with static mixer and a pipe with no mixer. These values are nearly equal to the wall temperature after the flow passes the fourth mixing element. For flow in a pipe with no mixer, when Re $=10$, a large difference between the averaged and minimum values of fluid temperature is distinguishable in all cross sections; however, for the flow in a pipe with static mixer, the difference between the averaged and minimum values of fluid temperature is considerably less, especially when the flow passes the sixth mixing element. The averaged temperature at the end of the sixth mixing element is 1.56 K less than the wall temperature, when the wall temperature is 318.15 K and it is 3.89 K less than the wall temperature when it is 348.15 K; for the pipe with no mixer the averaged temperature at the same flow cross section is 3.43 K (8.56 K) less than the wall temperature, when the wall temperature is 318.15 K (348.15 K). Although the differences between the averaged temperatures and the wall temperatures for the pipe with static mixer are less than those for the pipe with no mixer, the static mixer does not show a significant improvement. By increasing the flow Reynolds number these differences are more pronounced; for Re $=1000$, the averaged temperature at the end of the sixth mixing element is 11.01 K (27.53 K) less than the wall temperature, when the wall temperature is 318.15 K (348.15 K). For the pipe with no mixer the averaged temperature at the same flow cross section is 14.28 K (35.70 K) less than the wall temperature,

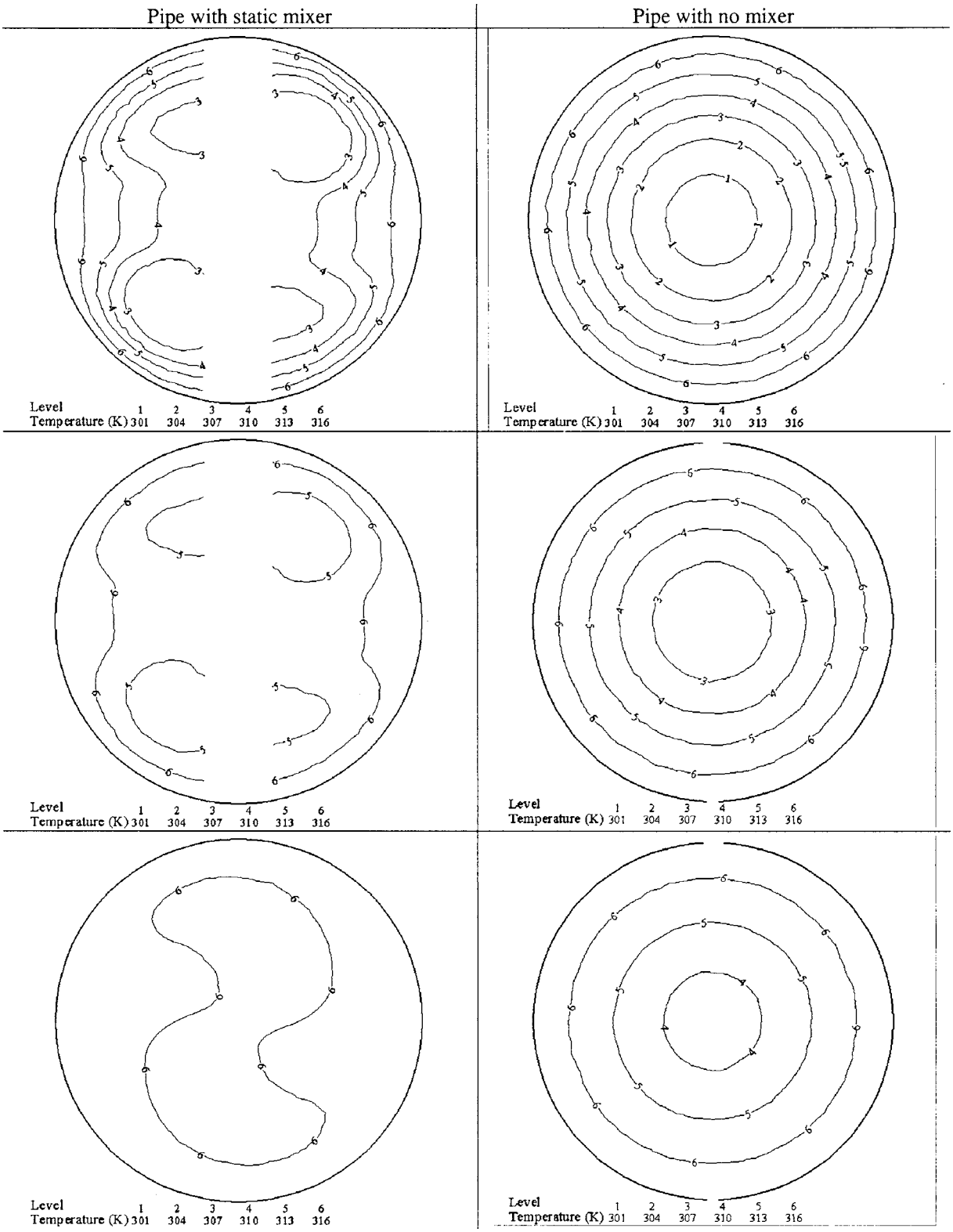

Fig. 3 Temperature at even numbered elements, Re=10 (T_W=318.15 K)

when the wall temperature is 318.15 K (348.15 K). For the case of Re=1, Br$\approx 8\times10^{-12}$ and for the case of Re=1000, Br$\approx 8\times10^{-6}$; therefore viscous dissipation effect is negligible in the cases studied here.

The ratio of the minimum temperature to the averaged temperature was calculated at a cross section located an $L/2$ distance downstream of the tailing edge of the last mixing element in a pipe with static mixer and at the same axial cross section with a pipe with no mixer, and are shown in Table 4.

When the difference between the fluid temperature at inlet and the wall temperature is 20 K, the static mixer produces almost no improvement in the temperature distribution. When the difference

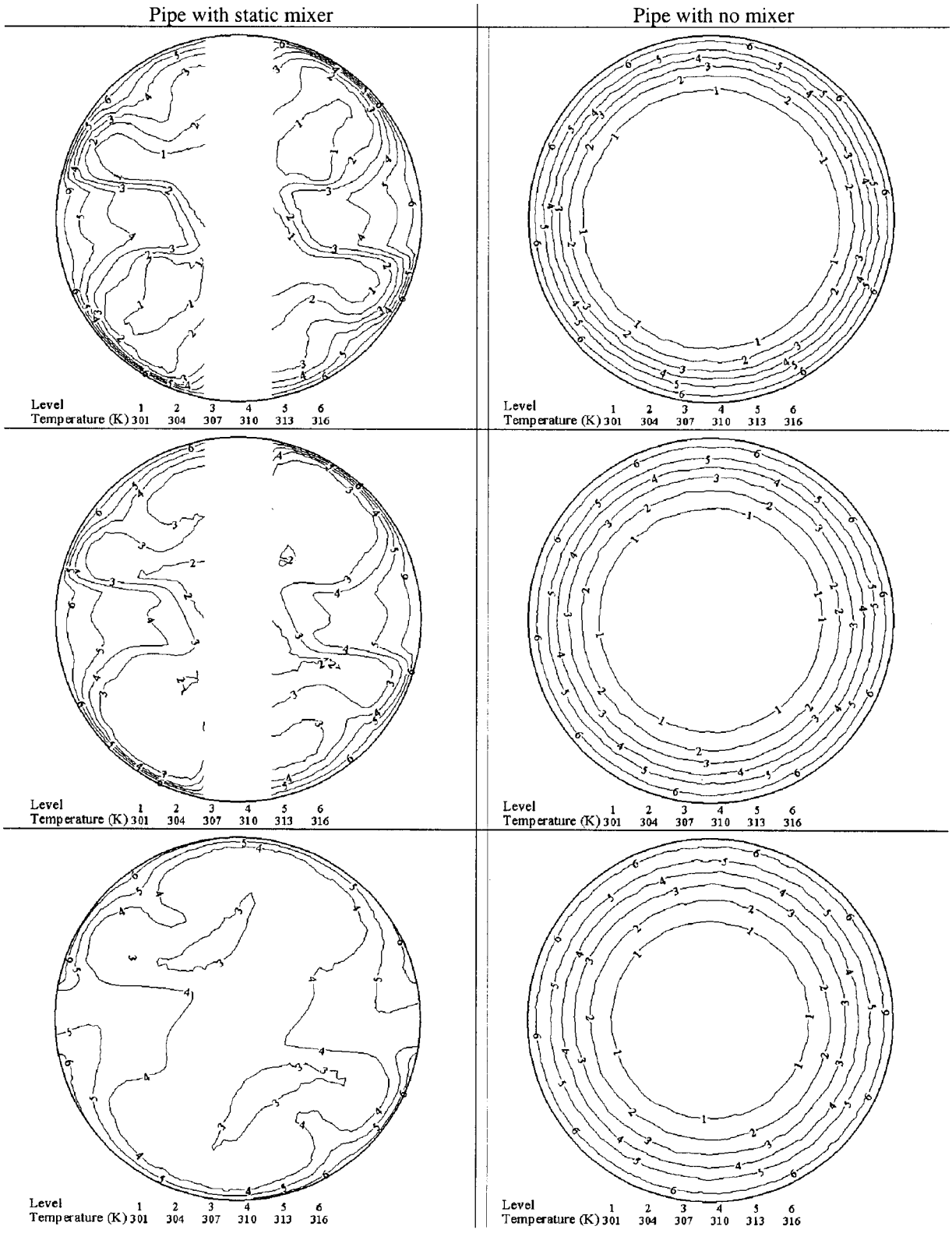

Fig. 4 Temperature at even numbered elements, Re=100 (T_W=318.15 K)

between the fluid temperature and the wall temperature is increased to 50 K, the static mixer shows a better ability to develop a more uniform temperature distribution within the fluid, especially for the case of Re=100. For Re=100, in which the fluid temperature at inlet and the wall temperature are set to 278.15 and 368.15 K, respectively, the minimum and the averaged temperature for a pipe with static mixer at a cross section located a distance $L/2$ downstream of the tailing edge of the last mixing element are 319.571 and 324.838 K, respectively. The minimum and the averaged temperature for a pipe with no mixer at the same axial cross sections are 278.306 and 313.564 K, respectively. When the difference between the fluid temperature at inlet and the

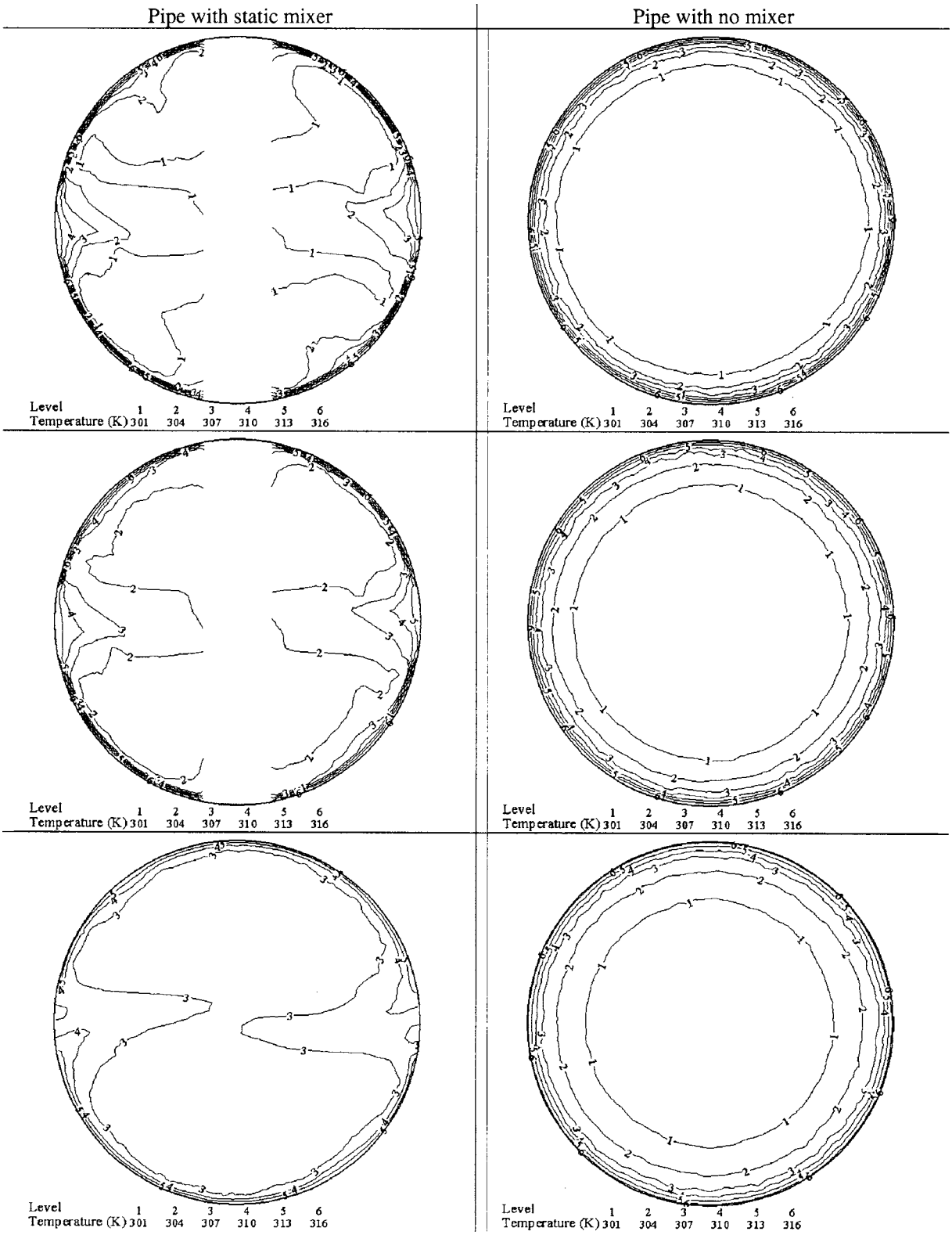

Fig. 5 Temperature at even numbered elements, Re=1000 (T_W=318.15 K)

wall temperature is increased to 90 K, the static mixer manifests a higher performance. It increases the minimum and the averaged fluid temperatures significantly and also it decreases the temperature gradient in a flow cross section significantly; the ratio of the minimum temperature to the averaged temperature is 0.984 for a pipe with static mixer, while it is only 0.888 for a pipe with no mixer.

The ratio of heat flux from the pipe wall into the fluid in a pipe with static mixer to the heat flux in a pipe with no mixer is presented at Table 5; two wall temperatures have been considered: 318.15 and 348.15 K. As expected, the wall temperature has no impact on the heat flux ratio.

For the case of Re=1, the heat flux is slightly less than 1 when

Table 2 Averaged and minimum fluid temperatures for a pipe with static mixer (wall temperature=318.15 K, adiabatic BC)

Re	Element number	Avg. T (K)	Min. T (K)
1	2	317.978	317.747
1	4	318.148	318.144
1	6	318.148	318.145
10	2	311.692	304.653
10	4	315.110	311.990
10	6	316.594	315.204
100	2	307.304	299.511
100	4	309.255	303.523
100	6	310.357	306.624
1000	2	303.383	299.620
1000	4	305.519	302.675
1000	6	307.139	304.939

the pipe is equipped with static mixer. The area of the heated surface in a pipe with static mixer is 88.08% of the area of heated surface in a pipe with no mixer. This is because of the material thickness of the static mixer studied here. It is noticed that for a standard Kenics mixer, the mixer thickness is 4.17% of the mixer length; however, as mentioned before, for the TAH static mixer, this ratio is 22%. In this flow condition, the static mixer is not able to bring a high degree of mixing to the fluid and therefore decreasing the heat transfer surface between the fluid and the heated surface leads to lower heat flux being transferred to the flow field. By increasing the Reynolds number to 10, the static mixer manifests a higher capability of fluid mixing, leading to higher convective heat exchange to the core fluid inside the tube and increases

Table 3 Averaged and minimum fluid temperatures for a pipe with no mixer (wall temperature=318.15 K, adiabatic BC)

Re	Cross section	Avg. T (K)	Min. T (K)
1	2	317.835	317.260
1	4	318.137	318.113
1	6	318.148	318.147
10	2	310.872	299.659
10	4	313.282	304.639
10	6	314.725	308.811
100	2	305.415	298.150
100	4	306.774	298.151
100	6	307.603	298.173
1000	2	302.104	298.150
1000	4	303.306	298.155
1000	6	303.869	298.222

Table 4 Minimum to averaged temperature ratio (adiabatic BC)

	Re	Temp. ratio T_W=318.15 K	Temp. ratio T_W=348.15 K
Static mixer	10	0.998	0.995
	100	0.996	0.991
	1000	0.999	0.997
No mixer	10	0.987	0.969
	100	0.975	0.940
	1000	0.988	0.971

Table 5 Heat flux ratio (adiabatic BC)

Re	Heat flux ratio T_W=318.15 K	Heat flux ratio T_W=348.15 K
1	0.999	0.999
10	1.219	1.219
100	2.172	2.172
1000	2.740	2.740

Table 6 Heat flux and mass flux ratios

Pressure drop (Pa)	Heat flux ratio	Mass flux ratio
0.174	10.042	16.460
1.811	2.728	13.112
42.437	2.115	10.673

the rate of heat transfer to the flow. By increasing the Reynolds number from 10 to 100, the heat flux ratio increases significantly (2.17 for Re 100, compared to 1.22 for Re=10). By increasing the Reynolds number to 1000, again, the heat flux is increased, however, the rate of its increase is not as significant as for the case of Re=100. In fact, when the Reynolds number is increased from 10 to 100, the heat flux ratio is increased by 78.19%, whereas, when the Reynolds number is increased from 1 to 10, the heat flux ratio is increased by 22.0% and when the Reynolds number is increased from 100 to 1000, the heat flux ratio is increased by 26.18%.

This can be explained by fluid mixing performance of the helical static mixer. By increasing the number of the mixing elements, the mixing of fluid increases; also, when the flow regime changes from creeping flow to laminar flow, the rate of increase of mixing is also increased [25].

It is possible to compare the heat flux rate to the flow in a pipe with static mixer to the heat flux rate to a flow in a pipe with no mixer, which has the same pressure drop as the pressure drop across the mixer. For a flow in a pipe with no mixer with the same pressure drop as a flow across a six-element helical mixer, with Reynolds numbers of 1, 10, and 100, the ratios of heat flux rate in a pipe with no mixer to the heat flux rate in a pipe with a six-element mixer are shown in Table 6, for the constant temperature boundary conditions. Also the ratio of mass flux in a pipe with static mixer to the mass flux in a pipe with no mixing element is presented in this table. The mass ratio is equal to the ratio of flow Reynolds numbers. For a laminar flow in a pipe, the length of thermal entrance region is given by [47]:

$$\left(\frac{X}{D}\right) \approx 0.05 \,\mathrm{Re}\,\mathrm{Pr} \tag{11}$$

For a laminar flow in a fully thermally developed region the heat flux ratio is independent of the Reynolds number [47]. Therefore, the rate of heat flux from the wall pipe to the fluid in that region is constant, as far as the flow is laminar. However, for the case studied here, a large portion of the flow is in the entrance region. In that region, the temperature gradient at the solid surface is high and therefore the heat flux rate is high compared to the heat flux rate in fully thermally developed region. For the case of the pressure drop of 0.174 (1.811) Pa, the length of thermal entrance region in a pipe with no mixer is about 16.5 (13.1) times the length of thermal entrance region in a pipe with the mixer, which explains the reason why that heat flux rate in a pipe with no mixer is higher. When the pressure increases to about 42.4 Pa (which is the pressure drop for flow across the static mixer, when Reynolds number is set 100), the ratio of heat flux decreases to about 2.1. In that case the flow rate, as well as the Reynolds number, in a pipe with no mixer is about 10.6 times of that in a pipe with a six-element helical static mixer. It is mentioned that in most cases in industry, the length of heat exchanger element is much higher than the length of the thermal entrance region and therefore most of heat flow occurs in the fully developed region.

It is important to note that using the first-order upwind method to solve the energy equation leads to an overestimation of the heat flux; for the case of Re=100, first-order upwind predicts a heat flux 17.92% higher in a pipe with a six-element mixer. Also it was observed that using a constant value for thermal conductivity leads to an underestimation of heat flux; for the case of Re

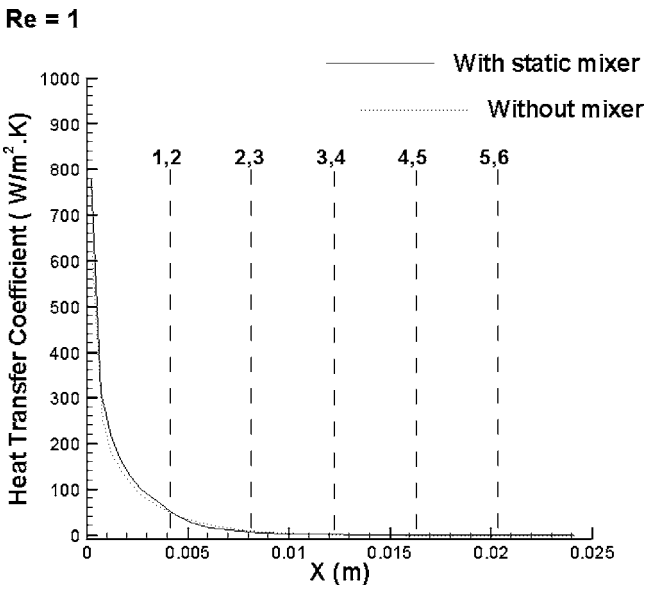

Fig. 6 Heat transfer coefficient in a pipe (Re=1, adiabatic BC)

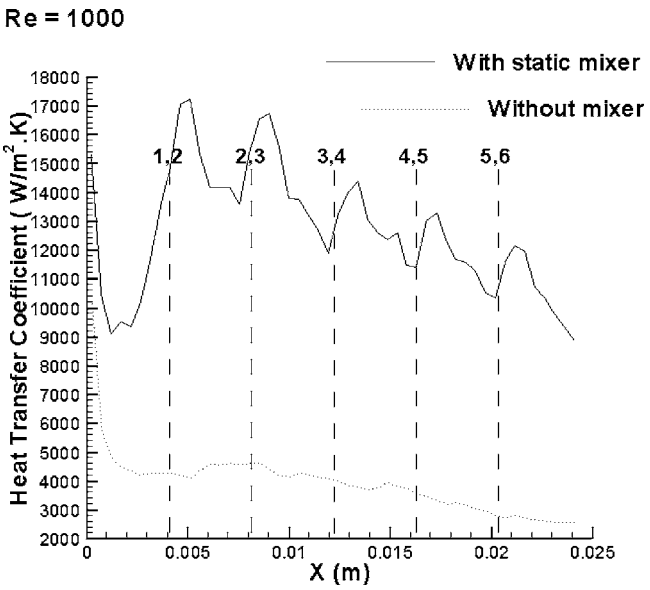

Fig. 8 Heat transfer coefficient in a pipe (Re=1000, adiabatic BC)

=1000, a constant thermal conductivity assumption results in a heat flux 3.3% smaller in a pipe with a six-element mixer.

The heat transfer coefficients for flow in a pipe that contains a six-element static mixer, with the adiabatic boundary condition, and for flow in a pipe with no mixer, are compared in Figs. 6–8. The dashed lines in these figures show the axial location of the contact point of each two mixing elements and are numbered by the numbers of those elements. As can be seen, for the case of Re=1, the heat transfer coefficients for both flows are the same; static mixer produces no increase in the heat transfer coefficient. When the Reynolds number is increased, the static mixer manifests a significant improvement to the heat transfer coefficient. Also, it is seen that the heat transfer coefficient has local maximums around the contact point of each two mixing elements. Thus, in these transition areas the effective rate of heat transfer is higher due to mixing of fluid elements.

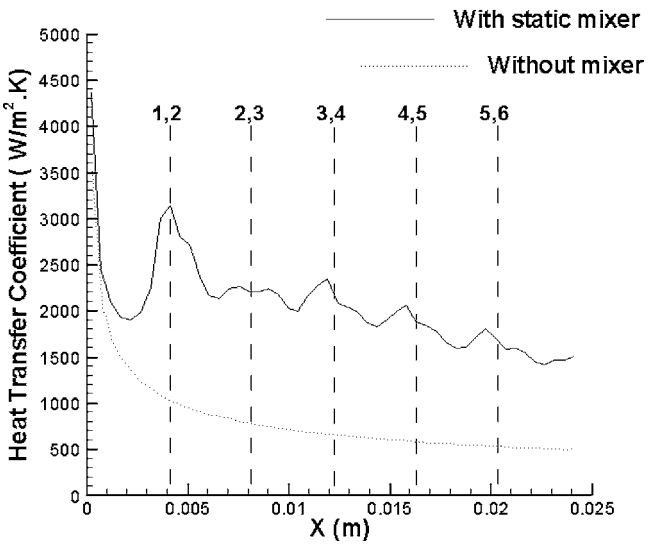

Fig. 7 Heat transfer coefficient in a pipe (Re=100, adiabatic BC)

Figures 9 and 10 show contours of temperature at the end of the second, the fourth, and the sixth mixing element, from top to bottom, respectively, for a pipe that contains a six-element static mixer, applying the constant temperature boundary condition. For Re=1, the temperature at these flow cross sections is equal to the wall temperature. For Re=10, only temperature contours are distinguishable at the end of the second helical element; at the fourth and the sixth elements, the temperature gradient in the flow cross section is extremely small and virtually all fluid elements reach the wall temperature. For the case of Re=100, the area of the low temperature region, at the end of the second mixing element, is significantly smaller compared to the results obtained for the same Reynolds number using the adiabatic boundary condition. Also, the minimum temperature is higher for the case of the constant temperature boundary condition, compared to the case of the adiabatic boundary condition. The same pattern can be observed at the end of the fourth and the sixth helical mixing elements. By increasing the Reynolds number to 1000, the difference of fluid temperature distribution in a cross section between a static mixer with the adiabatic boundary condition and static mixer with the constant temperature boundary condition is more pronounced.

Applying the constant temperature boundary condition to the mixer surface, the flow field was studied for different flow conditions. Averaged and the minimum fluid temperatures at different flow cross section are presented in Table 7. The minimum to averaged temperature ratios at the end of even numbered mixing element for different flow Reynolds number are given in Table 8. For Re=1 and Re=10, the averaged temperature and the minimum temperature are almost the same for both cases of a pipe with static mixer and a pipe with no mixer. These values are nearly equal to the wall temperature after the flow passes the fourth mixing element. For flow in a pipe with no mixer, for Re =100 and Re=1000, a large difference between the averaged and minimum values of fluid temperature is distinguishable in all cross sections; however, for the flow in a pipe with static mixer, the difference between the averaged and minimum values of fluid temperature is considerably less, especially when the flow passes the sixth mixing element. Comparing these results, obtained by applying the constant temperature boundary condition, to the results obtained by applying the adiabatic boundary condition, shows that the mixer has a higher performance under the constant temperature boundary condition, especially for higher Reynolds numbers.

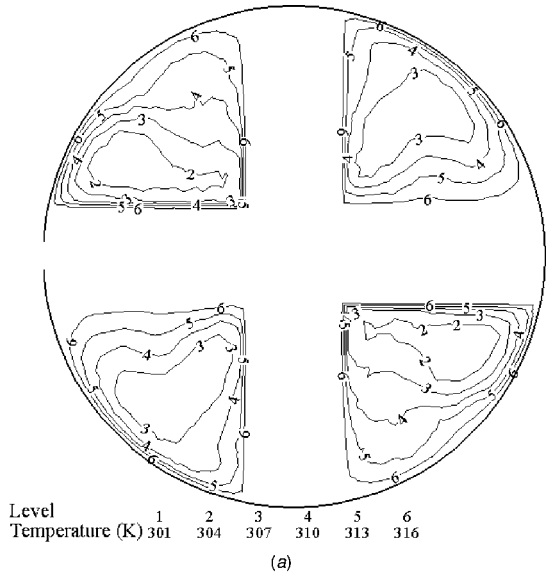

(a)

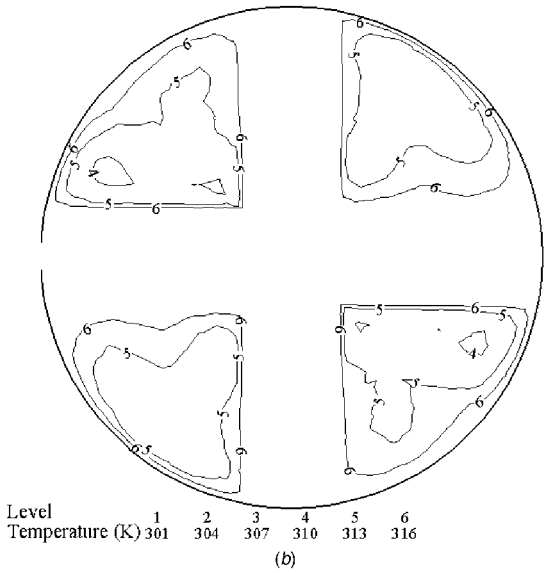

(b)

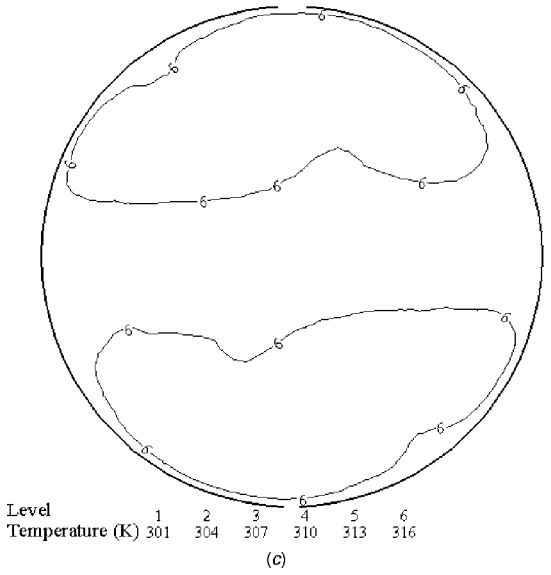

(c)

Fig. 9 Temperature contours, constant temperature BC, Re =100

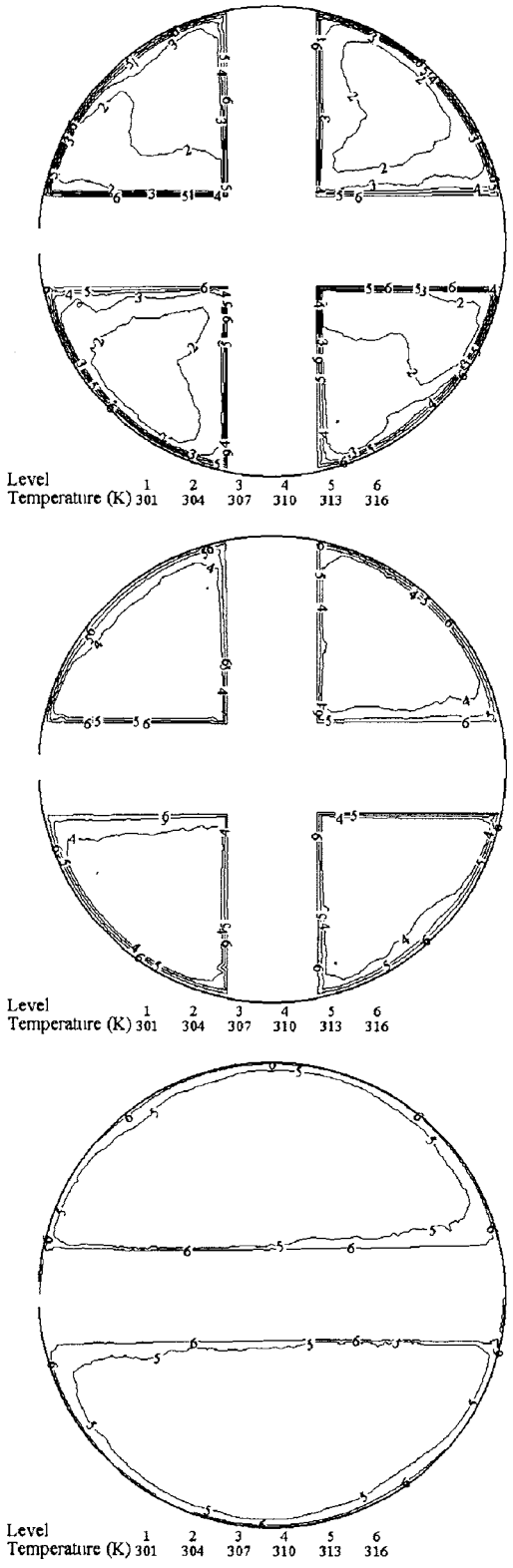

Fig. 10 Temperature contours, constant temperature BC, Re =1000

Table 9 presents the maximum to minimum temperature ratios at the end of each even numbered element, for Re=1000. When Reynolds number is small, this ratio is one at all flow cross sections. For higher Reynolds numbers this ratio increases when the wall temperature is increased. As the flow passes through the mixing elements the ratio decreases and therefore fluid temperature is

Table 7 Averaged and minimum fluid temperatures for a pipe with static mixer (wall temperature=318.15 K, constant temperature BC)

Re	Element number	Avg. T (K)	Min. T (K)
1	2	318.150	318.150
1	4	318.150	318.150
1	6	318.150	318.150
10	2	317.22	312.739
10	4	318.021	317.412
10	6	318.130	318.046
100	2	313.781	301.774
100	4	315.595	309.641
100	6	316.434	313.300
1000	2	311.113	302.352
1000	4	313.159	307.098
1000	6	314.359	310.600

more uniform. The rate of decrease of the temperature ratio is higher when the wall temperature is higher, indicating that the helical static mixer has better performance for such cases.

The performance of the helical static mixer under turbulent flow regime, Re=3000, was studied when the difference between the fluid temperature at inlet and the wall temperature is 90 K. The left column of Fig. 11 shows contours of temperature at the end of the second, the fourth, and the sixth mixing element, from top to bottom, respectively, for a pipe that contains a six-element static mixer. The right column shows the temperature contours at the same axial cross sections in a pipe with no mixer. At the end of the second mixing element, although the area of the low temperature region is smaller compared to the same cross section in a tube with no mixer in it, still a large portion of flow cross section is filled with low temperature fluid elements. This region decreases after the fourth element; however, the high temperature region is still a narrow ring adjacent to the pipe wall. At the end of the sixth mixing element the area of the low temperature fluid is noticeably smaller when compared to the same flow cross section for the case of a tube with no mixer in it.

The heat transfer coefficients for flow in a pipe that contains a six-element static mixer, with the adiabatic boundary condition, and for flow in a pipe with no mixer are compared in Fig. 12, for Re=3000. When the flow regime is turbulent, the static mixer increases the heat transfer coefficient significantly. Again, it is seen that the heat transfer coefficient has local maximums around the contact point of each two mixing elements. The heat flux ratio is 3.167, when the adiabatic boundary condition is applied to the surface of mixer, and it is 5.734, when the constant temperature boundary condition is applied.

Table 8 Minimum to averaged temperature ratio (T_W =318.15 K, constant temperature BC)

Re	Temp. ratio 2nd element	Temp. ratio 4th element	Temp. ratio 6th element
10	0.986	0.998	1.000
100	0.962	0.981	0.990
1000	0.972	0.981	0.988

Table 9 Maximum to minimum temperature ratio (Re=1000, constant temperature BC)

T_W (K)	Temp. ratio 2nd element	Temp. ratio 4th element	Temp. ratio 6th element
318.15	1.052	1.036	1.024
348.15	1.128	1.086	1.057
368.15	1.177	1.117	1.077

Figure 13 shows contours of temperature at the end of the second, the fourth, and the sixth mixing element, from top to bottom, respectively, for a pipe that contains a six-element static mixer, applying the constant temperature boundary condition. The area of the low temperature region, at the end of the second mixing element, is significantly smaller compared to the results obtained at the same cross section using the adiabatic boundary condition. At the end of the fourth element, the minimum temperature is higher for the case of the constant temperature boundary condition, compared to the case of the adiabatic boundary condition. The area of low temperature region at the end of the fourth element, when the constant temperature boundary condition is applied, is even smaller than the area of low region temperature at the end of the sixth element, when the adiabatic boundary condition is applied. At the sixth helical mixing element, a large portion of flow cross section is filled with high temperature fluid elements.

The minimum to averaged temperature ratios at the end of even numbered mixing element for the adiabatic and the constant temperature boundary conditions are given in Table 10. The closer this ratio to one, the lower temperature gradient in the flow cross section. As expected, this ratio increases as the flow goes through mixing elements. Overall, the difference between the impacts of the boundary conditions (mixer material) on this ratio is not significant.

Table 11 shows the heat flux ratio, which is the heat flux obtained by applying the constant temperature boundary condition, divided by the heat flux obtained by applying the adiabatic boundary condition. As was mentioned before, these two boundary conditions on the mixer surface model two extreme (ideal) limits for the mixing element: one with no thermal conductivity and one with infinite thermal conductivity. The real cases (mixing element with different thermal conductivity) fall somewhere between two hypothetic cases. Therefore, these two extreme boundary conditions can be used to determine the two borders of the mixer effectiveness.

For low Reynolds number flows, this ratio is almost one. For such a case the static mixer material has a minimal impact on the rate of heat transfer. The heat flux ratio increases about 10%, when Reynolds number increases from 1 to 10. For Re=100, the rate of heat transfer to the working fluid is about 60% greater, when the mixer surface has a temperature equal to the pipe wall. When Reynolds number increases from 100 to 1000, again the heat flux ratio increases, although the rate of increase is not as high as the one when Reynolds number increased from 10 to 100. When the flow regime is turbulent, the ratio of heat flux with the constant temperature boundary condition to heat flux with the adiabatic boundary condition is again enhanced. By increasing the Reynolds number from 100 to 1000 (ten times), this ratio increases almost 7%; and by increasing the Reynolds number from 1000 to 3000 (three times), this ratio increases almost 6%. This suggests that the heat conductivity of the material of mixer has a major impact on the heat transfer rate in a helical static mixer under turbulent flow conditions.

Table 12 presents TDR values at the end of the last mixing element for different flow Reynolds numbers. When Re=1, TDR is equal to zero for the adiabatic boundary condition. For such a case, TDR is 1.0 for the constant temperature boundary condition; as was mentioned previously, in this situation the TDR value cannot reveal any information about the mixer performance. For the case studied here, the difference between maximum and minimum temperatures for a pipe with no mixer is only 0.005 K. Therefore, the static mixer does not improve the temperature blending process in this case either. When Re=10, TDR is about 0.68, for the adiabatic boundary condition. By increasing the Reynolds number, TDR values decrease. This suggests that the helical static mixer is more effective for lower Reynolds number in laminar flows. When Reynolds number increases from 1000 to 3000, TDR increases about 16%, suggesting that when the flow regime becomes turbulent mixer performance is improved again. When the

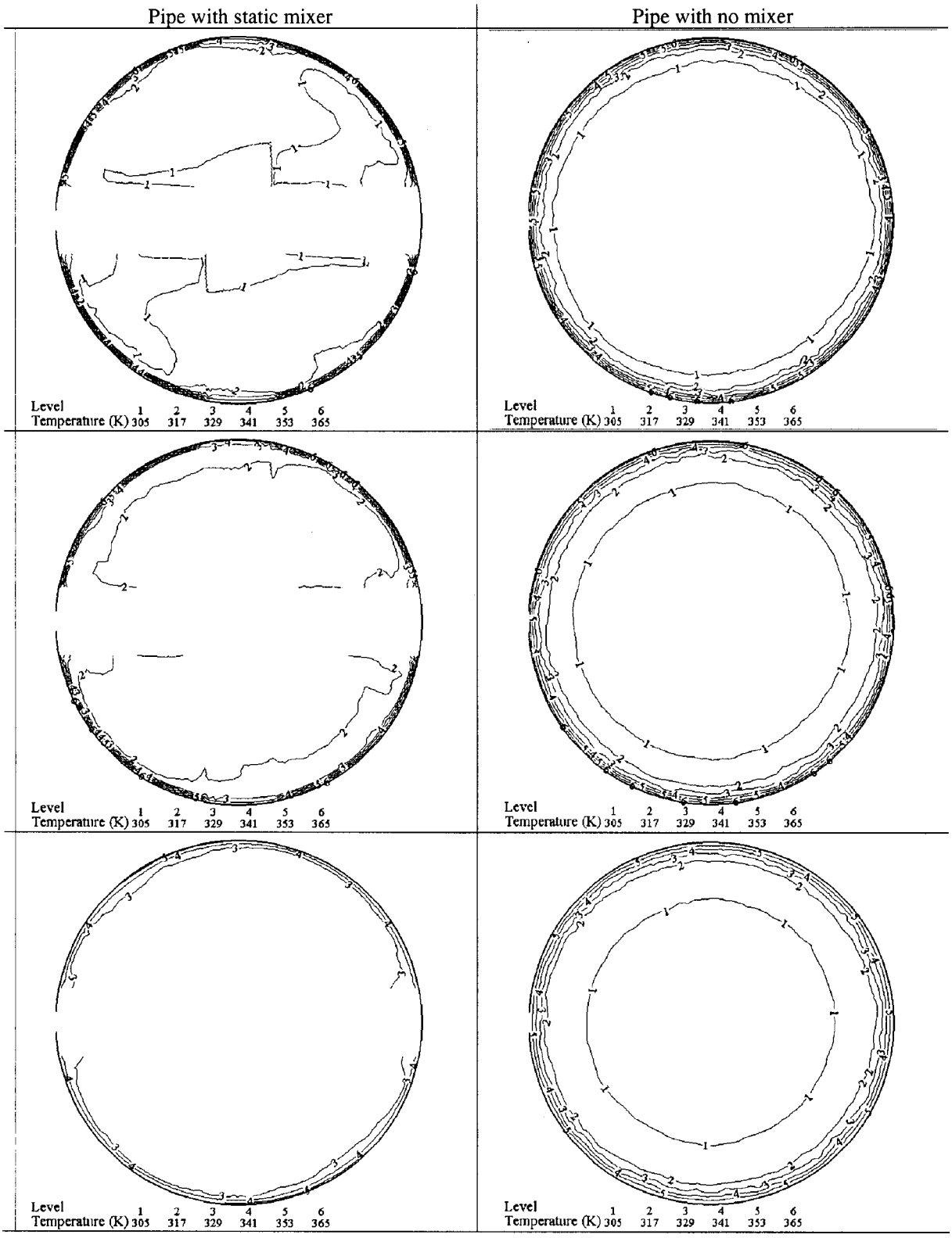

Fig. 11 Temperature at even numbered elements, Re=3000 (T_W=368.15 K)

constant temperature boundary condition is applied, the TDR value is high for all Reynolds numbers from 10 to 1000. Using a heat conductive material for the static mixer enhances the temperature blending process significantly in laminar flows. For Re =3000, although the TDR is higher when the constant temperature boundary condition is applied, the difference between TDR values is not that significant.

Figure 14 shows the distribution function for water, calculated

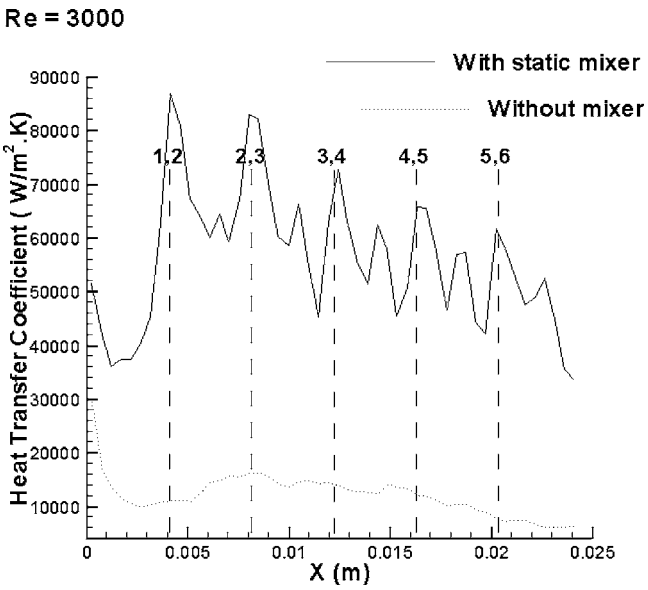

Fig. 12 Heat transfer coefficient in a pipe (Re=3000, adiabatic BC)

for Re=1, 10, and 100. For Re=1, 10, and 100, the majority of fluid particles have a similar t^*, which is less than 2. For higher Reynolds number the distribution function is a less important factor, because the nature of the flow regime causes a narrow range of t^*, e.g., when Re=3000, the majority of fluid elements, associated with streamlines that occupy a large portion of the flow, have a similar t^*, between 0.5 and 1.5.

Conclusions

Thermal performance of a helical static mixer was numerically studied using two different boundary conditions for the mixer surface: Adiabatic and constant temperature. The considered working fluid is water. It was shown that helical static mixers can decrease the temperature gradient in fluid elements and can produce a more uniform temperature distribution within the fluid; however, the mixer's effect on the uniformity of the temperature distribution is not significant, when the difference between the wall temperature and the inlet fluid is small.

Heat flux rate is not improved by using the helical static mixer in very low Reynolds number flows. For laminar flows with Reynolds numbers of 10 to 1000, use of helical static mixer increases the heat flux to the flow significantly. The static mixer studied here shows high performance in laminar flow regime for Reynolds numbers of the order of 10^2.

For very low Reynolds number flows, the static mixer surface boundary conditions show minimal impact on the rate of heat transfer. A helical static mixer gives a heat flux ratio of 2.2–2.7 for a non-creeping laminar flow, when the adiabatic boundary condition is applied to the surface of mixer. The heat flux increases significantly in non-creeping flow, when constant temperature boundary condition is applied.

Helical static mixer can improve the heat transfer rate in turbulent flow regime. For a typical turbulent flow in a helical mixer, Re=3000, the heat flux ratio is about 3.2, when adiabatic boundary condition is applied to the mixer. By applying a constant temperature boundary condition to the surface of the mixer, heat flux ratio is increased by a factor of 1.8.

Acknowledgment

This research was sponsored by Illinois Tool Works, Inc.

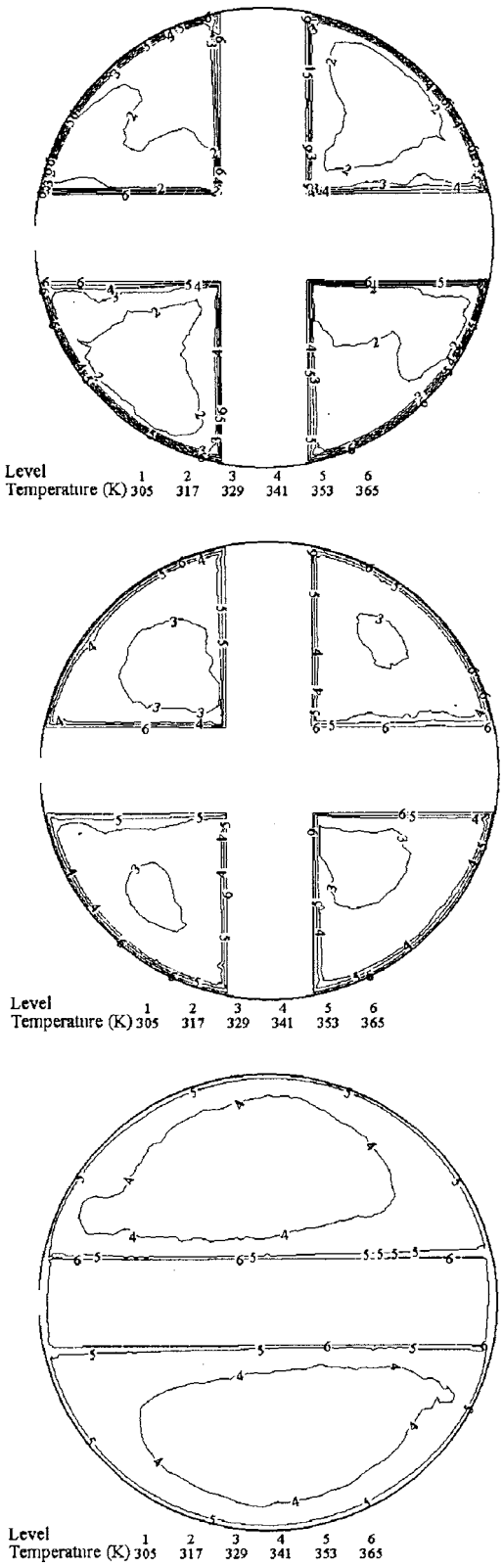

Fig. 13 Temperature contours, Constant temperature BC, Re =3000

Nomenclature

Br = Brinkman number ($=2\mu U^2/K(T_w-T_e)$)
c_p = specific heat
d = pipe diameter

Table 10 Minimum to averaged temperature ratio (Re=3000)

Mixing element	Temp. ratio (adiabatic BC)	Temp. ratio (Constant temp. BC)
2	0.965	0.868
4	0.979	0.906
6	0.975	0.956

E = total energy
F_i = external force vector ($i=1,2,3$)
g = acceleration due to gravity
h = enthalpy
K = thermal conductivity
k = turbulence kinetic energy
L = mixing element length
p = pressure
Pr = Prandtl number ($=c_p\mu/k$)
Re = Reynolds number ($=\rho Ud/\mu$)
t^* = non-dimensional residence time
T = temperature
T_0 = reference temperature
T_e = entrance temperature

Table 11 Ratio of heat flux with constant temperature BC to heat flux with adiabatic BC

Re	Heat flux ratio
1	1.003
10	1.107
100	1.587
1000	1.705
3000	1.810

Table 12 Temperature difference ratio (T_W=348.15 K)

Re	TDR (adiabatic BC)	TDR (constant temperature BC)
1	0.000	1.000
10	0.684	0.988
100	0.441	0.971
1000	0.396	0.959
3000	0.459	0.557

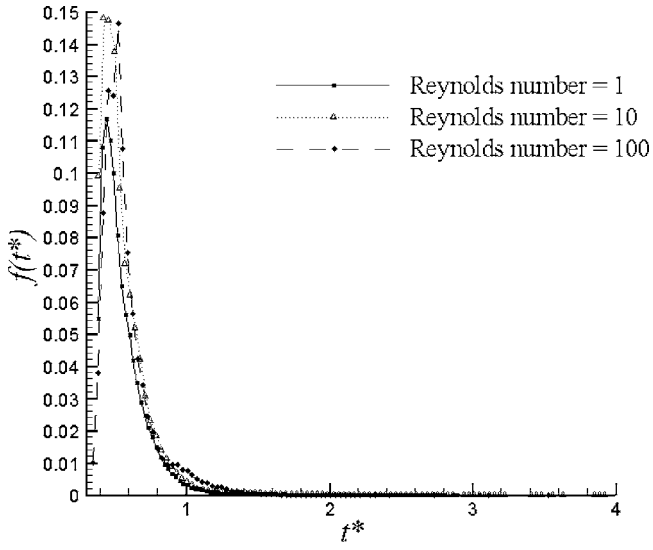

Fig. 14 Distribution function for laminar flow in a six-element static mixer (dt^*=0.01)

T_W = wall temperature
U = bulk velocity
u_i = velocity vector ($i=1,2,3$)
X = length of thermal entrance region
x_i = position vector ($i=1,2,3$)
δ_{ij} = Kronecker delta (=1 if $i=j$, =0 if $i\neq j$)
μ = molecular viscosity
ρ = density
$-\overline{\rho u_i' u_j'}$ = Reynolds stresses ($i,j=1,2,3$)
τ_{ij} = stress tensor ($i,j=1,2,3$)
ω = specific dissipation

References

[1] Shah, N. F., and Kale, D. D., 1991, "Pressure Drop for Laminar Flow of Non-Newtonian Fluids in Static Mixers," Chem. Eng. Sci., **46**, pp. 2159–2161.
[2] Chandra, K. G., and Kale, D. D., 1992, "Pressure Drop for Laminar Flow of Viscoelastic Fluids in Static Mixers," Chem. Eng. Sci., **47**, pp. 2097–2100.
[3] Xu, G., Feng, L., Li, Y., and Wang, K., 1997, "Pressure Drop of Pseudo-Plastic Fluids in Static Mixers," Chin. J. Chem. Eng., **5**(1), pp. 93–96.
[4] Pahl, M. H., and Muschlknautz, E., 1982, "Static Mixers and Their Applications," Int. Chem. Eng., **22**, pp. 197–205.
[5] Boss, J., and Czastkiewicz, W., 1982, "Principles of Scale-Up for Laminar Mixing Process of Newtonian Fluids in Fluids in Static Mixer," Int. Chem. Eng., **22**, pp. 362–367.
[6] Morris, W. D., and Misson, P., 1974, "An Experimental Investigation of Mass Transfer and Flow Resistance in the Kenics Static Mixer," Ind. Eng. Chem. Process Des. Dev., **13**, pp. 270–279.
[7] Middleman, S., 1974, "Drop Size Distributions Produced by Turbulent Pipe Flow of Immiscible Fluids Through a Static Mixer," Ind. Eng. Chem. Process Des. Dev., **13**, pp. 78–83.
[8] Morris, W. D., and Proctor, R., 1977, "The Effect of Twist Ration on Forced Convection in the Kenics Static Mixer," Ind. Eng. Chem. Process Des. Dev., **16**, pp. 406–412.
[9] Joshi, P., Nigam, K. D. P., and Nauman, E. B., 1995, "The Kenics Static Mixer: New Data and Proposed Correlations," Chem. Eng. J., **59**, pp. 265–271.
[10] Li, H. Z., Fasol, C., and Choplin, L., 1996, "Hydrodynamics and Heat Transfer of Rheologically Complex Fluids in a Sulzer SMX Static Mixer," Chem. Eng. Sci., **51**(10), pp. 1947–1955.
[11] Qi, Y., Kawaguchi, Y., Christensen, R. N., and Zakin, J. L., 2003, "Enhancing Heat Transfer Ability of Drag Reducing Surfactant Solutions With Static Mixers and Honeycombs," Int. J. Heat Mass Transfer, **46**, pp. 5161–5173.
[12] Lang, E., Drtina, P., Streiff, F., and Fleishli, M., 1995, "Numerical Simulation of the Fluid Flow and the Mixing Process in a Static Mixer," Int. J. Heat Mass Transfer, **38**(12), pp. 2239–2250.
[13] Visser, J. E., Rozendal, P. F., Hoogstraten, H. W., and Beenackers, A. A. C. M., 1999, "Three-Dimensional Numerical Simulation of Flow and Heat Transfer in the Sulzer SMX Static Mixer," Chem. Eng. Sci., **54**, pp. 2491–2500.
[14] Khakhar, D. V., Franjione, J. G., and Ottino, J. M., 1987, "A Case Study of Chaotic Mixing in Deterministic Flows: The Partitioned-Pipe Mixer," Chem. Eng. Sci., **42**, pp. 2909–2926.
[15] Kusch, H. A., and Ottino, J. M., 1992, "Experiments on Mixing in Continuous Chaotic Flows," J. Fluid Mech., **236**, pp. 319–348.
[16] Hobbs, D. M., and Muzzio, F. J., 1998, "Reynolds Number Effects on Laminar Mixing in the Kenics Static Mixer," Chem. Eng. J., **70**, pp. 93–104.
[17] Jones, S. C., Sotiropoulos, F., and Amirtharajah, A., 2002, "Numerical Modeling of Helical Static Mixer for Water Treatment," J. Environ. Eng., **128**, pp. 431–440.
[18] Byrde, O., and Sawley, M. L., 1999, "Optimization of a Kenics Static Mixer for Non-Creeping Flow Conditions," Chem. Eng. J., **72**, pp. 163–169.
[19] Byrde, O., and Sawley, M. L., 1999, "Parallel Computation and Analysis of the in a Static Mixer," Comput. Fluids, **28**, pp. 1–18.
[20] Yesilata, B., 2002, "Effect of Viscous Dissipation on Polymeric Flows Between Two Rotating Coaxial Parallel Disks," Int. Commun. Heat Mass Transfer, **29**(5), pp. 589–600.
[21] Aydin, O., 2005, "Effects of Viscous Dissipation on the Heat Transfer in a Forced Pipe Flow. Part 2: Thermally Developing Flow," Energy Convers. Manage., **46**, pp. 3091–3102.
[22] Murakami, Y., and Mikić, B. B., 2003, "Parametric Investigation of Viscous Dissipation Effects on Optimized Air Cooling Microchanneled Heat Sinks," Heat Transfer Eng., **24**(1), pp. 53–62.
[23] Xu, B., Ooi, K. T., Mavriplis, C., and Zaghloul, M. E., 2003, "Evaluation of Viscous Dissipation in Liquid Flow in Microchannels," J. Micromech. Microeng., **13**(1), pp. 53–57.
[24] White, F. M., 1991, *Viscous Fluid Flow*, McGraw–Hill, New York, NY.
[25] Rahmani, R. K., Keith, T. G., and Ayasoufi, A., 2005, "Three-Dimensional Numerical Simulation and Performance Study of an Industrial Helical Static Mixer," ASME J. Fluids Eng., **127**(3), pp. 467–483.
[26] Warming, R. F., and Beam, R. M., 1975, "Upwind Second-Order Difference Schemes and Applications in Unsteady Aerodynamic Flows," *Proc. AIAA Sec-*

ond Computational Fluid Dynamics Conference, Hartford, CT, pp. 17–28.
[27] Barth, T. J., and Jespersen, D., 1989, "The Design and Application of Upwind Schemes on Unstructured Meshes," Technical Report No. AIAA-89–0366, AIAA 27th Aerospace Sciences Meeting, Reno, NV.
[28] Vandoormaal, J. P., and Raithby, G. D., 1984, "Enhancements of the SIMPLE Method for Predicting Incompressible Fluid Flows," Numer. Heat Transfer, **7**, pp. 147–163.
[29] Hinze, J. O., 1975, *Turbulence*, McGraw–Hill, New York, NY.
[30] Wilcox, D. C., 1998, *Turbulence Modeling for CFD*, DCW Industries, Inc., La Canada, CA.
[31] Mathieu, J., and Scott, J., 2000, *An Introduction to Turbulent Flow*, The Press Syndicate of The University of Cambridge, Cambridge, UK.
[32] Pope, B. S., 2000, *Turbulent Flows*, Cambridge University Press, Cambridge, UK.
[33] Kolmogorov, A. N., 1942, "Equations of Turbulence Motion of Incompressible Fluid," Izvestia Academy of Sciences, USSR; Physics, 6, pp. 56–58.
[34] Sotiropoulos, F., and Patel, V. C., 1995, "On the Role of Turbulence Anisotropy and Near-Wall Modeling in Predicting Three-Dimensional Shear-Flows," AIAA J., **33**, pp. 504–514.
[35] Sotiropoulos, F., and Ventikos, Y., 1998, "Flow Through a Curved Duct Using Nonlinear Two-Equation Turbulence Model," AIAA J., **36**, pp. 1256–1262.
[36] Lin, F. B., and Sotiropoulos, F., 1997, "Strongly-Coupled Multigrid Method for 3-D Incompressible Flows Using Near-Wall Turbulence Closures," J. Fluid Mech., **119**, pp. 314–324.
[37] Menter, F. R., 1994, "Two-Equation Eddy-Viscosity Turbulence Models for Engineering Applications," AIAA J., **32**(8), pp. 1598–1605.
[38] Wilcox, D. C., 1988, "Reassessment of the Scale-Determining Equation for Advanced Turbulence Models," AIAA J., **26**(11), pp. 1299–1310.
[39] Tung, T. T., 1976, "Low Reynolds Number Entrance Flows: A Study of a Motinless Mixer," Ph.D. thesis, University of Massachusetts, Amherst, MA.
[40] Kemblowski, Z., and Pustelnik, P., 1988, "Residence Time Distribution of a Power-Law Fluid in Kenics Static Mixers," Chem. Eng. Sci., **43**(3), pp. 473–478.
[41] Hobbs, D. M., and Muzzio, F. J., 1997, "The Kenics Static Mixer: A Three-Dimensional Chaotic Flow," Chem. Eng. J., **67**, pp. 153–166.
[42] Nauman, E. B., 1991, "On Residence Time and Trajectory Calculations in Motionless Mixers," Chem. Eng. J., **47**, pp. 141–148.
[43] Rahmani, R. K., Keith, T. G., and Ayasoufi, A., 2006, "Numerical Simulation and Mixing Study of Pseudoplastic Fluids in an Industrial Helical Static Mixer," ASME J. Fluids Eng., **128**(3), pp. 467–480.
[44] Smirnov, A., Shi, S., and Celik, I., 2001, "Random Flow Generation Technique for Large Eddy Simulations and Particle Dynamics Modeling," ASME J. Fluids Eng., **123**, pp. 359–371.
[45] Incropera, F. P., and Dewitt, D. P., 1985, *Introduction to Heat Transfer*, Wiley, New York, NY.
[46] Sieder, E. N., and Tate, G. E., 1936, "Heat Transfer and Pressure Drop of Liquids in Tubes," Ind. Eng. Chem., **28**, pp. 1429–1435.
[47] Kays, W. M., and Crawford, M. E., 1980, *Convective Heat and Mass Transfer*, McGraw–Hill, New York, NY.

Heat Transfer Analysis in Metal Foams With Low-Conductivity Fluids

Nihad Dukhan
Department of Mechanical Engineering,
University of Detroit Mercy,
4001 W. McNichols Rd.,
Detroit, MI 48221
e-mail: nihad.dukhan@udmercy.edu

Rubén Picón-Feliciano
Department of Mechanical Engineering,
University of Puerto Rico-Mayagüez,
Mayagüez, Puerto Rico 00681

Ángel R. Álvarez-Hernández
NASA Johnson Space Center,
Houston, TX 77058

The use of open-cell metal foam in contemporary technologies is increasing rapidly. Certain simplifying assumptions for the combined conduction/convection heat transfer analysis in metal foam have not been exploited. Solving the complete, and coupled, fluid flow and heat transfer governing equations numerically is time consuming. A simplified analytical model for the heat transfer in open-cell metal foam cooled by a low-conductivity fluid is presented. The model assumes local thermal equilibrium between the solid and fluid phases in the foam, and neglects the conduction in the fluid. The local thermal equilibrium assumption is supported by previous studies performed by other workers. The velocity profile in the foam is taken as non-Darcean slug flow. An approximate solution for the temperature profile in the foam is obtained using a similarity transform. The solution for the temperature profile is represented by the error function, which decays in what looks like an exponential fashion as the distance from the heat base increases. The model along with the simplifying assumptions were verified by direct experiment using air and several aluminum foam samples heated from below, for a range of Reynolds numbers and pore densities. The foam samples were either 5.08- or 20.32-cm-*thick in the flow direction. Reasonably good agreement was found between the analytical and the experimental results for a considerable range of Reynolds numbers, with the agreement being generally better for higher Reynolds numbers, and for foam with higher surface area density.* [DOI: 10.1115/1.2217750]

Keywords: convection, heat transfer, porous media, metal foam

Introduction

The use and applications of metal foams have been widening. They have been used in aerospace systems [1,2], geothermal operations, and in petroleum reservoirs [3]. Nickel foams have been used in high-power batteries for lightweight cordless electronics [2]. Thermal management applications of foams include compact heat exchangers for airborne equipment, air-cooled condenser towers, and compact heat sinks for power electronics [1]. The open high porosity (often greater than 0.9 [4]), low relative density, high thermal conductivity of the ligaments, the large accessible surface area per unit volume, and the ability to mix the cooling fluid by promoting eddies [5], all make metal foam heat exchangers efficient, compact, and lightweight. Metal foams have also been used successfully as thermal conductivity enhancers of phase change materials in thermal control devices [6,7].

Open-cell metal foam consists of tortuous flow passages. Convection heat transfer takes place between the surface of the solid ligaments and the fluid. The flow recirculates at the back of the ligaments, and turbulence and unsteady flows may occur [8]. The geometric complexity and the random orientation of the solid ligaments in the foam prevent exact solutions of the transport equations inside the pores [3,9].

Due to their novelty and random structure, metal foams are still incompletely characterized. Only in the past 15 years or so, transport phenomena in metal foam have received more attention. Prior work in the porous media had been focused on packed spheres and other types of porous materials. Although the knowledge base is improving with time, the recent upsurge of utilizing high porosity media in contemporary technologies makes the need for fully characterizing them, and assessing their performance in various applications, more urgent. In terms of heat transfer, simple reliable models of the heat transfer inside metal foams would certainly help the engineering research, design, and application communities.

Many workers focused on determining the effective thermal conductivity of metal foam. Bhattacharya et al. [4], for example, provided analytical and experimental results for the effective thermal conductivity for high porosity metal foam. The analytical model represented the foam by a two-dimensional array of hexagonal cells. Results showed that the effective thermal conductivity depended strongly on the porosity. Boomsma and Poulikakos [10] showed that changing the fluid conductivity in saturated high-porosity metal foam had a relatively small effect on the effective thermal conductivity of the foam, i.e., the solid conductivity controlled the effective conductivity despite the high porosity of the metal foam.

Bastawros [5] provided experimental measurements and modeling of the thermal and hydraulic aspects of cellular metals subject to transverse airflow. Results showed that at low velocities, the heat flux was governed by the convective heat transfer to the flowing fluid. At higher velocities, the heat flux was limited by the heat conduction from the substrate to the foam block through the constricted nodal passages of the foam. Calmidi and Mahajan [11] conducted experimental and numerical work to study forced convection in high porosity metal foam over a range of porosity and pore densities using air as the working fluid. They presented a correlation for the Nusselt number based on the pore Reynolds number. Hwang et al. [12] conducted a numerical and experimental study on aluminum foam with air as the coolant over a range of porosities and Reynolds numbers. They showed that both the friction and the volumetric heat transfer coefficient increased with decreasing the foam density at a fixed Reynolds number.

Lu et al. [13] provided a general analytical model for the heat transfer in open-cell metal foam. They discussed the hydraulic and the thermal entry lengths for a channel filled with foam. They also

Contributed by the Heat Transfer Division of ASME for publication in the JOURNAL OF HEAT TRANSFER. Manuscript received May 8, 2005; final manuscript received February 6, 2006. Review conducted by A. Haji-Sheikh.

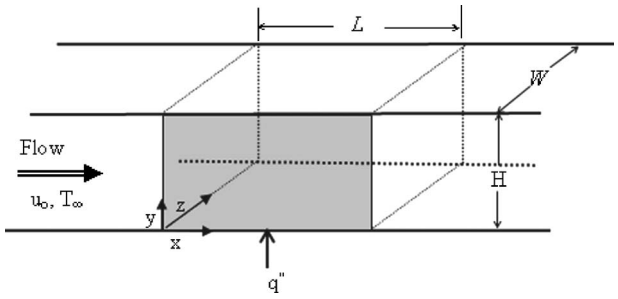

Fig. 1 Schematic and nomenclature of a foam block

presented a correlation for the heat transfer coefficient and a guide for the optimum foam structure for maximum heat transfer. The foam was characterized by its relative density, which equals to one minus the porosity.

Lee and Vafai [14] presented an analytical model for the solid and the fluid temperatures in porous media. They identified three regimes each dominated by one of the three mechanisms: fluid conduction, solid conduction, and internal heat exchange between the solid and the fluid. They used the Darcy flow model for the velocity distribution inside the foam. There was no experimental validation of the analytical results.

Angirasa [15] reported numerical results for convection heat transfer in metallic fibrous heat dissipaters using water as the cooling fluid. The heat transfer rate increased with the stagnant thermal conductivity.

Poulikakos and Renken [16] presented numerical simulation results for a channel filled with a fluid-saturated porous medium. They proved that the Darcy flow model underpredicted the heat transfer rate. Poulikakos and Kazmierczak [17] studied forced convection in a duct partially filled with a porous material.

Kim and Jang [18] studied the effects of the Darcy number, the Prandtl number, and the Reynolds number on the local thermal nonequilibrium between the solid and the fluid in a porous medium. They reported that the thermal equilibrium assumption was always valid when the solid conduction was the dominant heat transfer mode.

The present work provides an approximate model for the heat transfer in open-cell metal foams, when they are used in a forced convective mode with a low conductivity fluid such as air. As a simplification, the model ignores the conduction in the fluid. The analysis uses the typical parameters reported by the foam manufacturers and other relevant engineering parameters. The model assumes and justifies that there is local thermal equilibrium between the solid and the fluid. The simplicity and applicability of the present approach eliminates the need for rigorous microscopic analytical or numerical modeling of the three-dimensional flow and the heat transfer in and around the pores. Another advantage is that the current model is easily verified by experiments, as described in this paper. Direct temperature measurements inside the foam are also reported, which, to the knowledge of the authors, have not been performed before, or are not available in the open literature.

Heat Transfer Model. Consider a rectangular block of porous foam having a constant cross-sectional area and heated from below with a constant uniform heat flux q″. Let the block have a thickness L in the flow direction, width W and height H, as shown in Fig. 1. Assume there is a confined one-dimensional fluid flow in the positive x direction with an average velocity u_o entering the foam. We make the following assumptions:

- Radiation is negligible. For moderate temperatures, the ratio of radiation to the total heat transfer is very small and can be neglected [19]. An order of magnitude analysis revealed that radiation heat transfer may become significant (10% of the total heat transfer) if the base temperature is in the order of 800 K. This is valid for some typical metal foam heat transfer designs having a height of a few centimeters and using ambient air as the coolant.
- Constant thermophysical properties of the solid and the fluid phases. This is a pretty good assumption for applications in which the temperatures do not reach high levels, and/or for materials that do not exhibit significant variations in their properties over the given range of temperature of interest.
- The porous medium is isotropic and homogeneous with constant porosity [12,19]. Duocel aluminum foam produced by ERG Inc., for example, has a matrix of cells and ligaments that is completely repeatable, regular, and uniform. Visual inspection of such foam does not reveal any nonuniformity in its structure.
- Flow is steady and fully developed. Kaviany [20] stated that the hydraulic entrance length in porous media is about one pore size for Reynolds number 10^3–10^4, where this Reynolds number is based on the pore diameter as the length scale. Lu et al. [13] stated that for metal foam, the hydraulic entrance length is much shorter than that for a nonporous medium and generally negligible. Hwang et al. [12] used this assumption for a foam sample 6 cm long in the flow direction at moderate Reynolds numbers.
- The longitudinal conduction terms for both of the phases are negligible (high Péclet number) [21,22]. The case where axial conduction is important was considered by Minkowycz and Haji-Sheikh [23].

Applying conservation of energy for steady-state conditions to the solid and the fluid within a control volume inside the foam, we obtain

$$k_{s,\text{eff}}\frac{\partial^2 T_s}{\partial y^2} - h\sigma(T_s - T_f) = 0 \tag{1}$$

$$k_{f,\text{eff}}\frac{\partial^2 T_f}{\partial y^2} + h\sigma(T_s - T_f) = \varepsilon\rho c_p u\frac{\partial T_f}{\partial x} \tag{2}$$

where the temperatures are volume-averaged quantities and u is the volume-averaged velocity in the pores. These equations are not new but have been used by many researchers, e.g., Calmidi and Mahajan [11], Hwang et al. [12], Lee and Vafai [14], Narasimhan [21], Krishnan et al. [24], Amiri and Vafai [25], Hwang and Chao [26], Amiri et al. [27], Alazmi and Vafai [28], Kim and Kim [29] and Kim and Kim [30].

Many models in the literature include an extra term in the fluid's energy equation called thermal dispersion [9,11,24,31,32]. However, Calmidi and Mahajan [11] have shown that this term is extremely low for metal foam-air combinations due to the relatively high condctivity of the solid matrix.

We would like to make a new simplifying assumption. For commercial open-cell aluminum foam systems with air as the coolant at a pore velocity of a few meters per second, order-of-magnitude analysis (see, for example, Neild and Bejan [33]) shows that the conduction term in the fluid is a few orders of magnitude smaller than the convection and the bulk flow terms in Eq. (2). This is also true even if the dispersion conductivity is included along with the air conductivity. This is mainly due to the very low conductivity of air (0.026 W/m K at 25°C). Lee and Vafai [14] alluded to this simplification, and Younis and Viskanta [34] made a similar assumption. Equation (2) then becomes

$$h\sigma(T_s - T_f) = \varepsilon\rho c_p u\frac{\partial T_f}{\partial x} \tag{3}$$

In other words, the heat is transferred primarily from the solid to the fluid by convection and is manifested as an increase in the fluid's temperature in the flow direction. The heat transfer by conduction from the heated base to the fluid can also be

Table 1 Foam parameters

ppi	ε %	d (mm)	d_p (mm)	σ (m^2/m^3)	$k_{s,eff}$ (W/m/K) [40]	f	$K\times10^7$ (m^2)
10	92.9	0.40	3.2	810	5.36	0.082	1.146
20	92.5	0.35	2.9	1720	6.07	0.104	1.170
40	93.5	0.20	2.0	2700	4.98	0.090	0.568

neglected [13].

For an aluminum foam-air combination, the temperature of the solid and the fluid are very close in value due to the high rate of convection between them [11]. Kim and Jang [18] studied the effects of the Darcy number, the Prandtl number, and the Reynolds number on the local thermal nonequilibrium between the solid and the fluid in a porous medium. They reported that the thermal equilibrium assumption was always valid when the solid conduction was the dominant heat transfer mode.

Lee and Vafai [14] stated that, for the case where the Biot number was high and the ratio of the fluid to the solid conductivity was very small (named Regime II in Ref. [14]), which is the case for an aluminum foam-air combination, the temperature difference between the solid and the fluid would be nearly uniform over the foam cross section. They also stated that for this case, the solid and the fluid temperatures were approximately the same. In Calmidi and Mahajan [11], who solved the complete governing equations, the fluid and the solid temperatures are seen to be very close in magnitude and to have the same slope. This is also seen in the results reported by Kim and Jang [18], Krishnan et al. [24] and Kim and Kim [29]. For a discussion on the departure from local thermal equilibrium, see [35].

In light of the above discussion, it is therefore fair to invoke the local thermal equilibrium assumption: $T_f=T_s$. This allows for replacing the fluid temperature by the solid temperature on the right hand side of Eq. (3). Adding Eqs. (1) and (3) eliminates the convection term and leads to

$$k_{s,\text{eff}}\frac{\partial^2 T_s}{\partial y^2}=\varepsilon\rho c_p u\frac{\partial T_s}{\partial x} \tag{4}$$

The boundary conditions are:

$$T_s\big|_{y=H}=T_\infty \tag{5}$$

$$T_s\big|_{y=0}=T_b \tag{6}$$

$$T_s\big|_{x=0}=T_\infty \tag{7}$$

where T_b is the base temperature at $y=0$.

The boundary conditions in Eqs. (5) and (6) warrant some discussion. With regard to Eq. (5), we make the observation that the heat transfer in heated metal foams is concentrated in the proximity of the heated wall. This means that the temperature front does not reach the tip of the foam block at $y=H$. Therefore, we can assume that for high enough Reynolds numbers and far away from the heated base, the temperature inside the foam reaches that of the ambient air. This was observed during preliminary experimental runs. As such, we can let y approach infinity in Eq. (5).

As for Eq. (6), we observe that for typical applications of metal foam in heat sink designs (few cm blocks of foam brazed to a solid aluminum base, with a fan providing a few meters-per-second air velocity), and for a high constant heat flux applied at the base, the base temperature stays approximately constant: It only changes by less than 2°C. This is shown in the results of Ref. [11], for example, and was verified by preliminary runs of the current investigators. Therefore, the constant heat flux condition could be replaced by a constant temperature boundary condition, without significant compromise of accuracy.

In a nondimensional form, Eqs. (4)–(7) take the form

$$\frac{\partial^2\theta_s}{\partial\eta^2}=\frac{1}{\alpha}\frac{\partial\theta_s}{\partial\chi} \tag{8}$$

$$\theta_s(\chi,0)=1 \tag{9}$$

$$\theta_s(\chi,\eta\to\infty)=0 \tag{10}$$

$$\theta_s(0,\eta)=0 \tag{11}$$

where $\theta_s=(T_s-T_\infty)/(T_b-T_\infty)$, $\eta=y\sqrt{\varepsilon U/K}$, $\chi=x\varepsilon/(\text{Re}_K\sqrt{K})$, $U=u/u_D$, $\alpha=k_{\text{seff}}/(\varepsilon\ \mu\ c_p)$ and u_D is the Darcean velocity defined by $u_D=1/A\int_A udA$. The parameter α is similar to the diffusivity: It represents the ratio of the heat conduction by the solid to the heat stored by the fluid.

The solution to Eqs. (8)–(11) is

$$\theta_s=1-\text{erf}(\psi) \tag{12}$$

where $\psi=\eta/2\sqrt{\alpha\chi}$ is a similarity transform.

For aluminum foam, several experiments confirmed that the Forchheimer-extended Darcy flow model is valid. See, for example, Boomsma et al. [36], Dukhan and Alvarez [37], Boomsma et al. [38], and Seguin et al. [39]. Using the Forchheimer-extended Darcy model, the momentum equation reduces to a nonlinear second order differential equation for the velocity profile:

$$\frac{d^2U}{d\eta^2}=\frac{\varepsilon}{Da^2}(U-1)+\frac{\text{Re}_K}{Da^2}f\varepsilon^2(U^2-1) \tag{13}$$

This was given and solved by Vafai and Kim [19], and was used by Calmidi and Mahajan [11] in their numerical solution for heat transfer in high porosity metal foam. When plotted, the solution shows dependence on the transverse direction only in a small region very close to the solid boundaries. See also Angirasa [15] and Kim and Jang [18]. This allows for neglecting the boundary term in the momentum equation and the use of slug-flow approximation as used by [9,12]. With this assumption, the solution to Eq. (13), is simply $U=1$.

In regards to the effective thermal conductivity, many models exist [10–12,18,20,25,27,28,33,40–42]. Determining the effective thermal conductivity for the current study will be discussed later.

Experiment

In order to verify the above model and its assumptions, five samples of commercially available open-cell aluminum foam were tested. The samples covered the range of pore density of the commercially available aluminum foam: 10, 20, and 40 ppi. The samples were made from aluminum alloy 6101-T6 having a material density of 2700 kg/m^3. The foam parameters, shown in Table 1, were obtained from ERG Materials and Aerospace [43] or estimated from reported values of Bhattacharya et al. [4], Calmidi and Mahajan [11], and Boomsma and Poulikakos [36]. The foam samples used in the current work were very comparable to the ones used by [4,11,36].

The dimensions of the cross section of each sample were $W=10.16$ cm (4 in.) and $H=24.13$ cm (9.5 in.). The thickness in the flow direction was either $L=5.08$ or 20.32 cm (2 or 8 in.). The small thickness is suitable for small foam cooling designs such as those used in electronics cooling, while the large thickness is com-

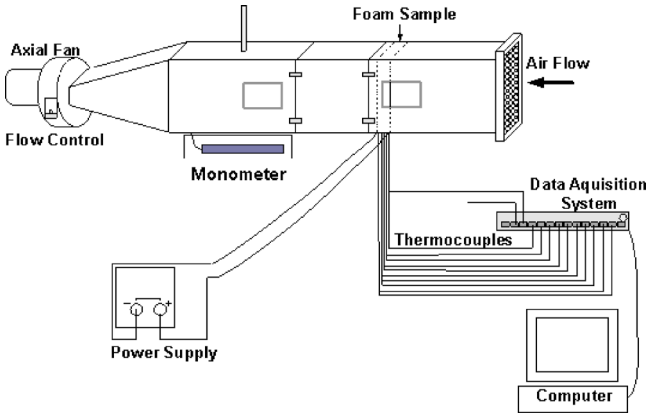

Fig. 2 Schematic of the experimental setup

parable to what would be used in larger heat exchanger designs. Each sample was brazed to a 12.7 mm (0.5 in.) thick solid aluminum base. The brazing minimized the thermal contact resistance between the solid base and the foam ligaments.

Experiments were performed in the Porous Media Research Lab of the authors' using an open-loop wind tunnel shown schematically in Fig. 2. Room air was forced to flow into this tunnel by a suction fan located close to its exit. The exit had a sliding plate that changed the size of the exit area, thus controlling the volumetric flow rate through the tunnel. A 5-cm (2 in.)-thick section of flow straighteners was placed close to the entrance. The size of the tunnel's test section was 14.9 cm by 30.2 cm (5.875 by 11.875 in.); and it had an integrated manometer for pressure measurements in mm of water.

Each foam sample was provided with a thin thermofoil heater having a surface area identical to its solid aluminum base. The heat flux provided by the heater was 4.6 W/cm^2 for a thin sample and 3.2 W/cm^2 for a thick sample. The heater was connected to a dc power supply to provide some electrical power. The four sides of each foam sample that constituted its outer perimeter were insulated using 1 in.-thick Styrofoam insulation, and the sample was placed in the tunnel's test section. The other two sides were perpendicular to the flow direction and remained open to the airflow. The insulation material ensured that the flow would travel through the foam only, allowing only a negligible flow between the insulation and the tunnel walls.

Due to the complex structure of metal foam, intricate internal temperature measurements are rather difficult to perform. However, inserting the bead of a thermocouple inside the foam would measure a temperature. For local thermal equilibrium conditions, the solid and the fluid temperatures are almost identical, and the measured temperature can represent any of them.

A total of 13 thermocouples were used to measure the steady-state temperature at different strategic locations inside each foam sample, as well as the ambient and the base temperatures. Steady-state conditions were achieved after about 30 min for the thin samples and after about 40 min for the thick ones. The temperature measurement in each thin sample were performed at the axial locations $x=2.54$, 3.81, and 4.44 cm (1, 1.5, and 1.75 in.), while for each thick sample at $x=5.08$, 10.16 and 15.24 cm (2, 4 and 6 in.). The y locations of the thermocouples for all samples were 0.64, 1.27, 1.91, 2.54, 3.18, 3.81, 4.44, 5.08, 6.35, 8.89, and 13.97 cm (0.25, 0.50, 0.75, 1.00, 1.25, 1.50, 1.75, 2.00, 2.50, 3.50 and 5.50 in.). Smaller spacing of the thermocouples (0.64 cm) was used closer to the base to capture the anticipated steep drop in temperature. All the measurements were performed in the $z=5.08$ cm (2 in.) plane. The dependence of temperature on the z direction was eliminated based on the symmetry of the boundary conditions, i.e., insulation at $z=0$ and at $z=10.16$ cm (4 in.), and on the fact that any boundary layers would be extremely thin. Actually, preliminary measurements were performed for this direction to verify this assumption.

The thermocouples were attached to the channels of an automatic data acquisition system, which was connected to a computer, where the temperature readings were recorded, as shown in Fig. 2.

The average velocity through the tunnel was measured by an Omega HH-30A digital anemometer with a range of 0.2–40 m/s (0.6–131.2 ft/s). Temperature measurements were taken at three different flow rates of the tunnel. The resulting permeability-based and pore-diameter-based Reynolds numbers are shown in Table 2. The Péclet number based on the effective Prandtl number is also shown in the table. We notice that the value of Péclet number for four of the cases is below unity. These values are underlined in the table. This may become an issue as the assumption of ingnoring axial conduction becomes suspect. These low values are due to the low velocities produced by the limited suction power of the fan of the wind tunnel, when the foam sample thickness was large in the flow dirction.

Uncertainty Analysis. Small holes were drilled in the foam to house the bead of each thermocouple for the temperature measurements. Due to the porous structure of the foam, the drill had a tendency to travel small distances around the intended hole's position. Also, the flexibility of the thermocouple wires added to the uncertainty of the exact location of the bead. The combined uncertainty in the location was estimated to be 3.2 mm (1/8 in.). Therefore, the relative uncertainty in the length was $\upsilon_L = \pm 12.5\%$ and it was obtained using a reference length of 1 in.

Table 2 Reynolds and Péclet numbers

Sample No.	*ppi*	Thickness L (cm)	Re_K	Re_p	Pe	Optimal $k_{s,eff}$ (W/m K)
1	10	5.08	165.4	1563.5	5.76	11.00
			192.9	1823.4	6.72	
			216.3	2044.6	7.54	
2	20	5.08	134.6	1141.2	3.71	8.53
			157.4	1334.5	4.34	
			180.9	1533.7	4.99	
3	10	20.32	47.1	445.2	1.64	6.12
			51.2	484.0	1.78	
			55.3	522.7	1.93	
4	20	20.32	29.1	246.7	0.80	4.40
			32.8	278.1	0.91	
			63.9	541.8	1.76	
5	40	20.32	20.1	168.7	0.67	5.01
			29.8	250.1	0.99	
			43.9	368.4	1.46	

The average air velocity in the tunnel was measured using a digital anemometer. The uncertainties reported by the manufacturer included a fixed error of ±0.25% of the full scale and an error of ±0.75% of the reading. The resolution error was 0.01 m/s. The root-sum-squares method states that an estimate of the uncertainty in a measurement, v_x, caused by J elemental errors, $e_j s$, is [44]

$$v_x = \pm \sqrt{\sum_{j=1}^{J} e_j^2} \tag{15}$$

Combining the above uncertainties according to Eq. (15), and using a velocity of 1 m/s, the maximum relative total uncertainty in the air velocity was $v_{u_o} = \pm 11.2\%$.

For the temperature terminal block in the data acquisition system, the manufacturer reported an accuracy of 1.2°C and a repeatability of 0.4°C. Combining these using Eq. (15), the total uncertainty for the temperature card was $v_B = \pm 1.26$°C. The uncertainty in the thermocouple was estimated as $v_{Th} = \pm 1.50$. Therefore, the total average uncertainty of the temperature measurement according to Eq. (15) was ±1.96°C. Using the ambient temperature (21°C) as a reference, the average relative uncertainty in temperature was $v_T = \pm 9.3\%$.

The uncertainty propagation in the reported non-dimensional quantities ψ and θ_s can be calculated as follows. First we can write $\psi = y/2(\varepsilon\rho c_p u/xk_{\text{seff}})^{1/2}$. The total uncertainty in ψ is the sum of the uncertainty in the variables that make up ψ according to:

$$v_\psi = \pm \left[\left(\frac{\partial\psi}{\partial y} v_y\right)^2 + \left(\frac{\partial\psi}{\partial\varepsilon} v_\varepsilon\right)^2 + \left(\frac{\partial\psi}{\partial\rho} v_\rho\right)^2 + \left(\frac{\partial\psi}{\partial c_p} v_{cp}\right)^2 + \left(\frac{\partial\psi}{\partial u} v_u\right)^2 + \left(\frac{\partial\psi}{\partial x} v_x\right)^2 + \left(\frac{\partial\psi}{\partial k_{\text{seff}}} v_{k\text{seff}}\right)^2 \right]^{1/2} \tag{16}$$

Performing the partial derivative and dividing by ψ, the percent uncertainty in ψ is:

$$\frac{v_\psi}{\psi} = \pm \left[\left(\frac{v_y}{y}\right)^2 + \left(\frac{v_\varepsilon}{2\varepsilon}\right)^2 + \left(\frac{v_\rho}{2\rho}\right)^2 + \left(\frac{v_{cp}}{2c_p}\right)^2 + \left(\frac{v_u}{2u}\right)^2 + \left(\frac{v_x}{2x}\right)^2 + \left(\frac{v_{k\text{seff}}}{2k_{\text{seff}}}\right)^2 \right] \tag{17}$$

As stated above, the uncertainty in location was $v_y = v_x = 0.032$ m. For the porosity, density, specific heat of air, we assume 10% of the reported values: $v_\varepsilon = 0.0929$, $v_\rho = 0.0116$ kg/m^3, $v_{cp} = 0.01007$ kJ/kg K (air at 25°C). For the velocity, we use $v_u = 0.336$ m/s using a reference velocity of 3 m/s, and for the effective conductivity, we use $v_{k\text{seff}} = 0.53$ W/m K, assuming 10% of the reported value for the 10 ppi sample. Also using an average distance in the y direction of $H/2 = 0.12$ m and $x = 0.0254$ m in the x direction, and substituting all of these into Eq. (17), yields $v_\psi/\psi = \pm 11.5\%$.

Next, we perform the same analysis for the dimensionless temperature. We first write $\theta_s = \Delta T_s/\Delta T_b$, where $\Delta T_s = T_s - T_\infty$ and $\Delta T_b = T_b - T_\infty$. The uncertainty in θ_s is given by:

$$\frac{v_{\theta s}}{\theta_s} = \pm \left[\left(\frac{v_{\Delta Ts}}{\Delta T_s}\right)^2 + \left(\frac{v_{\Delta Tb}}{\Delta T_b}\right)^2 \right] \tag{18}$$

The estimated uncertainty in the temperature measurement as given above was 1.96°C, thus, according to Eq. (15), $v_{\Delta Ts} = v_{\Delta T\infty} = 2.77$°C. Using an average temperature difference of 40°C and substituting in Eq. (18), we obtain $v_{\theta s}/\theta_s = \pm 9.8\%$.

Results and Discussion

Many models for the effective thermal conductivity exist in the literature. Some of them are rather simple and depend on the porosity [12,18,25,27,28]. Other more complex models are also available, such as the one based on the equivalent thermal-circuit described by Kaviany [20], or by the weighted geometric mean given by Nield and Bejan [33], and others [10,11,40–42]. The effective conductivities of the foam samples were calculated using each of the above models. There was a substantial disagreement among the resulting values. The optimal effective thermal conductivity values that minimized the error between the experimental temperature profiles and the theoretical profiles, given by Eq. (12), were also calculated. These optimal values were closest to the values obtained by employing the model of Calmidi and Mahajan [40], with the difference being smaller for lower Reynolds number. The effective conductivities calculated based on [40] are listed in Table 1, while the average optimal values are listed in Table 2. The optimal values changed depending on the Re inside the foam sample, and were generally higher for higher Reynolds numbers. It seems that the flow may have been laminar for the cases where Re_p was less than approximately 500. For this case the agreement between the effective conductivity based on [40] and the optimal value is relatively good. As the Re_p increased, the optimal effective conductivity was substantially larger than that obtained by employing the model of [40]. It therefore seems that for Re_p greater than 500, the effect of turbulence (or transition to turbulence) increased the rate of convection and produced larger thermal conductivity values.

The average values at the intermediate Reynolds numbers were employed in the figures. The analytical solution (Eq. (12)) using the optimal effective thermal conductivity value will be given by a solid line, while the analytical solution using the effective thermal conductivity according to [40] will be given by a dotted line in the following plots.

Figure 3 contains plots of the measured temperature profiles inside the 10 ppi sample which had a thickness of 5.08 cm in the flow directions. Parts (*a*), (*b*), and (*c*) are for permeability Reynolds numbers 165, 193, and 216, respectively. The experimental data are given for the axial distances 2.54, 3.81, and 4.44 cm from the inlet. The experimental temperature data lie on the same curve when plotted against the similarity transform ψ. This validates the similarity approach given by the error function solution. The agreement between the analytical and the experimental results is very good, especially when using the optimal thermal conductivity to calculate ψ.

The temperature inside the foam reaches the ambient temperature at $\psi = 3.5$ approximately. This corresponds to the physical distance $y = 3$ cm from the heated base. The height of each foam sample perpendicular to the flow direction was 24.13 cm. So treating the foam as a semi-infinite medium, as we did with the second temperature boundary condition Eq. (10), is justified. The analytical solution using the effective thermal conductivity according to Ref. [40] clearly underestimates the temperature in the foam, because it underestimates the conductivity itself for this 10 ppi foam, as shown in Table 1.

The agreement seems to improve as the Reynolds number increases, as seen in parts (*b*) and (*c*) of this figure. This may be attributed to the fact that the flow and the heat transfer are more developed and the Pe is higher for the higher Reynolds numbers. Also, as the Reynolds number increases, the heat transfer by convection from the solid to the fluid increases [11], which increases the fluid temperature and makes it closer to the solid temperature. For such case, the assumption of local thermal equilibrium is more valid.

In all three cases, there is some scatter for $\psi = 1$, approximately. This seems to be an experimental error associated with the hole that housed the bead of the thermocouple in that location.

Figure 4 shows plots of the measured temperature profiles inside the 20 ppi sample which had a thickness of 5.08 cm in the flow direction. Parts (*a*), (*b*) and (*c*) are for permeability Reynolds numbers 134.6, 157.4, and 180.9, respectively. The experimental data are given for axial distance of 2.54, 3.81, and 4.44 cm from the inlet. Again the similarity in the three temperature profiles is

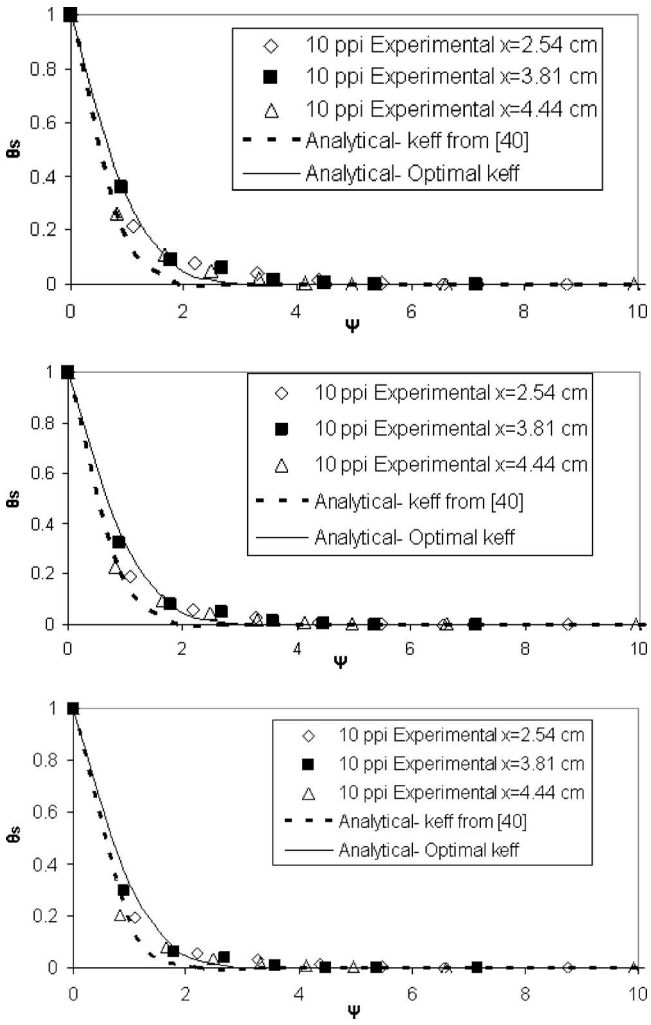

Fig. 3 Temperature distribution for 10 ppi thin foam sample: (*a*) Re_k=165.4, (*b*) Re_k=192.9, (*c*) Re_k=216.3

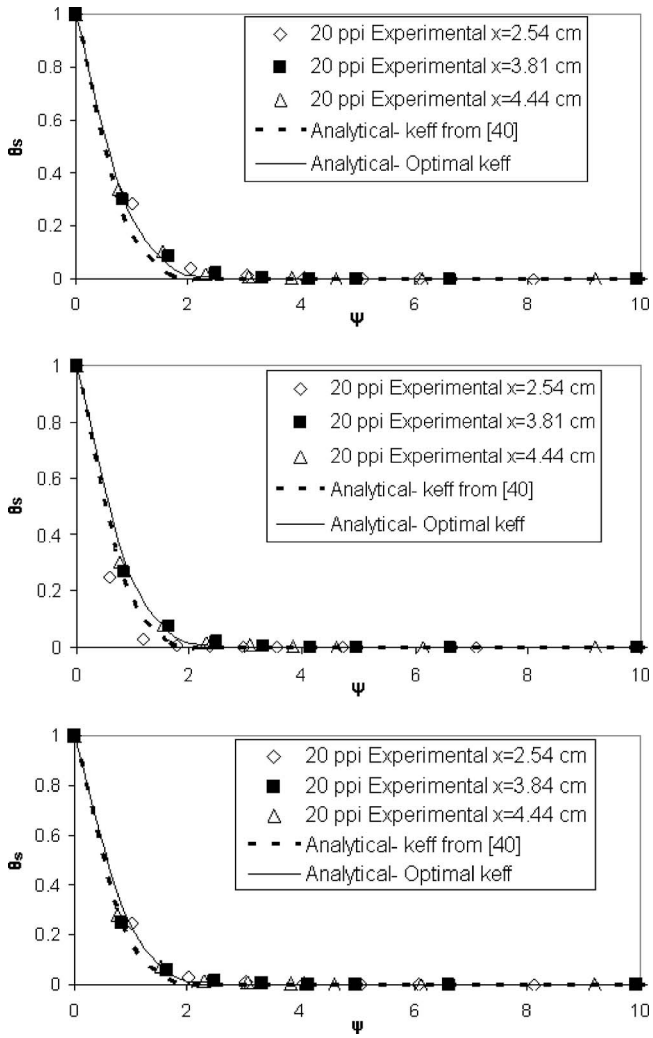

Fig. 4 Temperature distribution for 20 ppi thin foam sample: (*a*) Re_k=134.6, (*b*) Re_k=157.4, (*c*) Re_k=180.9

obvious as they lie on the same curve. There is some scatter in part (*b*) for Reynolds number 157.4 and the axial distance 2.54 cm at ψ=1 and 1.5, approximately. This is believed to be due to experimental error.

The analytical solution using the optimal thermal conductivity for this 20 ppi sample is given by the solid line. The agreement between the analytical and the experimental results is very good, especially for parts (*a*) and (*c*). The agreement at the low Reynolds number of 134.6 is not as good, as can be seen in part (*a*) of the figure.

The agreement between the analytical and the experimental data is generally better for this 20 ppi sample compared to the previous 10 ppi sample of the same thickness and almost the same porosity. This may be explained by the fact that the surface area density is larger for the current sample compared to the 10 ppi sample. See Table 2. This increase in the surface area results in an increased convection heat transfer from the solid to the fluid. This leads to closer temperatures of the fluid and the solid, i.e., the assumption of local thermal equilibrium is a better approximation.

The analytical solution using the effective thermal conductivity according to Ref. [40] again underestimates the temperature in the foam, because it underestimates the conductivity itself for this 20 ppi foam, as shown in Table 1. However, the difference between the two analytical curves using the optimal thermal conductivity and the one based on Ref. [40] is smaller for this foam compared to the 10 ppi foam. The estimated thermal conductivities are closer, as shown in Table 1.

The following figure, Fig. 5, shows the results for a significantly thick 10 ppi foam sample: 20.32 cm in the flow direction. Such thickness may be desirable for larger foam heat exchanger designs. Due to the large pressure drop, only moderate Reynolds numbers could be achieved for the airflow through this thick foam. The temperature profiles for axial distances of 5.08, 10.16, and 15.24 cm from the inlet are plotted against the similarity transform ψ. For the high Reynolds numbers of 51.2 and 55.3, as shown in parts (*b*) and (*c*) of this figure, the agreement between the experimental results and the analytical solution given by the solid lines is good. The error function solution generally underestimates the temperature.

For this thick sample, there seems to be a weak dependence on the axial distance that is not captured by the similarity transform ψ. This is amplified for the low Reynolds numbers of 47.1 and 51.2, as shown in parts (*a*) and (*b*) of Fig. 5. The scatter in the data can be attributed to uncertainties in the distance measurements associated with the location of the bead of the thermocouples. The pores of 10 ppi foam are relatively large (3.2 mm as given in Table 1). This increased the uncertainty in the location, as the bead was free to move a little. It is the opinion of the authors,

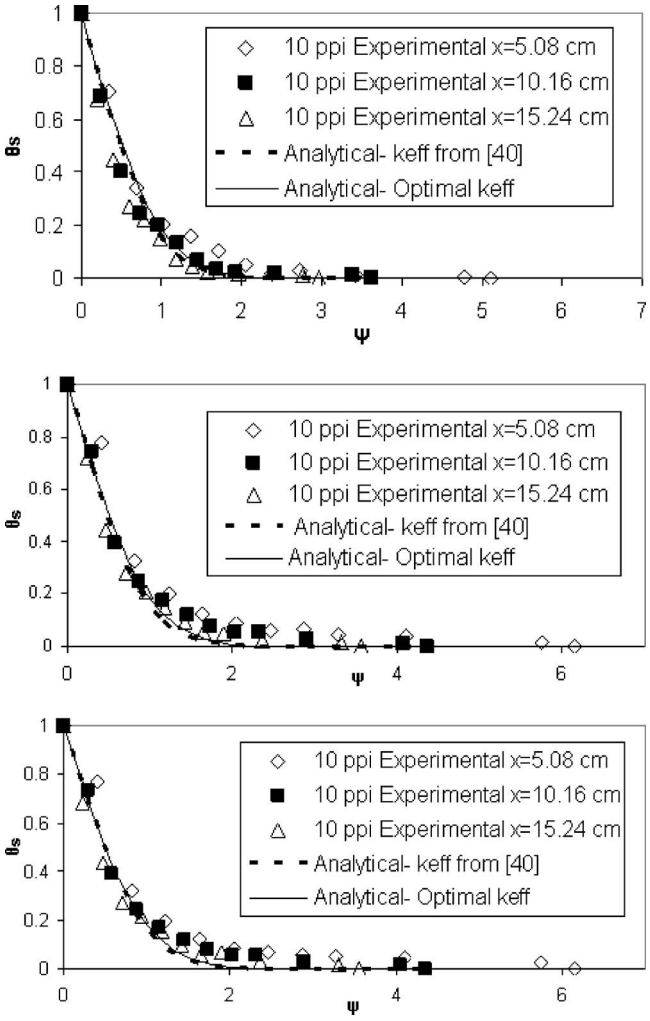

Fig. 5 Temperature distribution for 10-ppi-thick foam sample: (*a*) Re_k=47.1, (*b*) Re_k=51.2, (*c*) Re_k=55.3

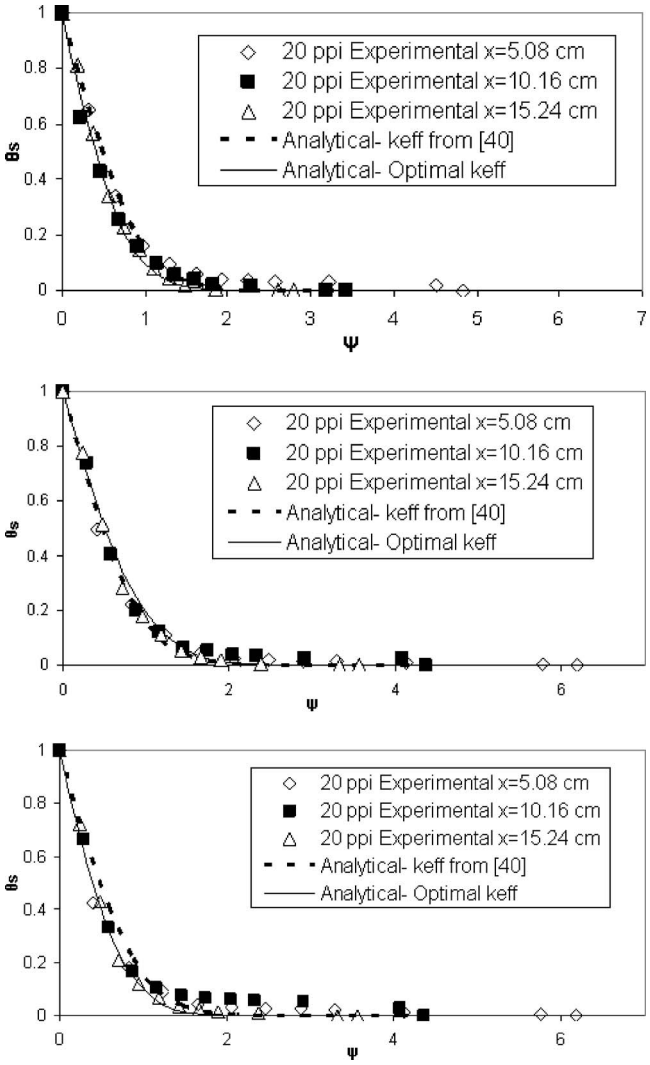

Fig. 6 Temperature distribution for 20-ppi-thick foam sample: (*a*) Re_k=29.1, (*b*) Re_k=32.8, (*c*) Re_k=63.9

however, that the approximation given by the analytical solution can still be used for preliminary heat exchanger designs but with care.

The results for the 20 ppi 22.32-cm-thick sample are given in Fig. 6. Parts (*a*), (*b*) and (*c*) are for Reynolds numbers 29.1, 32.8, and 63.9, respectively. The agreement between the experimental results and the analytical solution for this case is pretty good in general. The experimental results are certainly similar and lie on the same curve when plotted against the similarity transform ψ. There is some deviation of the experimental data for the axial location of 10.16 cm (4 in.) for the high Reynolds number of 63.9, as shown in part (*c*). This is attributed to the experimental errors.

For the 20.32-cm-thick 40 ppi sample, Fig. 7 parts (*a*), (*b*) and (*c*) show the experimental temperature profiles versus the similarity transform at the axial distances 5.08, 10.16, and 15.24 cm, for the Reynolds numbers 20.1, 29.8, and 43.9. It is clear in these plots that the similarity solution is a good approximation. The experimental results for the three axial locations lie approximately on the same curve. The agreement between the experimental results and the analytical solution is generally better for this 40 ppi sample compared to the previous 10 and 20 ppi samples. This may be attributed to some fine geometrical differences in the structure of the 40 ppi foam. The agreement is weaker for the low Reynolds number of 20.1. For this case the Pe is 0.67 as shown in Table 2. For such a low value of Pe, the local thermal equilibrium may not be a good assumption. The better agreement could be explained by the very large surface area density for the 40 ppi foam compared to the 10 ppi foam, as shown in Table 1.

The analytical solution using the effective thermal conductivity according to Ref. [40] agrees with the analytical solution based on the optimum effective thermal conductivity. This is expected because the values of the effective thermal conductivities are almost identical, as listed in Table 1. The ability of the method of Ref. [40] to predict the effective thermal conductivity seems to be best for the 40 ppi foam. This may be due to the nature of the internal geometry of this type of foam, and how true the representation of this geometry by the model of [40].

Conclusion

The heat transfer in open-cell metal foam with a low conductivity fluid as the coolant was investigated. An analytical model was developed utilizing the typical parameters usually reported by the foam manufacturers as well as the thermophysical properties of the foam and the coolant. The model utilized the thermal equilibrium assumption between the solid and the fluid phases in the foam. A similarity solution for the temperature profile was obtained using the error function. The model and its underlying assumptions were verified by experiment for several aluminum foam samples using air as the coolant. The results generally

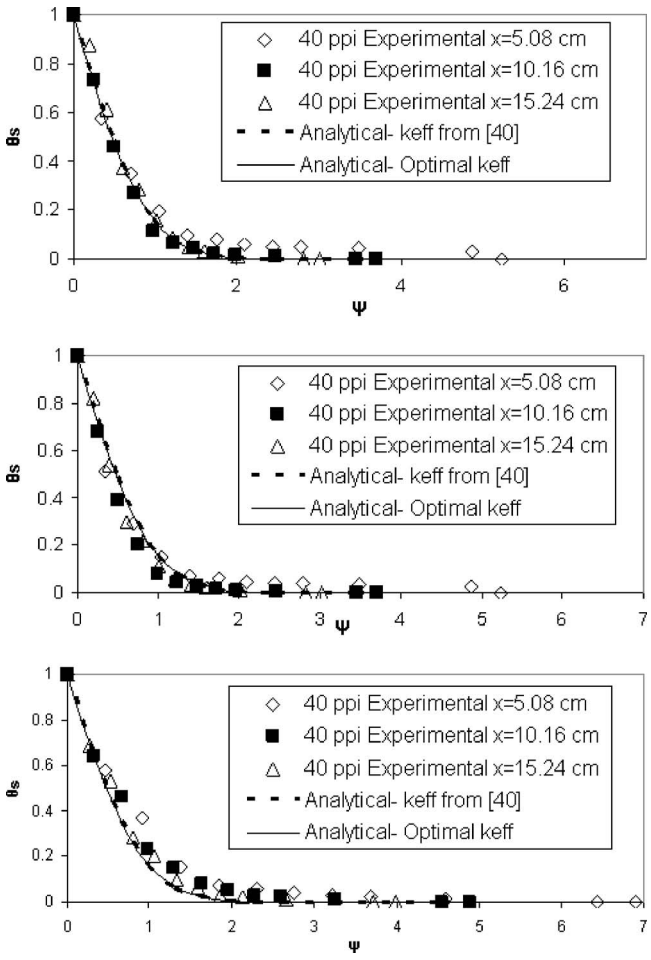

Fig. 7 Temperature distribution for 40-ppi-thick foam sample: (*a*) $Re_k=20.1$, (*b*) $Re_k=29.8$, (*c*) $Re_k=43.9$

showed good agreement between the model's prediction and the experimental data for a range of permeability Reynolds numbers. The model was generally more accurate for higher Reynolds numbers, and for foams with higher surface area densities.

Acknowledgment

This work was supported in part by the ERC Program of the National Science Foundation under Award No. EEC-9731677 with the help of Dr. Miguel Vélez and Dr. Elaine Scott; and also by Pratt & Whitney with the help of David Cloud, for which the authors are very thankful. Pablo D. Quiñones-Ramos, currently at the University of Michigan, has been instrumental in providing many of the references needed for completing this paper, for which the authors are deeply grateful.

Nomenclature

d = ligament diameter
d_p = pore diameter
c_p = heat capacity of fluid
Da = Darcy number $=\sqrt{K}/H$
f = friction factor
h = convection heat transfer coefficient
H = height of foam sample
k = thermal conductivity
K = permeability
Pr = Prandtl number of air at room temperature
Pr_{eff} = effective Prandtl number $=Pr k_f/k_{eff}$
Pe = Péclet number $=Re_p Pr_{eff}$
ppi = number of pores per inch
Re_K = Reynolds number based on permeability $=u_D\sqrt{K}/\nu$
Re_p = Reynolds number based on pore diameter $=u_D d_p/\nu$
q'' = heat flux
T = temperature
L = thickness of foam sample in flow direction
W = width of foam sample
U = nondimensional velocity $=u/u_D$
u = volume-averaged pore velocity
u_D = Darcean velocity
u_o = average tunnel velocity entering foam
x = axial coordinate along the flow direction
y = transverse coordinate along foam sample
z = coordinate along width of foam sample

Greek

α = non-dimensional parameter in Eq. (8)
χ = non-dimensional coordinate in flow direction
ε = porosity
η = non-dimensional transverse coordinate
μ = dynamic viscosity
ν = kinematic viscosity
θ = dimensionless temperature
ρ = density of fluid
σ = surface area per unit volume of foam
υ = uncertainty
ψ = similarity transform, Eq. (12)

Subscripts

b = at the base ($y=0$)
eff = effective value
f = fluid
s = solid
∞ = ambient

References

[1] Ashby, M. F., Evans, A. G., Fleck, N. A., Gibson, L. J., Hutchinson, J. W., and Wadley, H. N. G., 2000, *Metal Foams, A Design Guide*, Butterworth-Heinemann, Woburn, MA, pp. 181–188.
[2] Sullines, D., and Daryabeige, K., 2001, "Effective Thermal Conductivity of High Porosity Open Cell Nickel Foam," *Proc. 35th AIAA Thermophysics Conference*, Anaheim, CA, January 11–14, AIAA Paper No. 2819, p. 12.
[3] Vafai, K., and Tien, C. L., 1982, "Boundary and Inertia Effects on Convective Mass Transfer in Porous Media," Int. J. Heat Mass Transfer, **25**(8), pp. 1183–1190.
[4] Bhattacharya, A., Calmidi, V. V., and Mahajan, R. L., 2002, "Thermophysical Properties of High Porosity Metal Foams," Int. J. Heat Mass Transfer, **45**, pp. 1017–1031.
[5] Bastawros, A. F., 1998, "Effectiveness of Open-Cell Metallic Foams for High Power Electronic Cooling," *Proc. Symposium on the Thermal Management of Electronics, IMECE*, Anaheim, CA, November 15–20, ASME HTD Vol. 361-3, pp. 211–217.
[6] Alawadhi, E. M., and Amon, C. H., 2003, "PCM Thermal Control Unit for Portable Electronic Devices: Experimental and Numerical Studies," IEEE Trans. Compon. Packag. Technol., **26**(1), pp. 116–125.
[7] Vesligaj, M. J., and Amon, C. H., 1999, "Transient Thermal Management of Temperature Fluctuations During Time Varying Workloads on Portable Electronic," IEEE Trans. Compon. Packag. Technol., **22**(4), pp. 541–550.
[8] Bastawros, A. F., Evans, A. G., and Stone, H. A., 1998, "Evaluation of Cellular Metal Heat Transfer Media," MECH, 325, Harvard University, Cambridge, MA.
[9] Hunt, M. L., and Tien, C. L., 1988, "Effect of Thermal Dispersion on Forced Convection in Fibrous Media," Int. J. Heat Mass Transfer, **31**(2), pp. 301–309.
[10] Boomsma, K., and Poulikakos, D., 2001, "On the Effective Thermal Conductivity of Three-Dimensionally Structured Fluid-Saturated Metal Foam," Int. J. Heat Mass Transfer, **44**, pp. 827–836.
[11] Calmidi, V. V., and Mahajan, R. L., 2000, "Forced Convection in High Porosity Metal Foams," ASME J. Heat Transfer, **122**, pp. 557–565.
[12] Hwang, J. J., Hwang, G. J., Yeh, R. H., and Chao, C. H., 2002, "Measurement of the Interstitial Convection Heat Transfer and Frictional Drag for Flow Across Metal Foam," ASME J. Heat Transfer, **124**, pp. 120–129.
[13] Lu, T. J., Stone, A., and Ashby, M. F., 1998, "Heat Transfer in Open-Cell Metal Foam," Acta Mater., **46**(10), pp. 3619–3635.
[14] Lee, D. Y., and Vafai, K., 1999, "Analytical Characterization and Conceptual

Assessment of Solid and Fluid Temperature Differentials in Porous Media," Int. J. Heat Mass Transfer, **42**, pp. 423–435.
[15] Angirasa, D., 2002, "Forced Convective Heat Transfer in Metallic Fibrous Materials," ASME J. Heat Transfer, **124**, pp. 739–745.
[16] Poulikakos, D., and Renken, K., 1987, "Forced Convection in a Channel Filled With Porous Medium, Including the Effect of Flow Inertia, Variable Porosity, and Brinkman Friction," ASME J. Heat Transfer, **109**, pp. 880–888.
[17] Poulikakos, D., and Kazmierczak, M., 1987, "Forced Convection in a Duct Partially Filled With a Porous Material," ASME J. Heat Transfer, **109**, pp. 653–662.
[18] Kim, S. J., and Jang, S. P., 2002, "Effects of the Darcy Number, the Prandtl Number and the Reynolds Number on the Local Thermal Non-Equilibrium," Int. J. Heat Mass Transfer, **45**, pp. 3885–3896.
[19] Vafai, K., and Kim, S. J., 1989, "Forced Convection in a Channel Filled With a Porous Medium: An Exact Solution," ASME J. Heat Transfer, **111**, pp. 1103–1106.
[20] Kaviany, M., 1995, *Principles of Heat Transfer in Porous Media*, 2nd ed., Springer, New York, pp. 17, 18, 30, 70, 415.
[21] Narasimhan, A., Lage, J., and Nield, D. A., 2001, "New Theory for Forced Convection Through Porous Media by Fluids With Temperature-Dependent Viscosity," ASME J. Heat Transfer, **123**, pp. 1045–1051.
[22] Ingham, D. B., and Pop, I., 1998, *Transport Phenomena in Porous Media*, Elsevier Science, Oxford, UK, p. 103.
[23] Minkowycz, W. J., and Haji-Sheikh, A., 2006, "Heat Transfer in Parallel Plates and Circular Porous Passages With Axial Conduction," Int. J. Heat Mass Transfer (in press).
[24] Krishnan, S., Murthy, J. Y., and Garimella, S. V., 2004, "A Two-Temperature Model for the Analysis of Passive Thermal Control System," ASME J. Heat Transfer, **126**, pp. 628–637.
[25] Amiri, A., and Vafai, K., 1994, "Analysis of Dispersion Effects and Non-Thermal Equilibrium, Non-Darcian, Variable Porosity Incompressible Flow Through Porous Media," Int. J. Heat Mass Transfer, **37**(6), pp. 939–954.
[26] Hwang, G. J., and Chao, C. H., 1994, "Heat Transfer Measurement and Analysis for Sintered Porous Channels," ASME J. Heat Transfer, **116**, pp. 456–464.
[27] Amiri, A., Vafai, K., and Kuzay, T. M., 1995, "Effects of Boundary Conditions on Non-Darcian Heat Transfer Through Porous Media and Experimental Comparisons," Numer. Heat Transfer, Part A, **27**, pp. 651–664.
[28] Alazmi, B., and Vafai, K., 2002, "Constant Wall Heat Flux Boundary Conditions in Porous Media Under Local Thermal Non-Equilibrium Conditions," Int. J. Heat Mass Transfer, **45**, pp. 3071–3087.
[29] Kim, S. J., and Kim, D., 1999, "Forced Convection in Microstructures for Electronic Equipment Cooling," ASME J. Heat Transfer, **121**, pp. 639–645.
[30] Kim, S. J., and Kim, D., 2001, "The Thermal Interaction at the Interface Between a Porous Medium and an Impermeable Wall," ASME J. Heat Transfer, **123**, pp. 527–533.
[31] Quintard, M., Kaviany, M., and Whitaker, S., 1997, "Two-Medium Treatment of Heat Transfer in Porous Media: Numerical Results for Effectvive Properties," Adv. Water Resour., **20**(2–3), pp. 77–94.
[32] Deleglise, M., Simacek, P., Binetruy, C., and Advani, S., 2003, "Determination of the Thermal Dispersion Coefficient During Radial Filling of a Porous Medium," ASME J. Heat Transfer, **125**, pp. 875–880.
[33] Nield, D. A., and Bejan, A., 1999, *Convection in Porous Media*, 2nd ed., Springer, New York, p. 25.
[34] Younis, L. B., and Viskanta, R., 1993, "Experimental Determiniation of the Volumetric Heat Transfer Coefficient Between Stream of Air and Ceramic Foam," Int. J. Heat Mass Transfer, **36**(6), pp. 1425–1434.
[35] Minkowycz, W. J., Haji-Sheikh, A., and Vafai, K., 1999, "On Departure From Local Thermal Equilibrium in Porous Media Due to a Rapidly Changing Heat Source: The Sparrow Number," Int. J. Heat Mass Transfer, **42**, pp. 3373–3385.
[36] Boomsma, K., and Poulikakos, D., 2002, "The Effect of Compression and Pore Size Variations on the Liquid Flow Characteristics in Metal Foam," ASME J. Fluids Eng., **124**, pp. 263–271.
[37] Dukhan, N., and Alvarez, A., 2004, "Pressure Drop Measurements for Air Flow Through Open-Cell Aluminum Foam," *Proc. ASME International Engineering Congress*, Anaheim, CA, November 13–19, Paper No. IMECE2004-60428.
[38] Boomsma, K., Poulikakos, D., and Ventikos, Y., 2003, "Simulations of Flow Through Open Cell Metal Foams Using an Idealized Periodic Cell Structure," Int. J. Heat Fluid Flow, **24**, pp. 825–834.
[39] Seguin, D., Montillet, A., and Comiti, J., 1998, "Experimental Characterization of Flow Regimes in Various Porous Media-I: Limit of Laminar Flow Regime," Chem. Eng. Sci., **53**(21), pp. 3751–3761.
[40] Calmidi, V. V., and Mahajan, R. L., 1999, "The Effective Thermal Conductivity of High Porosity Fibrous Metal Foam," ASME J. Heat Transfer, **121**, pp. 466–471.
[41] Zhao, C. Y., Lu, T. J., and Jackson, J. D., 2004, "The Temperature Dependence of Effective Thermal Conductivity of Open-Cell Steel Alloy Foams," Mater. Sci. Eng., A, **367**, pp. 123–131.
[42] Zumbrunnen, R., Viskanta, R., and Incropera, F. P., 1986, "Heat Transfer Through Porous Solids With Complex Internal Geometries," Int. J. Heat Mass Transfer, **29**(2), pp. 275–284.
[43] ERG Materials and Aerospace, 2003, www.ergaerospace.com, Oakland, CA.
[44] Figliola, R., and Beasly, D., 2000, *Theory and Design for Mechanical Measurements*, 3rd ed., Wiley, New York, pp. 124, 310.

Direct Simulation of Transport in Open-Cell Metal Foam

Shankar Krishnan
Jayathi Y. Murthy
Suresh V. Garimella

NSF Cooling Technologies Research Center,
School of Mechanical Engineering,
Purdue University,
West Lafayette, IN 47907

Flows in porous media may be modeled using two major classes of approaches: (a) a macroscopic approach, where volume-averaged semiempirical equations are used to describe flow characteristics, and (b) a microscopic approach, where small-scale flow details are simulated by considering the specific geometry of the porous medium. In the first approach, small-scale details are ignored and the information so lost is represented in the governing equations using an engineering model. In the second, the intricate geometry of the porous structures is accounted for and the transport through these structures computed. The latter approach is computationally expensive if the entire physical domain were to be simulated. Computational time can be reduced by exploiting periodicity when it exists. In the present work we carry out a direct simulation of the transport in an open-cell metal foam using a periodic unit cell. The foam geometry is created by assuming the pore to be spherical. The spheres are located at the vertices and at the center of the unit cell. The periodic foam geometry is obtained by subtracting the unit cell cube from the spheres. Fluid and heat flow are computed in the periodic unit cell. Our objective in the present study is to obtain the effective thermal conductivity, pressure drop, and local heat transfer coefficient from a consistent direct simulation of the open-cell foam structure. The computed values compare well with the existing experimental measurements and semiempirical models for porosities greater than 94%. The results and the merits of the present approach are discussed. [DOI: 10.1115/1.2227038]

Introduction

Metal foams are a class of materials with low densities and novel physical, mechanical, thermal, electrical, and acoustic properties. They offer great potential for use as lightweight structures, and for energy absorption and thermal management applications [1]. Metal foams can offer effective solutions to many thermal management problems because of their large surface area to volume ratio and high permeability to fluids [2–4].

Flows in porous media may be modeled using two major approaches: (a) a macroscopic approach, where volume-averaged semiempirical equations are used to describe flow characteristics, and (*b*) a microscopic approach, where the small-scale flow details are simulated by considering the specific geometry of the porous medium. In the former approach, small-scale details are ignored and the information so lost is represented in the governing equations using an engineering model. In the latter approach, the intricate geometry of the porous structures is accounted for and the flow through these structures is computed. The latter approach is computationally expensive if the entire physical domain were to be simulated. Computational time can be reduced by exploiting periodicity in situations where periodicity is obtained.

Resolution of flow and heat transfer at the pore scale is necessary for a number of reasons when modeling metal foams. Detailed modeling of pore-scale heat transfer has been used to yield the effective thermal conductivity of the foam for situations with no flow. Existing models have frequently used idealized (and approximate) geometries assuming one-dimensional conduction heat transfer with a free parameter that is adjusted to match experimental results [5,6]. Another use for pore-scale models is to better characterize the pressure drop and local heat transfer coefficient during flow and convective heat transfer through the foam. Though there have been a few studies that take this approach [7,8], the range of Reynolds numbers considered does not adequately cover metal-PCM systems where the pore Reynolds numbers are very small ($\mathrm{Re} < 1$) [9]. The geometric representation of the foam varies greatly in the literature. Past investigators have represented the open-celled foam structure using (i) simple cubic unit cells consisting of slender circular cylinders [3], (ii) cubic unit cells consisting of square cylinders [10], (iii) truncated tetrakaidecahedron unit cells with triangular strands (fibers) [7], and (iv) a Weaire-Phelan unit cell [8]. Results from these models have included effective thermal conductivity and pressure drop calculations, but no information has been reported on local heat transfer. The local heat transfer coefficients are very important for closing (coupling) the solid and fluid energy equations in the two-medium volume-averaged models [9,11–13]. Also, the unit cell used to predict effective thermal conductivity is frequently different from the ones used for flow calculations [14]. Our objective in the present study is to obtain the effective thermal conductivity, pressure drop, and local heat transfer coefficient from a consistent direct simulation of the open-cell foam structure.

Foam Geometry

A three-dimensional periodic module is identified for the direct simulation of open-cell foams. The geometry chosen should be space filling and should have minimum surface energy. This is required because of the nature of the foaming process. A popular method for foaming metals such as aluminum is by blowing a foaming gas through molten metal with ceramic particles (used for stabilization) from below [1]. The gas bubbles developed are free to move around and pack themselves. The liquid metal accumulates at the interstices of the bubbles. For the process to reach a steady state, the bubbles must attain an equilibrium, i.e., a minimum surface energy state. Once the molten foam is solidified, the open-cell foam is rolled into sheets or into any other desired form [1]. Until recently, the body-centered-cubic (BCC) structure (similar to Kelvin's tetrakaidecahedron unit cell [15,16]), has been shown to have minimum surface-area to volume ratio compared to all other space filling structures [17]. Figure 1 shows a schematic diagram of a BCC unit cell. Though other choices such as the Weaire-Phelan (WP) unit cell are possible to model, a BCC unit cell model is used here for simplicity.

Contributed by the Heat Transfer Division of ASME for publication in the JOURNAL OF HEAT TRANSFER. Manuscript received July 6, 2005; final manuscript received January 9, 2006. Review conducted by N. K. Anand. Paper presented at the 2005 ASME International Mechanical Engineering Congress (IMECE2005), November 5–11, 2005, Orlando, Florida, USA.

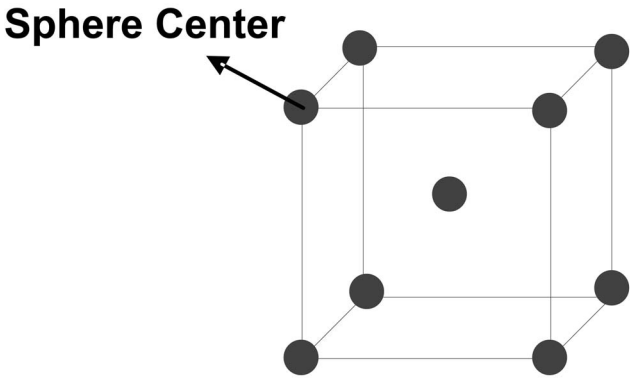

Fig. 1 Schematic of the body-centered-cubic model

In the present approach for foam geometry creation, the shape of the pore is assumed to be spherical and spheres of equal volumes are located at the vertices of the cell and at the center of the unit cell. The ideal periodic foam geometry is obtained by subtracting the unit cell cube from the spheres located at the body centers and vertices of the cube, as shown in Fig. 2. For open-cell structures, the sphere radius must be larger than half the side of the cube. The cross section of the foam ligaments are convex triangles (Plateau borders) and they all meet at symmetric tetrahedral vertices [17]. It may be noted that there is a nonuniform distribution of metal mass along the length of the ligament with more mass accumulating at the vertices (nodes), resulting in a thinning at the center of the ligament, as experimentally observed in foam samples by many authors [1,6,14,18]. Figure 3 shows some sample open-cell structures. The distinguishing feature of this approach is that (i) the geometry creation is simple; (ii) it captures many of the important features of real foams; and (iii) meshing of the geometry is easier compared to the approach carried out in [8] for modeling pressure drop. In [8], the foam was represented by an ideal Weaire-Phelan unit-cell obtained using Surface Evolver, a surface minimization software package. The idealized geometry was exported to a mesh generation program. After a series of post-processing steps on the geometry obtained from Surface Evolver, an unstructured volume mesh was generated for CFD calculations.

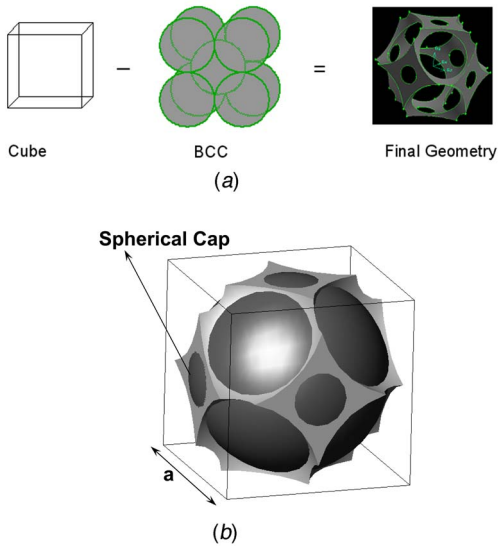

Fig. 2 Schematic diagram of (*a*) the geometry creation and (*b*) a periodic unit cell

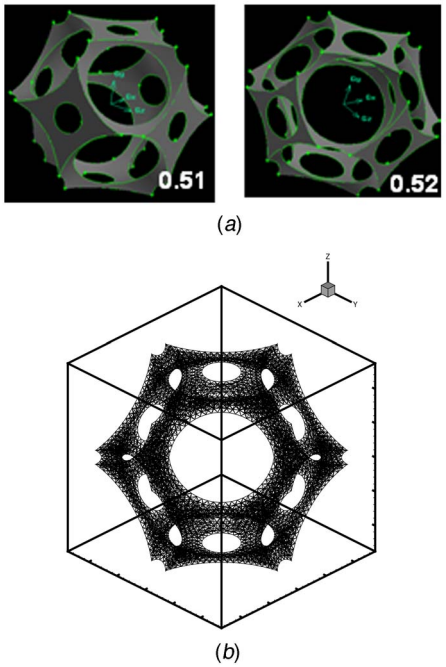

Fig. 3 Sample images of (*a*) the Representative Elementary Volume (REV) and (*b*) the computational mesh of the solid-foam (fluid zone grid points are omitted for clarity)

The expression for the porosity of the periodic module and the fluid inlet area of the periodic face can be obtained by accounting for the overlapping sphere volumes and circle areas, respectively. The intersection volume (lens volume) between two overlapping spheres is given by the relation

$$V_{\text{int}} = \frac{\pi}{12}(4R + s)(2R - s)^2, \tag{1}$$

where s is the center-to-center distance between the in-line spheres and R is the radius of the sphere. The body-centered sphere intersects with eight spheres on the vertices of the cube and hence the volume of the sphere at the body center of the cube is

$$V'_{bc} = \frac{4\pi}{3}R^3 - 8\left(\frac{V_{\text{int}}}{2}\right) \tag{2}$$

In addition to the sphere at the body center, there is one additional sphere volume contributed by the eight segments of the sphere at the vertices. Hence the total sphere volume not accounting for the spherical caps (see Fig. 2(*b*)) at the intersection between the face of the cube (plane) and the spheres is twice the V'_{bc} given in Eq. (2). The volume occupied by the spherical cap (the protruding volume from the unit cube for sphere diameter larger than length of the cube) due to a sphere intersecting a plane is given by the expression

$$V'_{\text{sc}} = \frac{\pi}{3}(R - a/2)^2(2R + a/2)$$

There are six spherical caps for the six corresponding faces of the cube and hence the volume of the fluid space in the cube is given by the expression

$$V'_f = 2\left(\frac{4\pi}{3}R^3 - \frac{\pi}{3}(4R + s)(2R - s)^2 - 2\pi(R - a/2)^2(2R + a/2)\right)$$

and, hence, the porosity is given by the relation

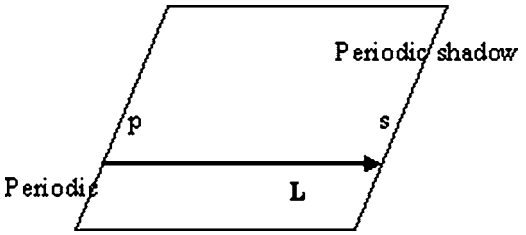

Fig. 4 Schematic illustration of a periodic domain

$$\varepsilon = \frac{V_f'}{V} = \frac{2\left(\frac{4\pi}{3}R^3 - \frac{\pi}{3}(4R+s)(2R-s)^2 - 2\pi(R-a/2)^2(2R+a/2)\right)}{a^3} \tag{3}$$

In the above expressions, a is the length of the side of the unit cell. Similarly, the inlet face area for the fluid can be obtained by subtracting the circle area and the intersection area between the sphere and the plane from the face area. The inlet face area is given by the expression

$$A_{\text{in},f} = \pi R^2 - 2\left[2R^2\cos^{-1}\left(\frac{s}{2R}\right) - \frac{1}{2}s\sqrt{4R^2-s^2}\right] + \pi\left(\frac{4R^2-a^2}{4}\right) \tag{4}$$

It should be noted that the center-to-center distance ($\sqrt{3}a/2$) for the volume (porosity) calculation is different from the center-to-center distance ($a/2$) for the area calculation. An effective pore diameter was extracted, setting Eq. (4) equal to the area of an equivalent circle. It should be noted that exactly at a sphere radius of 0.5, the BCC structure ceases to be a complete open structure, and the corresponding porosity at this condition is 0.94. The implications of this porosity on model fidelity will be discussed later in this paper.

Mathematical and Numerical Modeling

Flow and Temperature Periodicity. Consider a module with periodic boundaries separated by a constant translation vector ($\vec{L}$), as shown in Fig. 4. For simplicity, a two-dimensional domain is shown. This module represents one of a series of periodic modules translated by $\vec{L}$. It should be noted that there may be other periodic boundaries in the module, but there is no net inflow through any of these boundaries. For periodic boundaries, according to [19], the following relationship holds for the velocity and the pressure at any position $\vec{r}$:

$$u_i(\vec{r}) = u_i(\vec{r}+\vec{L}) = u_i(\vec{r}+2\vec{L}) = \cdots$$

$$P(\vec{r}) - P(\vec{r}+\vec{L}) = P(\vec{r}+\vec{L}) - P(\vec{r}+2\vec{L}) = \cdots$$

For periodic flows, the pressure gradient can be divided into two components – the gradient of the periodic component, $\partial\hat{p}/\partial x_i$, and the gradient of a linearly varying component, $(\partial\overline{p}/\partial x_i)\vec{e}_L$:

$$\frac{\partial P}{\partial x_i} = -\frac{\partial\overline{p}}{\partial x_i}\vec{e}_{L,i} + \frac{\partial\hat{p}}{\partial x_i}$$

where $e_{L,i}$ is the ith component of the unit vector in the direction $\vec{L}$.

For given heat-flux boundary conditions, the shape of the temperature field becomes constant from module to module. Consequently, the periodic condition for the temperature is given by

$$T(\vec{r}) - T_b(\vec{r}) = T(\vec{r}+\vec{L}) - T_b(\vec{r}+\vec{L}) = T(\vec{r}+2\vec{L}) - T_b(\vec{r}+2\vec{L}) = \cdots$$

Here the bulk temperature T_b is defined as

$$\frac{\int\int_A |u_i e_{L,i}| T\,\mathrm{d}A}{\int\int_A |u_i e_{L,i}|\,dA} = 0$$

where A is the area of the cross section.

Governing Equations. The governing flow and heat transfer equations for periodic fully developed incompressible, steady flow of a Newtonian fluid are [19,20]

$$\frac{\partial}{\partial x_i}(\rho u_i) = 0 \tag{5}$$

$$\frac{\partial}{\partial x_j}(\rho u_i u_j) = \frac{\partial p}{\partial x_i} + \frac{\partial}{\partial x_j}\left(\mu\frac{\partial u_i}{\partial x_j}\right)_i - \frac{\partial\overline{p}}{\partial x_i}e_{L,i} \tag{6}$$

$$\frac{\partial}{\partial x_i}(\rho u_i C_p T) = \frac{\partial}{\partial x_i}\left(k\frac{\partial T}{\partial x_i}\right) \tag{7}$$

The above equations assume that the flow is thermally and hydrodynamically fully developed. In Eq. (6), the terms involving $\partial^2/\partial x^2$ have been included to account for the large local streamwise gradients that may occur in periodically fully developed flows. The quantity $\partial\overline{p}/\partial x_i$ in Eq. (6) is assigned a priori, and controls the mass flow rate through the module, and hence the pore Reynolds number. In order to sustain periodicity, all fluid properties are assumed to be independent of temperature. It should be noted that on the solid bounding walls a no-slip boundary condition is imposed for the velocities and a constant heat flux is specified for the energy equation. Details of the mathematical model are available in [19]. An extensive treatment of the numerical method for the periodic flow and heat transfer on unstructured meshes along with the implementation is given in [20].

The periodic unit cell geometry was created using the commercial software GAMBIT [21]. The geometry was meshed using hybrid (tetrahedral and hexagonal) elements in GAMBIT by specifying the minimum edge length. The mesh so created was exported to the commercial code FLUENT [22] for flow simulations. A second-order upwind scheme was used for the flow and heat transfer calculations. A colocated pressure-velocity formulation in conjunction with the SIMPLE algorithm was used for obtaining the velocity fields, and the linearized systems of equations are solved using an algebraic multigrid algorithm. Details of the numerical method may be found in [23]. The calculations were terminated when the (scaled) residual [22] had dropped below 10^{-7} for all governing equations.

Grid independence of the solution for the meshes used in the present simulations was established. A pore Reynolds number of 20, a Prandtl number of 0.71, and a porosity of 0.965 were used for this set of calculations. Grid sensitivity was tested on three different grids: grid 1 (106,520 cells), grid 2 (188,885 cells), and grid 3 (383,230 cells). For grid 1, deviations of 2.6% and 0.5% in the friction factor and Nusselt number were found with respect to grid 3. For grid 2, the corresponding deviations with respect to grid 3 were 0.9% and 0.4%. The calculations reported in this paper were therefore performed on grid 2.

Results and Discussion

Effective Thermal Conductivity. In addition to the friction factor and Nusselt number results described above, the effective thermal conductivity of the foam is computed by considering heat conduction through the solid structure, in the absence of fluid flow. The effective thermal conductivity is computed numerically

by solving the conduction heat transfer equation ($\nabla \cdot k \nabla T = 0$). Only a single periodic module is used in the analysis. Using the periodicity assumption, each module in the heat flow direction experiences an equal temperature drop, i.e.,

$$\nabla T(\vec{r}) = \nabla T(\vec{r} + \vec{L}) = \nabla T(\vec{r} - \vec{L})$$

The numerical implementation of this type of periodic condition in the unstructured finite volume framework is described in [24]. Computations are performed by choosing an arbitrary temperature drop ΔT across the module in the heat flow direction and finding the resulting heat transfer rate at the periodic boundaries from the simulation results. The effective thermal conductivity of the module is then given by the expression

$$k_{eff} = \frac{-\int_{A_p} \mathbf{J} \cdot d\mathbf{A}}{\Delta T A_p} \tag{8}$$

In the above equation, **J** is the diffusion flux vector at the periodic face obtained from the simulation, dA is the outward pointing elemental face, area vector on the periodic face, and A_p is the area of the periodic face. Computations are performed using a modified version of the commercial code FLUENT [22]. It is noted that conduction through the solid foam and the fluid are considered for the calculation of the effective thermal conductivity of the module.

Lemlich Theory. Lemlich [25] developed a theory to predict the electrical conductivity of a polyhedral liquid foam of high porosity. The electrical conduction is viewed as occurring only through the Plateau border (ligament in the case of solid foams) along its axis, and not through its periphery. He found that the effective electrical conductivity of the foam was related to the electrical conductivity of the liquid through the following relation:

$$\sigma_{\text{eff}} = \sigma_l \frac{(1-\varepsilon)}{3} \tag{9}$$

This expression can be used for the effective thermal conductivity of the solid foam by exploiting the analogy between Ohm's law and Fourier's law, so that

$$k_{\text{eff}} = k_s \frac{(1-\varepsilon)}{3} \tag{10}$$

Figures 5(a) and 5(b) show the predicted effective thermal conductivity from the simulations as a function of porosity for an open cell foam saturated with air and water, respectively. Also plotted in Fig. 5 are measured experimental values [6,26] and results from semiempirical models in the literature [6]. It can be seen from Fig. 6 that the present model compares well with the experiments (both air and water) and the other models for porosities above 0.94. The foam geometry ceases to be "open" celled for porosities below 0.94, as previously discussed. It may be recalled that the models of Boomsma and Poulikakos [5], Calmidi and Mahajan [6], and Bhattacharya et al. [14] employ an adjustable free parameter to match the experiments of Calmidi and Mahajan [6]. The computations in this paper employ no such adjustable parameter; here, the attempt is to directly compute the effective conductivity from a detailed description of the foam geometry. It may be noted, however, that deviations from experimental data reflect the inadequacy of the present geometric model at lower porosities.

The Lemlich theory predicts the thermal conductivity values well when the interstitial fluid is air (Fig. 5(a)), but is less successful with water saturation (Fig. 5(b)). This deviation for water is primarily due to the assumption of negligible heat exchange to the interstitial fluid in the model, and also due to the ignored contribution of nodal resistance at the tetrahedral vertices. In the case of water (whose thermal conductivity is an order of magnitude higher than that of air) the heat exchange between the foam ligament and interstitial fluid is significant. Equation (10) may thus be used for very satisfactory order-of-magnitude estimates of effective thermal conductivity of open cell foams.

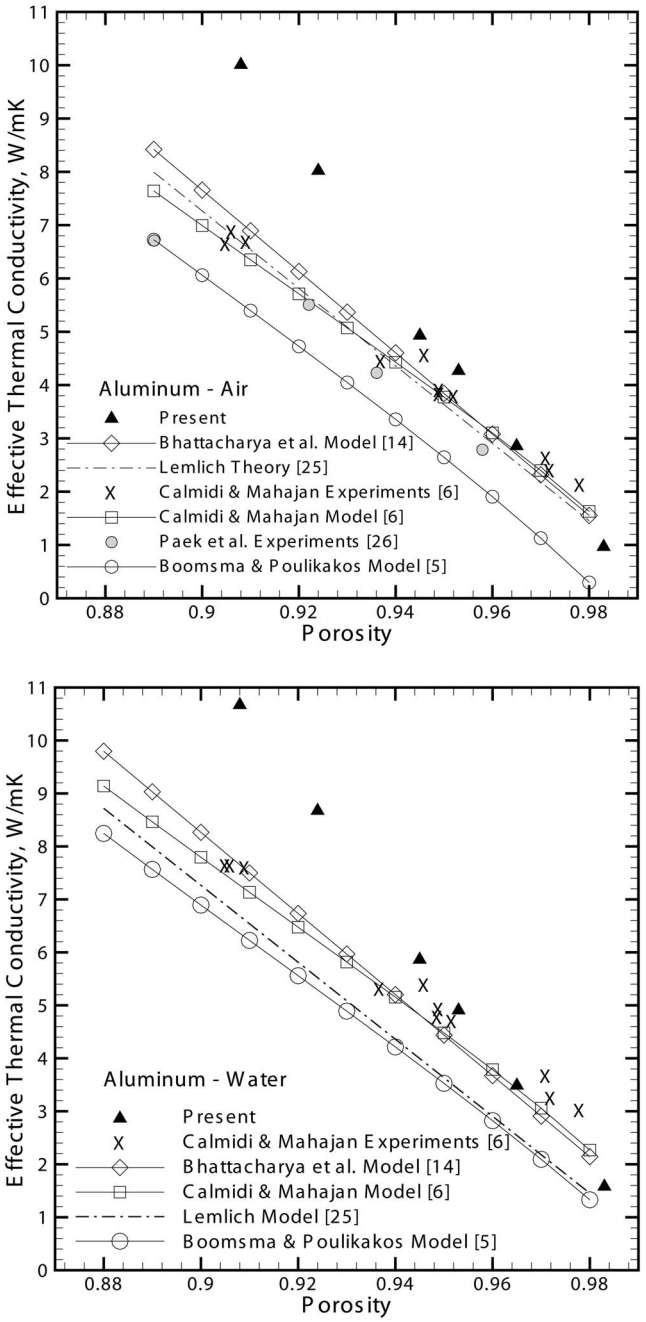

Fig. 5 Effective thermal conductivity as a function of porosity for aluminum foam saturated with (*a*) air and (*b*) water. The thermal conductivity values used for aluminum, air, and water are 218, 0.0265, and 0.613 W/mK, respectively [5]

Pressure—Drop and Heat Transfer Coefficient. For the calculations presented in this section, a constant heat flux boundary condition was imposed on the ligament walls. Hence, conduction through the ligaments of the foam is neglected. The streamwise diffusion term is retained in the momentum and energy equations which govern the generalized fully developed regime [19].

For a fluid flowing through a porous medium, boundary layer growth is significant only over an axial length of order $(\rho \mathrm{Ku_D})/\mu$, where u_D is $(K/\mu)dP/dx$. Similarly, the thermal boundary layer

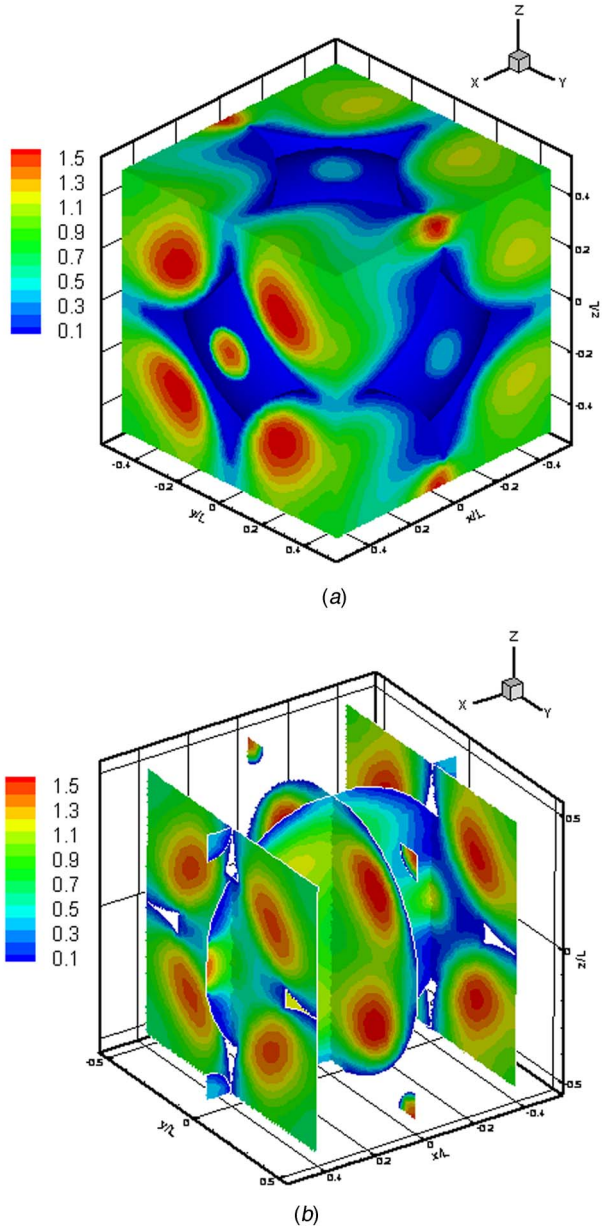

Fig. 6 Predicted results for (*a*) dimensionless velocity field, and (*b*) dimensionless velocity field at different locations ($x/L=-0.4$, 0.0, 0.4, and $y/L=0$)

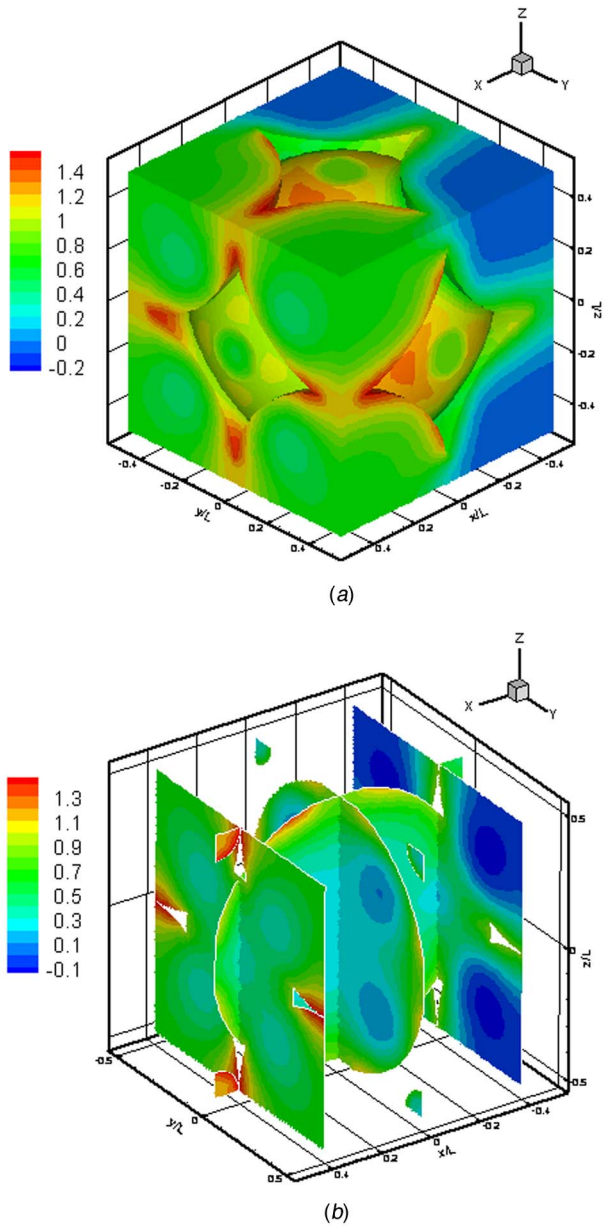

Fig. 7 Predicted results for (*a*) dimensionless temperature field and (*b*) dimensionless temperature maps at different locations ($x/L=-0.4$, 0 and 0.4, and $y/L=0$)

development length is on the order of $\mathrm{Ku_D}/\alpha$. The flow penetration is usually on the order of $\sqrt{\mathrm{K}}$, the characteristic length scale. It should be noted that unlike packed beds of spheres, the porosity and permeability for open-cell foams are constant even close to the solid boundary, i.e., the porosity does not change near the boundaries. In this section, a representative case of porosity $=0.965$ with air being the interstitial fluid is explained first. In the later part of the section we discusses the predicted variation of the friction factor and local Nusselt number.

Figure 6 shows the predicted dimensionless *u*-velocity field normalized using the mean velocity for a porosity of 0.965. The Reynolds number based on the effective diameter of the pore is 50 and the Prandtl number is 0.7. The effective diameter for all the computations is obtained by setting Eq. (4) equal to that of the area of a circle and backing out the effective diameter. Figure 6(*b*) shows the dimensionless velocity field on slices at discrete locations along the axial direction of flow. Also plotted in Fig. 6(*b*) is the velocity field at $y/L=0$ to illustrate the axial flow. The flow enters at the periodic inlet, $x/L=-0.5$. Periodic conditions are specified on all the boundary faces of the cubic unit cell. The solid boundaries are demarcated in white in the figure. From Fig. 6 the boundary layer development at the solid boundaries can be seen. Due to the resistance offered by the foam ligaments, the mean velocities are higher in some regions. Figure 7 shows the dimensionless temperature distribution $[(T-T_b)/(\overline{T_s}-T_b)]$ in the fluid for a porosity value of 0.965. As expected, the dimensionless temperature at the periodic inlet is low and thermal boundary layers can be clearly seen in Fig. 7(*b*). For $\mathrm{Pe}>1$, thermal dispersion effects become important [27,28]. The calculation of thermal dispersion conductivity is beyond the scope of this paper and is being considered in ongoing work.

Figure 8 shows the predicted normalized permeability of the foam as a function of porosity. Also shown are the reported ex-

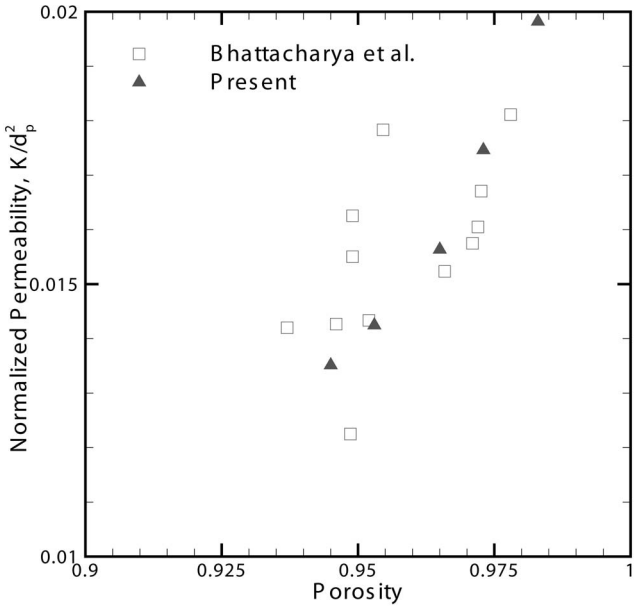

Fig. 8 Predicted normalized permeability of the foam as a function of the porosity of the foam. Also plotted are experimental data points from Bhattacharya et al. [14].

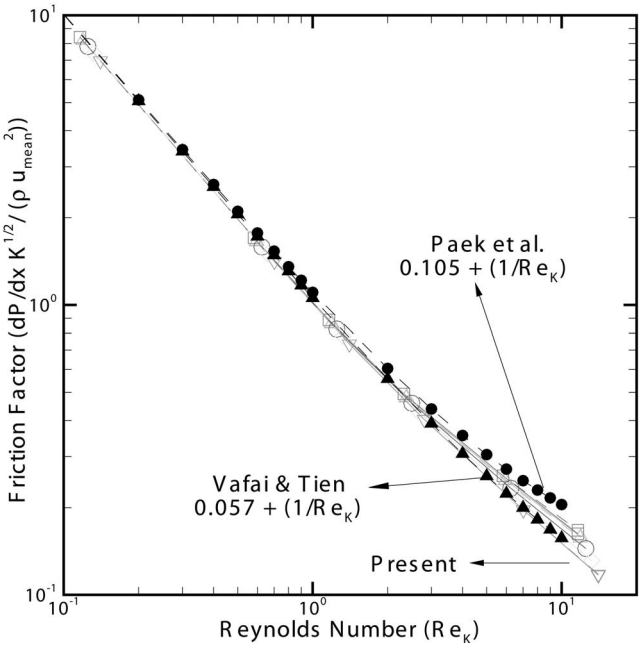

Fig. 9 Predicted friction factor as a function of Reynolds number based on the flow penetration length ($\sqrt{K}$). Also plotted are experimental correlations from Paek et al. [26] and Vafai and Tien [29]. Symbols are defined in Fig. 10.

perimental measurements from Bhattacharya et al. [14]. The permeability was normalized with the mean pore diameter of the open cell. The permeability was calculated from Darcy's law, $K = -(\mu u_{\text{mean}})/(\partial \overline{p}/\partial x_i)$ where the u_{mean} was obtained from the specified periodic inlet mass flow rate and using Eq. (4). The pressure drop was obtained as an output from the simulations. It should be noted that the reported permeability values are averaged values over a Reynolds number range of 1 to 10, i.e., in the linear Darcy regime.

Friction factors for the different cases considered are shown in Fig. 9 for porosities greater than 0.94. Also plotted in Fig. 9 are the experimental correlations from Paek et al. [26] and Vafai and Tien [29]. The friction factor is defined as

$$f = \frac{\left(-\frac{\partial \overline{p}}{\partial x_i}\right)\sqrt{K}}{\rho u_{\text{mean}}^2}$$

and in the Darcy regime, the friction factor (f) scales as the inverse of the modified Reynolds number based on the flow penetration length ($f = 1/\text{Re}_K$). From Fig. 9, it can be seen that for the porosity and modified Reynolds number ($\text{Re}_K \approx 1-10$) ranges considered in this study, the flow of both air and water through the foam is still in the Darcy regime. Deviations from $1/\text{Re}_K$ behavior were observed near a modified Reynolds number of approximately 20 for both air and water.

The Nusselt number for the foam was also calculated for the different cases considered and is defined as

$$\text{Nu} = \frac{hD}{k_f} = \frac{q''D}{k_f(\overline{T_s} - T_b)}$$

In the above equation $\overline{T_s}$ is the averaged temperature of the foam. Figure 10 shows the predicted Nusselt number as a function of the square root of the Peclet number. This scale is readily obtained by balancing the convective and axial diffusive fluxes. Also plotted in Fig. 10 is the correlation from Calmidi and Mahajan computed for air and for a porosity of 0.973 [30]. While their original correlation was based on the fiber diameter, it is rescaled here in terms of the mean pore diameter, with 0.00402 and 0.0005 m as the fiber and pore diameters, respectively [30]. The curves for air and water, respectively, are seen to collapse to a single line (unique slope) for $\text{Pe}_d < 30$, but they have different slopes due to the difference in the Prandtl number.

Conclusions

In this paper we present a consistent approach to the simulation of open-cell foam geometries for the study of effective thermal conductivity, friction factor, and Nusselt number. A BCC unit cell

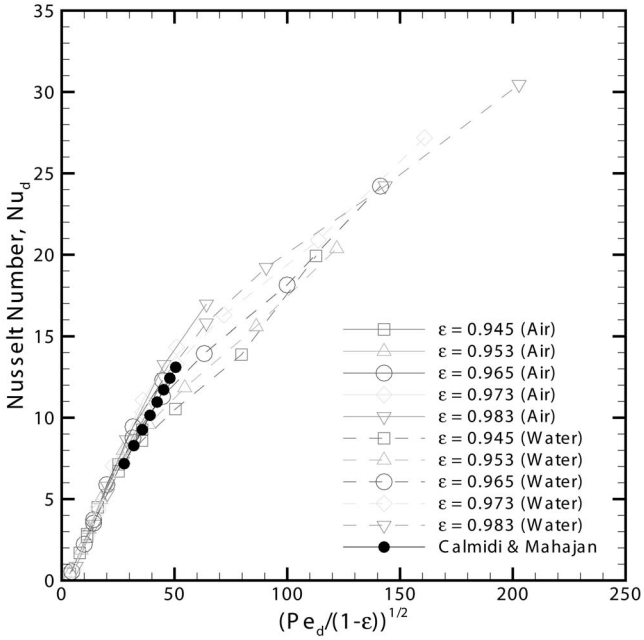

Fig. 10 Predicted Nusselt number based on effective diameter of the pore as a function of the square root of the Peclet number [$\text{Re}_d \text{Pr}/(1-\varepsilon)$]. Also plotted is the correlation from Calmidi and Mahajan [30].

model is used with no adjustable geometric parameters to match experiments for all three computations, unlike previous published work. For porosities higher than 94% ($\varepsilon > 0.94$), the predicted effective thermal conductivity, friction factor, and Nusselt number from the simulations compare reasonably well with the existing experimental and semiempirical models. However, the predicted effective thermal conductivity departs from measurements for low-porosity foams that are no longer open-celled; alternative geometric descriptions must be investigated at these lower porosities. For $\varepsilon > 0.94$, the effective thermal conductivity scales as $k_s(1-\varepsilon)/3$ for the range of porosities investigated, while the friction factor and Nusselt number scale as $1/\mathrm{Re}_K$ and $[\mathrm{Pe}/(1-\varepsilon)]^{1/2}$, respectively. It is expected that thermal dispersion effects will be significant for $\mathrm{Pe} > 1$ [27,28]. The present study may be extended to evaluate thermal dispersion effects, as is being done in ongoing work.

Acknowledgment

Support for this work from industry members of the Cooling Technologies Research Center, an NSF Industry/University Cooperative Research Center (www.ecn.purdue.edu/CTRC), is gratefully acknowledged. The authors wish to thank Dr. Dawei Sun for his help with AutoCAD.

Nomenclature

a = edge length of the unit cell, m
A = area, m^2
C_p = specific heat capacity, $J\,kg^{-1}\,K^{-1}$
D = diameter of the pore, m
Da = Darcy number
f = friction factor
h = heat transfer coefficient, $Wm^{-2}\,K^{-1}$
J = diffusion flux vector, $m^2\,s^{-1}$
K = permeability, m^2
k = thermal conductivity, $Wm^{-1}\,K^{-1}$
L = length of the periodic module, m
Nu = Nusselt number
q'' = heat flux, Wm^{-2}
Pr = Prandtl number
Pe = Peclet number
R = radius of the pore, m
Re = Reynolds number
s = center-to-center distance, m
T = temperature, K
t = time, s
u,v,w = velocities along x,y,z directions, ms^{-1}
V = volume, m^3
x,y,z = Cartesian coordinates

Greek Symbols

α = thermal diffusivity, $m^2\,s^{-1}$
ε = porosity
μ = dynamic viscosity, $kg\,m^{-1}\,s^{-1}$
ρ = density, $kg\,m^{-3}$

Superscripts

$-$ = average or mean

Subscripts

b = bulk
bc = body center
D = Darcian
eff = effective
f = fluid
in = inlet
int = intersection
s = solid
sa = surface area
sc = spherical cap

References

[1] Ashby, M. F., Evans, A., Fleck, N. A., Gibson, L. J., Hutchinson, J. W., and Wadley, H. J. G., 2000, *Metal Foams: A Design Guide*, Butterworth-Heinemann, Boston.
[2] Boomsma, K., Poulikakos, D., and Zwick, F., 2003, "Metal Foams as Compact High Performance Heat Exchangers," Mech. Mater., **35**, pp. 1161–1176.
[3] Lu, T. J., Stone, H. A., and Ashby, M. F., 1998, "Heat Transfer in Open-Cell Metal Foams," Acta Mater., **46**, pp. 3619–3635.
[4] Ozmat, B., Leyda, B., and Benson, B., 2004, "Thermal Applications of Open-Cell Metal Foams," Mater. Manuf. Processes, **19**, pp. 839–862.
[5] Boomsma, K., and Poulikakos, D., 2001, "On the Effective Thermal Conductivity of a Three-Dimensionally Structured Fluid-Saturated Metal Foam," Int. J. Heat Mass Transfer, **44**, pp. 827–836.
[6] Calmidi, V. V., and Mahajan, R. L., 1999, "The Effective Thermal Conductivity of High Porosity Fibrous Metal Foams," ASME J. Heat Transfer, **121**, pp. 466–471.
[7] Fourie, J. G., and Du Plessis, J. P., 2002, "Pressure Drop Modeling in Cellular Metallic Foams," Chem. Eng. Sci., **57**, pp. 2781–2789.
[8] Boomsma, K., Poulikakos, D., and Ventikos, Y., 2003, "Simulations of Flow Through Open Cell Foams Using an Idealized Periodic Cell Structure," Int. J. Heat Fluid Flow, **24**, pp. 825–834.
[9] Krishnan, S., Murthy, J. Y., and Garimella, S. V., 2005, "A Two-Temperature Model For Solid-Liquid Phase Change in Metal Foams," ASME J. Heat Transfer, **127**, pp. 995–1004.
[10] DuPlessis, P., Montillet, A., Comiti, J., and Legrand, J., 1994, "Pressure Drop Prediction For Flow Through High Porosity Metallic Foams," Chem. Eng. Sci., **49**, pp. 3545–3553.
[11] Krishnan, S., Murthy, J. Y., and Garimella, S. V., 2004, "A Two-Temperature Model For the Analysis of Passive Thermal Control Systems," ASME J. Heat Transfer, **126**, pp. 628–637.
[12] Kaviany, M., 1995, *Principles of Heat Transfer in Porous Media*, Springer-Verlag, New York.
[13] Amiri, A., and Vafai, K., 1994, "Analysis of Dispersion Effects and Non-Thermal Equilibrium, Non-Darcian, Variable Porosity Incompressible Flow Through Porous Media," Int. J. Heat Mass Transfer, **37**, pp. 939–954.
[14] Bhattacharya, A., Calmidi, A. A., and Mahajan, R. L., 2002, "Thermophysical Properties of High Porosity Metal Foams," Int. J. Heat Mass Transfer, **45**, pp. 1017–1031.
[15] Thomson, W., 1887, "On the Division of Space With Minimum Partitional Area," Philos. Mag., **5**, pp. 645–654.
[16] Weaire, D., 2001, "A Philomorph Looks at Foam," Proc. Am. Philos. Soc., **145**, pp. 564–574.
[17] Phelan, R., Weaire, D., and Brakke, K., 1995, "Computation of Equilibrium Foam Structures Using the Surface Evolver," Exp. Math., **4**, pp. 181–192.
[18] Dharmasena, K. P., and Wadley, H. N. G., 2002, "Electrical Conductivity of Open-Cell Metal Foams," J. Mater. Res., **17**, pp. 625–631.
[19] Patankar, S. V., Liu, C. H., and Sparrow, E. M., 1977, "Fully Developed Flow and Heat Transfer in Ducts Having Streamwise-Periodic Variations of Cross-Sectional Area," ASME J. Heat Transfer, **99**, pp. 180–186.
[20] Murthy, J. Y., and Mathur, S., 1997, "Periodic Flow and Heat Transfer Using Unstructured Meshes," Int. J. Numer. Methods Fluids, **25**, pp. 659–677.
[21] Fluent Inc., User's Guide for GAMBIT 2.0, 2002.
[22] Fluent Inc., User's Guide for FLUENT 6.0, 2002.
[23] Mathur, S. R., and Murthy, J. Y., 1997, "A Pressure-Based Method for Unstructured Meshes," Numer. Heat Transfer, Part B, **31**, pp. 195–216.
[24] Kumar, S., and Murthy, J. Y., 2005, "A Numerical Technique For Computing Effective Thermal Conductivity of Fluid-Particle Mixtures," Numer. Heat Transfer, Part B, **47**, pp. 555–572.
[25] Lemlich, R., 1978, "A Theory For the Limiting Conductivity of Polyhedral Foam at Low Density," J. Colloid Interface Sci., **64**, pp. 107–110.
[26] Paek, J. W., Kang, B. H., Kim, S. Y., and Hyun, J. M., 2000, "Effective Thermal Conductivity and Permeability of Aluminum Foam Materials," Int. J. Thermophys., **21**, pp. 453–464.
[27] Koch, D. L., and Brady, J. F., 1985, "Dispersion in Fixed Beds," J. Fluid Mech., **154**, pp. 399–427.
[28] Koch, D. L., and Brady, J. F., 1985, "The Effective Diffusivity of Fibrous Media," AIChE J., **32**, pp. 575–591.
[29] Vafai, K., and Tien, C. L., 1982, "Boundary and Inertia Effects on Convective Mass Transfer in Porous Media," Int. J. Heat Mass Transfer, **25**, pp. 1183–1190.
[30] Calmidi, V. V., and Mahajan, R. L., 2000, "Forced Convection in High Porosity Metal Foams," ASME J. Heat Transfer, **122**, pp. 557–565.

Drag and Heat Transfer Reduction Phenomena of Drag-Reducing Surfactant Solutions in Straight and Helical Pipes

Wael I. A. Aly

Hideo Inaba
e-mail: inaba@mech.okayama-u.ac.jp

Naoto Haruki

Akihiko Horibe

Graduate School of Natural Science and Technology,
Okayama University,
Okayama 700-8530, Japan

Flow drag and heat transfer reduction phenomena of non-ionic aqueous surfactant solutions flowing in helical and straight pipes have been experimentally investigated at surfactant solution concentration range of 250–5000 ppm *and temperature range of* 5–20°C. *The helically coiled pipes have curvature ratios range of 0.018–0.045. Experimental findings indicate that the friction factors and the heat transfer coefficients of the surfactant solution in helical pipes are significantly higher than in a straight pipe and lower than Newtonian fluid flow like water through the same coils in the turbulent drag reduction region. Drag reduction and heat transfer reduction increase with an increase in surfactant solution concentration and temperature in the measured concentration and temperature ranges. On the other hand, they decrease with increasing of the curvature ratio. A set of empirical expressions for predicting the friction factor and the average Nusselt number for the surfactant solution's flow through helical and straight pipes have been regressed based on the obtained data in the present experiments.*
[DOI: 10.1115/1.2217751]

Keywords: drag reduction, surfactant, convective heat transfer, helical pipe, secondary flow, curvature ratio

1 Introduction

The drag reduction phenomenon has been known for more than five decades. In the pioneering study of Toms and Mysels [1], they independently observed that at constant pressure gradient, the turbulent flow rate could be increased by the addition of polymer or surfactant to a Newtonian solvent. Nowadays, there are a great number of practical engineering applications that make use of this phenomenon. One of the most attractive applications is to reduce the pumping power of circulating flows like district heating and cooling (DHC) systems, especially by using surfactant additives. Surfactants (a very convenient abbreviation of "Surface-active agents") have a definite advantage over other drag reducing additives, like polymers, that their structures are thermodynamically stable and self-assemble quickly after degradation, which allows them to be reused in circulation flows [1,2]. However, accompanying the drag reduction is a heat transfer reduction; this heat transfer reduction is beneficial for long distance transport of hot or cold fluids, but detrimental for the applications utilizing heat exchange devices where heat exchange is essential, like DHC systems. Methods to temporarily enhance the heat transfer ability of drag reducing surfactants in heat exchangers and regaining drag reduction properties downstream of the heat exchangers have been reviewed by Qi et al. [3]. Much more is known about flow drag and heat transfer reduction in straight channels and pipes than about phenomenon in helical pipes, despite the fact that flow in helical pipes is a fundamental problem.

Due to the occurrence of a secondary flow in planes normal to the main flow, heat and mass transfer in helical pipes are significantly higher than a straight pipe. Also, because of their compact structure and high heat transfer coefficient, helical pipes have been introduced as one of the passive heat transfer enhancement techniques. Helical pipes are frequently used in many engineering applications to enhance the process of heat and mass transfer, including domestic hot water heaters, chemical process reactors, industrial and marine boilers, well drilling, completion, and stimulation operations in the petroleum industry, kidney dialysis devices, and blood oxygenators, among many others [4,5].

It is rather surprising to find that, despite its important applications, the flow of drag-reducing fluids in curved and helical pipes has received much less attention in the literature than its Newtonian counterpart.

In the present article the flow drag and heat transfer reduction characteristics of nonionic aqueous surfactant solution in helically coiled pipes are investigated experimentally and compared to a straight pipe.

2 Experimental Facility and Procedure

A schematic diagram of the experimental apparatus featuring its main components and instrumentation is shown in Fig. 1. A 2 m-long straight entrance section was used to provide a well developed and stable inlet velocity distribution. Three helical stainless steel pipe test sections of different coil diameters were used in the experiments with an outer pipe diameter of 16 mm and inner diameter of $d=14.4$ mm, with ten turns. The curvature ratios (pipe-to-coil diameter ratio $\delta=d/D$) are $\delta=0.045$, 0.027, and 0.018. Otherwise, a 1.5 m length straight pipe test section was prepared to measure the straight pipe friction factor and heat transfer. The details of the geometry of the helical pipes are illustrated in Fig. 2. The geometric parameters of the helical pipes and the straight pipe test sections are provided in Table 1. Water or the aqueous oleyldihydroxyethylamineoxide (ODEAO) surfactant solution as a test fluid from a constant temperature tank was circulated by a centrifugal pump with variable-speed controller through a 5 m pipe length to the straight entrance section before entering the test sections; the test liquid flow rate was measured using a magnetic flow meter with measuring accuracy of ±0.5% and repeatability of ±0.1%.

Contributed by the Heat Transfer Division of ASME for publication in the JOURNAL OF HEAT TRANSFER. Manuscript received May 17, 2005; final manuscript received January 23, 2006. Review conducted by Raj M. Manglik.

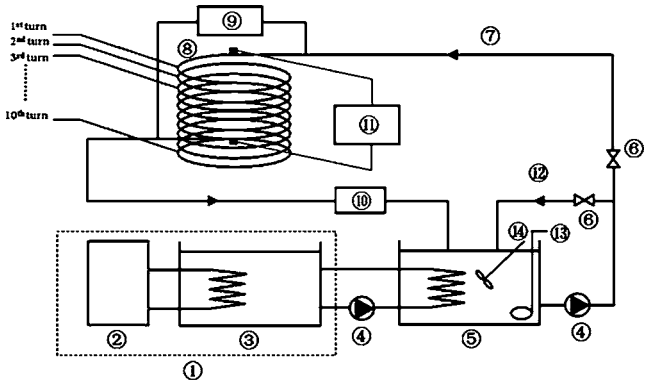

① Brine chiller
② Condensing unit
③ Brine tank
④ Centrifugal pump
⑤ Constant temperature tank
⑥ Valve
⑦ Hydrodynamic entry length
⑧ Helically coiled pipe test section
⑨ Differential pressure gauge
⑩ Magnetic flow meter
⑪ AC power supply
⑫ By-pass line
⑬ Heater
⑭ Agitator

Fig. 1 Schematic diagram of the experimental apparatus

Pressure-loss ΔP in the axial direction of the test sections was measured using a calibrated differential pressure transducer connected with pressure taps mounted on the inlet and exit of the test sections, and in cases of low pressure loss using manometers. The estimated accuracy of pressure-loss measurements is ±1.5% of the full range chosen considering the pressure transducer accuracy. The friction factor f was calculated by the following equation:

$$f = \frac{\Delta P}{(L/d)(1/2)\rho U_m^2} \tag{1}$$

where ρ is the test liquid density at mean bulk temperature and U_m is the mean axial velocity of the test liquid.

The heat transfer experiments were carried out under uniform heat flux boundary condition. The test sections were heated directly by passing an electric current through the test sections. The constant heating currents provided by an alternative current (ac) power supply connected directly to the inlet and outlet of the test sections by means of customized copper clamps providing very good electrical contact that allowed for varying the heating power. The boundary condition of a uniform heat flux could reasonably be assumed for the current study. The heat flux of the series of experiments ranged from 0.67 to 8.9 kW/m^2 for the straight pipe and from 0.14 to 5.0 kW/m^2 for the helical pipes.

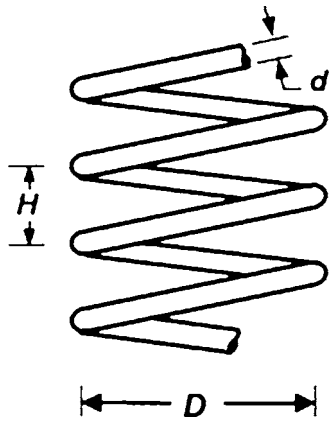

Fig. 2 Geometry of the helical pipe test section

Table 1 Geometrical parameters of the test sections

Test Sect.	d (mm)	d_o (mm)	D (mm)	H (mm)	$\delta = d/D$	L/d	No. of Turns
Coil 1	14.4	16	320	32	0.045	694	10
Coil 2	14.4	16	540	32	0.027	1180	10
Coil 3	14.4	16	800	32	0.018	1746	10
S.P.	16	22	⋯	⋯	⋯	94	⋯

The wall temperature of the coils was measured along the heated length at 40 axial stations with axially increasing spacing utilizing *T*-type thermocouples mounted on the top side of the coils. Pre-experiments have been done to check the validity of setting the wall temperature thermocouples on the top position by setting thermocouples on the top, bottom, outer, and inner sides of the helical pipe periphery in some sections along the coils. The maximum deviation of the top position wall temperature from the average wall temperature was within ±0.5% and the maximum temperature difference between the inner and outer walls in the pre-experiments was 0.7°C. It is concluded from the pre-experiments that the top position wall temperature is representative of the average wall temperature in the periphery direction. Moreover, two previous studies [6,7] under the constant heat flux wall condition also observed that the local heat transfer coefficient (or Nusselt number) is the highest on the outer side of the coiled pipe, the lowest on the inner side, and average value on the top and the bottom sides. It should be emphasized, however, that if the difference between the inner and outer walls temperature is large enough, then selecting the top position depending on simple averaging might not be accurate to calculate the local heat transfer coefficients.

Another two *T*-type thermocouples were set in the inlet and outlet of the test coils for test liquid bulk temperature measurements. Due to the method of heating, it was reasonable to assume a linear increase in the bulk temperature across the heated length. All thermocouples were connected to a data acquisition system. Before installation, all thermocouples were calibrated against a standard precision thermometer and demonstrated an accuracy of ±0.1°C. After the thermocouples were installed, the test section was wrapped with 100 mm thickness of glass wool insulating material to minimize the heat loss from the test coil to the environment. The maximum heat loss was estimated within ±3.0% of the amount of heat evolved from the heated coil.

Heat transfer experiments were performed for water and ODEAO surfactant solution at different temperatures and concentrations. Each test run started after achieving the steady state of the differential pressure, temperatures, and flow rate at each measuring point. For the constant heat flux boundary condition, the local Nusselt number is defined as:

$$\mathrm{Nu}_x = \frac{q''d}{k(T_w - T_b)} \tag{2}$$

where T_w is the local wall temperature, T_b is the test liquid bulk temperature at the same cross section, q'' is the power input per unit area at the coil-liquid interface, and k is the thermal conductivity of the test liquid. The thermophysical properties of the surfactant solution were estimated at the mean bulk temperature. Except viscosity, it is a common practice to use the thermophysical properties (density, specific heat, and thermal conductivity) of the solvent (here it is water) in data reduction of surfactant solutions. To minimize the variation in the test liquid properties and the effect of natural convection, the bulk temperature increases $(T_{b,\mathrm{out}} - T_{b,\mathrm{in}})$ during the experiments were strictly controlled and kept below 4.5°C, and the maximum temperature difference between the inlet temperature of the test fluid and the wall temperature at the exit from the helical pipe test sections was less than 6°C. Average Nusselt number was calculated by integrating the local values over the entire length of the helical pipe test sections.

Based on the measurements of different variables, the major parameter uncertainties were estimated by the method recom-

Table 2 Experimental uncertainties

Flow rate	±0.5%	Pipe diameter	±0.7%
Temperature	±0.1°C	Velocity	±1.5%
Heat flux	±1.5%	Friction factor	±3.4%
Density	±0.25%	Reynolds number	±2.2%
Conductivity	±0.2%	Dean number	±2.4%
Viscosity	±1.9%	Nusselt number	±11%

mended by Moffat [8]. The uncertainties of the thermoproperties (except ODEAO solution viscosity) were determined by comparing the correlations used in data reduction with the tabulated values in handbooks plus the uncertainties of the original data if available. Table 2 summarized the uncertainties results.

3 Rheological Properties of Surfactant Solution

The drag-reducing surfactant used in the present study was a mixture of the non-ionic surfactant oleyldihydroxyethylamineoxide (ODEAO, $C_{22}H_{45}NO_3=371$) in the amount of 90% and the zwitterionic surfactant cetyldimethylaminoaciticacidbetaine (CDMB, $C_{20}H_{41}NO_2=327$) in the amount of 10%, CDMB was added to the ODEAO in order to avoid the chemical degradation due to ionic impurities existing in tap water [9]. The chemical structure of the surfactant is shown in Fig. 3. From this point forward, the used surfactant will be abbreviated as ODEAO. Non-ionic surfactants like ODEAO are known as environmentally acceptable drag-reducing additives. The proposed ODEAO solution has a less eco-toxicity (lethal dose (LD_{50}) of 5000 mg/kg and lethal concentration (LD_{50}) of 0.6 mg/L in 24 h), and better biodegradability (elimination percentage of 62% (OECD) test) than many other surfactants.

Many authors who studied drag-reducing surfactant systems [10–12] have stated that viscoelastic rheological properties of the surfactant solutions are responsible for the occurrence of drag reduction. However, Lu et al. [13] reported an effective drag-reducing surfactant system which lacks normal viscoelasticity characteristics. It did, however, exhibit high apparent extensional viscosity. On the other hand, there are strong indications for a relationship between drag reduction and extensional viscosity [13,14].

Due to the difficulties in measuring both viscoelasticity and extensional viscosity of dilute and semi-dilute surfactant solutions, only the shear viscosity of the surfactant solution was measured in the present study using a Brookfield viscometer. Surfactant concentration range for the surfactant solution used in the present study was from $C=250$ ppm to 5000 ppm and temperature range from $T=5$ to 20°C. The measuring accuracy of the viscometer was examined by using distilled water as a reference fluid. The obtained results of the distilled water agreed with the reference data within a standard deviation of 1.9%. The viscous characteristic of the ODEAO surfactant solution is expressed by the following power law model with two constants:

$$\tau = K\dot{\gamma}^n \tag{3}$$

where τ is the shear stress and $\dot{\gamma}$ is the shear rate. The consistency index (or pseudoplastic viscosity) K and the power law exponent (or flow behavior index) n for the ODEAO surfactant solution were determined using the shear stresses and shear rates measured using the viscometer at different concentrations and temperatures.

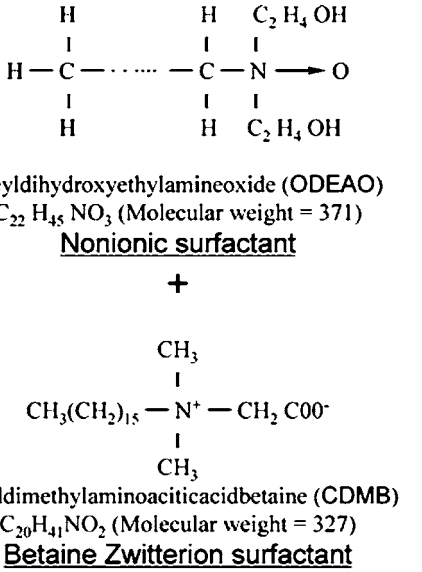

Fig. 3 Chemical structure of surfactant

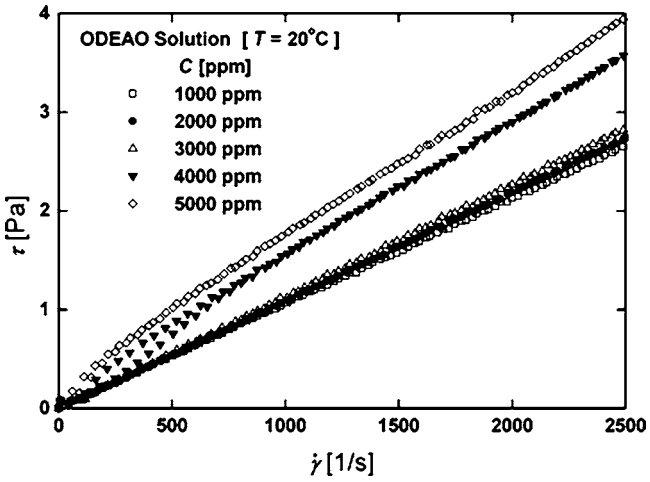

Fig. 4 Relationship between τ and $\dot{\gamma}$

Figure 4 shows the relation between τ and $\dot{\gamma}$ for the ODEAO solution at 20°C and different concentrations, data for concentrations $C=1000$ ppm up to 3000 ppm indicates Newtonian behavior (having a slope of unity). The relationship between both of K and n and the surfactant solution temperature at different concentration C is shown in Fig. 5. It is seen from Fig. 5 that the consistency index K value increases drastically with increasing concentration C in the range of $C>3000$ ppm and temperature $T<25$°C. The value of K decreases with an increase in temperature at the same concentration. Figure 5 shows that the ODEAO surfactant solution almost behaves as a Newtonian fluid ($n=1$) for C up to 3000 ppm, and behaves as a pseudoplastic fluid ($n<1$) for $C>3000$ ppm.

It is intriguing that even if the ODEAO surfactant solution behaves as a Newtonian fluid for surfactant concentrations up to 3000 ppm, the turbulent drag reduction effect appears, as will be shown later in the present study.

4 Results and Discussion

4.1 Flow Drag Reduction. The pressure drop measurements have been conducted along the helical and straight pipes. Figure 6 shows the relationship between the friction factor f and the Reynolds number Re or the modified Reynolds number Re′ (Re in case of water and Re′ in case of ODEAO surfactant solution) for the helical pipes and the straight pipe at surfactant concentration of $C=1275-1756$ ppm and at temperature of 20°C. The modified Reynolds number Re′ introduced by Metzner and Reed [15] is defined as follows:

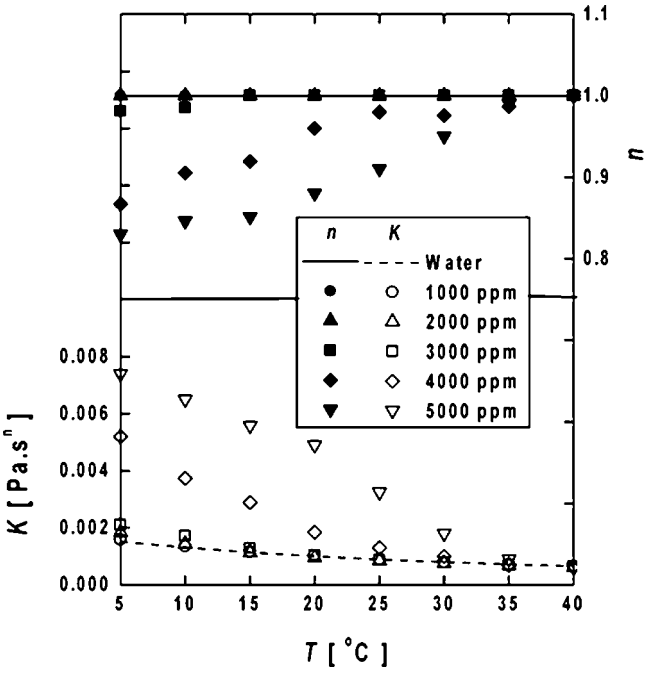

Fig. 5 Relationship between *K* and *n* with temperature, at different concentrations

$$\mathrm{Re}' = 8^{1-n}\left(\frac{3n+1}{4n}\right)^{-n}\left(\frac{\rho U_m^{2-n} d^n}{K}\right) \tag{4}$$

If n is equal to one, Eq. (4) becomes the conventional relationship for Newtonian fluids. The dashed lines in Fig. 6 show calculated water friction factor f in the straight pipe for laminar flow ($f_{SL}=64/\mathrm{Re}$) and turbulent flow ($f_{ST}=0.3164/\mathrm{Re}^{0.25}$). The solid lines in Fig. 6 represent Eq. (5) proposed by Manlapaz and Churchill [16] and Eq. (6) introduced by Mishra and Gupta [17] for Newtonian fluid flow through helical pipes for laminar and turbulent flow, respectively. The obtained data of friction factor for water in the present experiments agree well with straight pipe Newtonian equations and both Eqs. (5) and (6).

$$f_{CL} = f_{SL}\left[1 + \left(1 + \frac{\delta}{3}\right)^2 \frac{\mathrm{Dn}}{88.33}\right]^{1/2} \tag{5}$$

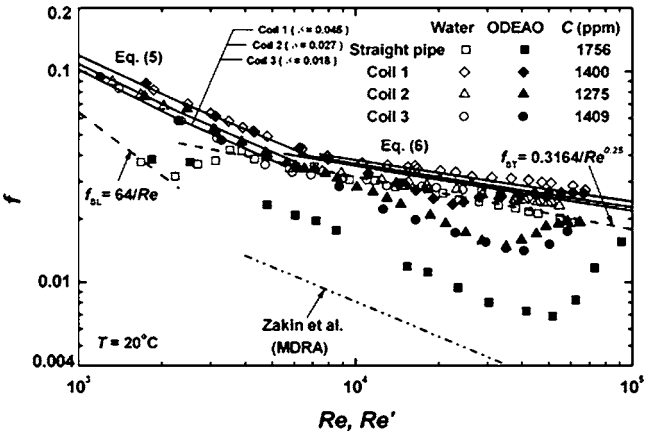

Fig. 6 Friction behavior of aqueous ODEAO solution in the helical and straight pipes

$$f_{CT} = f_{ST} + 0.03(\delta)^{1/2} \tag{6}$$

where δ is the curvature ratio ($\delta=d/D$, pipe-to-coil diameter ratio) and Dn is the Dean number defined as:

$$\mathrm{Dn} = \mathrm{Re}\,\delta^{1/2} \tag{7}$$

Equation (5) available for $\mathrm{Dn}>40$, and Eq. (6) provided that $\mathrm{Re}_{crit}<\mathrm{Re}<10^5$, $0.289\times10^{-2}<\delta<0.15$, and $0<H/D<25.4$, where Re_{crit} is the critical Reynolds number from laminar flow to turbulent flow through helical coils proposed by Ito [18] ($\mathrm{Re}_{crit}=2\times10^4\ \delta^{0.32}$).

Both Equations (5) and (6) should account for pitch effect using the diameter of curvature instead of the coil diameter when the pitch H is greater than the coil radius $D/2$ [16], which is not applicable in the present study.

It is evident from Fig. 6 that the present experimental data for water and the ODEAO surfactant solution agree well with the Newtonian fluid flow correlations in the straight pipe ($\mathrm{Re}<2300$) and the helical pipes ($\mathrm{Re}<\mathrm{Re}_{crit}$) in the laminar region. On the other hand, the turbulent friction factor data of the ODEAO surfactant solution falls below the Newtonian fluid flow correlations in the straight pipe and the helically coiled pipes.

It is clear that transition from laminar flow to turbulent flow in the helical pipes as well as the straight pipe happened at higher Re' values than water, the laminar flow line is extended up to $\mathrm{Re}'=5.17\times10^4$, 2.25×10^4, 3.5×10^4, and 4.1×10^4 according to straight pipe, coil 1, coil 2, and coil 3, respectively. Therefore, the ODEAO surfactant solution has the flow drag reduction effect in the helically coiled pipes as well as in the straight pipe. This effect can be explained by the turbulence suppression (or flow laminarization) of the turbulent energy dissipation due to the high ordered networks of the rod-like micelles structure of the ODEAO surfactant in the solution. Transition to turbulent flow occurs when the surfactant solution exceeds the critical wall shear stress under the strong mechanical load at high velocity. Also, the maximum drag reduction asymptote for surfactant solutions flow through straight pipes proposed by Zakin et al. [19] is indicated in Fig. 6. This maximum drag reduction asymptote is approximately valid in the range between $4000<\mathrm{Re}<130,000$ and is based on the solution shear viscosity:

$$f = 1.26\mathrm{Re}^{-0.55} \tag{8}$$

Unfortunately, such an equation is not yet available for helically coiled pipes flow. However, it seems that from Fig. 6 the extension of the laminar flow line may be the maximum drag reduction asymptote for coiled pipe flow if the laminar flow behavior could be sustained.

4.1.1 Temperature Effect. The friction behavior in the turbulent-flow regime depends strongly on the temperature. Figure 7 shows the friction behavior of aqueous ODEAO solution for various temperatures in coil 3 and the straight pipe. It is understood that the critical modified Reynolds number Re'_{crit} increases with an increase in temperature in the measured range ($T=5-20°\mathrm{C}$). This would be related to the critical wall shear stress. The wall shear stress τ_w as a function of the mean flow velocity U_m is shown in Fig. 8 for the ODEAO surfactant solution flow through coil 3 and the straight pipe at concentration $C=1409$ and 1756 ppm, respectively, and different temperatures. The wall shear stress given by

$$\tau_w = \frac{d\Delta P}{4L} \tag{9}$$

The critical wall shear stress τ_{wc} is the stress which is reached at the critical velocity when drag reduction starts to decrease and can be identified in Fig. 8 as a sudden change in the shear stress slope. It is noticed that the τ_{wc} increases with temperature at the same concentration in both helical pipe ($\tau_{wc}=2.0$, 2.3, 5.8, and 14.9 Pa at $T=5$, 10, 15, and 20°C, respectively) and the straight pipe

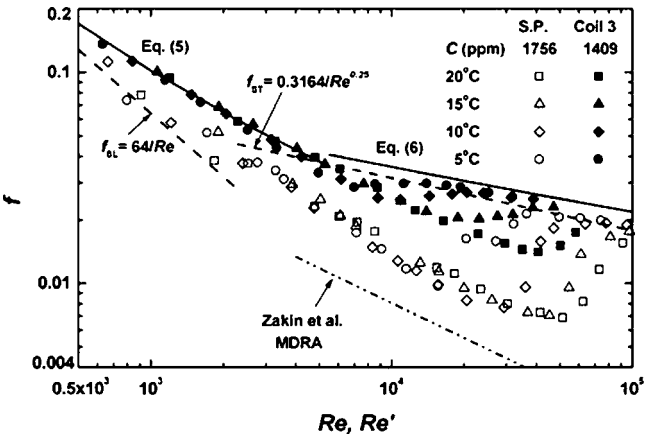

Fig. 7 Temperature effect on friction behavior of aqueous ODEAO solution in coil 3 and the straight pipe

(τ_{wc}=3.1, 3.4, 6.4, and 9.7 Pa at T=5, 10, 15, and 20°C, respectively).

4.1.2 Concentration Effect. ODEAO surfactant concentration C effect on the friction factor is shown in Fig. 9 with the relation between the friction factor f and the Reynolds number Re or the modified Reynolds number Re′ for laminar and turbulent flow through the straight pipe (Fig 9(*a*)) and coil 1 (Fig. 9(*b*)) at temperature T=10°C and different concentrations. It can be noticed that the increase in concentration of the surfactant results with an increase in the critical modified Reynolds number Re'_{crit}, since the increase in concentration strengthens the network's structure of the rod-like surfactant micelles. It is seen in Fig. 9 that for concentrations up to about 1400 ppm the drag reduction effect is small. On the other hand, for higher concentrations (1760–3440 ppm) the effect is strong. However, increasing the concentration from 1760 up to 3440 ppm has a little effect on drag reduction. A possible reason is the network's structure of the rod-like surfactant micelles became saturated and increasing the concentration more will not be effective.

4.1.3 Curvature Effect. Curvature is an essential parameter of a helical pipe. It creates the secondary flow inside the pipe. The effect of curvature can be seen in Fig. 6. It can be observed that the friction factors for all the coils are higher than the friction factor in case of the straight pipe due to the secondary flow at the same Reynolds number or the modified Reynolds number. Also,

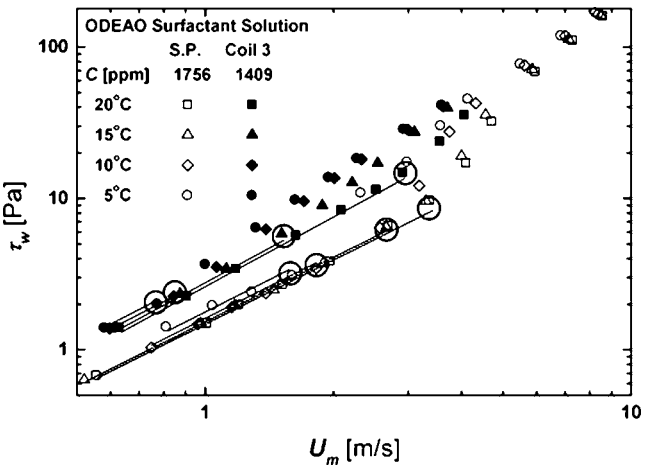

Fig. 8 Wall shear stress τ_w as a function of the mean flow velocity U_m

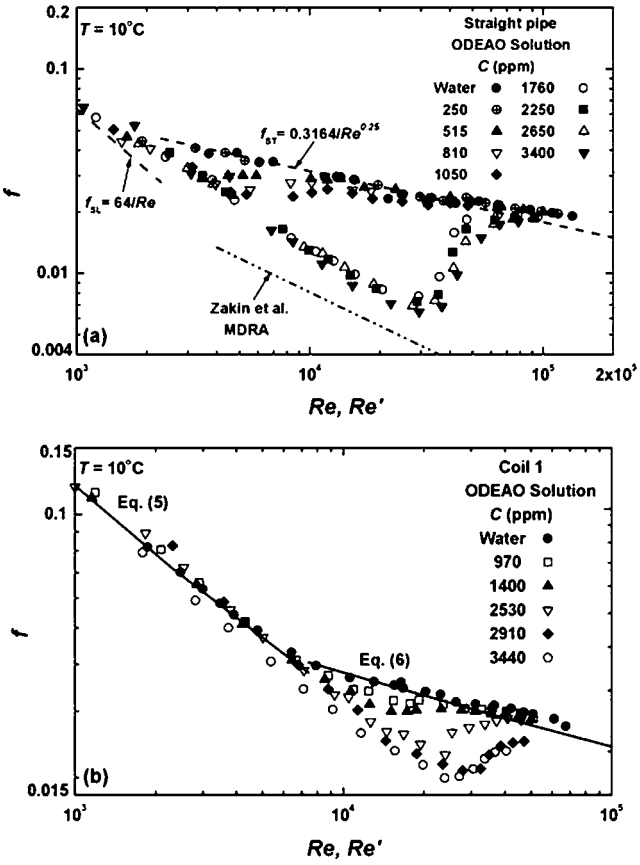

Fig. 9 Concentration effect on friction factor: (*a*) Straight pipe (*b*) coil 1 (T=10°C)

the higher the curvature ratio (δ=d/D), the larger the friction factor, since the increase in curvature ratio increases the secondary flow intensity, thereby increasing the pressure drop or the wall shear stress τ_w at the same Re′.

4.2 Wall Temperature Distribution. The axial variation in wall temperature is presented in Fig. 10 for water and surfactant solution flow through coil 1 and coil 2. The following definitions were used for the dimensionless variables, X and θ:

$$X = \frac{x}{L_t} \quad \text{and} \quad \theta = \frac{T_w - T_{b,\text{in}}}{T_{b,\text{out}} - T_{b,\text{in}}} \tag{10}$$

where x denotes the distance from the entrance of the helical pipe; L_t represents the pipe length of one turn of the test section; T_w is the wall temperature at the location x; and $T_{b,\text{in}}$ and $T_{b,\text{out}}$ are the inlet and outlet bulk temperatures, respectively. The obtained results in Fig. 10 reveal that the temperature field exhibits cyclic oscillations in the thermal entrance region of the coiled pipes for water (Fig. 10(*a*)) and the ODEAO surfactant solution (Fig. 10(*b*)) too.

The cyclic behavior of the temperature field along the length of the coils with Newtonian fluids was reported by the previous investigations (Seban and McLaughlin [20], Janssen and Hoogendoorn [21], Dravid et al. [22], and Austen and Soliman [23]). The amplitude of the oscillations is seen to increase as the Dean number Dn or the modified Dean number Dn′ (Dn′=Re′$\delta^{1/2}$) increases. These oscillatory characters of the wall temperature are due to the circulatory secondary flows resulting from the centrifugal force. The sharp variation in the wall temperature appears since the strong secondary flow brings the test liquid particles from different temperatures regions into the heating wall under the

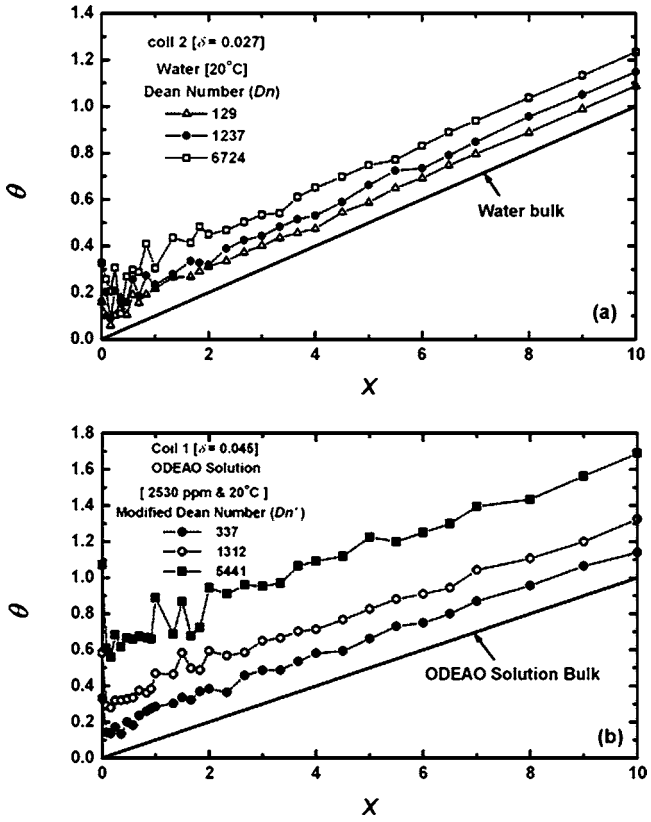

Fig. 10 Dimensionless wall temperature distribution along the coiled pipes: (*a*) Coil 2 water at 20°C (*b*) Coil 1 ODEAO solution 2530 ppm and 20°C

constant wall heat flux.

It can be noted from the results that the achievement of the fully developed temperature field is indicated by the wall temperature rising steadily parallel to the linearly increasing fluid bulk temperature. Also, it is seen that after two turns ($X>2$), the temperature distributions along the wall are almost parallel to the linear water or surfactant solution bulk temperatures, which suggest that the temperature field within the helical pipes is fully developed. This finding has been confirmed in a previous study of convective heat transfer characteristics in helical pipes under the constant heat flux condition by Xin and Ebadian [6].

4.3 Nusselt Number Distribution. The development of the local Nusselt number Nu_x with axial location in the three coils, with surfactant solution at almost the same concentration at 20°C, is depicted in Fig. 11. In the early developing stage, which is known by the Leveque region [22], Nu_x reaches its minimum value since the thermal boundary layer is very thin, and the temperature field penetration into the secondary flow field is insufficient for the effect of the latter to become significant. The previous reports [22,24,25] mentioned that this early stage should happen in a very short distance of ($x/d<5-8$) from the entrance to test sections. After the early stage, Nu_x experiences an oscillatory state, in which the value of Nu_x is oscillatory with the axial distance along the coils before it is fully developed. It is noted that for the case of smaller δ (Fig. 11(*c*)), one obvious peak value of Nu_x appears. On the other hand, for the case of larger δ (Fig. 11(*a*)), two obvious peak values of Nu_x are found with the higher Re′. It has been confirmed that the oscillation of Nu_x is due to the secondary flow in helical pipes. The oscillatory behavior of Nu_x had been reported previously in the numerical studies by Acharya et al. [24], Lin and Ebadian [25], and Patankar et al. [26].

The effects of Re′ on the Nu_x are shown in Fig. 11. With the increase of Re′, the value of Nu_x at every axial location increases and the oscillation of Nu_x is strengthened. It is revealed that the oscillation of Nu_x is enhanced and its magnitude increased with the higher curvature ratio δ.

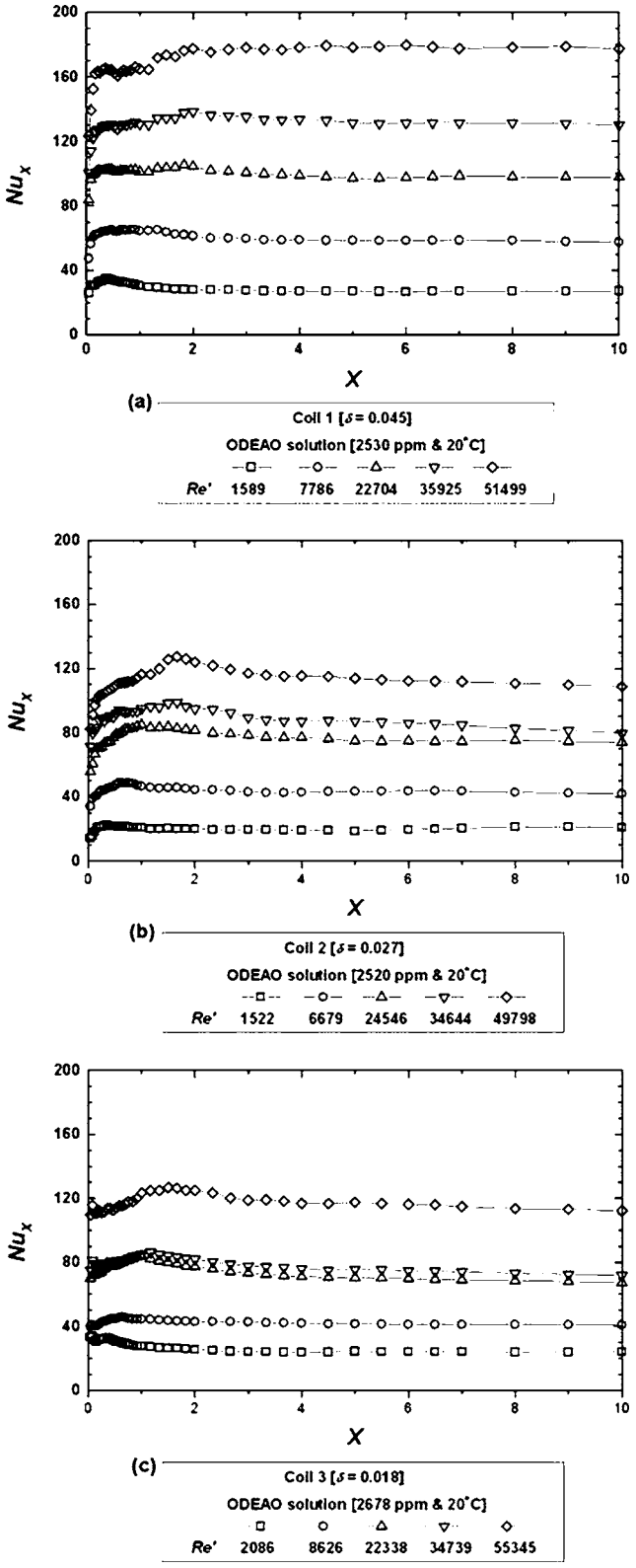

Fig. 11 Variation of Nusselt number Nu_x with axial distance along the coiled pipes at almost same concentration and at 20°C: (*a*) Coil 1, (*b*) coil 2, (*c*) coil 3

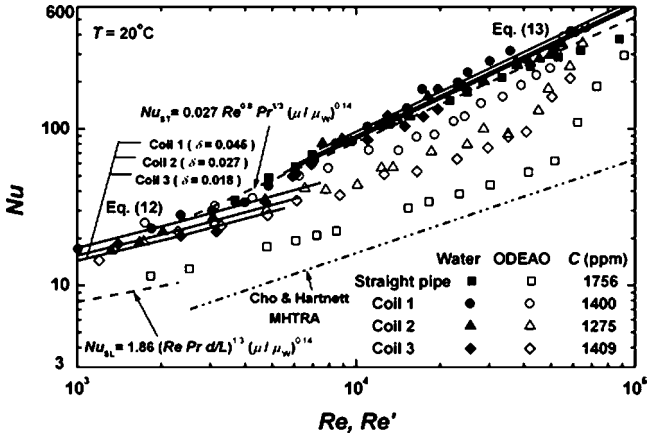

Fig. 12 Nusselt number Nu behavior of aqueous ODEAO solution in the helical and straight pipes

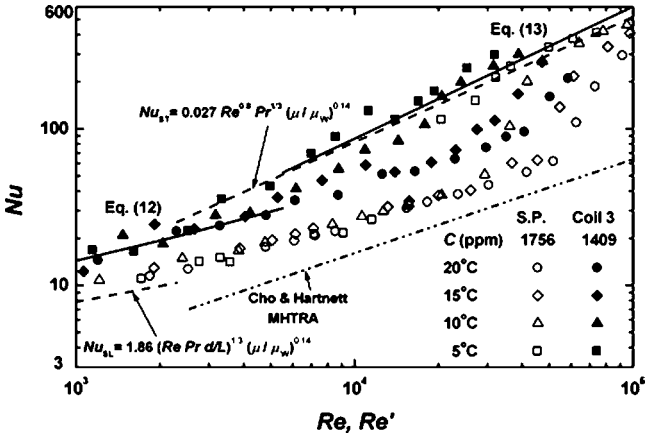

Fig. 13 Temperature effect on average Nusselt number Nu behavior of aqueous ODEAO solution in coil 3 and the straight pipe

4.4 Heat Transfer Reduction.

4.4.1 Average Nusselt Number. The average Nusselt number Nu can be determined by integrating the local values over the entire length of the helical pipe test sections using the following equation:

$$\mathrm{Nu} = \frac{1}{L}\int_0^L \mathrm{Nu}_x dx \tag{11}$$

The relationship between the average Nusselt number Nu and Re for water and Re′ for the surfactant solution flow through the coils and the straight pipe is shown in Fig. 12.

The dashed line shows the predicted Nu for Newtonian fluids in a straight pipe for both laminar ($\mathrm{Nu_{SL}}=1.86\,(\mathrm{Re\,Pr}\,d/L)^{1/3}(\mu/w)^{0.14}$) and turbulent ($\mathrm{Nu_{ST}}=0.027\,\mathrm{Re}^{0.8}\,\mathrm{Pr}^{1/3}(\mu/\mu_w)^{0.14}$) flow, and the solid lines indicate the Nu for Newtonian fluids in helical pipes for both laminar and turbulent flow with uniform heat flux condition by the following Eq. (12) proposed by Manlapaz and Churchill [27], and turbulent flow by Eq. (13) given by Mori and Nakayama [28].

$$\mathrm{Nu}_{CL} = \left[\left(\frac{48}{11} + \frac{51/11}{\left[1+\dfrac{1342}{\mathrm{Pr\,Dn}^2}\right]^2}\right)^3 + 1.816\left(\frac{\mathrm{Dn}}{1+\dfrac{1.15}{\mathrm{Pr}}}\right)^{3/2}\right]^{1/3} \tag{12}$$

$$\mathrm{Nu}_{CT} = \frac{\mathrm{Pr}^{0.4}}{41.0}\mathrm{Re}^{5/6}\delta^{1/12}[1+0.061(\mathrm{Re}\,\delta^{2.5})^{-1/6}] \tag{13}$$

Also, the maximum heat transfer reduction asymptote for flow through straight pipes proposed by Cho and Hartnett [15] is indicated in Fig. 12, which is given by

$$\mathrm{Nu} = 0.13\left(\frac{x}{d}\right)^{-0.3}(\mathrm{Re}')^{0.6}(\mathrm{Pr}')^{1/3} \tag{14}$$

Equation (14) is recommended for viscoelastic aqueous polymer solutions for $\mathrm{Re}'>6000$ and for $x/d<450$. Pr′ is the modified Prandtl number which is defined as [15]:

$$\mathrm{Pr}' = \frac{C_P\left(\dfrac{3n+1}{4n}\right)^n K\left(\dfrac{8U_m}{d}\right)^{n-1}}{k} \tag{15}$$

The obtained water data in the present experiments agree with these equations for laminar and turbulent flow within a maximum deviation of ±9%. It is also seen that the Nu data of the ODEAO surfactant solution are slightly over the prediction Eq. (12) in the laminar flow region. On the other hand, the Nu data of the surfactant solution are remarkably below Eq. (13) in the turbulent flow region since the ODEAO surfactant as a turbulent drag reducing additive suppresses the turbulence velocity fluctuations as mentioned in the former part 4.1 on flow drag reduction, dampening the turbulence velocity fluctuations results in a decreased transport of energy due to mixing. Moreover, Sellin et al. [29] argued the heat transfer reduction that accompanied the drag reduction is caused by the thickening of the viscous sublayer near the heated wall which causes an increase in the thermal resistance between the wall and the bulk fluid and therefore a reduction in the rate of heat transfer.

4.4.2 Temperature Effect. From Fig. 13, it is noticed that the Re′ region of heat transfer reduction increases with increasing temperature from $T=5$ to 20°C at the same concentration. This can be explained by the increase of the critical wall shear stress τ_{wc} with temperature as shown in Fig. 8.

4.4.3 Concentration Effect. As mentioned before, the increase in concentration of the surfactant in the solution results in the increase in the critical wall shear stress and the critical modified Reynolds number Re'_{crit}, since the increase in concentration strengthens the network's structure of the rod-like surfactant micelles. This in turn decreases transport of energy due to mixing effect. Moreover, increasing the concentration increases the resistance to heat transfer in the viscous sublayer near the heated wall. Figure 14 shows that an increase in concentration increases the turbulent heat transfer reduction range in coil 1 as well as the straight pipe.

4.4.4 Curvature Effect. The effect of curvature on Nu can be seen in Fig. 12. The higher the curvature ratio δ, the larger the average Nusselt number in the laminar and the turbulent flow regions, based on the same Re and Re′ for water and the ODEAO surfactant solution, respectively. The enhancement of Nu is due to the increase in the secondary flows with the increase of δ.

4.5 Drag Reduction and Heat Transfer Reduction Ratios. Drag reduction ratio (DR) and heat transfer reduction ratio (HTR) are the most often used parameters for quantifying the variation in friction or heat transfer relative to the level of turbulent friction factor or heat transfer for a corresponding non-drag reducing "Newtonian" fluid at constant flow rate [1]. These are usually expressed as the following percentages:

$$\mathrm{DR} = \frac{f_N - f_{\mathrm{DR}}}{f_N}\times 100; \quad \mathrm{HTR} = \frac{\mathrm{Nu}_N - \mathrm{Nu}_{\mathrm{DR}}}{\mathrm{Nu}_N}\times 100 \tag{16}$$

The relation between DR and HTR as functions of Re′ for the ODEAO surfactant solution flow through coil 1, coil 3, and the

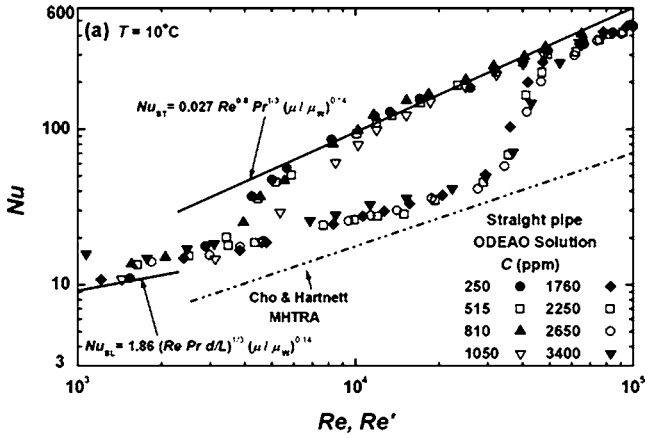

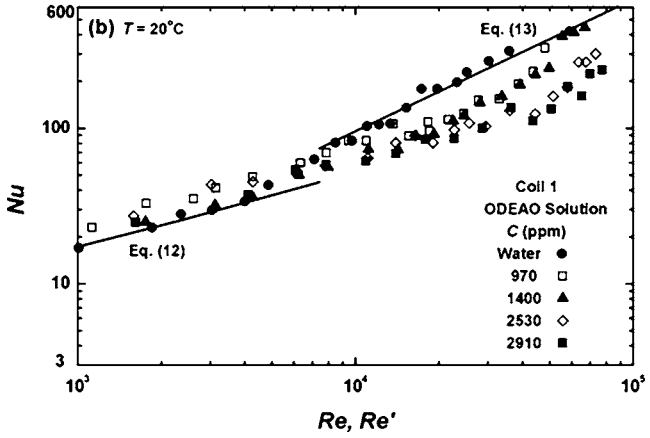

Fig. 14 Concentration effect on average Nusselt number Nu behavior of aqueous ODEAO solution: (*a*) Straight pipe, (*b*) coil 1

straight pipe at almost the same concentration and at different temperatures is shown in Fig. 15. It is obvious that an increase in solution temperature extends the DR and HTR ranges of drag and heat transfer reduction, and increases the maximum values of DR and HTR, and after reaching the maximum values, both of DR and HTR diminish as Re′ increases.

Figure 16 shows the relationship between DR and HTR for the ODEAO surfactant solution flow through the coils and the straight pipe at almost the same concentration and at 20°C as a function

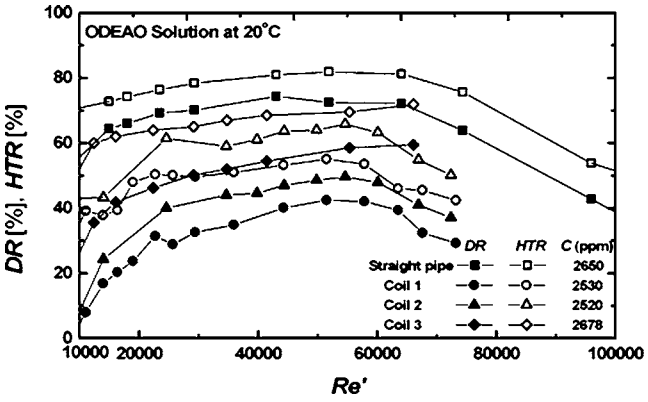

Fig. 16 DR and HTR as a function of Re′

of the modified Reynolds number Re′. It is clear that both the drag reduction ratio and the heat transfer reduction ratio in the straight pipe flow are higher than those in the coiled pipes. The decrease in DR and HTR in the coiled pipes flow in comparison with the straight pipe flow would be caused by the secondary flow resulting from the effective centrifugal force. In other words, the lower DR and HTR of the coiled pipes than the straight pipe is due to the fact that the differences between the extension of the laminar flow and the turbulent flow friction factor and Nusselt number lines are much greater for the straight pipe than for the coiled pipes.

Aguilar et al. [30] suggested the use of turbulent reduction parameters (turbulent reduction drag TRD and turbulent reduction heat TRH) which reflect the degree of turbulence reduction with respect to full laminarization rather than to an artificial zero-viscosity fluid; they are defined as:

$$\mathrm{TRD} = \frac{f_{NT} - f_{\mathrm{DR}}}{f_{NT} - f_{NL}} \times 100; \quad \mathrm{TRH} = \frac{\mathrm{Nu}_{NT} - \mathrm{Nu}_{\mathrm{DR}}}{\mathrm{Nu}_{NT} - \mathrm{Nu}_{NL}} \times 100 \tag{17}$$

where T and L are denoting turbulent and laminar flow of the Newtonian solvent, respectively. The use of the turbulence reduction parameters allows us to compare only the turbulence levels in the helical and straight pipes independently of the secondary flow issues, since drag-reducing additives should affect turbulence primarily and less so secondary flows in curved pipes [31]. Table 3 presents a comparison between the usual DR and HTR parameters and the turbulence reduction parameters (TRD and TRH). It is clear that TRD representation is better than DR in case of helical

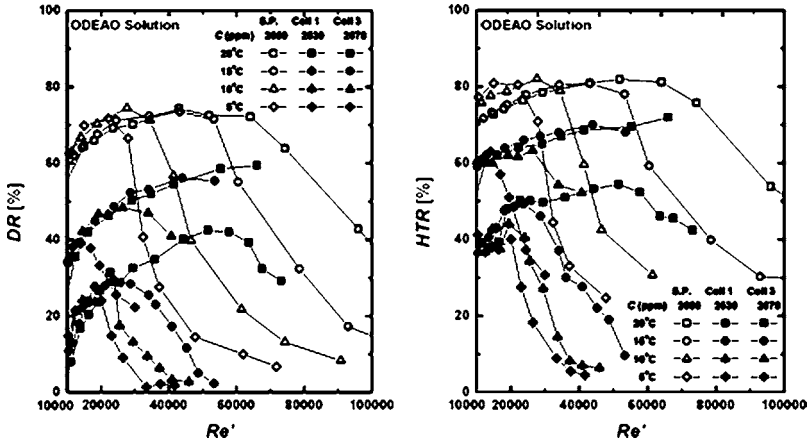

Fig. 15 Effect of temperature on DR and HTR in coil 1, coil 3, and the straight pipe

Table 3 Comparison between drag and heat transfer reduction parameters

Test sect.	Re′	*C*[ppm]	*DR*%	HTR%	TRD%	TRH%	HTR/DR	TRH/TRD
Coil 1	51500	2530	42	56	81	88	1.34	1.09
Coil 2	54600	2520	50	66	87	93	1.32	1.07
Coil 3	55350	2678	59	70	90	95	1.19	1.06
S.P.	51900	2650	73	82	77	90	1.12	1.17

pipes. On the other hand, the difference between the representations is small in case of the straight pipe. Also, it is clear that the secondary flow effect on heat transfer is diminished when using TRH, as the values are close for the straight and helical pipes. In addition, the HTR/DR and TRH/TRD ratios are shown in Table 3.

It is observed that both of the HTR and TRH are significantly higher than the DR and TRD, respectively. Kostic [32] explained this discrepancy by a non-homogenous turbulence due to the flow-induced anisotropicity of the high ordered rod-like micelles structure and properties of surfactant solution. That is, the DR depends on the fluctuating velocity components of main flow and the cross flow, while the HTR depends on the cross-flow velocity components only. Since the cross-flow components are more suppressed by the flow-induced anisotropic fluid structure than the main-flow components, as a result the values of HTR are over the DR.

ODEAO surfactant concentration has the same effect on DR and HTR as the temperature. Figure 17 represents DR and HTR as a function of Re′ of the ODEAO surfactant solution flow through the straight pipe at different surfactant concentrations and at constant temperature, it is seen that as the concentration increases the DR and HTR ranges increase in the measured temperature and concentration ranges, since the increase in concentration strengthens the network's structure of the rod-like surfactant micelles and increases the critical wall shear stress τ_{wc}.

As mentioned before, increasing the curvature ratio δ increases the secondary flow which increases the pressure loss and enhances the heat transfer for water and surfactant solution flow through a coiled pipe as seen in Figs. 15 and 16.

4.6 Prediction of Friction Factor and Nusselt Number. Useful correlations to the practical applications for predicting the friction factor and the average Nusselt number for aqueous ODEAO surfactant solutions flow through both straight and helical pipes have been derived in terms of the modified Reynolds number Re′, a non-dimensional concentration (*Cc*) defined as the ratio of the actual surfactant concentration in the solution to the lower critical concentration in a straight pipe of $C=250$ ppm for the ODEAO surfactant at which the rod-like micelles cannot be formed and there is no drag reduction effect, a non-dimensional temperature (*Tc*) defined as the ratio of the actual surfactant absolute temperature to the lower critical absolute temperature of 275 K (2°C) where there is no drag reduction effect, and the mdified Prandtl number Pr′. For the helical pipe there are two more extra parameters, namely the modified Dean number Dn′ and the curvature ratio δ.

Straight pipe correlations

$$f_{S.P.} = 4.31\,\mathrm{Re}'^{-0.63} Cc^{0.042} Tc^{0.14} \tag{18}$$

$$\mathrm{Nu}_{S.P.} = 0.127\,\mathrm{Re}^{0.5}\mathrm{Pr}'^{0.33} Cc^{-0.047} Tc^{2.4} \tag{19}$$

Correlations (18) and (19) could predict the present data within a standard deviation of 11%, and they are applicable for $Tc=1-1.065$, $Cc=2-14$, and $\mathrm{Re}'=1000-\mathrm{Re}'$ at the critical wall shear stress.

Helical pipes correlations

$$f_{C.P.} = \frac{1376\delta^{0.62}(1 + 0.94Cc^{-0.34}Tc^{-1.57})}{(1.56 + \log \mathrm{Dn}')^{5.73}} \tag{20}$$

$$\mathrm{Nu}_{C.P.} = 1.12\mathrm{Dn}'^{0.55}\mathrm{Pr}'^{0.60} Cc^{-0.176} Tc^{0.72}\delta^{0.32} \tag{21}$$

Correlation (20) could predict the present data within a standard deviation of 10%, and correlation (21) with 17%, and they are applicable for $Tc=1-1.065$, $Cc=4-14$, $\mathrm{Dn}'=100-\mathrm{Dn}'$ at the critical wall shear stress, and $\delta=0.018-0.045$.

Figure 18 shows comparisons between experimental data and predicted values from correlation Eq. (18)–(21); a fairly good agreement between experiments and prediction is clear.

It should be noted that Eqs. (18)–(21) may not be suitable for some other surfactant systems. For example, in some surfactant systems drag reduction increases as temperature decreases.

For Newtonian fluid flow, the Reynolds number includes the effect of pipe diameter. However, for drag-reducing fluids, this is not the case. The friction factor is a function of both Re and pipe diameter [1]. The diameter effect issue has not been investigated in the present study and to the author's knowledge there is only one investigation in the literature that has dealt with the diameter effect in curved pipes. In this investigation, Imao [33] investigated experimentally the flow drag reduction of TTAB aqueous surfac-

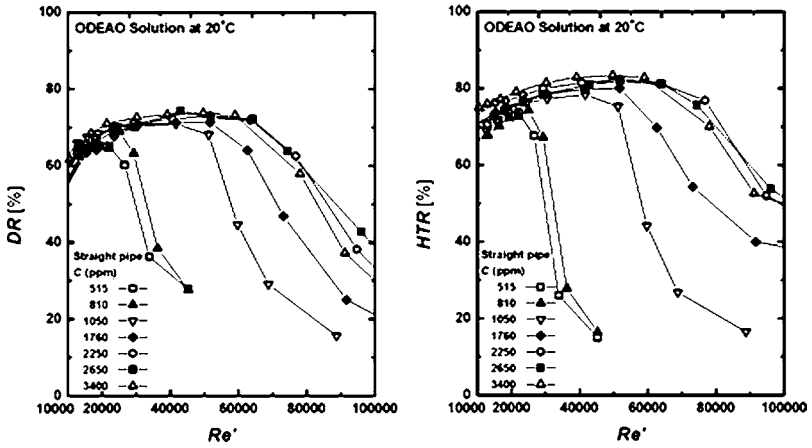

Fig. 17 Effect of surfactant concentration on DR and HTR in the straight pipe

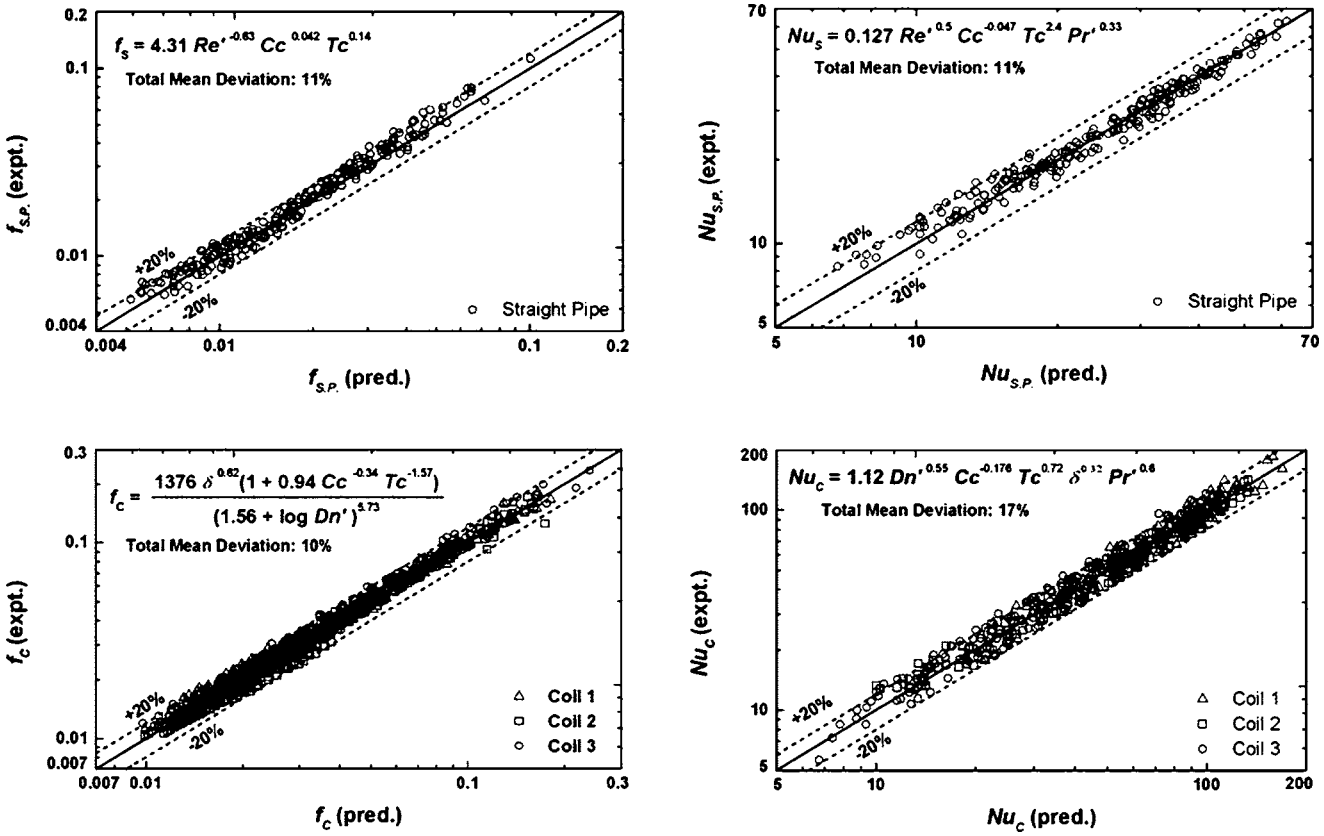

Fig. 18 Comparisons of experimental values of the friction factor and Nusselt number with those predicted with the proposed correlations 18–21

tant solutions in 180° bends with different pipe diameters (5, 10, 15 mm) and curvature ratios (0.01 to 0.05). He found that total bend loss coefficients for the surfactant solution are independent of the pipe diameter, but they depend on the curvature ratio. However, the pipe diameter range (5–15 mm) was very narrow and a larger range should be investigated to confirm this result, in addition to using helical pipes.

5 Conclusions

The characteristics of flow and heat transfer of a non-ionic turbulent drag-reducing surfactant solution have been investigated experimentally in helical and straight pipes.

1. Even the ODEAO surfactant solution behaved as a Newtonian fluid for surfactant concentrations up to 3000 ppm; it is a typically drag-reducing fluid.
2. The friction factors and the heat transfer coefficients of both water and the ODEAO surfactant solution in helical pipes are significantly higher than in a straight pipe. This is because of the secondary flow caused by the centrifugal forces in helical pipes.
3. The temperature distributions along the length of the coils show cyclic behavior in an early stage, then, after two turns, become almost parallel to the linear water or surfactant solution bulk temperatures, which suggest that the temperature within the helical pipes is fully developed after the second turn of the coil.
4. Experimental results showed that both the drag reduction DR and heat transfer reduction HTR in helical pipes are lower than in a straight pipe. It is not surprising that the surfactant drag reduction DR and heat transfer reduction HTR effects are lower for the helical pipes than for straight pipes, indeed the surfactant solute acts as a turbulence suppressor of the fluid-dynamic instability self-inducing vortices inside the fluid. No effects (or very low ones) can be seen if the turbulence is induced by dynamic instabilities due to geometrical shapes of the pipe, which is much stronger then self-induced ones.
5. DR and HTR are increasing with an increase in surfactant solution concentration and temperature in the measured concentration and temperature ranges. On the other hand, they decrease with larger curvature ratio.
6. A set of empirical correlations for predicting the friction factor and the average Nusselt number for the ODEAO surfactant solution flow through helical and straight pipes has been regressed based on the present data. These correlations are dependent on the modified Reynolds number Re′ or the modified Dean number Dn′, modified Prandtl number Pr′, curvature ratio δ, a non-dimensional concentration *Cc*, and a non-dimensional temperature *Tc*.
7. The main conclusion, from an engineering point of view, is that drag-reducing surfactants could be effectively applied to district cooling systems, since the long-straight pipes of the distribution system have high benefits from DR and HTR, while the same effects are not so negative in the heat transfer devices. However, possible solutions to the heat transfer reduction problem in the heat transfer devices might be applied [3]. Moreover, potentially, helical pipes might be used for heat transfer enhancement for drag-reducing fluids.

Acknowledgment

The first author gratefully acknowledges the support of the Egyptian Government/Ministry of Higher Education during his study in Japan.

Nomenclature

C = mass concentration of surfactant, ppm
Cc = non-dimensional surfactant concentration
C_P = specific heat at constant pressure, J/kg K
D = coil diameter, m
Dn = Dean number, $\mathrm{Dn}=\mathrm{Re}\,\delta^{0.5}$
Dn′ = modified Dean number, $\mathrm{Dn}'=\mathrm{Re}'\,\delta^{0.5}$
DR = drag reduction ratio, %
d = pipe diameter, m
f = friction factor
H = coil pitch, m
HTR = heat transfer reduction ratio, %
h = heat transfer coefficient, $\mathrm{W/m^2\,K}$
K = consistency index of power law fluid, $\mathrm{Pa\,s^n}$
k = thermal conductivity of test fluid, W/m K
L = length of the pipe, m
L_t = length of one turn of the coil, m
n = power law exponent of power law fluid
Nu = Nusselt number, $\mathrm{Nu}=h\,d/k$
p = pressure, Pa
ppm = parts per million (mass basis)
Pr = Prandtl number, $\mathrm{Pr}=C_p\,\mu/k$
Pr′ = modified Prandtl number, defined in Eq. (15)
q'' = heat flux, $\mathrm{W/m^2}$
Re = Reynolds number, $\mathrm{Re}=\rho U_m d/\mu$
Re′ = modified Reynolds number, defined in Eq. (4)
T = temperature, °C
Tc = non-dimensional surfactant solution temperature
TRD = turbulent reduction drag ratio, %
TRH = turbulent reduction heat ratio, %
U_m = mean velocity of test fluid, m/s
X = dimensionless axial distance along the coil, $X=x/L_t$
x = axial distance of the coil, m

Greek Symbols

$\dot{\gamma}$ = shear rate, 1/s
δ = curvature ratio, $\delta=d/D$
Δ = difference operator
μ = Newtonian fluid dynamic viscosity, Pa s
ρ = density of test fluid, $\mathrm{Kg/m^3}$
τ_w = shear stress, $\mathrm{N/m^2}$
θ = dimensionless temperature, defined in Eq. (10)

Subscripts

b = bulk value
C = coil
c = critical value
DR = drag reducing fluid
expt. = experimental value
L = laminar flow
N = Newtonian fluid solvent
pred. = predicted value
S = straight pipe
T = turbulent flow
W = wall condition
X = local value at axial distance of coil

References

[1] Zakin, J. L., Lu, B., and Bewersdorff, H. W., 1998, "Surfactant Drag Reduction," Rev. Chem. Eng., **14**, pp. 253–320.
[2] Inaba, H., 2000, "New Challenge in Advanced Thermal Energy Transportation Using Functionally Thermal Fluids," Int. J. Therm. Sci., **l39**, pp. 991–1003.
[3] Qi, Y., Kawaguchi, Y., Christensen, R., and Zakin, J. L., 2003, "Enhancing Heat Transfer Ability of Drag Reducing Surfactant Solutions With Static Mixers and Honeycombs," Int. J. Heat Mass Transfer, **46**, pp. 5161–5173.
[4] Bejan, A., and Kraus, A. D., 2003, *Heat Transfer Handbook*, Wiley, New Jersey, pp. 1088–1091.
[5] Zhou, Y., and Shah, S. N., 2004, "Rheological Properties and Friction Pressure Loss of Drilling, Completion, and Stimulation Fluids in Coiled Tubing," ASME J. Fluids Eng., **126**, pp. 153–161.
[6] Xin, R. C., and Ebadian, M. A., 1997, "The Effects of Prandtl Numbers on Local and Average Convective Heat Transfer Characteristics in Helical Pipes," ASME J. Heat Transfer, **119**, pp. 467–473.
[7] Bai, B., Guo, L., Feng, Z., and Chen, X., 1999, "Turbulent Heat Transfer in a Horizontal Helically Coild Tube," Heat Transfer Asian Res., **28**, pp. 395–403.
[8] Moffat, R. J., 1988, "Describing Uncertainties in Experimental Results," Exp. Therm. Fluid Sci., **1**, pp. 3–17.
[9] Nakata, T., Inaba, H., Horibe, A., Haruki, N., and Sato, K., 2004, "The Influence of Impurities in a Water Solution with Drag Reducing Surfactants on the Flow Drag Reduction and a Recovering Method of its Decreased Drag Reduction Effect," Trans. JSRAE, **21**(1), pp. 33–43.
[10] Bewersdorff, H. W., and Ohlendorf, D., 1988, "The Behavior of Drag-Reducing Cationic Surfactant Solutions," Cell Calcium, **266**, pp. 941–953.
[11] Rose, G. D., and Foster, K. L., 1989, "Drag Reduction and Rheological Properties of Cationic Viscoelastic Surfactant Formulations," J. Non-Newtonian Fluid Mech., **31**, pp. 59–85.
[12] Gyr, A., and Bewersdorff, H. W., 1995, *Drag Reduction of Turbulent Flows by Additives*, Kluwer, Dordrecht, The Netherlands.
[13] Lu, B., Li, X., Talmon, Y., and Zakin, J. L., 1997, "A Non-Viscoelastic Drag Reducing Cationic Surfactant System," J. Non-Newtonian Fluid Mech., **71**, pp. 59–72.
[14] Pinho, F. T., 2003, "A GNF Framework for Turbulent Flow Models of Drag Reducing Fluids and Proposal for a k-ε Type Closure," J. Non-Newtonian Fluid Mech., **114**, pp. 149–184.
[15] Cho, Y. I., and Hartnett, J. P., 1982, "Non-Newtonian Fluids in Circular Pipe Flow," Adv. Heat Transfer, **15**, pp. 59–141.
[16] Manlapaz, R. L., and Churchill, S. W., 1980, "Fully Developed Laminar Flow in a Helically Coiled Tube of Finite Pitch," Chem. Eng. Commun., **7**, pp. 57–78.
[17] Mishra, P., and Gupta, S. N., 1979, "Momentum Transfer in Curved Pipes: Newtonian Fluids," Ind. Eng. Chem. Process Des. Dev., **18**, pp. 130–137.
[18] Ito, H., 1959, "Friction Factors for Turbulent Flow in Curved Pipes," ASME J. Basic Eng., **81**, pp. 123–134.
[19] Zakin, J. L., Myska, J., and Chara, Z., 1996, "New Limiting Drag Reduction and Velocity Profile Asymptotes for Nonpolymeric Additives Systems," AIChE J., **42**(12), pp. 3544–3546.
[20] Seban, R. A., and McLaughlin, E. F., 1963, "Heat Transfer in Tube Coils with Laminar and Turbulent Flow," Int. J. Heat Mass Transfer, **6**, pp. 387–395.
[21] Janssen, L. A. M., and Hoogendoorn, C. J., 1978, "Laminar Convective Heat Transfer in Helical Coiled Tubes," Int. J. Heat Mass Transfer, **21**, pp. 1197–1206.
[22] Dravid, A. N., Smith, K. A., Merrill, and Brain, P. L. T., 1971, "Effect of Secondary Flow Motion on Laminar Flow Heat Transfer in Helically Coiled Tubes," AIChE J., **17**, pp. 1114–1122.
[23] Austen, D. S., and Soliman, H. M., 1988, "Laminar Flow and Heat Transfer in Helically Coiled Tubes with Substantial Pitch," Exp. Therm. Fluid Sci., **1**, pp. 183–194.
[24] Acharya, N., Sen, M., and Chang, H., 1994, "Thermal Entrance Length and Nusselt Numbers in Coiled Tubes," Int. J. Heat Mass Transfer, **37**(2), pp. 336–340.
[25] Lin, C. X., and Ebadian, M. A., 1997, "Developing Turbulent Convective Heat Transfer in Helical Pipes," Int. J. Heat Mass Transfer, **40**(16), pp. 3861–3873.
[26] Patankar, S. V., Pratap, V. S., and Spalding, D. B., 1974, "Prediction of Laminar Flow and Heat Transfer in Helically Coiled Pipes," J. Fluid Mech., **62**(3), pp. 539–551.
[27] Manlapaz, R. L., and Churchill, S. W., 1981, "Fully Developed Laminar Convection from a Helical Coil," Chem. Eng. Commun., **9**, pp. 185–200.
[28] Mori, Y., and Nakayama, W., 1967, "Study on Forced Convective Heat Transfer in Curved Pipes (Second Report, Turbulent Region)," Int. J. Heat Mass Transfer, **10**, pp. 37–59.
[29] Sellin, R. H. J., Hoyt, J. W., and Scrivener, O., 1982, "The Effect of Drag Reducing Additives on Fluid Flows and Their Industrial Applications: Basic Aspects," J. Hydraul. Res., **20**, pp. 29–68.
[30] Aguilar, G., Gasljevic, K., and Matthys, E. F., 1999, "Coupling Between Heat and Momentum Transfer Mechanisms for Drag-Reducing Polymer and Surfactant Solutions," ASME J. Heat Transfer, **121**, pp. 796–802.
[31] Gasljevic, K., and Matthys, E. F., 1999, "Improved Quantification of the Drag Reduction Phenomenon Through Turbulence Reduction Parameters," J. Non-Newtonian Fluid Mech., **84**, pp. 123–130.
[32] Kostic, M., 1994, "On Turbulent Drag and Heat Transfer Phenomena Reduction and Laminar Heat Transfer Enhancement in Non-Circular Duct Flow of Certain non-Newtonian Fluids," Int. J. Heat Mass Transfer, **37**(Suppl. 1), pp. 133–147.
[33] Imao, S., 2003, "Bend Loss Coefficient of Drag-Reducing Surfactant Solution," *Proc. ASME, Fourth ASME-JSME* Joint Fluid Engineering Conference, Honolulu, Hawaii, July 6–10, Paper No. FEDSM2003–45767.

Experimental Estimate of the Continuous One-Dimensional Kernel Function in a Rectangular Duct With Forced Convection

Jinny Rhee
Mechanical and Aerospace Engineering Department,
San Jose State University,
One Washington Square,
San Jose, CA 95192-0087
e-mail: jrhee@email.sjsu.edu

Robert J. Moffat
Mechanical Engineering Department,
Stanford University,
Stanford, CA 94305-3030
e-mail: rmoffat@stanford.edu

The continuous, one-dimensional kernel function in a rectangular duct subject to forced convection with air was experimentally estimated using liquid crystal thermography techniques. Analytical relationships between the kernel function for internal flow and the temperature distribution resulting from a known heat flux distribution were manipulated to accomplish this objective. The kernel function in the hydrodynamically fully developed region was found to be proportional to the streamwise temperature gradient resulting from a constant heat flux surface. In the hydrodynamic entry region of the rectangular duct, a model for the kernel function was proposed and used in its experimental determination. The kernel functions obtained by the present work were shown to be capable of predicting the highly nonuniform surface temperature rise above the inlet temperature resulting from an arbitrary heat flux distribution to within the experimental uncertainty. This is better than the prediction obtained using the analytically derived kernel function for turbulent flow between parallel plates, and the prediction obtained using the conventional heat transfer coefficient for constant heat flux boundary conditions. The latter prediction fails to capture both the quantitative and qualitative nature of the problem. The results of this work are relevant to applications involving the thermal management of nonuniform temperature surfaces subject to internal convection with air, such as board-level electronics cooling. Reynolds numbers in the turbulent and transition range were examined. [DOI: 10.1115/1.2227039]

Introduction

The kernel function or its equivalent, the inverse Green's function, is the mathematically invariant relationship between surface heat flux and temperature distribution for forced convection problems. The heat transfer coefficient, which is traditionally used for this purpose, is the descriptor of choice for constant temperature and heat flux surfaces, as well as applications where the average surface temperature and heat transfer are sufficient for the objective at hand. However, because the traditional heat transfer coefficient is typically defined with temperatures far from the surface as the reference temperature (e.g., the mean fluid temperature or freestream temperature), it is highly variable when the surfaces are not uniform in temperature or heat flux. It can be made to vary between $-\infty$ and $+\infty$ by simply changing the heat flux boundary conditions at a constant Reynolds number. This dependence makes the traditional heat transfer coefficient an inconvenient choice for applications requiring accurate characterization of nonuniform surface temperatures and heat fluxes.

The kernel function, on the other hand, characterizes the convective abilities of a hydrodynamic environment regardless of thermal boundary conditions. Kernel functions are described in advanced convection textbooks (e.g., Ref. [1]) and are equivalent to the Stieltjes integral using the Graetz solution adapted for variable heat flux at the wall in an internal flow [2]. Typically, the analytically derived, one-dimensional kernel functions for simple flow conditions are presented, such as: a flat plate with laminar or turbulent boundary layer; circular tubes with hydrodynamically fully developed flow; and flow between parallel plates [3]. Various assumptions are used to model turbulence, resulting in small discrepancies between analogous solutions. For the steady-state solution of the continuity, momentum, and energy equations with constant fluid properties, the relationship of the kernel function to heat flux and surface temperature is indicated in Eq. (1)

$$T(x) - T_{in} = \frac{1}{k\,\mathrm{Re}\,\mathrm{Pr}} \int_0^x \tilde{g}(x,\xi)\dot{q}_0''(\xi)\,d\xi \tag{1}$$

The physical interpretation of the kernel function, $\tilde{g}(x,\xi)$, is the surface temperature rise at location x, resulting from a unit heat flux at location ξ, multiplied by the appropriate constants to render it dimensionless. At a given distance x from the inlet, the total surface temperature rises above the inlet temperature, $T(x)-T_{in}$, is the integral of the temperature wakes weighted by the upstream heat flux values that produced them. The variable, $\dot{q}_0''(\xi)$, represents the heat flux at the specified location, ξ. The remaining variables, k, Re, and Pr are the fluid conductivity, Reynolds number, and Prandtl number, respectively. The Reynolds number is defined with an appropriate characteristic length scale, L, which we shall discuss later.

The shortcomings of the conventional heat transfer coefficients and the advantages of invariant descriptors have been well documented in the literature [4]. The kernel function's invariance to thermal boundary conditions gives it significant advantages in advanced heat transfer problems such as conjugate convection-conduction analysis, validation of compact models, and convergence of numerical solutions. In conjugate convection-conduction problems, a unique kernel function unambiguously describes the hydrodynamic environment at the interface, unlike the heat transfer coefficient which varies with the temperature solution at the boundary. This information should allow the difficult simultaneous solution of both sets of governing equations to be separated into a conduction problem and a convection problem, reducing iteration and convergence issues arising from the conjugate problem. The kernel function can be experimentally determined, and has the potential to contribute to the validation and formulation of

Contributed by the Heat Transfer Division of ASME for publication in the JOURNAL OF HEAT TRANSFER. Manuscript received July 8, 2005; final manuscript received January 17, 2006. Review conducted by Bengt Sunden.

compact models involving transition and turbulent flow, which are subject to modeling ambiguities. Last, kernel function algorithms have been shown to be numerically stable and computationally efficient, especially in comparison to more traditional methodologies [5].

Several studies have experimentally quantified a kernel function using discrete elements. Anderson and Moffat [6,7] studied the flow between two closely spaced walls with a uniformly spaced array of flat packs on one wall, modeling a board-level electronics-cooling situation. Each discrete flat pack was uniform in temperature and characterized by its total power dissipation. A row of flat packs was heated, and the resulting temperature distributions on the remaining rows of unheated flat packs were recorded. The induced temperature distribution from a unit heat release from the heated row is the one-dimensional, discrete kernel function (DKF). In addition, the adiabatic heat transfer coefficient, so-called because its unpowered equilibrium temperature is used as the reference temperature, was measured on the powered row. With this significant distinction, the adiabatic heat transfer coefficient is invariant to thermal boundary conditions, and only needs to be measured once for a given hydrodynamic situation.[1] A range of channel heights and inlet velocities were characterized in the references cited. In addition, a temperature prediction methodology for using the two-dimensional DKF, i.e., the resulting temperature distribution on all unheated array elements resulting from a unit heat release on one element, was presented.

Hacker and Eaton [8] studied the application of kernel function concepts to separated flow downstream of a backward-facing step, with applicability to dump combustor design. A programmable radiative lamp was used to impose discrete surface temperature steps enabling the measurement of a discrete one-dimensional kernel function. Liquid crystal thermography and transient analysis techniques were used to quantify surface temperature and heat flux. The discrete Green's function, an invariant descriptor in matrix form, was measured. It was shown that the inverse discrete Green's function is equivalent to the DKF studied by Anderson and Moffat [6,7].

Batchelder and Eaton [9] measured a discrete one-dimensional inverse Green's function on a flat plate subjected to a turbulent boundary layer with and without freestream turbulence. These conditions might be present in a heat exchanger or gas turbine blade environment. A steady state measurement technique with liquid crystal thermography improved upon the high measurement uncertainties that were present in previous work [8]. It was shown that the measured inverse Green's function could successfully predict the surface temperature resulting from an arbitrary heat flux distribution such as a sinusoid, as was imposed in this study.

Some investigators have applied Green's function principles to analytically solve convection and diffusion problems for relatively simple geometries. Khon'kin [10] found the Green's function for the longitudinal dispersion of particles in a round tube using an asymptotic method. Bokota and Iskierka [11] used a superposition of Green's functions to solve the diffusion-convection equation applicable to laser hardening of long rectangular elements. The temperature solutions were used to determine the phase transformations and thermal stresses on the surface during the heating and cooling processes.

Mitrovic et al. [12] performed numerical experiments using direct numerical simulation of two-dimensional turbulent flow between parallel plates. They used Lagrangian scalar tracking techniques to quantify the trajectories of thermal markers from a line source of heat, which yields the essence of the continuous one-dimensional kernel function described in this paper. A large range of Prandtl numbers are examined in this study. In addition, unified correlations for the heat and mass transfer coefficients are proposed based on their work.

Mukerji et al. [13] performed steady-state experiments to measure the surface temperature responses to one-dimensional and two-dimensional temperature steps in a turbulent external boundary layer, with and without freestream turbulence. This study concluded from the comparison of the resulting thermal wakes that spanwise turbulent diffusion is not a significant heat transport mechanism, except for very small heated spots under conditions of low freestream turbulence. This conclusion provides strong evidence that the continuous, one-dimensional kernel function may be sufficient to characterize the two-dimensional surface temperature problem. However, because some applications like electronics cooling often does involve small heated spots, and because fully developed internal flow differs in some fundamental ways from external flow, this conclusion should be reverified before its widespread use in related flows.

Objectives

The present study seeks to build upon the previous work in several important aspects. The objective is to determine the continuous, one-dimensional kernel function in hydrodynamic situations modeling board-level electronics-cooling applications using experimental methods. The continuous kernel function will allow greater resolution of the surface temperature and heat flux than the discrete version, and the use of experimental methods will provide material for comparison with analytical results using turbulence models. Internal flow of air in a rectangular duct at transition (2300–10,000) and turbulent ($>$10,000) Reynolds numbers will be studied, as is typical of this application.

Analysis for Kernel Function Measurement in a Rectangular Channel

Upon examination and manipulation of Eq. (1), we discovered an intriguing and fairly simple relationship between the kernel function and the surface temperature gradient resulting from a constant heat flux surface in hydrodynamically fully developed flow. For hydrodynamically fully developed flow, the kernel function does not change as the location of unit heat release is varied, i.e., the pattern of streamwise temperature decay is invariant with location. Therefore, the kernel function reduces to a function of one variable only, which is the distance between the considered location and the location of upstream heating, $(x-\xi)$. With the heat flux, $\dot{q}_0''$, equal to a constant, Eq. (1) becomes:

$$T(x) - T_{in} = \frac{\dot{q}_0''}{k\,\mathrm{Re}\,\mathrm{Pr}} \int_0^x \tilde{g}_{fd}(x-\xi)\,d\xi \tag{2}$$

Both sides of Eq. (2) can be differentiated with respect to x using Leibniz' rule, and the derivative with respect to x is recognized as being the negative derivative with respect to ξ for the variable, $(x-\xi)$. The integral term is evaluated and the remaining expression can be rearranged for the kernel function as shown in Eq. (3)

$$\tilde{g}_{fd}(x) = \frac{k\,\mathrm{Re}\,\mathrm{Pr}}{q_0''} \frac{dT(x)}{dx} \tag{3}$$

This remarkable result states that the kernel function in hydrodynamically fully developed flow is simply proportional to the streamwise temperature gradient resulting from a constant heat flux surface! The simplicity of the physical setup and measurements required suggests great potential for its experimental determination. Furthermore, this kernel function should be able to predict the surface temperature resulting from any arbitrary heat flux distribution in hydrodynamically fully developed flow, regardless of the fact that it was measured on a constant heat flux surface.

[1]The adiabatic heat transfer coefficient and the unpowered component temperature are actually extensions of the DKF. In the limit as the component size approaches zero in the streamwise direction, all that remains is the continuous one-dimensional (1D) kernel function. Both the DKF and the 1D kernel are used in the appropriate sum/integral to evaluate the surface temperature rise above the inlet temperature.

In the entry region, the kernel function is no longer solely a function of $(x-\xi)$. The streamwise temperature distribution on a constant heat flux plate in the entry region is described by

$$T(x) - T_{in} = \frac{\dot{q}_0''}{k\,\mathrm{Re}\,\mathrm{Pr}} \int_0^x \tilde{g}(x,\xi)d\xi \tag{4}$$

As the kernel function is no longer solely a function of $(x-\xi)$, it cannot be obtained from this equation using the method used to obtain the fully developed kernel function. An assumption about the entry region kernel function is made at this point to allow us to evaluate it.

A model for the kernel function in the entry region of a duct is proposed based on the behavior of the one-dimensional DKF measured by Anderson and Moffat [6,7]. There are three characteristics of the DKF that are noted for the present model: first, the surface temperature rise approaches the mean air temperature rise far downstream of heat flux application; second, the kernel function achieves its fully developed state by the third row from the upstream edge, at which point it is solely a function of the number of rows downstream of the heated row; and third, the kernel functions for the rows in the entry region seem to be scaled versions of the fully developed kernel functions minus the contributions from the mean air temperature rise above inlet temperature. These observations of the discrete kernel function suggest the following model for the continuous kernel function in the entry region of an internal flow

$$\tilde{g}(x,\xi) = f(\xi)[\tilde{g}_{fd}(x-\xi) - D] + D$$

$$f(\xi) \neq 1,\ \xi \text{ in entry region}$$

$$f(\xi) = 1,\ \xi \text{ in fully developed region} \tag{5}$$

The function, $f(\xi)$, is a weighting function that will be equal to unity when hydrodynamically fully developed conditions are achieved. The constant, D, reflects the resulting mean air temperature rise per amount of heat flux applied. Equivalently, it can also be interpreted as the value of the fully developed kernel function, $\tilde{g}_{fd}(x-\xi)$, at large values of $(x-\xi)$. Plugging Eq. (5) into Eq. (1) yields the following interpretation of the entry region kernel function model

$$T(x) - T_{in} = \underbrace{\frac{1}{k\,\mathrm{Re}\,\mathrm{Pr}} \int_0^x f(\xi)[\tilde{g}_{fd}(x-\xi) - D]\dot{q}_0''(\xi)d\xi}_{T(x)-T_m(x)} + \underbrace{\frac{D}{k\,\mathrm{Re}\,\mathrm{Pr}} \int_0^x \dot{q}_0''(\xi)d\xi}_{T_m(x)-T_{in}} \tag{6}$$

With this model, the integral form of the surface temperature rise above inlet temperature is seen to be comprised of the surface temperature rise above the mean temperature plus the mean temperature rise above the inlet temperature. The mean air temperature rise at location x resulting from the energy per duct width added upstream of it is easily expressed as the inverse of the product of the mass flow rate of air per duct width and its specific heat using an energy balance. The constant, D, can then be determined as follows

$$D = \frac{k\,\mathrm{Re}\,\mathrm{Pr}}{\dot{m}c_p/W} \tag{7}$$

Again, the kernel function is invariant with thermal boundary conditions; hence, the constant D is also invariant, regardless of the thermal boundary conditions used for its determination.

Equations for Slowly Varying Heat Flux. In actual practice, it is not easy to establish a uniform heat flux on a real surface, even using the common technique of electrically heating thin foil surfaces. As the surface becomes hotter in the downstream direction, it loses a greater percentage of its heat flux to conduction and radiation. Therefore, the convective heat flux from an electrically heated plate is not truly uniform, but decreases slowly in the downstream direction. To obtain an analogous expression to Eq. (3) for this scenario, Eq. (1) can be integrated using Leibniz' rule and then integrated by parts to produce the following expression for the hydrodynamically fully developed region

$$\tilde{g}_{fd}(x) = \frac{k\,\mathrm{Re}\,\mathrm{Pr}}{q_0''(0)}\frac{dT(x)}{dx} - \frac{1}{q_0''(0)}\int_0^x \tilde{g}_{fd}(x-\xi)\frac{dq_0''(\xi)}{d\xi}d\xi \tag{8}$$

In principle, this equation can be used to measure the fully developed kernel function for any known heat flux distribution. In practice, however, solution techniques are only well behaved when the heat flux is slowly varying in the streamwise direction.

Once the fully developed kernel functions are determined, Eqs. (6) and (7) can be used to determine $f(\xi)$ and D in the entry region, yielding the complete set of kernel functions.

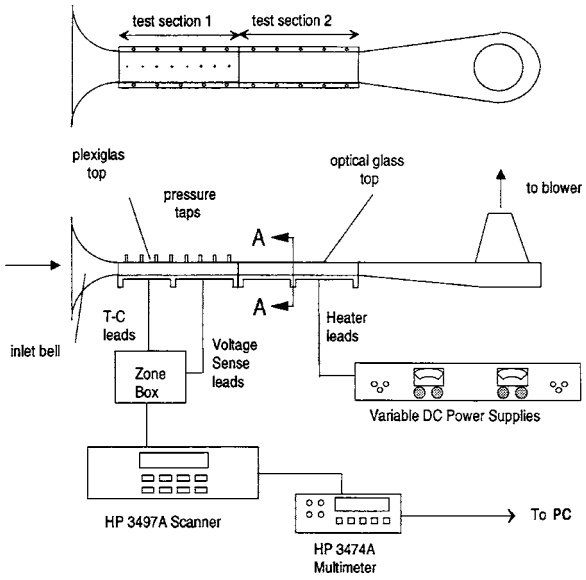

Fig. 1 Schematic of wind tunnel and experimental setup

Experimental Apparatus

An experimental apparatus was designed to enable the measurement of the kernel function in a rectangular duct flow using the outlined analysis. It consisted of an open-loop suction wind tunnel with a rectangular duct test section and an image processing system capable of full-field temperature measurements. The construction and instrumentation of the experimental apparatus are detailed in this section.

Wind Tunnel. A schematic of the wind tunnel is shown in Fig. 1. The inlet bell was fabricated from a 36 cm diameter PVC pipe. The curvature of the inlet bell was chosen to be greater than $(\pi+2)/\pi$ times the greatest cross-sectional dimension of the test section. This criterion ensured attached flow at the beginning of the test section. A pitot static tube (1.7 mm diam) was inserted in a section of the inlet bell adjoining the test section to measure inlet velocity, and removed prior to each data run. Turbulent trips were located on the bottom and top walls of the inlet bell directly downstream of the port for the pitot static tube. Air flow was induced in the tunnel by a 15 hp regenerative blower (EG&G rotron blower model DR 6R with Eaton Dynamic 20 hp motor model AS211001-0001 and Eaton Dynamatic controller model 4000).

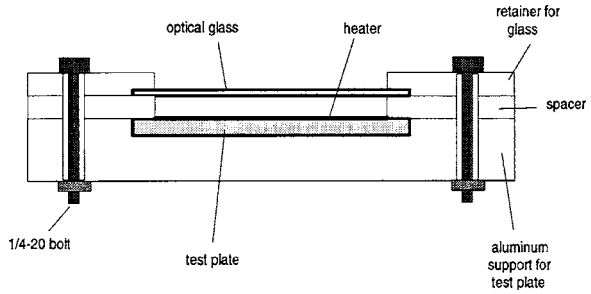

Fig. 2 Cross-sectional view of test section assembly

Test Sections. The cross-sectional view of the test section indicated by the line *A-A* Fig. 1 is shown in Fig. 2. Each of the two test sections required for this study were rectangular ducts 10 cm×1 cm in cross section and 35 cm long. The length of one test section corresponded to 19.3 hydraulic diameters, which exceeded the recommendation of 10–15 hydraulic diameters for fully developed heat transfer behavior in turbulent flow [1]. The test sections were interchangeable to allow a given heater to be placed in the entry or fully developed region of the channel. The top surface of either test section could be fitted with a Plexiglas top, or a sheet of low reflectivity glass (Invisiglas® by Optical Coatings Laboratory) as shown in the figure. The Plexiglas top was instrumented with 36-gauge *K*-type thermocouples and static pressure taps every 4 cm in the streamwise direction. All of the thermocouples in this experiment were multiplexed by an HP3497A scanner to an HP3474A multimeter. Both of these instruments were controlled via a general purpose interface bus interface to a personal computer.

Test Plates. The test plate surfaces formed the bottom wall of the test section and are sketched in Fig. 3. They were made of balsa wood on an isothermal aluminum layer, the temperature of which could be measured for the accurate determination of the conduction heat loss. The aluminum layer was purposely designed to decrease the time required to achieve steady state temperature on and throughout the test plates. The test plates where equipped with one of two heaters designed to produce known heat flux distributions: The first test plate produced a uniform heat flux over the entire surface; and the second produced a uniform heat flux only over the streamwise intervals from 4.6 to 9.7 cm and from 12.2 to 14.8 cm. The heaters were constructed of mylar sheets with a vacuum-deposited gold layer as implemented by other authors [14,15]. Copper busbars made contact at the leading and trailing edges of the heater with silver loaded epoxy. Heater leadwires and voltage sense wires were soldered onto the busbars, and

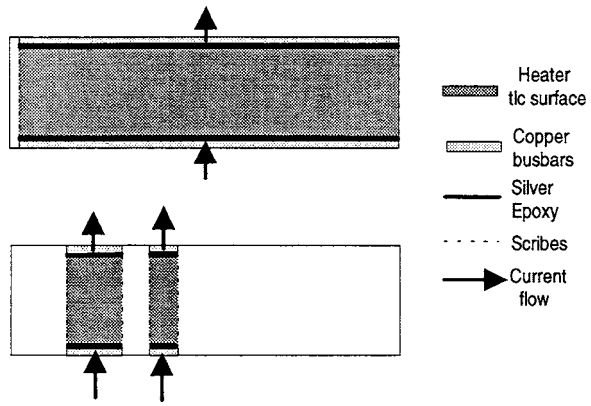

Fig. 3 Top view of two test plates used for present work: constant heat flux on entire surface (35 cm in the streamwise direction); and constant heat flux on two strips only (4.6–9.7 cm and 12.2–14.8 cm in the streamwise direction)

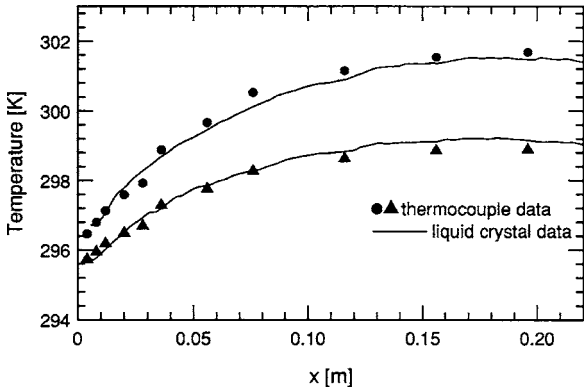

Fig. 4 Temperature calibration of liquid crystal paint verified by concurrent thermocouple measurements

power was supplied to the heaters from a 1 to 30 V, 0 to 3 A direct current power supply. The top surfaces of the heaters were coated with thermochromic liquid crystal paint, Hallcrest R20C5W, which is active between 21 and 31°C. The liquid crystal paint was applied using the technique described in Farina et al. [16]. In addition, sixteen 36-gauge *K*-type thermocouples were epoxied at various streamwise locations 4 cm from the centerline of the duct on the underside of the constant heat flux heater. These thermocouples were well away from the centerline of the duct, and were used to verify the liquid crystal temperature measurements at the start of each data run.

Image Processing System. The digital image processing system consisted of a charge coupled device camera and a personal computer equipped with Matrox image processing boards. Temperature acquisition by image processing involved the use of a temperature-hue angle calibration determined by the image processing software. The image processing software, calibration schemes, and the calibration rig used are described in detail in Farina et al. [16]. The use of low reflectivity glass top reduced the interference with the image due to reflections, but was not necessary for obtaining repeatable temperature measurements. To validate the temperature calibration, the temperatures 4 cm from the centerline of the duct were measured using the image processing system and compared to the measurements from the underlying thermocouples for each Reynolds number in the present study. A sample verification run is shown in Fig. 4. It is interesting to note a slight but consistent surface temperature dip at the locations of the thermocouple beads, indicating a small amount of conduction loss through the thermocouple wires.

Data Processing and Analysis

The steps in the computation of the kernel function distribution are described in this section. The measured quantities and the data reduction schemes are outlined.

Convective Heat Flux. Accurate measurement of the convective heat flux over the test plates was necessary for use in the computation of the kernel function. The convected heat flux was taken to be the electrical power density minus the local conduction and radiation losses, or

$$\dot{q}''_{\text{conv}} = \dot{q}''_{\text{tot}} - \dot{q}''_{\text{cond}} - \dot{q}''_{\text{rad}} \tag{9}$$

The electrical power density was computed as the product of the voltage drop across the heater multiplied by the current divided by the surface area. For the constant heat flux plate, the conduction loss was calculated assuming a 1D loss through the balsa wood test plate to the isothermal aluminum layer. A comparison of this estimate to the solution of a full two-dimensional (2D) finite difference calculation showed negligible differences. For the strip heater test plate, the conduction loss was determined using a 2D

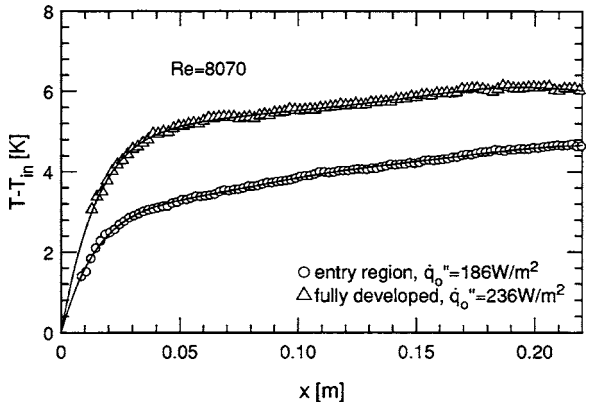

Fig. 5 Centerline temperature measurements on constant heat flux surface as a function of distance from onset of heating

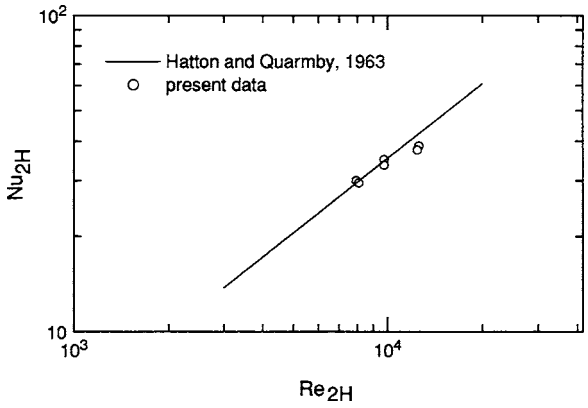

Fig. 6 Nusselt and Reynolds numbers from present work compared to analytical solution of flow between parallel plates with constant heat flux on one side (see Ref. [3])

finite difference conduction solver to handle the sharp gradients in temperature on the surface of the plate. Radiation from the test plate to the glass ceiling was computed numerically on an Excel spreadsheet using the temperatures measured on the test plate and channel ceiling. The emissivity of the liquid crystal paint was measured to be 0.9 with an emissometer (Devices and Services Co., model AE), and the emissivity of the glass was 0.94. Conduction and radiation losses accounted for about 15% of the electrical power density at the downstream end of the test plate.

Centerline Temperatures and Curve Fits. The temperatures on a 3 cm wide strip at the centerline of the heated wall were measured using the image processing system for each run. The centerline temperatures were calculated as the spanwise average of 100 frames from the image processing system on the 3 cm strip. It was necessary to curve fit the measured centerline temperature distributions resulting from the constant heat flux heaters to reduce the scatter in the temperature derivatives. An eighth order polynomial was used to fit the temperature measurements. The liquid crystal data in the entry region and fully developed region for a Reynolds number of 8070 and its corresponding curve fit is shown in Fig. 5. An eighth order polynomial was the lowest order polynomial that sufficiently well fit the data close to the onset of heating. The temperature at $x=0$ was forced to equal the inlet temperature. Alternative curve fitting schemes were not examined in this study. In this figure, $x=0$ was taken to be the onset of heating for the test plate in both the entry and fully developed regions. The temperature data for Reynolds numbers of 9750 and 12,500 (figures omitted for brevity) were also curve fit with similar results. All of the curve fits are within ±1% of the wall temperature rise above ambient of the liquid crystal data.

Kernel Functions. Equation (8) describes the relationship between the surface temperature, heat flux, and fully developed kernel function. The centerline surface temperature and heat flux in the hydrodynamically fully developed section were measured and quantified by the experimental apparatus and appropriate calculations. The fluid properties were evaluated at the inlet temperature. Therefore, the kernel function is the only unknown, and can be determined from the known quantities. Because Eq. (8) is implicit for the kernel function, an iterative approach was used. The first estimate of the fully developed kernel function was the right-hand side of Eq. (3) which is easily computed from the centerline temperature measurements. This estimate was then used to evaluate the integral term on the right hand side of Eq. (8), and to produce a more refined estimate accounting for variable heat flux. The process of further refining the fully developed kernel function in this manner was continued until convergence was obtained. The number of iterations required was on the order of 10–50 for the range of Reynolds numbers examined.

The fully developed kernel function was then used to determine the weighting function, $f(\xi)$, in the hydrodynamically developing section to yield the kernel function in the entry region. This was accomplished by numerical integration of Eq. (6). The centerline surface temperature and heat flux distributions in the entry region test section as well as the fully developed kernel function previously obtained were sampled at sufficiently small intervals so that Eq. (6) yielded the following system of linear equations:

$$T(n) - T_{in} - \sum_{m=1}^{n} \frac{\dot{q}_0''(m)\Delta x D}{k\,\mathrm{Re}\,\mathrm{Pr}} = \frac{\Delta x}{k\,\mathrm{Re}\,\mathrm{Pr}} \sum_{m=1}^{n} \left[\tilde{g}_{fd}\left(n - m + \frac{1}{2}\right) - D \right] \dot{q}_0''(m) f(m) \quad (10)$$

The variable Δx is the stepsize. The variable, n, varies from 0 to N, where N is the number of steps on a constant heat flux test plate. The left-hand side of this equation represents the wall temperature rise above the inlet temperature minus the mixed mean air temperature rise at discrete step, n. The summation term representing the mixed mean air temperature rise is moved to the left-hand side in the discrete formulation. The fully developed kernel function is evaluated at a distance $(n-m+1/2)$, which is the midpoint of the discrete step, n, in relation to a unit heat release on upstream step, m. For example, on the first discrete step at the inlet of the channel, the fully developed kernel function would be evaluated at its midpoint, or $(1-1+1/2)$. For subsequent discrete steps n, the surface temperature minus the mixed mean air temperature is equal to the sum of the heat flux weighted kernel functions originating from all upstream locations, $m<n$.

In our experiment, a stepsize of 1 mm was used for Δx. Equation (10) yields N number of linear equations to solve for the weighting function, $f(m)$, at N number of discrete locations, m. The linear system of equations was solved using the commercial package, MATLAB®4.0.

Uncertainty. The experimental uncertainties in the centerline surface temperature measurement, convective heat flux calculation, and all fluid properties and nondimensional numbers were evaluated using traditional uncertainty analysis [17]. The reported uncertainties are equivalent to the 95% confidence interval incorporating both bias and fluctuation measurement errors.

Experimental Results and Discussion

The proposed method of determining the kernel function distribution was applied for developing turbulent rectangular duct flows at various Reynolds numbers. The resulting kernel functions were then examined and their utility assessed by using them in a temperature prediction of an arbitrarily heated surface.

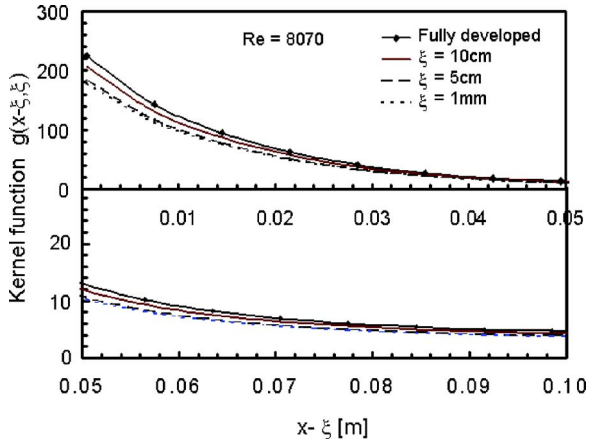

Fig. 7 Continuous one-dimensional kernel function in the hydrodynamically developing section of rectangular duct flow for a Reynolds number of 8070

Figure 6 shows the fully developed Nusselt number versus the Reynolds number from the present work in comparison to data from the literature. Although the hydraulic diameter is typically chosen as the characteristic length in symmetrically heated internal convection in noncircular ducts, the dissimilarity in thermal boundary conditions from having only one wall heated in the present work suggests that a better comparison would be to flow between parallel plates with one wall heated, unless of course a thermally congruent rectangular duct flow study is found in the prior work. Because this was not the case, the length scale for the Reynolds number was chosen to be twice the channel height for the sake of consistent comparison to flow between parallel plates. Because of this distinction, the Reynolds number is denoted Re_{2H} in the figure. Similarly, the same length scale is used for the Nusselt number, denoted Nu_{2H}. The mean heat transfer coefficients in the Nusselt numbers from the current work were obtained by computing the mean heat transfer coefficients measured at locations 13–17 hydraulic diameters from the onset of heating. The solid line in this figure represents the correlation for the analytical study of fully developed turbulent flow between parallel plates with uniform heat flux on one side [3]. Exact agreement is not expected because of the influence of secondary flow in the corners of the rectangular duct. Nevertheless, the agreement shown is not bad, and validates at least the power and temperature measurements.

With this definition of the Reynolds number, the constant, D, can be evaluated using Eq. (7). For constant fluid properties, the following constant is obtained

$$D = \frac{k\,\mathrm{Re}\,\mathrm{Pr}}{\dot{m}c_p/W} = \frac{k(U_{in}2H/\nu)(\nu/\alpha)}{\rho U_{in}Hc_p} = 2 \tag{11}$$

Figure 7 plots the kernel function versus $(x-\xi)$ parametric in ξ for a Reynolds number of 8070. The kernel function achieves 95% of the fully developed kernel function at the streamwise location corresponding to about nine hydraulic diameters. This length is denoted the kernel function entry region. It is slightly shorter than the criterion of 10–15 hydraulic diameters proposed for a fully developed heat transfer coefficient based on mean air temperature [1]. This observation is consistent with the fact that the heat transfer coefficient based on mean air temperature can be expressed using an integral of the upstream kernel functions weighted by the heat flux distribution, or

$$h_m(x) \equiv \frac{\dot{q}_0''(x)}{T(x) - T_m} = \frac{\dot{q}_0''(x)}{\dfrac{1}{k\,\mathrm{Re}\,\mathrm{Pr}}\displaystyle\int_0^x [\tilde{g}_{fd}(x-\xi) - D]f(\xi)\dot{q}_0''(\xi)d\xi} \tag{12}$$

Since the expression for the mean heat transfer coefficient contains an integral of the upstream kernel functions, the kernel function must achieve the fully developed state before the mean heat transfer coefficient.

In addition to showing that the kernel function entry region is relatively short, this figure also shows that the difference between the fully developed kernel and the entry region kernel is small. These observations justify the use of the kernel function model, Eq. (5). Because of the limited influence of the heated areas in this region, the model need only be a reasonable approximation of the actual kernel function.

The uncertainty in the kernel function measurement is infinite at an $(x-\xi)$ of zero, but rapidly decreases to between 5% and 10% at an $(x-\xi)$ value of 8.3 hydraulic diameters. The uncertainty at the leading edge often does not greatly affect the accuracy of the temperature predictions downstream of it.

Figure 8 compares the fully developed kernel functions for the three Reynolds numbers examined in this study in the range of $(x-\xi)$ where the curves are distinct. This figure clearly shows that the fully developed kernel functions are a function of the Reynolds number. This finding is consistent with Hatton and Quarmby [3] who found that the analytically derived eigenvalues required for the determination of the kernel function for turbulent hydrodynamically developed flow between parallel plates are also a function of the Reynolds number. In comparison, the eigenvalues for laminar internal flows are not.

Although the fully developed kernel functions are clearly functions of Reynolds number, the Reynolds number dependence seems to be limited to small values of $(x-\xi)$, or about 1.7 hydraulic diameters in this case. Furthermore, all three kernel functions approach the value of the constant D at large $(x-\xi)$ within the experimental uncertainty as we expect.

Figure 9 compares the weighting functions, $f(\xi)$, obtained for the three Reynolds numbers. The weighting function should asymptotically approach the value of 1 as the fully developed region is approached. Again, the experimental uncertainties at the leading edge make the values of $f(\xi)$ unreliable there, but the influence of this large uncertainty in most temperature predictions is small. The weighting function curves for all three Reynolds numbers lie within the experimental uncertainty of their mean curve. This unexpected result suggests that the weighting functions, and thus the lengths of the kernel function entry regions, are relatively insensitive to Reynolds number for the range studied.

The utility of the kernel function can be judged by its ability to predict the temperature distribution resulting from an arbitrary heat flux distribution. The strip heater test plate provided uniform heat flux only over the streamwise intervals from 4.6 to 9.7 cm and from 12.2 to 14.8 cm in the hydrodynamically fully devel-

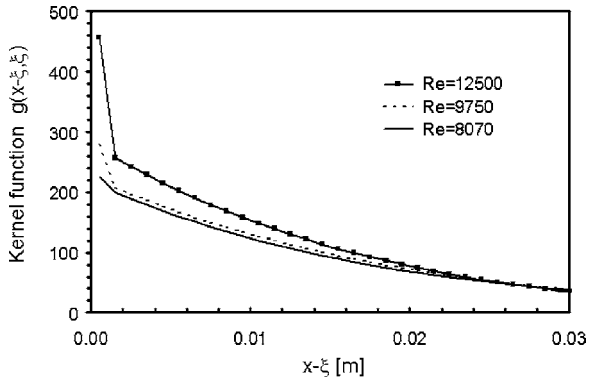

Fig. 8 Comparison of one-dimensional kernel functions for hydrodynamically fully developed flow at various Reynolds numbers

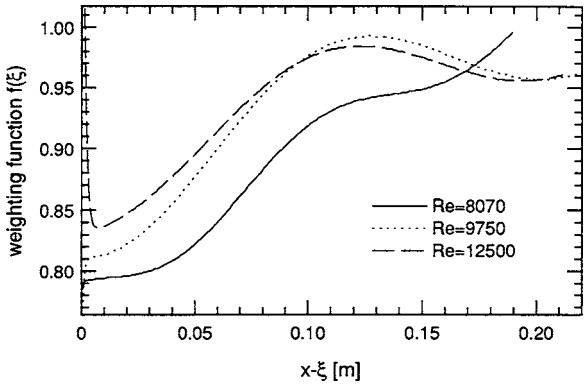

Fig. 9 Weighting function, $f(\xi)$, in the hydrodynamically developing section of rectangular duct flow at various Reynolds numbers

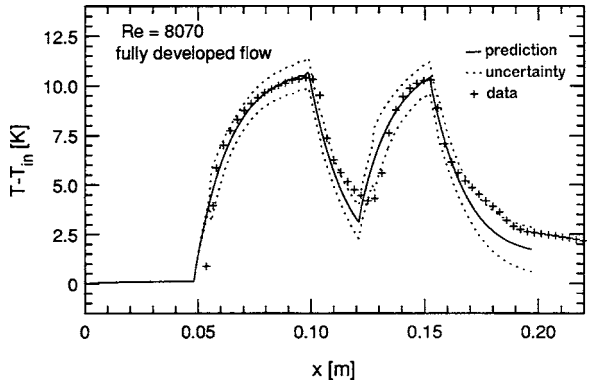

Fig. 11 Comparison of surface temperature data for arbitrary heat flux distribution with temperature prediction using present kernel function

oped test section for the Reynolds number of 8070. Figure 10 plots the convective heat flux in the streamwise direction for this test plate. The total electrical power density dissipated by the heaters is plotted as a comparison. The difference between the total and convective heat fluxes is an indication of the magnitude of the conduction and radiation corrections. The convective heat flux is negative in the regions where no electrical power is provided downstream of the heaters. The reason for this is that the surface is hotter than the opposite wall of the channel and the aluminum plate under the balsa wood, and thus loses heat to radiation and conduction, which must be made up by convection.

The measurement uncertainties in the temperature and heat flux measurements contribute to the uncertainty in the kernel function computation, which ultimately contribute to uncertainty in the temperature predictions. Figure 11 compares the temperature measurement data with the temperature prediction using the kernel function and the uncertainty interval around the prediction. The measured temperature distribution on the strip heaters falls almost entirely within the uncertainty interval. This result explains any discrepancy between the temperature data and the prediction, and provides evidence that the sources of uncertainty in the experiment are nearly accounted for in their entirety. The uncertainty in the prediction is about 6% of the surface temperature rise above inlet temperature at both peaks.

Finally, the temperature data and kernel function temperature prediction are compared to the prediction obtained using the analytical kernel functions for flow between parallel plates, and the prediction obtained using the conventional heat transfer coefficient for a constant heat flux surface in Fig. 12. In this figure, the point of using the proper kernel function for nonuniform temperature surfaces is clearly illustrated. The analytically derived kernel function by Hatton [3] for turbulent fully developed flow between parallel plates underpredicts the rate of streamwise temperature rise and decay. Although the surface temperature prediction is qualitatively correct in shape, its poor comparison to the data suggests that the assumptions used in its derivation such as turbulence models are not general enough to apply to closely related geometries such as a rectangular duct flow. The predicted temperature downstream of heating does agree with the mean air temperature, lending evidence that the kernel function prediction was applied as intended.

The fully developed heat transfer coefficient from a constant heat flux rectangular duct with the mean temperature used as the reference temperature (denoted h_m) is unsuccessful at predicting both the peak temperatures and the qualitative shape of streamwise temperature rise and decay. The use of this descriptor models the surface temperature in proportion to the convective heat flux (seen to be influenced by radiation and conduction losses in this figure), which is in direct conflict with the data. This model ignores the thermal wake from surface heating, which is clearly significant directly downstream of heating in this Reynolds number range. Strictly speaking of course, the traditional heat transfer coefficients only apply to the heat flux distribution from which it was measured, and should be remeasured for every new heat flux distribution for a fair comparison. This limitation only further illustrates the disfunctionality and tedious application of the conventional heat transfer coefficient in nonuniform heat flux and surface temperature situations.

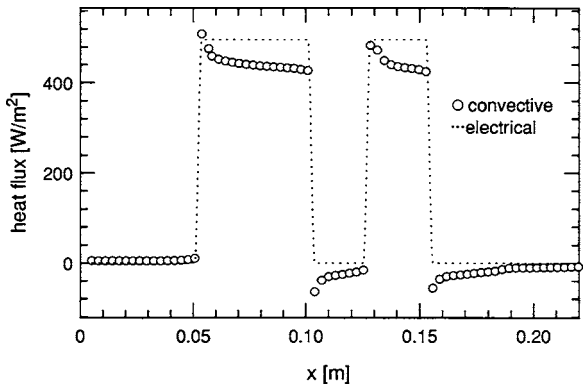

Fig. 10 Convective heat flux pattern in the streamwise direction for test plate with strip heaters

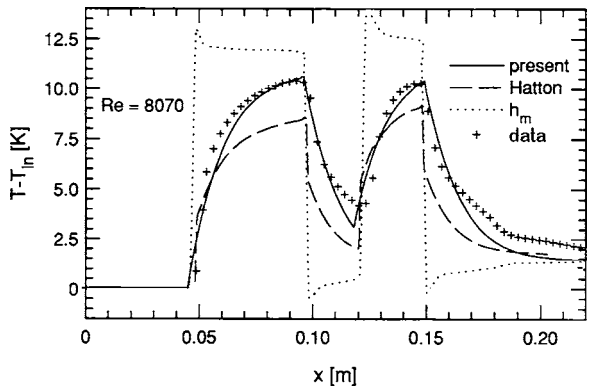

Fig. 12 Comparison of temperature predictions resulting from application of present kernel function, analytical kernel function by Hatton and Quarmby (see Ref. [3]), and the heat transfer coefficient with the mean temperature as the reference temperature

Conclusions

We have presented a method for estimating the continuous, one-dimensional kernel function for a two-dimensional internal flow with constant properties subject to forced convection. We have also demonstrated the measurement of the kernel function in a rectangular duct using a liquid crystal thermography technique. The Reynolds numbers were chosen to provide insight into turbulent internal flow as well as the transition region. The uncertainty interval was sufficiently low to allow for acceptable surface temperature prediction on an arbitrary heated surface. The surface temperature prediction using the kernel functions from the present work was shown to be more accurate than the analytically derived kernel functions for turbulent flow between parallel plates. This evidence suggests that significant differences exist between the two flow scenarios, impacting applications such as board-level electronics cooling.

The advantages of using the kernel function over the conventional heat transfer coefficient were illustrated. The kernel function's invariance to thermal boundary conditions is a key property for highly nonuniform temperature or heat flux distributions. The traditional heat transfer coefficient, strictly speaking, needs to be remeasured for each heat flux distribution to yield accurate results needed for a variety of applications. Once the kernel function is determined as a function of Reynolds number and Prandtl number, it can be used to predict the nonuniform surface temperature rises from any heat flux distribution on the order of 6% or so, as shown by the present work. The empirical correlations for heat transfer coefficient, on the other hand, typically come with an uncertainty of 25% at best, even for well-matched boundary conditions, and are sometimes different for heated and cooled flows. The invariance to thermal boundary conditions should make the kernel function the forced convection descriptor of choice in conjugate conduction-convection problems, which are often used to compute highly nonuniform temperature and thermal stress distributions.

The next step in this research would be to measure the continuous, two-dimensional kernel function for a two-dimensional internal flow, such as a rectangular channel. With this accomplished, the convection and thermal wakes from a two-dimensional arbitrarily heated surface can be easily quantified. Although there is some prior work that suggests that spanwise diffusivity is small for relatively large heated rectangles in a turbulent boundary layer, this conclusion needs to be validated for small heated spots in internal flow situations. In the meantime, linearly scaling the heat flux prediction in the spanwise direction using a one-dimensional kernel function might be a reasonable compromise.

Nomenclature

Cp = specific heat of fluid (J/kg C)
D = constant used in continuous one-dimensional kernel function model in the hydrodynamic entry region (-)
DKF = discrete kernel function (-)
$f(\xi)$ = weighting function for kernel function in entry region (-)
$\tilde{g}(x,\xi)$ = continuous one-dimensional kernel function in x direction from unit heat flux at ξ (-)
$\tilde{g}_{fd}(x-\xi)$ = continuous, fully developed, one-dimensional kernel function as a function of distance from heat flux location (-)
$h_m(x)$ = heat transfer coefficient, $\dot{q}''_{\text{conv}}(x)/(T(x)-T_m(x))$ (W/m^2 K)
H = channel height (m)
k = conductivity of fluid (W/mK)
L = characteristic length scale (m)
m = index (-)
$\dot{m}$ = mass flow rate of air, $\rho U_{in} WH$ (kg/s)
n = index (-)
N = number of steps on heated surface (-)
Nu_{2H} = Nusselt number for flow between parallel plates, $h_m 2H/k$ (-)
Pr = Prandtl number, ν/α (-)
$\dot{q}''_0(\xi)$ = surface heat flux at location, ξ (W/m^2)
$\dot{q}''_{\text{cond}}$ = surface heat flux due to conduction (W/m^2)
$\dot{q}''_{\text{conv}}$ = surface heat flux due to convection (W/m^2)
$\dot{q}''_{\text{rad}}$ = surface heat flux due to radiation (W/m^2)
$\dot{q}''_{\text{tot}}$ = total heat flux from electrical power (W/m^2)
Re = Reynolds number, $U_{in}L/\nu$ (-)
Re_{2H} = Reynolds number for flow between parallel plates, $U_{in}2H/\nu$ (-)
$T(x)$ = temperature at location x (K)
T_{in} = inlet temperature (K)
$T_m(x)$ = mixed mean fluid temperature at location, x (K)
U_{in} = inlet velocity (m/s)
W = width of duct (m)
x = distance from leading edge (m)

Greek Symbols

α = thermal diffusivity, $k/(\rho Cp)$ (m^2/s)
Δx = stepsize (mm)
ρ = density (kg/m^3)
ν = kinematic viscosity (m^2/s)
ξ = variable of integration, typically denotes location of heat flux (m)

References

[1] Kays, W. M., and Crawford, M. E., 1980, *Convective Heat and Mass Transfer*, 2nd ed., McGraw-Hill, New York.
[2] Sellars, J. R., Tribus, M., and Klein, J. S., 1956, "Heat Transfer to Laminar Flow in a Round Tub or Flat Conduit—The Graetz Problem Extended," Trans. ASME, **78**, pp. 441–448.
[3] Hatton, A. P., and Quarmby, A., 1963, "The Effect of Axially Varying and Unsymmetrical Boundary Condition on Heat Transfer With Turbulent Flow Between Parallel Plates," Int. J. Heat Mass Transfer, **33**, pp. 2659–2670.
[4] Moffat, R. J., 1998, "What's New in Convective Heat Transfer?," Int. J. Heat Fluid Flow, **19**, pp. 90–101.
[5] Crittenden, P. E., and Cole, K. D., 2002, "Fast-Converging Steady-State Heat Conduction in a Rectangular Parallelepiped," Int. J. Heat Mass Transfer, **45**, pp. 3585–3596.
[6] Anderson, A. M., and Moffat, R. J., 1992, "The Adiabatic Heat Transfer Coefficient and the Superposition Kernel Function: Part 1—Data for Arrays of Flatpacks for Different Flow Conditions," ASME J. Electron. Packag., **114**(1), pp. 14–21.
[7] Anderson, A. M., and Moffat, R. J., 1992, "The Adiabatic Heat Transfer Coefficient and the Superposition Kernel Function: Part 2—Modeling Flatpack Data as a Function of Channel Turbulence," ASME J. Electron. Packag., **114**(1), pp. 22–28.
[8] Hacker, J. M., and Eaton, J. K., 1996, "Measurements of Heat Transfer in Separated and Reattaching Flow With Spatially Varying Thermal Boundary Conditions," Int. J. Heat Fluid Flow, **18**, pp. 131–141.
[9] Batchelder, K. A., and Eaton, J. K., 2001, "Practical Experience With the Discrete Green's Function Approach to Convective Heat Transfer," ASME J. Heat Transfer, **123**(1), pp. 70–76.
[10] Khon'kin, A. D., 2000, "The Taylor and Hyperbolic Models of Unsteady Longitudinal Dispersion of a Passive Impurity in Convection-Diffusion Processes," J. Appl. Math. Mech., **64**(4), pp. 607–617.
[11] Bokota, A., and Iskierka, S., 1997, "Numerical Simulation of Transient and Residual Stresses Caused by Laser Hardening of Slender Elements," Comput. Mater. Sci., **7**, pp. 366–376.
[12] Mitrovic, B. M., Le, P. M., and Papavassilious, D. V., 2004, "On the Prandtl or Schmidt Number Dependence of the Turbulent Heat or Mass Transfer Coefficient," Chem. Eng. Sci., **59**(3), pp. 543–555.
[13] Mukerji, D., Eaton, J. K., and Moffat, R. J., 2004, "Convective Heat Transfer Near One-Dimensional and Two-Dimensional Wall Temperature Steps," ASME J. Heat Transfer, **126**(2), pp. 202–210.
[14] Simonich, J. C., and Moffat, R. J., 1982, "New Technique for Mapping Heat Transfer Coefficient Contours," Rev. Sci. Instrum., **53**(5), pp. 678–683.
[15] Baughn, J. W., Takahashi, R. K., Hoffman, M. A., and McKillop, A. A., 1985, "Local Heat Transfer Measurements Using an Electrically Heated Thin Gold-Coated Plastic Sheet," ASME J. Heat Transfer, **107**(4), pp. 953–959.
[16] Farina, D. J., Hacker, J. M., Moffat, R. J., and Eaton, J. K., 1994, "Illuminant Invariant Calibration of Thermochromic Liquid Crystals," Exp. Therm. Fluid Sci., **9**(1), pp. 1–12.
[17] Moffat, R. J., 1982, "Contributions to the Theory of Single-Sample Uncertainty Analysis," ASME J. Fluids Eng., **104**, pp. 250–260.

Effects of Intersection Angles on Flow and Heat Transfer in Corrugated-Undulated Channels With Sinusoidal Waves

Jixiang Yin[1]
e-mail: yjxiangwise@hotmail.com

Guojun Li

Zhenping Feng

School of Energy and Power Engineering,
Xi'an Jiaotong University,
Xi'an 710049, P. R. C.

This paper reported three-dimensional numerical simulations of the steady laminar flow and heat transfer in corrugated-undulated channels with sinusoidal waves, aiming to investigate the effects of intersection angles (θ) between corrugated and undulated plate and Reynolds number (Re) on the flow and heat transfer. The simulations are conducted by using multi-channel computational domain for three different geometries. The code is validated against experimental results and then data for Nusselt number (Nu) and friction factor (f) are presented in a Re range of 100–1500, and intersection angle range of 30–150 deg. The simulation confirms the changes of Nuu (averaged over undulated plate) and Nuc (averaged over corrugated plate) with θ representing different characteristics. As θ increases, Nu (Nuu or Nuc) is about 2–16 times higher for the corrugated-undulated configurations CP-UH1 and CP-UP1 and the concomitant f is about 4–100 higher, when compared to a straight channel having square cross section. The minimum of local Nu (Nuu or Nuc) is situated at the four contact points where the top plate touches the bottom one, and the high Nu is located upstream of the crest of the conjugate duct. Performance evaluation for the CP-UH1 channel shows that the goodness factors (G) are larger than 1 with the straight channel having a square cross section as a reference, and the 30 deg geometry channel has optimal flow area goodness.
[DOI: 10.1115/1.2222378]

Keywords: heat transfer enhancement, intersection angle, three-dimensional computation, corrugated-undulated channel

Introduction

In compact heat exchangers, it is desirable to achieve the highest heat transfer rate with the smallest pressure loss. This requirement is especially important for the practical engineering devices, which are limited in size and efficient in operation, such as a recuperator in micro and miniturbines (approximate output power ranges from 5 to 500 kW) [1], the plate heat exchangers used for process industries, heating and cooling in evaporators, air-conditioning equipment and the areas of medical and biochemical engineering et al. [2]. The design compactness increase of heat exchanger promotes laminar flow through a trend toward smaller length scale and lower Reynolds numbers. And it is expected that an early transition from laminar flow to turbulent flow can be caused by a relatively simple rational redesign of the basic heat transfer elements to form complex flow passage.

One method to enhance heat transfer in laminar flow regime is to combine flow separation and reattachment of boundary layer so as to induce vortice to augment transverse fluid mixing, and to trigger free shear self-sustained oscillations by geometric modifications or structures of the wall. The destabilizing flow increases momentum transfer with a corresponding increase in the value of wall shear stress. This flow, at a much lower Re, yields heat transfer rates commensurate with those of a plane channel turbulent flow. Among the many different types of plate corrugations available, crossed-corrugated (CC) plate pattern [3,4] (see Fig. 1), whose upper and lower plates have the same scale, is the most commonly used and efficient corrugation configuration. Stasiek et al. [3] and Ciofalo et al. [4] performed a systematic investigation on the fluid flow and heat transfer characteristics by means of experimental and numerical methods. They not only measured the heat transfer and pressure drop, but also discussed the effects of various configurations and Reynolds number on flow and heat transfer. Their numerical prediction confirms the relative adaptability of different modeling approaches such as laminar, low-Re, k-ϵ and large-eddy simulation to simulate transitional and weakly turbulent flow by comparison of their results of local and overall heat transfer rate with the experimental data. Literature [5] investigated the effects of the corrugation angle on flow and heat transfer in cross corrugation channels with sinusoidal wave for $50 \leqslant \mathrm{Re} \leqslant 2000$, $30\ \mathrm{deg} \leqslant \theta \leqslant 150\ \mathrm{deg}$. Focke et al. [6] and Muley and Manglik [7] reported an experimental investigation of the effects of corrugation inclination angle relative to flow direction on the thermal-hydraulic performance. Blomerius, Holsken, and Mitra [8] investigated the effects of the ratio of corrugation wave length to amplitude on flow and heat transfer in sine-wave crossed-corrugated ducts for two symmetric and one mixed chevron plate arrangements. Blomerius and Mitra [9] have investigated the flow structure and heat transfer in corrugated channels, taking into consideration the influence of unsteadiness for the channels consisting of two-dimensional and three-dimensional corrugated plates in the laminar to transitional range of Reynolds numbers (600–2000). On the other hand, only few researchers have mentioned the corrugated-undulated (CU) geometry (see Fig. 2), a variant of crossed-corrugated geometry, because CU geometry has not been applied in rotary air preheaters until the last decade [10]. Stasiek [10] and Ciofalo, Piazza, and Stasiek [11] presented an experimental and numerical investigation of the heat transfer and fluid flow for corrugated-undulated geometry configuration (con-

[1]Corresponding author. Also at: Taiyuan University of Technology.

Contributed by the Heat Transfer Division of ASME for publication in the JOURNAL OF HEAT TRANSFER. Manuscript received May 23, 2005; final manuscript received January 7, 2006. Review conducted by Bengt Sunden.

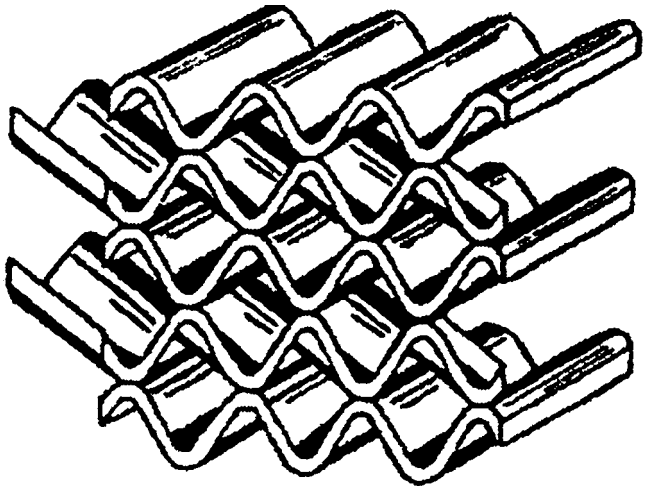

Fig. 1 Crossed-corrugated geometry (see Ref. [3])

figuration walls profiles are formed by a combination circular arc with straight line) with a Re range of 1500–10,000. But they provided some sparse results from a numerical study under transitional and weakly turbulent conditions. Owing to the complexities of the geometry configuration, the investigation of flow field is more difficult, that is why there are fewer flow field measurements than heat transfer in literature. Furthermore, the investigation was limited to transitional and turbulent flow regime because of the faint pressure drop signal in laminar flow regime.

Despite all the previous efforts, to the authors' knowledge, the numerical investigations of flow and heat transfer, whether for CC or for CU, are few in the laminar regime, and the few numerical simulations available adopted periodic boundary conditions in the inlet/outlet faces. For entry effects, little knowledge is available. A number of important issues remain to be explored regarding how heat transfer and pressure drop vary with intersection angle and Re for CU configuration.

The aim of this work is to provide information on the flow and heat transfer in the corrugated-undulated channel with sine-wave plates. The numerical investigation has been performed for several flow Reynolds numbers ranging from 100 to 1500 and for different intersection angles (from 30 deg to 150 deg) between corrugated and undulated plates. The present calculation adopts multichannel computational domain. Finally, the analysis of entry effects is presented, and performance evaluation is conducted with a straight channel having a square cross section as a reference.

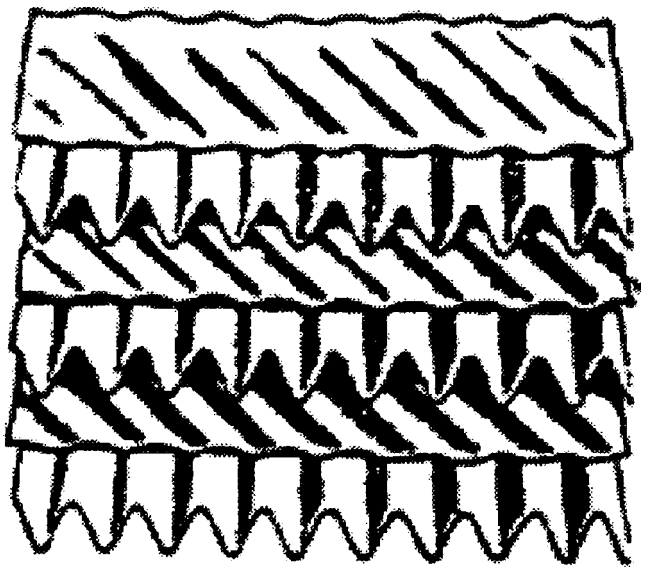

Fig. 2 Corrugated-undulated geometry (see Ref. [3])

Geometries Description

Figure 3 shows the detailed description for the geometry configuration considered in this study. It is composed of two different scale plates that bear sine-wave wall profiles. Plates bearing shallow furrows (undulated plates, subscript "*u*") alternate with plates bearing deeper furrows (corrugated plates subscript "*c*") at an angle to form communicating channel. The channel configuration of the fluid flow and heat transfer is decided by parameters such as pitch P, internal height H_i, intersection angle θ (between plates), and wall thickness S (S is neglected in this study).

In the present study, the corrugated plates are kept fixed (the furrows of the corrugated plates are parallel to this main flow direction), while the undulated plates with three different geometrical parameters intersect on the top of corrugated plates at an angle varied from 30 deg to 150 deg. Their characteristics are summarized in Table 1.

The geometry is expressed by using the pattern of the CP-U (CP stands for the corrugated plate and UH1, UP1, UCS for undulated plates).

Model and Methods

Physical Problem Description. The present calculation adopts 10×10 multiple channels computational domain (see Fig. 4), while the corresponding unitary cell is shown in Fig. 5. This domain has two inlets (D, W) and two outlets (U, E). The established complex flow channels may result in high heat transfer rates with relatively lower pressure losses. The inlet faces flow rate will be prescribed through specification of the Re and the fluid inlet temperature is assumed as constant. With the computation domain length extended, periodically fully developed flow and heat transfer will be attained eventually. The outlet faces are considered as a fully developed condition on which exist zero-normal derivatives of flow and heat transfer variables. The constant wall temperature is assumed and its value is higher than that of the fluid. The fluid medium is air with constant property.

Governing Equations. Under the assumption of steady, laminar, incompressible three-dimensional flow and heat transfer, the flow field and temperature field for constant property fluid are governed by these equations:

Continuity equation

$$\frac{\partial}{\partial x_i}(\rho u_i) = 0 \tag{1}$$

Navier-Stokes equation

$$\frac{\partial}{\partial x_i}(\rho u_i u_k) = \frac{\partial}{\partial x_i}\left(\mu\frac{\partial u_k}{\partial x_i}\right) - \frac{\partial p}{\partial x_k} \tag{2}$$

Energy equation

$$\frac{\partial}{\partial x_i}(\rho u_i T) = \frac{\partial}{\partial x_i}\left(\frac{\lambda}{C_p}\frac{\partial T}{\partial x_i}\right) \tag{3}$$

Grid Generation. The computation domain of Fig. 4 is covered with unstructured Tet/Hybrid grids. The commercial code GAMBIT has been selected to generate these grids due to its excellent merit of managing very complex 3D geometries. Depending on the intersection angle between corrugated and undulated plate and shape factor (pitch, height), approximately 25,000–30,000 grid points per unit cell are used to discretize the computation domains. Figure 6 shows the representative grid of adjacent channels along the mainstream direction for CP-UH1 with 60 deg intersection angle between corrugated and undulated plate. The sys-

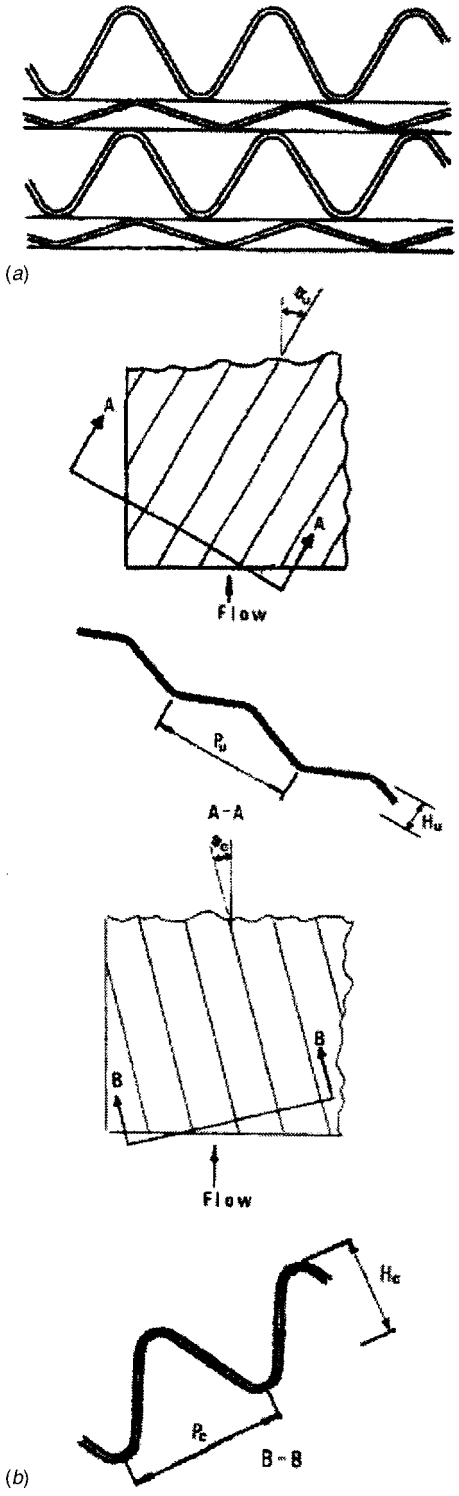

Fig. 3 Geometry of corrugated-undulated (CU) heat transfer element. (*a*) End view of element pack; (*b*) cross section and planform of undulated plate; (*c*) cross and planform of corrugated plate.

tematic grid refinement studies have been conducted by integrating the accuracy of the numerical results with the computational cost because the well-resolved three-dimensional computations will require considerably large CPU time to conduct parametric tests. To predict efficiently the larger gradients of velocity and temperature abutting the wall surfaces, more nodes are distributed in the vicinity of the upper and lower walls.

Table 1 Geometries considered

Corrugated plate		Undulated plates		
Geometry	CP	UP1	UH1	UCS
P(mm)	22.60	26.21	21.87	32.00
H(mm)	13.13	3.65	5.20	8.00
P/H	1.721	7.181	4.206	4.00
D_e(mm)		12.75	13.51	15.52

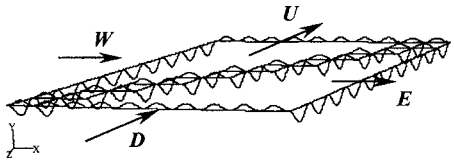

Fig. 4 Computational domain sketch

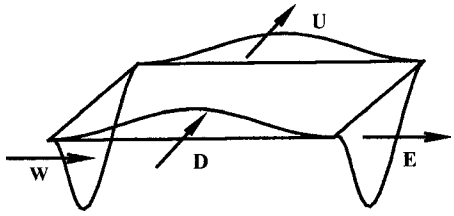

Fig. 5 Unitary cell (perspective view)

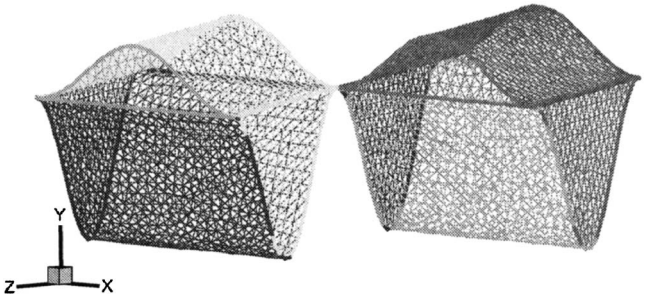

Fig. 6 Three-dimensional grid of adjacent channels along main flow direction

Numerical Solution. Three-dimensional numerical simulations of the fluid flow and heat transfer in the computation domain of Fig. 4 are conducted by the computer code FLUENT based on a finite volume technique. The discretization schemes of convective terms in momentum and energy equations adopt QUICK scheme with three-order precision. The SIMPLEC pressure-velocity coupling algorithm is used here. For all reported calculation results, the convergence criteria are the convergence residuals less than 10^{-4} for velocity equations and less than 10^{-7} for energy equations. The convergence became more and more difficult for these geometry channels whose intersection angles are larger or smaller.

Geometry and Performance Parameters. A corrugated-undulated geometry can be completely specified by the parameters marked in Fig. 3, from which the other relevant quantities required in the calculation can be derived. Figure 7 is a unitary cell projection plane with labeled main quantities. The relevant geometrical quantities are formulated by Eq. (4) and Eq. (5).

Flow cross section

$$A_c = [p_u H_u \sin\alpha + p_c H_c \sin(\theta - \alpha)]/\sin\theta \tag{4}$$

Inlet-to-outlet length

$$\Delta L = [p_u \cos\alpha + p_c \cos(\theta - \alpha)]/2 \sin\theta \tag{5}$$

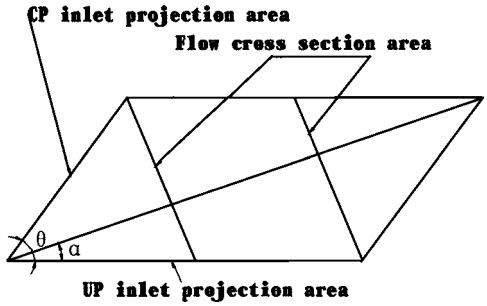

Fig. 7 Main geometrical quantities sketch

In heat exchanger design, the most relevant performance parameters are pressure drop and heat transfer rate. It is desirable that high heat transfer rates are obtained while pressure losses are as low as possible. The pressure losses are evaluated using dimensionless pressure gradient per unit length along the mainstream direction, and the defining equation is as follows:

Friction factor

$$f = \frac{|\Delta \mathbf{P}| D_e}{2\rho \Delta L u_{av}^2} \tag{6}$$

Heat transfer can be described by a dimensionless parameter Nusselt number. The local and surface-weighted averaged heat transfer rates can be defined as:

Local Nusselt number

$$\mathrm{Nu}_x = \frac{q_w D_e}{\lambda (T_w - T_f)} \tag{7}$$

Average Nusselt number

$$\mathrm{Nu} = \frac{\langle q_w \rangle D_e}{\lambda (T_w - T_f)} \tag{8}$$

Model Validation

The use of the experimental results is limited, not only because there is little literature on the CU geometry configurations, but also because the literature [10,11] provided no detailed data about the CU geometry studied. Moreover, the literature [10,11] did not present the experimental results in low Reynolds numbers. The present study confirms the validation of numerical code by comparing the numerical results predicted using 7×7 multi-channel domain with the experimental results presented by Utriainen and Sunden [1] for CC2.2-75 ($P/H_i=2.2$, inclination angle $\theta=75$ deg) geometry. The numerical results show that when consecutive cells along the main flow direction increase, the corresponding heat transfer rate and friction factor have basically been constant (up to the fourth channel along main flow direction), which means that a fully developed condition is attained, both hydrodynamically and thermally. Figure 8 illustrates the numerical data for the average Nu of the fourth cell wall surface and friction factor in the same channel and experimental results presented by literature [1], which exhibits a good agreement, indicating the validity of the present computation method.

Entry Effects

The present simulation adopts 10×10 multi-channel computational domain (see Fig. 4) in order to estimate the entry effects and to ascertain that the flow and heat transfer is fully developed. Because of the asymmetry of CU channel, the flow is more complex in CU channel than in the CC channel, so the length of computational domain should be extended to 10×10 (for CC channel 7×7). Figures 9(*a*) and 9(*b*) show the variations of average *Nuc* and *Nuu* with different geometries and Re versus unitary cell number along main flow direction. It is found that the changes of *Nuc* and *Nuu* are significant in the entrance, but the effects concern only the first few cells, and the changes are much less marked and finally keep constant basically up to the seventh cell from the entrance, which corresponds to fully developed flow and thermal conditions. That is to say, the flow pattern repeats itself from module to module, and the heat transfer coefficient has reached its asymptotic value [12]. So this paper will use the predicted seventh cell's results for the results analysis and discussion.

Results and Discussion

Flow Characteristics. The present work suggested that the flow behavior in the corrugated-undulated channel studied is different from the crossed-corrugated channel. Focke, Zachariades, and Olivier [6] used the flow visualization method to study the flow field in crossed-corrugated channel. They concluded that for $0\ \mathrm{deg}<\theta<160$ deg, apart from sidewall reflections, the fluid flow follows predominantly the furrow on each plate and two sets of different directional streams intersect in the neighborhood of midplane where the top plate and bottom one contact each other, which induces secondary swirling motions (see Fig. 10). Owing to the symmetric plate configuration, the oncoming fluid is forced to flow equally along the furrows of each plate of any given couple, independent of their skewness with respect to the main flow direction [11]. However, the asymmetric plate configuration makes fluid flow more intricate in the corrugated-undulated configuration considered in the present investigation. For $\theta<90$ deg, the deeper corrugated channels cause a larger and larger fraction of the fluid flow to be diverted from the shallower undulated channels with

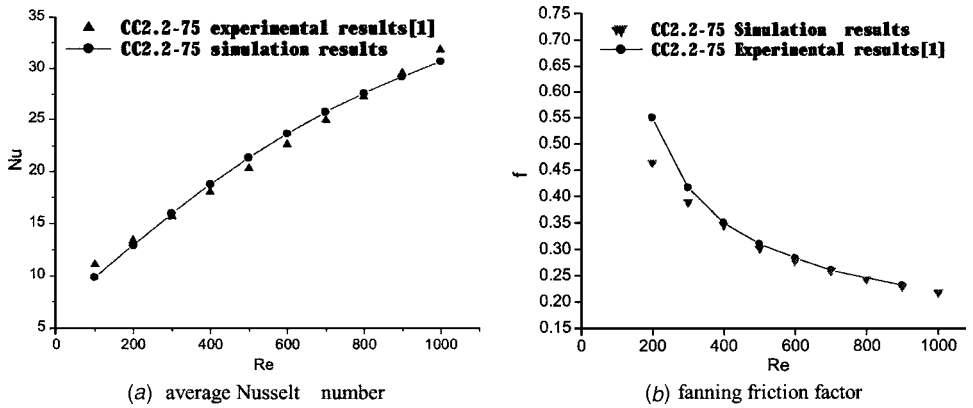

Fig. 8 Comparison between predicted and experimental results. (*a*) Average Nusselt number, (*b*) Fanning friction factor.

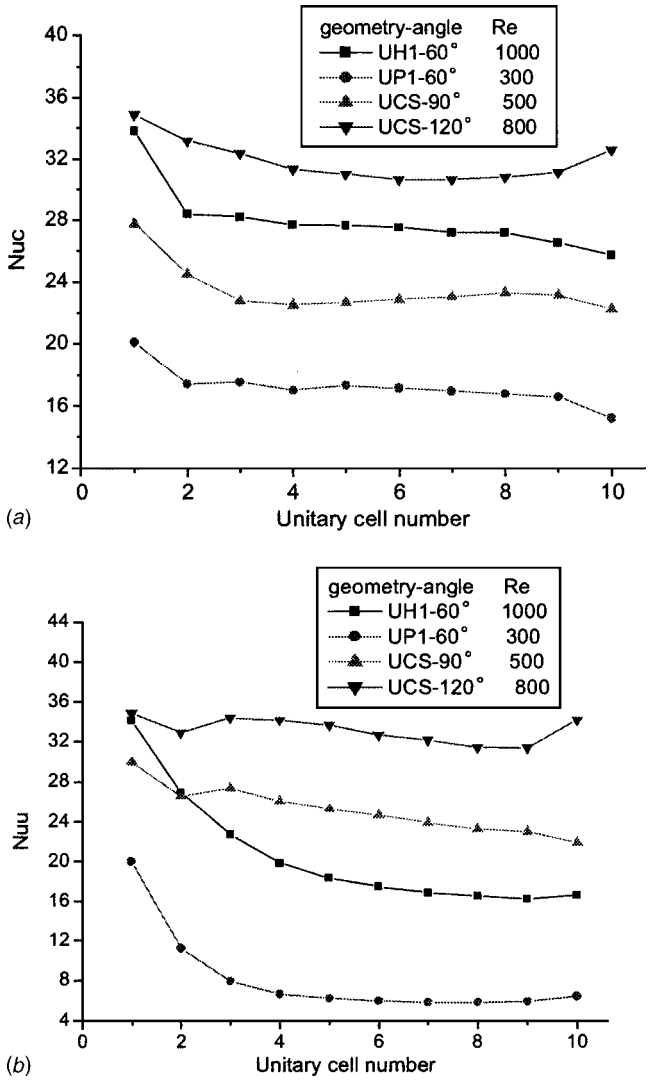

Fig. 9 (*a*) Average Nu in the main flow direction consecutive cell of corrugated plates; (*b*) average Nu in the main flow direction consecutive cell of undulated plates

increasing skewness with respect to the main flow direction. The opposite is true for $\theta > 90$ deg because the crossing streams between channels have a retarding function each other owing to their velocity components being in opposite directions. The retarding function makes the fluid flow diversion from the shallower channels decrease with increasing intersection angle (skewness). In conclusion, the fluid diversion from shallower to deeper channels decreases with increasing θ for the range of $\theta < 90$ deg or $\theta > 90$ deg, respectively.

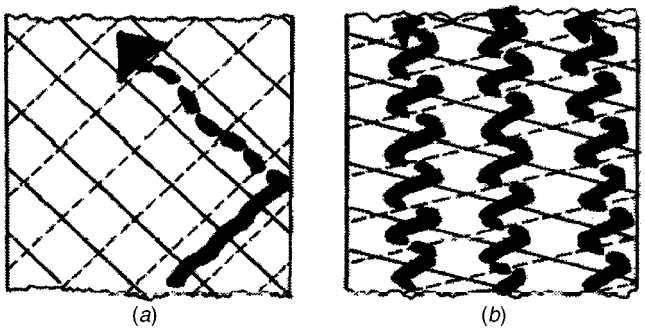

Fig. 10 Flow patterns in crossed-corrugated channel. (*a*) Moderate included angle; (*b*) Large included angle (see Ref. [5]).

Averaged Heat Transfer. It is important to record the heat transfer coefficients separately for the undulated and corrugated plates due to the asymmetric geometry. The heat transfer coefficient is evaluated by using the Nusselt number. Figure 11 shows the numerical results predicted for *Nuu* and *Nuc* for CP-UH1 and CP-UP1 configurations. It is evident that the *Nuu* and *Nuc* have similar change traits with Re, but different change traits with θ. For all intersection angles, the values of *Nuu* increase with increasing Re, but the change becomes less marked when the intersection angles become larger. Moreover, the increase in θ makes the *Nuu* increase because the fluid diversion from shallower to deeper channels decreases with increasing θ (except for 90 deg), thus the effect of heat transfer on 150 deg undulated wall plate is optimal and the 30 deg one is the worst.

On the other hand, the influence of the intersection angle on *Nuc* is less clear than that of Re. The change trend of *Nuc* with θ is similar to each other for CP-UH1 and CP-UP1. For $\theta \leq 90$ deg, the enhancement of *Nuc* associated with increasing Re is low for 60 deg geometry wall surface, intermediate for 30 deg geometry wall surface and high for 90 deg geometry wall surface, which is in agreement with the flow characteristics mentioned above. This is because the channel of 30 deg can cause the larger flow diversion from the shallower to the deeper channels than that of 60 deg channel, making the mixing more sufficient in the corrugated channel of 30 deg than that of 60 deg, and the *Nuc* on the 30 deg surface is larger than that of 60 deg. For $\theta > 90$ deg, the *Nuc* decreases with increasing θ (for CP-UP1, up to Re=1000, the *Nuc* on 120 deg geometry wall surface is higher than that of the 135 deg) so that the heat transfer effect is poorest on the 150 deg geometry wall surface.

The geometry CP-UCS (having minimum P/H), characterized by deep undulation height and large pitch, displays a different change with those two geometries mentioned above. Figure 12 shows the heat transfer rate versus intersection angle with different Reynolds numbers. Both *Nuu* and *Nuc* are increased with increasing θ for all intersection angles being investigated, and the heat transfer enhancement associated with increasing θ is more pronounced at low Re and large intersection angle, which means that it is more potent to intensify the heat transfer at such a region. By contrast, the changes of the *Nuu* and *Nuc* are less marked at larger Re and larger intersection angle. The same remarks hold as for the *Nuu* on the CP-UH1 and CP-UP1 geometries.

For all geometries investigated here, both *Nuu* and *Nuc* are higher than that of a straight channel having a square cross section (Nu=2.98) considered as a reference channel. The values of *Nuu* on CP-UH1 and CP-UP1 configurations increase by a maximum factor about 15 times higher at Re=1500, θ=150 deg than that of the reference channel. And that, the maximal increase values of *Nuc* on the CP-UH1 and CP-UP1 configuration is about 14 times higher than that of the same reference channel at Re=1500, θ=120 deg.

The effects of intersection angle on heat transfer on the corrugated plate are different with the CU configurations. The change in characteristics of *Nuc* with θ for the CP-UCS configuration is similar to crossed-corrugated (CC) configurations [3,4].

Local Heat Transfer. Figure 13 presents the local distribution of heat transfer coefficient expressed as Nu for CP-UCS configuration with two intersection angles of 60 deg and 120 deg on the seventh channel wall surfaces at Re=500. The following general qualitative remarks can be yielded.

- First, the similar characteristic can be found in the local distributions of *Nuu* and *Nuc* on different intersection angle plates. Low heat transfer is observed in the whole

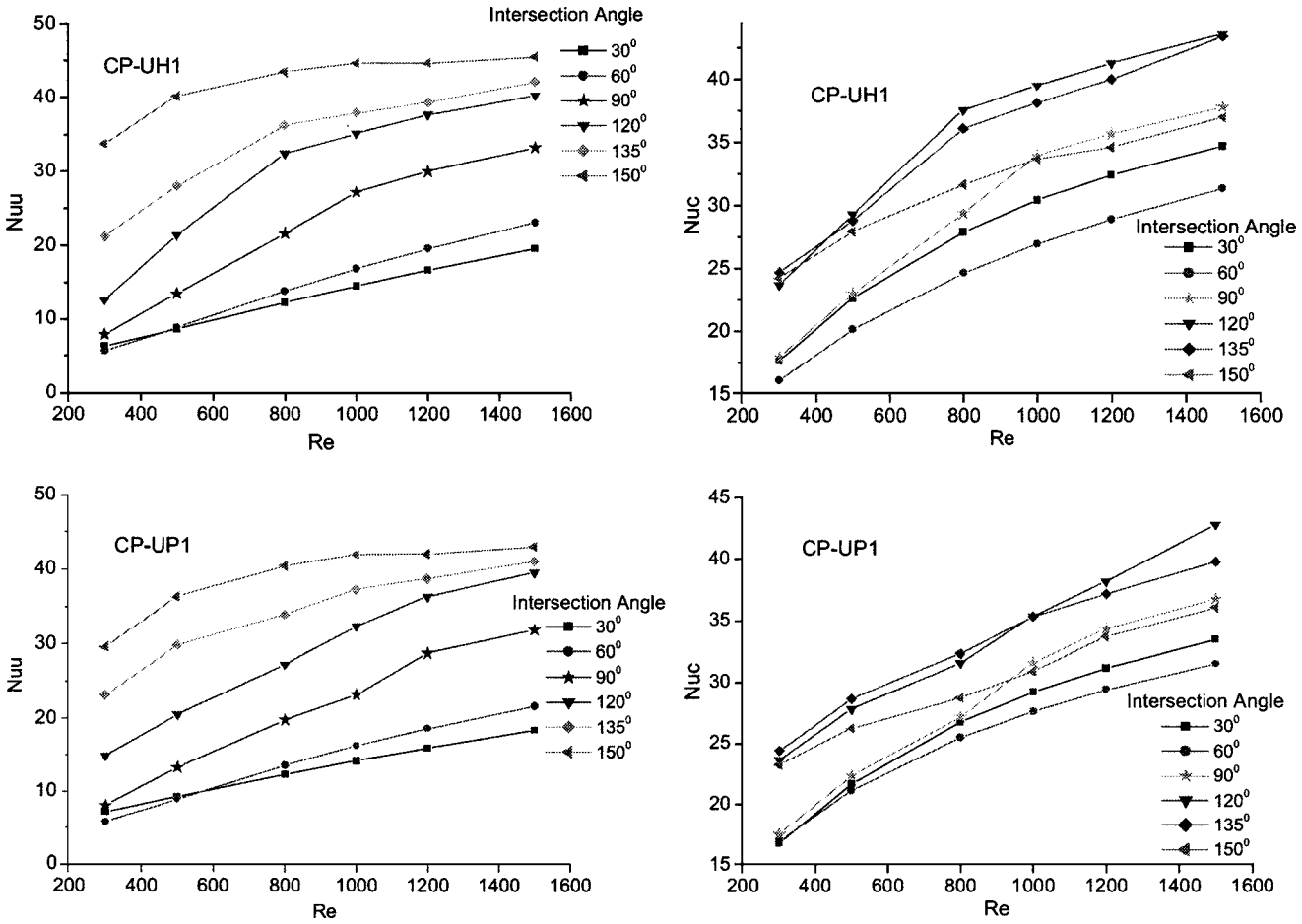

Fig. 11 Average Nusselt number on the undulated (*Nuu*) and corrugated (*Nuc*) plate as a function of the Re for different intersection angles and geometries

central corrugated (furrow) region due to almost undisturbed channel flow, however, on the undulated plate, the low heat transfer regime is shifted to the furrow one side close to the inlet neighborhood of the conjugate channel. This phenomenon is responsible for the asymmetry, which causes the change of flow structure.

- The maximal *Nuc* values are located in the inlet neighborhood of the conjugated channel exit and the exit neighborhood of the conjugated channel inlet, where the highest levels of mixing are generated by the interaction between two fluid streams; and the held region of maximum *Nuc* at large θ is larger than that of small θ. The secondary maximum *Nuc* occurs at the upstream of the trailing edge (main flow outflow). The effect of intersection angle on *Nuu* is larger than on that of *Nuc*. The largest *Nuu* distribution is the same as the *Nuc* for small intersection angle (θ=60 deg); but for large intersection angle (θ=120 deg), the maximum *Nuu* only occurs at the inlet neighborhood of the conjugated channels' exit.
- The minimum of Nusselt number is situated at four contact points where the top plate touches the bottom one where the flow is in the stagnation region. The fluid temperature of the trailing around the four contact points is close to the wall temperature because poor mixing there makes the heat transfer deteriorate. The smaller the intersection angle is, the broader the overspread of the trailing would be. Figure 14 represents the temperature distribution of the CP-UH1 configuration on the midplane for intersection angle 60 deg and 120 deg at Re=1200.

Flow Field. Figure 15 illustrates some characteristics of the flow field. This plot reports the velocity vector in two inlet faces of the seventh channel for the CP-UH1 configuration, θ =120 deg and Re=1500. A secondary flow pattern is visible and a swirling flow pattern can be observed in the deeper corrugated channel. Although the vortex induced by the interaction between fluid streams flowing in conjugate channels is relatively weak, the swirling may play an important role in the heat transfer enhancement by steadily transporting core fluid to near wall region and vice versa. The complex CU configuration is forcing the streamwise flow toward the walls at an angle so that the flow in the near wall region is disturbed by both the angled streamwise flow and the secondary flows, which leads to an increase of velocity and temperature gradients and the enhancement of heat transfer is achieved.

Pressure Drop. In present study, the pressure drop is characterized by a dimensionless pressure gradient per unit length along the main flow direction expressed by formula (6). Figure 16 shows the dependence of friction factor *f* upon Reynolds number for CP-UH1 and CP-UP1 with different intersection angles from 30 deg to 150 deg. Very small or large intersection angles are not considered because they could make the computational domain excessively distorted, therefore make it difficult to form the grids and calculation convergence.

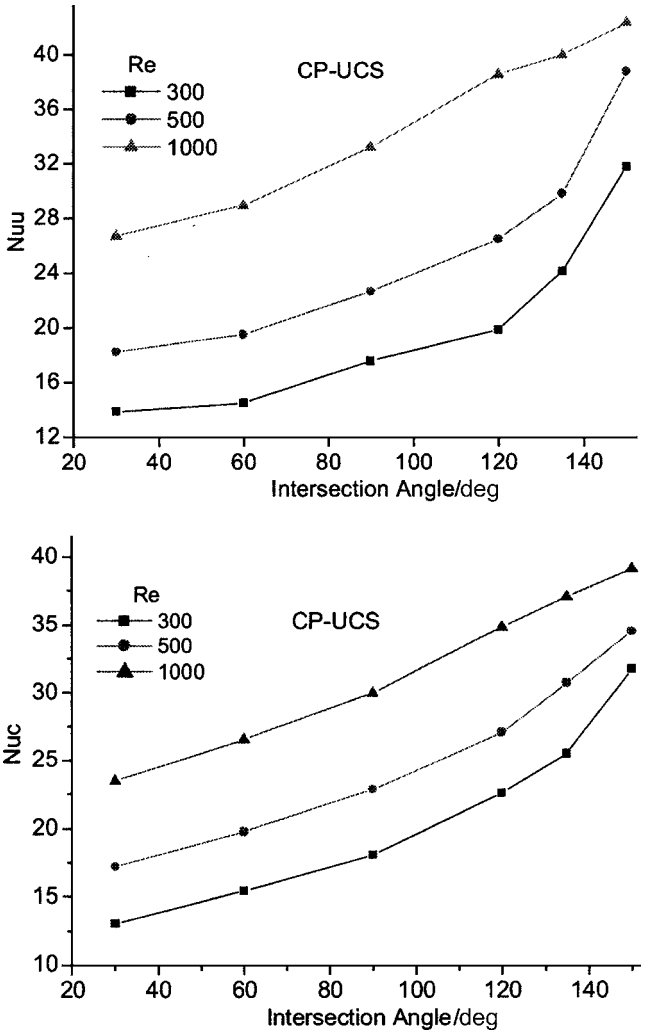

Fig. 12 Average Nu on undulated (Nuu) and corrugated (Nuc) plates of UCS geometry as a function of the intersection angle for different Reynolds numbers

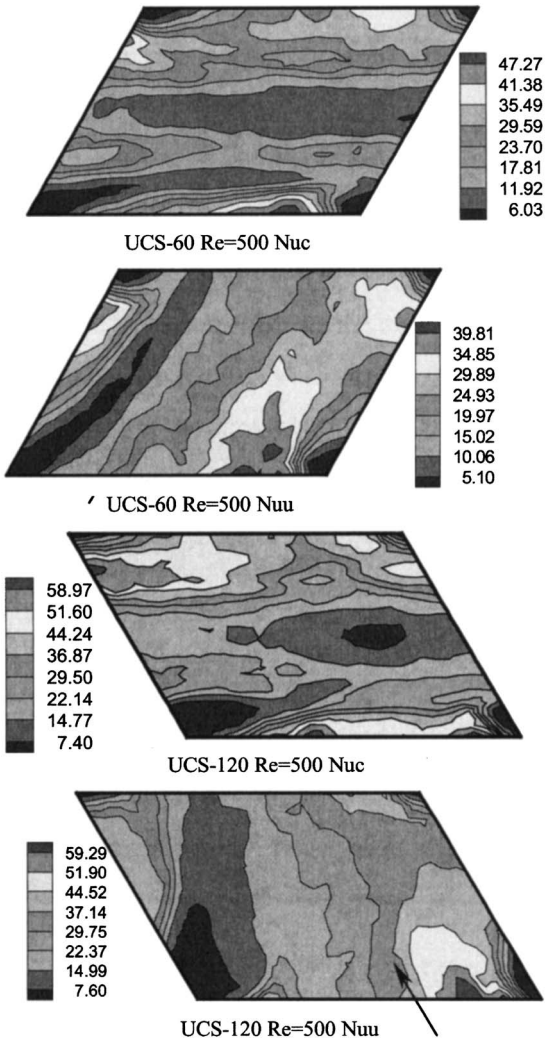

Fig. 13 Distribution of the local Nusselt number for the CP-UCS with intersection angle 60 deg, 120 deg and Re=500

It is clear that f decreases with increasing Re and the changes of f become more and more slower for large Re; moreover, this phenomenon is more pronounced in the case of $\theta > 90$ deg. The friction factors are increased about 4–100 times for the CP-UH1 or CP-UP1 compared with a straight channel having a square cross section.

The effect of shape factor on f is marked for $\theta > 90$ deg. The friction factors with a small P/H (CP-UH1, see Fig. 16, and CP-UCS, see Fig. 17) channel have an evident change with θ and Re; however, the effect of θ on f is very small and even almost died out for a large P/H (CP-UP1, see Fig. 16) channel. The non-linear behavior at higher Re for CP-UP1 could be due to the fact that the flow is in the transitional region and the laminar flow assumption may not be correct for the large Re regime. Figure 17 shows friction factor f as a function of intersection angle θ and three Reynolds numbers for CP-UCS channel, which displays the similar change traits to the CP-UH1.

For $\theta \leqq 90$ deg, the changes of f with θ and Re display similar traits for all considered channels. Friction factor increases with an increase in intersection angle due to the strength of the interaction between two streams fluid.

Performance Evaluation. In the design of heat exchanger, it is desirable to give the minimum pressure, and to obtain the highest heat transfer rate, though in practice the ease of manufacturability has to be taken into account. So it is important to carry out the performance evaluation. Numerous performance evaluation criteria have been suggested to compare the performance of heat exchanger surfaces according to different purposes for which a heat exchanger is designed [13]. In present study the goodness factor expressed as $G=(\mathrm{Nu}/\mathrm{Nu}_0)/(f/f_0)^{1/3}$ is used as the comparison criterion. It is based on the criterion of equal pumping power and fixed surface geometry, where the subscript 0 stands for the value of straight channel having a square cross section ($\mathrm{Nu}_0=2.98$, $f^*\mathrm{Re}=14.25$).

Figure 18 reports the goodness factor G versus Re with different intersection angles for the CP-UH1 configuration as a representative. A high position in this plot signifies a good performance, which means less pumping power is required to reach the same heat transport rate. It is difficult to separate from the influence of θ for the dependence of G on Re. It is observed that the G increases with increasing Re for $\theta < 90$ deg, and the goodness of the 30 deg channel is superior to that of the 60 deg one. For $\theta \geq 90$ deg, the G increases first with increasing Re, however, with further increase in Re the change of G is very faint, or even decreases for 150 deg channel; moreover, with Re up to about 800, the G decreases with increasing θ so that the performance of 150 deg channel is the worst. For all cases, the goodness factors are all larger than 1, which means the performance of the CP-UH1 geometry is superior to the straight channel having a square cross

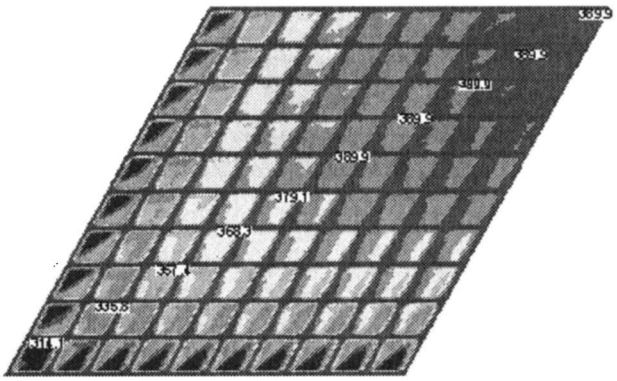

CH1-60 midplane temperature

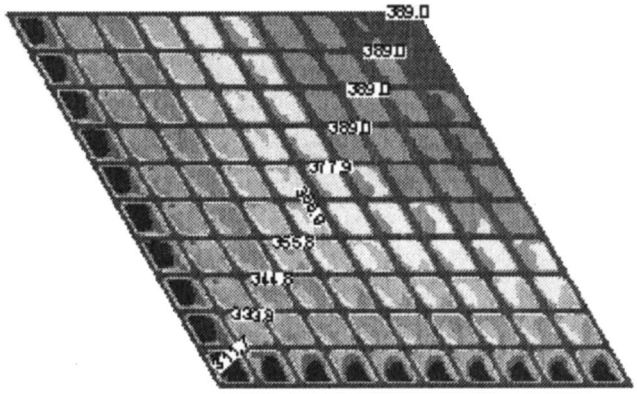

CH1-120 midplane temperature

Fig. 14 Temperature contour distributions of midplane for CP-UH1, intersection angle 60 deg, 120 deg and Re=1200

section.

Figure 19 shows the performance of the surfaces about flow area goodness factor comparison for the CP-UH1 geometry, where the ratio of the Colburn number to friction factor (j/f) is plotted versus the Reynolds number and intersection angle. A high position in this plot indicates a small flow area of the heat exchanger

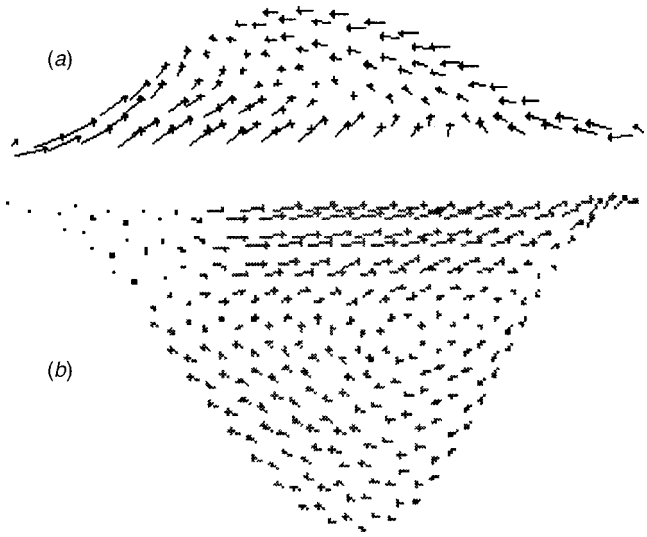

Fig. 15 Predicted velocity vector for the CP-UH1 inlet surface, intersection angle θ=120 deg, Re=1500. (*a*) Corrugation channel, (*b*) undulation channel.

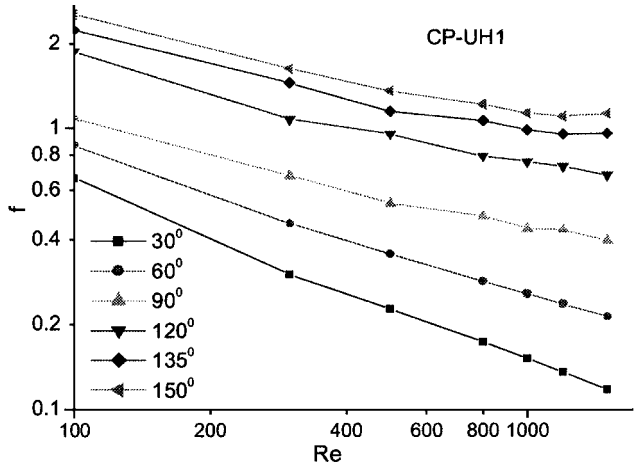

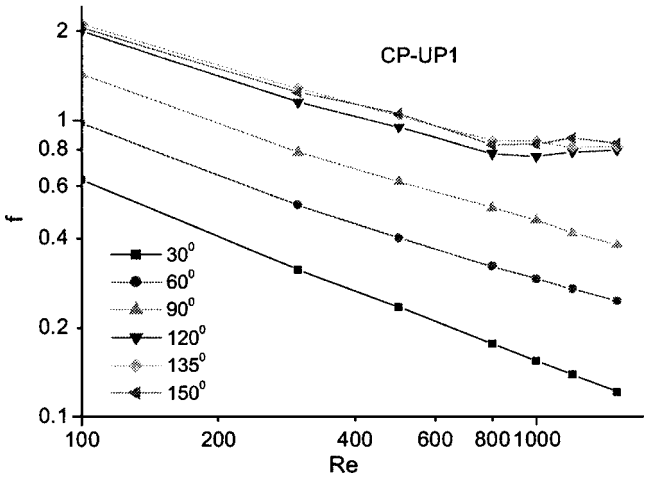

Fig. 16 Fanning friction factor as a function of Re for different intersection angles and geometries

[14]. This plot shows that the flow area goodness factor is decreased with increasing θ and the change is more pronounced in the range of $\theta<90$ deg than $\theta>90$ deg. The maximum goodness factor is obtained in the 30 deg geometry channel and the minimum in 150 deg one.

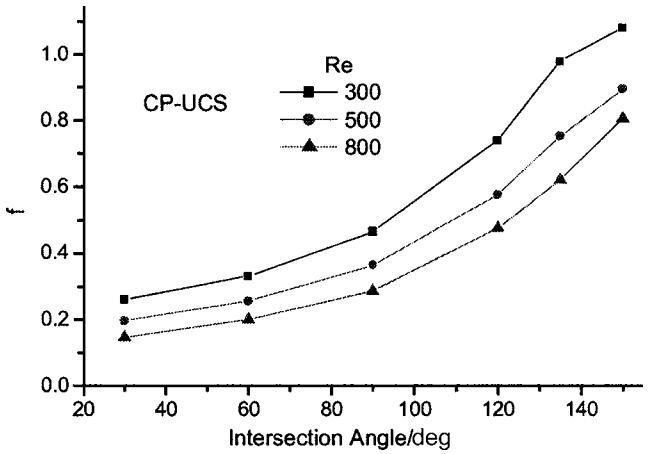

Fig. 17 Variation of *f* with intersection angle in the UCS channel for different Reynolds numbers

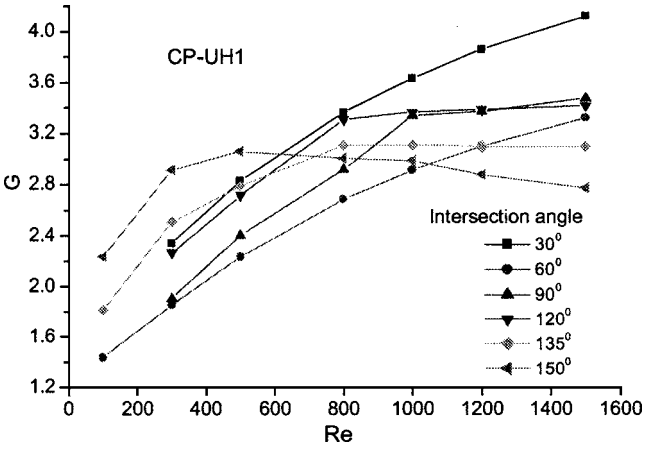

Fig. 18 Goodness factor *G* over Reynolds number with different intersection angles for CP-UH1

Conclusions

This study performs a three-dimensional numerical investigation on the heat transfer and pressure drop characteristics of the corrugated-undulated channel under laminar flow condition. The numerical prediction yields the following results:

The average *Nuu* and *Nuc* along the main flow direction consecutive cells for different geometries and intersection angles show that entry effects can be significant, however they mainly affect the first few cells and eventually the fully developed flow and thermal conditions are attained in the seventh channel.

The *Nuu* and *Nuc* are found to correlate positively with Reynolds number. The changes of *Nuu* and *Nuc* with θ represent different traits that are different with different geometries. The *Nuu* as well as the *Nuc* of the CP-UCS ($P/H=4.0$) increases with increasing θ. But the changes of *Nuc* for CP-UH1 ($P/H=4.206$) and CP-UP1 ($P/H=7.181$) with θ do not show a clear trend. The *Nuc* is smallest on 60 deg wall surface for $\theta \leq 90$ deg, while for $\theta > 90$ deg the minimal *Nuc* is obtained on 150 deg wall surface.

The local Nusselt number distributions show that the minimum Nu is situated at the four contact points where the top plate touches the bottom one; and the maximum values of Nu occur in a limited region located upstream of the crest of the conjugate channel. Low Nu is observed in the whole central corrugated (furrow) region, but it shifted to one side close to the inlet neighborhood of the conjugate duct on the undulated plate.

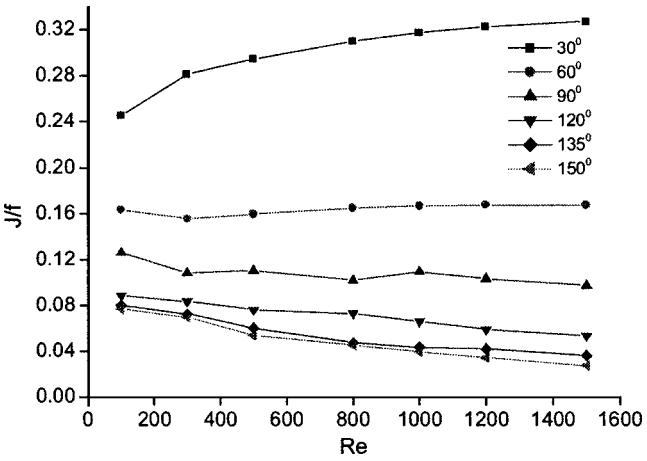

Fig. 19 The area goodness factor variation with intersection angles for CP-UH1

The friction factor f decreases with increasing Re. The change of f with θ differs with different geometries and different ranges of θ. For $\theta \leq 90$ deg, friction factors are increased with increasing θ for all geometries. For $\theta > 90$ deg, the effect of θ on f is very small for a large P/H (CP-UP1) channel; but f increases with increasing θ for the small P/H channels (CP-UH1 and CP-UCS).

The dependence of G upon Re and θ is faint. For all cases, G is larger than 1 with a straight channel having a square cross section as reference. The area goodness factor decreases with increasing θ and the change is more pronounced in the range of $\theta < 90$ deg than $\theta > 90$ deg. The 30 deg geometry channel has optimal flow area goodness, i.e., a small flow area of the heat exchanger.

Acknowledgment

The research was supported by the Hi-Tech Research and Development Program of China from 2003 to 2005 through its project on "the R&D of 100 kW Microturbine and Cogeneration System (2002AA503020)."

Nomenclature

Latin Symbols

A_c = cross section of unitary cell
A_d = heat transfer surface area
C_p = specific heat
D_e = equivalent diameter, $4V/A_d$
f = friction factor
H = external height of corrugation
H_i = internal height of corrugation
ΔL = extent of unitary cell along the main flow direction
$\dot{m}$ = mass flow rate in unitary cell
Nu = average Nusselt number
Nu_x = local Nusselt number
P = pitch of corrugation or undulation
$|\Delta \mathrm{P}|$ = pressure drop in unitary
Re = Reynolds number, $u_{av}D_e/\nu$
Pr = Prandtl number ($\mu^* Cp/\lambda$)
q_w = local wall heat flux
$\langle q_w \rangle$ = average wall heat flux
S = plate thickness [m]
T = temperature
T_f = fluid volume average temperature
u_{av} = average velocity, $G/\rho A_c$
u_i, u_k = velocity components
V = internal volume of unitary
x_i, x_k = generic variable

Greek Symbols

θ = intersection angle between corrugated and undulated plate
ρ = density of air
λ = fluid thermal conductivity
μ = dynamic viscosity
ν = kinematics viscosity

Subscripts

c = cross section
e = equivalent
f = fluid
i,k = indices of vector/internal p constant pressure
w = wall
x = local value

References

[1] Utriainen, E., and Sunden, B., 2002, "Evaluation of the Cross Corrugation and Some Other Candidate Heat Transfer Surface for Microturbine Recuperators," ASME J. Eng. Gas Turbines Power, **124**(4), pp. 550–560.

[2] Wirtz, R. A., Huang, F., and Greiner, M., 1999, "Correlation of Fully Developed Heat Transfer and Pressure Drop in a Symmetrically Grooved Channel," ASME J. Heat Transfer, **121**(1), pp. 236–239.
[3] Stasiek, J., Collins, M. W., Ciofalo, M., and Chew, P. E., 1996, "Investigation of Flow and Heat Transfer in Corrugated Passages—I. Experimental Results," Int. J. Heat Mass Transfer, **39**(1), pp. 149–164.
[4] Ciofalo, M., Stasiek, J., and Collins, M. W., 1996, "Investigation of Flow and Heat Transfer in Corrugated Passages—II. Numerical Simulations," Int. J. Heat Mass Transfer, **39**(1), pp. 165–192.
[5] Yin, J. X., Li, G. G., and Feng, Z. P., 2005, "The Effects of the Corrugation Angle on Flow and Heat Transfer in Cross Corrugation Channels With Sinusoidal Wave," ASME Paper No. GT2005-68282.
[6] Focke, W. W., Zachariades, J., and Olivier, I., 1985, "The Effect of the Corrugation Inclination Angle on the Thermohydraulic Performance of Plate Heat Exchangers," Int. J. Heat Mass Transfer, **38**(8), pp. 1469–1479.
[7] Muley, A., and Manglik, R. M., 1999, "Experimental Study of Turbulent Flow Heat Transfer and Pressure Drop in a Plate Heat Exchanger With Chevron Plates," ASME J. Heat Transfer, **121**(1), pp. 110–117.
[8] Blomerius, H., Holsken, C., and Mitra, N. K., 1999, "Numerical Investigation of Flow Field and Heat Transfer in Cross-Corrugated Ducts," ASME J. Heat Transfer, **121**(2), pp. 314–321.
[9] Blomerius, H., and Mitra, N. K., 2000, "Numerical Investigation of Convective Heat Transfer and Pressure Drop in Wavy Ducts," Numer. Heat Transfer, Part A, **37**, pp. 37–54.
[10] Stasiek, J. A., 1998, "Experimental Studies of Heat Transfer and Fluid Flow Across Corrugated-Undulated Heat Exchanger Surfaces," Int. J. Heat Mass Transfer, **41**(6-7), pp. 899–914.
[11] Ciofalo, M., Piazza, I. Di., and Stasiek, J. A., 2000, "Investigation of Flow and Heat Transfer in Corrugated-Undulated Plate Heat Exchangers," Heat Mass Transfer, **36**(5), pp. 449–462.
[12] Patanker, S. V., Liu, C. H., and Sparrow, E. M., 1977, "Fully Developed Flow and Heat Transfer in Ducts Having Streamwise-Periodic Variations of Cross-Sectional Area," J. Heat Transfer, **99**, pp. 180–186.
[13] Cowell, T. A., 1990, "A General Method for the Comparison of Compact Heat Transfer Surfaces," J. Heat Transfer, **112**, pp. 288–294.
[14] Utriainen, E., 2001, "Investigation of Some Heat Transfer Surface for Gas Turbine Recuperators," Ph.D. thesis, Department of Heat and Power Engineering, Lund Institute of Technology, Sweden.

Comparison of Various Methods for Simultaneous Retrieval of Surface Emissivities and Gas Properties in Gray Participating Media

M. Deiveegan
Research Scholar

C. Balaji
Associate Professor

S. P. Venkateshan[1]
Professor
e-mail: spv@iitm.ac.in

Heat Transfer and Thermal Power Laboratory,
Department of Mechanical Engineering,
Indian Institute of Technology Madras,
Chennai - 600 036, India

An inverse radiation analysis for simultaneous estimation of the radiative properties and the surface emissivities for a participating medium in between infinitely long parallel planes, from the knowledge of the measured temperatures and heat fluxes at the boundaries, is presented. The differential discrete ordinate method is employed to solve the radiative transfer equation. The present analysis considers three types of simple scattering phase functions. The inverse problem is solved through minimization of a performance function, which is expressed by the sum of squares of residuals between calculated and observed temperatures and heat fluxes at the boundaries. To check the performance and accuracy in retrieval, a comparison is presented between four retrieval methods, viz. Levenberg-Marquardt algorithm, genetic algorithm, artificial neural network, and the Bayesian algorithm. The results of the present analyses indicate that good precision in retrieval could be achieved by using only temperatures and heat fluxes at the boundaries. The study shows that the radiative properties of medium and surface emissivities can be retrieved even with noisy data using Bayesian retrieval algorithm and artificial neural network. Also, the results demonstrate that genetic algorithms are not efficient but are quite robust. Additionally, it is observed that an increase in the error in measurements significantly deteriorates the retrieval using the Levenberg-Marquardt algorithm.
[DOI: 10.1115/1.2227037]

Keywords: inverse radiation problem, parameter estimation, discrete ordinate method, Levenberg-Marquardt algorithm, genetic algorithm, artificial neural network, Bayesian algorithm

Introduction

The inverse analysis of radiation in a participating medium has a broad range of engineering applications, for example, remote sensing of the atmosphere, determination of the radiative properties of a medium, and the prediction of temperature distribution in combustion chambers, and so on. The inverse radiation problem considered here is concerned with a simultaneous estimation of the absorption, scattering coefficients, and surface emissivities for three types of scattering phase functions, in a plane-parallel slab, by utilizing the simulated, measured temperatures, and heat fluxes at the boundary.

In the forward problem the boundary conditions and the radiative properties of walls and medium are given and the temperature profile and heat fluxes at the boundaries are to be determined. The governing equation for describing the radiation intensity field in an absorbing, emitting, and scattering medium is the radiative transfer equation (RTE) [1], which is of the integro-differential type. In the present work the discrete ordinate method (DOM) [1–5] is employed to solve steady state radiative transfer in a participating medium. In the category of accurate radiative transfer algorithms, the DOM can provide the most flexible trade-off between precision and computation time [5]. In the discrete ordinate method, the general radiative transfer relations are represented by a discrete set of equations for the average intensity over a finite number of ordinate directions. Integrals over solid angles are replaced by a quadrature sum, which uses a set of the discrete ordinate directions and the corresponding weights. In the present work, the double Gauss quadrature rule is used to transform the integro-differential equation into a system of coupled first order ordinary differential equations with boundary conditions at the two end points, which can be solved by using readily available standard software routines.

A lot of work has been reported on the inverse analysis in participating medium [6–15] and estimation of radiative properties. Inverse radiation problems that deal with the prediction of the temperature distribution or source term in a medium from radiation measurements have been reported by many researchers [6–8]. Simultaneous estimation of optical thickness, single scattering albedo, and the coefficients of phase function for plane-parallel medium were also investigated [9,10]. The inverse analysis for the estimation of wall emissivities has been reported in Liu et al. [12]. Franca et al. [14] addresses various available methods for solving inverse problems in radiative transfer with participating media. The reviews by McCormick [15] reveal that most of the analysis of inverse radiation requires the knowledge of the moments of incident and emerging radiation at the boundaries, which are generally difficult to measure in practical applications. Although several techniques are available for the solutions of the radiation heat transfer problems, the radiative properties of the medium, such as the single scattering albedo, the extinction coefficient are uncertain. In this paper, the implementation of four inverse methods—Levenberg-Marquardt method (LMM), genetic algorithm (GA),

[1]Corresponding author.

Contributed by the Heat Transfer Division of ASME for publication in the JOURNAL OF HEAT TRANSFER. Manuscript received June 24, 2005; final manuscript received January 20, 2006. Review conducted by Walter W. Yuen.

artificial neural network (ANN), Bayesian algorithm, is presented to compare their accuracy, computational economy in the retrieval, for three types of scattering phase functions.

The convergence of the Levenberg-Marquardt method [16,17] for ill-posed problems has been proven by Hanke [18] and Hendricks and Howell [10]. The Levenberg-Marquardt method can be thought of as a combination of the steepest descent and the Gauss-Newton method. When the current solution is far from the correct one, the algorithm behaves like the steepest descent method: Slow, but guaranteed to converge. When the current solution is close to the correct solution, it becomes a Gauss-Newton method. The applicability of the conventional LMM for ill-posed problems is still an open research topic.

Genetic algorithms [19,20] are the search methods that combine the concept of survival-of-the-fittest among string patterns with a regulated yet randomized information exchange. Li and Yang [11] applied genetic algorithms to solve the inverse problem for simultaneously determining the single scattering albedo, the optical thickness and the phase function, from the knowledge of the exit radiation intensities.

In recent years, there has been a growing tendency to use data-driven approaches such as ANN to complement or even replace deterministic knowledge-based models. The use of ANN is particularly useful when the physical world is not fully defined, when the model has many uncertainties (model coefficients and/or input parameters), and when there is extensive data for training the network. Results of Tsintikidis et al. [21] showed that ANN gives better results when compared with regression models for atmosphere problems. The commonly used feed forward multilayer perceptron networks [22] are employed for training the ANN. Predictions made based on the simulated data, proves that the ANN prediction follows the observed trends quite well for both the training and testing data. The trained ANN is then used to retrieve the parameters.

In Bayesian inference, a prior distribution model is combined with the likelihood to formulate the posterior probability density function [23–25]. The Bayesian inference approach provides a complete probabilistic description of the unknown quantities given all related observations. The method regularizes the ill-posed inverse problem through prior distribution modeling [23] and in addition provides means to estimate the statistics of uncertainties. Sivia [24] gives a very good summary and practical applications of the Bayesian approach.

In the present work, the radiative properties of the medium and both surface emissivities are estimated simultaneously by inverse analysis, from the knowledge of temperature and heat flux at boundaries of a plane-parallel medium. Measured data are generated by adding random errors to the solutions to the forward problem. To assess the accuracy of predictions, a statistical analysis is made to establish the error bar for inverse solution. Error bars are useful not only for estimating the accuracy of predictions, but also determine whether any corrective measures are needed to improve the precision of prediction.

Analysis

The one-dimensional geometry used in the present analysis consists (Fig. 1) of two parallel, isothermal, diffuse, infinitely large plates separated by absorbing, emitting, scattering, gray medium that is in radiative equilibrium. The top and bottom plates are at temperatures T_t, T_b, having emissivities ϵ_b, ϵ_t, respectively, and are separated by distance L. The analysis of this inverse problem involves the following two basic steps: (a) The direct problem; (b) the inverse problem; these steps are described below.

The Direct Problem. The direct problem of concern here is to find the temperature profile and heat fluxes at the boundaries. In the present work the differential discrete ordinate method [4] is used to solve the direct problem. The equation of transfer for

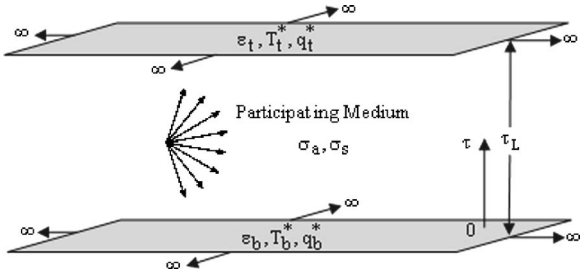

Fig. 1 Schematic of the physical model

azimuthally symmetric radiation in an absorbing, emitting, and scattering gray medium between plane parallel plates can be written [1] as

$$\mu\frac{\partial I(z,\mu)}{\partial z} = \sigma_a I_B[T(z)] - (\sigma_a + \sigma_s)I(z,\mu) + \frac{\sigma_s}{2}\int_{\mu'=-1}^{1} I(z,\mu')\Phi(\mu' \to \mu)d\mu' \tag{1}$$

where, I is the total intensity at an optical depth τ in the direction μ. Φ is the scattering phase function for azimuthally symmetric radiation. The one-dimensional domain is sub divided into N control volumes of length Δz in the z direction and the governing equations are evaluated for a discrete number of ordinate directions $2M$ and the integrals are replaced by a numerical quadrature [1] as follows:

$$\mu_i\frac{dI_i(\tau)}{d\tau} = -I_i(\tau) + (1-\tilde{\omega})I_B[T(\tau)] + \frac{\tilde{\omega}}{2}\sum_{j=1}^{2M} w_j I_j \Phi(\mu_j \to \mu_i) \tag{2}$$

where μ_i's are the quadrature points between −1 and +1 corresponding to a $2M$ order quadrature, and w_i's are the corresponding weights. For the case of radiative equilibrium I_B is given by

$$I_B[T(\tau)] = \frac{1}{2}\sum_{j=1}^{2M} w_j I_j(\tau) \tag{3}$$

Substituting the above expression into Eq. (2) yields a system of $2M$ first order ordinary differential equations. In matrix form

$$\frac{dI}{d\tau} = [A]I + B \tag{4}$$

where

$$A_{ij} = \frac{\delta_{ij}}{\mu_i} + \frac{\tilde{\omega}}{2\mu_i}w_j\Phi \tag{5}$$

$$B_i = \frac{(1-\tilde{\omega})}{2\mu_i}\sum_{j=1}^{2M} w_j I_j \tag{6}$$

The Jacobian of Eq. (4) is given by

$$\frac{\partial}{\partial I_j}\left[\frac{dI_i}{d\tau}\right] = A_{ij} \tag{7}$$

The boundary conditions for DOM are generated by expressing the intensity leaving the surface along ordinate direction M as the sum of emitted and reflected intensities. Out of $2M$ different intensities half originate from the bottom plate at $\tau=0$ (with $\mu_i > 0$), and the other half from the top plate at $\tau=\tau_L$ (with $\mu_i < 0$). Upward intensities (with $\mu_i > 0$) are used to find irradiation at the top plate, similarly the downward intensities (with $\mu_i < 0$) are used to find irradiation at bottom plate. At boundary $\tau=0$, it is

$$I_i(0) = \frac{\sigma T_b^4}{\pi} - 2\frac{(1-\varepsilon_b)}{\varepsilon_b}\sum_{j=1}^{M} w_j \mu_j I_j(0) \tag{8}$$

Similarly, at boundary $\tau = \tau_L$

$$I_i(\tau_L) = \frac{\sigma T_t^4}{\pi} + 2\frac{(1-\varepsilon_t)}{\varepsilon_t}\sum_{j=M+1}^{2M} w_j \mu_j I_j(\tau_L) \tag{9}$$

The temperature distribution is given by

$$T(\tau) = [\pi I_B(\tau)/\sigma]^{1/4} \tag{10}$$

The nondimensional heat flux is written as

$$q(\tau)^* = q(\tau)/\{\sigma(T_b^4 - T_t^4)\} \tag{11}$$

where the heat flux is given by

$$q(\tau) = \sum_{j=1}^{2M} w_j \mu_j I_j(\tau) \tag{12}$$

The present methodology uses the Gauss quadrature scheme of discrete ordinates to reduce the radiative transfer equations into a set of first order differential equations. The overall solution procedure for DOM is as follows:

(1) Compute Gauss quadrature points and weights;
(2) compute initial intensity field (from assumed temperature profile);
(3) calculate A and B according to Eqs. (5) and (6) (updated with every iteration);
(4) calculate the Jacobian matrix for Eq. (4) (updated with every iteration);
(5) solve the system of first order differential equations with two point conditions for intensity using DBVPFD (IMSL-FORTRAN) subroutine [26];
(6) calculate I_B using Eq. (3);
(7) calculate the temperature distribution from I_B, Eq. (10);
(8) calculate nondimensional flux using Eqs. (11) and (12).

The present scheme requires simple mathematics to set up equations and utilize the subroutine to solve the resultant system of equations. This commercially available DBVPFD (IMSL-FORTRAN 90) subroutine [26] has already been heavily tested for numerical accuracy and stability.

The scattering phase functions considered in the present analysis are as follows [27]:

Type 1: Phase function for the case of scattering of unpolarized incident radiation from a small sphere with refractive index tending to infinity

$$\Phi(\beta) = \tfrac{3}{5}\left[\left(1 - \tfrac{1}{2}\cos\beta\right)^2 + \left(\cos\beta - \tfrac{1}{2}\right)^2\right] \tag{13}$$

Type 2: Rayleigh scattering: $\Phi(\beta) = \frac{3}{4}(1 + \cos^2\beta)$ (14)

Type 3: Isotropic scattering: $\Phi(\beta) = 1.0$ (15)

Inverse Problem. The inverse radiation problem considered here is concerned with simultaneous estimation of the absorption, scattering coefficients and the surface emissivities, in a plane-parallel slab of optical thickness τ_L, by utilizing the simulated, measured temperatures and heat fluxes at the two boundaries. Assuming that the model is an accurate representation of the system, the measurements will differ from simulated data by measurement noise; the effect of noise is taken into account artificially as in the following equation:

$$y_i = Z_i + \sigma_{st,i}\xi \quad i = 1,2,3,4 \tag{16a}$$

Where σ_{st} is a standard deviation of measurement which is assumed to be same for all the measurements, and ξ is a standard normal distribution random number. Thus, the probability that ξ is included between −2.576 and 2.576 is 99%. The standard deviations of these parameters, σ_{st}, is chosen as

$$\sigma_{st,i} = \frac{Z_i \times \eta\%}{2.576} \tag{16b}$$

Levenberg-Marquardt Method. The formulation of the inverse problem considered here is similar to that for the direct problem, except that the absorption, scattering coefficients and two surface emissivities are unknown. Instead, measured temperature and heat flux at both surfaces of the plate (Y_i), are assumed to be available. Then the inverse problem consist of utilizing the measured data (Y_i) to determine the four elements of the unknown vector X defined as

$$R = \sum_{i=1}^{4} (y_i - Z_i(x_i))^2 = F^T F \tag{17}$$

where Z_i is the simulated data and F_i is the difference between the measured and simulated values. All of the arguments of X will be referred to as parameters. To minimize the norm R, the above equation is differentiated with respect to each of the unknown parameters $X = \{\kappa, \sigma_S, \epsilon_b, \epsilon_t\}$ to yield

$$\frac{\partial R}{\partial X} = \frac{\partial (F^T F)}{\partial X} = 0 \tag{18}$$

In this equation, the vector F is expanded in a Taylor series, and only the first order terms are retained. To improve convergence of the solution of the resulting system of equations, a damping parameter λ is added to yield the Levenberg-Marquardt algorithm [17]

$$(\zeta^T \zeta + \zeta\lambda)\Delta X = \zeta^T F \tag{19}$$

where ζ is the identity matrix and ζ_{ij} are the elements of the Jacobian matrix, i.e.,

$$\zeta_{ij} = \frac{\partial Z_i}{\partial X_j}; \quad i,j = 1,2,3,4 \tag{20}$$

Here $\partial Z_i / \partial X_j$ represents the sensitivity coefficient which is a measure of how the solution of a direct problem is affected by a change in any particular parameter. The iterative procedure starts with an initial guess for the vector of unknowns, X^0. Then the variation ΔX^k, at iteration level k, defined by

$$\Delta X^k = X^{k+1} - X^k \tag{21}$$

is calculated from Eq. (19), now written in a form suitable for iterative calculations

$$\Delta X^k = [(\zeta^k)^T \zeta^k + \zeta\lambda^k]^{-1} (\zeta^k)^T F^k \tag{22}$$

yielding the new estimated value for the unknowns

$$X^{k+1} = X^k + \Delta X^k \tag{23}$$

The iterative procedure of sequentially calculating ΔX^k and X^{k+1} from Eqs. (22) and (23), is continued until the convergence criteria

$$\Delta X_j^k < \varepsilon_c = 10^{-5} \quad \text{for } j = 1,2,3,4 \tag{24}$$

is satisfied.

Genetic Algorithm. The objective function without constraints is given by Eq. (17). Here, the optimization is carried out using GA. Since GA works with only maximization problems, the objective function is modified as

$$r = 1/(1 + R) \tag{25}$$

GA is a robust parameter search technique based on the mechanics of natural genetics and natural selection. Unlike calculus-based methods, GA does not depend on the existence of derivatives or on the initial values. Traditional optimization algorithms will con-

verge to the minimum only if the objective function has only one well defined minimum. Since the present objective function is highly nonlinear and multimodal, a traditional optimization algorithm as, for example, the sequential quadratic programming is used to validate the complexity of the objective function and it is found that the results converge to a local minimum based on the initial guess values. Thus GA, which is very attractive and used for applications where the objective function is highly nonlinear and multimodal, is employed for the process of optimization. GA works iteration (generation) by iteration, successively generating and testing a population of strings. In the first generation, an initial population, which is a set of individuals (design parameters) each of which is represented in binary-coded strings, is randomly generated within the range of parameters. After evaluating the fitness of each individual, fitter individuals are selected for reproducing offsprings for the next generation. The selection process is determined by the objective function values. Some of the selected individuals are chosen to find mates and undergo the crossover operation, which is a reproduction process that makes offsprings by exchanging their genes to improve the fitness of the next generation. Then, some of the offsprings are chosen for the operation of mutation that preserves the diversity of a population, while searching the design space that cannot be represented with the present population by changing some of the genes of selected individuals within the range of the design space. Because there is no guarantee that GA will produce a monotonic improvement in the objective function value with variance of generation, due to its stochastic nature, an elitist strategy is used to ensure a monotonic improvement by copying the best individual of the present generation on to the next generation. Once the first generation is completed, the iterations will not stop until a satisfactory solution is reached. The highlights of the GA code [28] used in the present study are (i) in the reproduction phase, fitter individuals are selected using tournament selection operator (ii) uniform crossover operator is used (iii) instead of mutation, micro-GA is implemented. Here, the bits of the best fitness parameter set are compared with corresponding bits of all other parameter sets, and if the number of bits which are different from the best parameter set are less than 5% of the total number of bits present in the total population, then the algorithm considers the population as converged and retains only the best fitness parameter set and replaces all other parameter sets with a new parameter set created, randomly as was done in the first step. Hence the micro-GA implementation will not occur in every generation, but only if this condition arises.

Artificial Neural Network. Applications of neural networks have two distinct phases: Training and simulation. In the training phase, many pairs of inputs and outputs are shown to the network and the weights within the network are adjusted until the network produces the desired output. In the simulation phase, the training algorithm is deactivated, and the network merely computes the output based on the given inputs.

In this study, feed-forward multilayer perceptron networks are employed for training the ANN. These networks are widely used due to their simplicity and excellent performance [22]. A network with four inputs and four outputs is created, and two hidden layers with 40 neurons each is employed. Already available data set of 20,000 profiles along with radiative properties of medium and surface emissivities are used to train the network. Figure 2 shows the layout of the network used in the present study. The left most layer in the Fig. 2 corresponds to the input variable. All the input variables are normalized with respect to their maximum possible values, to ensure that the range of all the variables lie in the same range of the activation function used for each node in the neural network and hence helps in the process of reducing the effort to link the input and output values in the ANN. This also helps in reducing some effort needed to code the variable limits in the optimization analysis, which is used for solving the inverse problem in the current study. In this study, the number of hidden layers

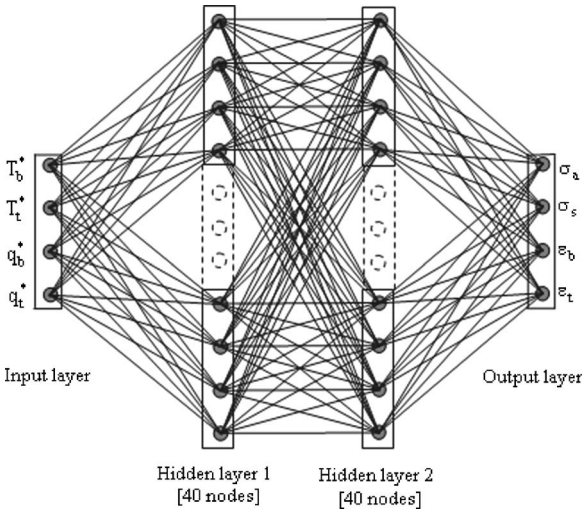

Fig. 2 A two hidden layer feed-forward neural network architecture

used is two, and 40 nodes are placed in each hidden layer. The rightmost nodes in the network give the retrieval parameters corresponding to the input temperatures and heat fluxes at boundaries. The above configuration of the network is selected based on the performance of the network that predicts the parameters well in comparison with that of other configurations.

Bayesian Retrieval Algorithm. The Bayesian retrieval algorithm uses a database of precalculated temperatures and heat fluxes for many possible values of radiative properties of medium and emissivities of surfaces, and integrates over the points in the database with the Bayes theorem. Bayesian inversion methods formally add prior information to that provided by the measurements to obtain a well posed retrieval and corresponding uncertainty estimate [24]. The Bayes theorem can be stated mathematically for the retrieval problem as

$$p_{\text{post}}(x|y) = \frac{p_f(y|x)p_{pr}(x)}{\int p_r(y|x)p_{pr}(x)dx} \tag{26}$$

where x represents the state vector $(\kappa, \sigma_s, \epsilon_b, \epsilon_t)$ and y represents the vector of observations (temperatures and heat fluxes at the boundaries). $p_p(x)$ is the prior probability density function (PDF) of the state x, $p_f(y|x)$ is the conditional probability density function of the measurements given the state vector, and $p_{\text{post}}(x|y)$ is the posterior probability density function of the state vector. The prior PDF represents our knowledge of the parameters.

The retrieved parameter x_{ret} is calculated by integrating over the posterior PDF to find the mean state

$$x_{\text{ret}} = \frac{\int x p_f(y|x)p_{pr}(x)dx}{\int p_r(y|x)p_{pr}(x)dx} \tag{27}$$

This is a Monte Carlo integration because the database points are chosen randomly. In practice, this integral is replaced by a sum over the cases in the database. One advantage of the Bayesian framework is that the uncertainties in retrieved parameters are naturally defined by the variance of the posterior PDF

Table 1 Validation of the DOM solutions for isotropic scattering for a plane medium

ϵ_b	ϵ_t	τ_L	q*(Exact) [29]	q*(DOM) [Present]	Percent Error[a]
1.0	1.0	0.1	0.9157	0.9160	0.031
		1.0	0.5532	0.5535	0.054
		2.0	0.3900	0.3901	0.025
		5.0	0.2077	0.2076	−0.048
0.8	1.0	0.1	0.7451	0.7455	0.045
		1.0	0.4859	0.4863	0.057
		3.0	0.2804	0.2805	0.032
0.8	0.5	0.1	0.4269	0.4271	0.025
		1.0	0.3271	0.3272	0.037
		3.0	0.2190	0.2190	0.009
0.8	0.1	0.1	0.0967	0.0967	0.002
		1.0	0.0904	0.0905	0.011
		3.0	0.0796	0.0796	0.012

[a]Percent Error = (Present − Exact) / Exact × 100.

$$\sigma_x^2 = \frac{\int (x - x_{\text{ret}})^2 p_f(y|x) p_{pr}(x) dx}{\int p_r(y|x) p_{pr}(x) dx} \tag{28}$$

where σ_x is the one sigma error bar in x and x_{ret} is the mean x of the posterior PDF.

The conditional PDF $p_f(y|x)$ is the probability density of the measurement vector given an state vector. The forward PDFs of the measurement vector are normally distributed about the simulated vector for each observation.

$$p_f(y|x) = \prod_{j=1}^{4} \frac{1}{\sqrt{2\pi\sigma_j^2}} \exp\left[- \frac{(y_j - Z_j(x))^2}{2\sigma_j^2} \right], \tag{29}$$

where y_j is the jth channel in the measurement vector, $Z_j(x)$ is the radiative transfer simulation for channel j, and σ_j is the standard deviation for channel j. This formulation assumes that the uncertainty in each channel is independent of the other channels, which is a good assumption for random measurement noise, but may be less viable for representing the radiative transfer modeling error. It is assumed that the uncertainty σ_j is due to the measurement errors. Since the conditional distribution is effectively zero if the measurement vector is far from the observed one, the Bayesian algorithm interpolates between those points in the database that are reasonable matches to the observations.

The prior probability distribution is a way of introducing other known information about the parameters. If a inversion is not completely well posed, then the addition of a priori information can serve as a constraint. In addition, the prior distribution gives a good indication of how to choose the random cases for the database. In fact, by choosing the database points in parameter space x_i distributed according to the prior PDF, the Monte Carlo integration simplifies to

$$x_{\text{ret}} = \frac{\sum_i x_i p_f(y|x_i)}{\sum_i p_f(y|x_i)} \tag{30}$$

The sums in the Bayesian retrieval algorithm span all points in the database. Including all the database points wastes computation time calculating the conditional PDF for points where the PDF is effectively zero, (i.e., where the measurement is far from that of the database case). The conditional PDF is the product of exponentials, and, thus, is also the exponential of χ^2

$$x_{\text{ret}} = \frac{\sum_i x_i \exp\left[- \frac{1}{2}\chi_i^2 \right]}{\sum_i \exp\left[- \frac{1}{2}\chi_i^2 \right]}; \quad x_i \text{ from } p_p(x) \tag{31}$$

where χ^2 is a measure of the difference between the measurement vector and database simulated vector

$$\chi^2 = \sum_{j=1}^{4} \left(\frac{y_j - Z_j}{\sigma_{\text{st},j}} \right)^2 \tag{32}$$

One way to speed up the Bayes integration is to stop the χ^2 summation and not calculate the posterior PDF when the χ^2 exceeds a maximum, user specified value, $\chi^2 > \chi^2_{\max}$. In the present work $\chi^2_{\max} = 30$ is used.

Results and Discussion

For all of the cases, the parameters considered are $T_b = 373$ K, $T_t = 573$ K, $L = 1.0$ m, and grid sensitivity studies have been carried out. It is noted that the error monotonically reduces when the number of ordinate directions is increased. By noting the change in the solution as the number of ordinate directions increases (for a fixed number of control volumes) the rate of convergence is inferred and, therefore, the number of ordinate directions corresponding to desired accuracy is obtained. For the present problem numbers of ordinate directions 24 is sufficient since the corresponding relative error is approximately 0.1%. In addition, the optimum number of control volume was obtained, by fixing the number of ordinate directions and then varying the control volumes. Finally, grid sensitivity studies show that optimum number of directions and control volumes for the DOM are 24×32, respectively.

Validation. In order to validate the present codes of the DOM, several preliminary calculations were performed and compared with the exact solutions [29] available in literature for a one dimensional planar absorbing and emitting medium contained between black plates under radiative equilibrium (Table 1). Table 1 shows the nondimensional radiative heat flux (Eq. (11)) values for discrete ordinate methods in comparison with the exact solutions for various optical thicknesses for the case of isotropic scattering with gray and diffuse type boundaries. It can be observed that the result predicted by the DOM is in good agreement with the exact solution. In the aforementioned case, the largest error between the exact and the DOM is about 0.057%. The present DOM is clearly

Table 2 Results for the case of single layer of the participating medium using mode 1 type of scattering (Mean ± standard deviation)

η [%]	Actual value	σ_a, m^{-1} 0.75	σ_s, m^{-1} 0.25	ϵ_b 0.6	ϵ_t 0.9	CPU Time, s
0	LMM	0.7500	0.2500	0.6000	0.9000	1.80
	ANN	0.7495	0.2508	0.6019	0.9021	0.01
	GA	0.7503	0.2494	0.6001	0.9002	28.90
	BAYESIAN	0.7526	0.2499	0.5999	0.9021	0.64
0.1	LMM	0.7487±0.0066	0.2502±0.0008	0.5997±0.0013	0.9004±0.0025	1.84
	ANN	0.7484±0.0013	0.2520±0.0007	0.6055±0.0003	0.9072±0.0004	0.01
	GA	0.7426±0.0157	0.2533±0.0106	0.6010±0.0041	0.8977±0.0093	28.79
	BAYESIAN	0.7559±0.0016	0.2498±0.0008	0.5998±0.0005	0.9065±0.0004	0.65
1.0	LMM	0.7370±0.0657	0.2522±0.0078	0.5974±0.0126	0.9042±0.0255	1.81
	ANN	0.7453±0.0131	0.2530±0.0068	0.6052±0.0031	0.9076±0.0043	0.01
	GA	0.7351±0.0447	0.2375±0.0337	0.5918±0.0192	0.9075±0.0266	28.97
	BAYESIAN	0.7515±0.0162	0.2512±0.0076	0.5999±0.0046	0.9064±0.0041	0.64
2.0	LMM	0.7247±0.1311	0.2546±0.0157	0.5956±0.0251	0.9092±0.0510	1.94
	ANN	0.7420±0.0262	0.2541±0.0137	0.6049±0.0062	0.9080±0.0086	0.01
	GA	0.7231±0.1199	0.2397±0.0363	0.5893±0.0249	0.9134±0.0508	29.60
	BAYESIAN	0.7466±0.0315	0.2535±0.0150	0.6005±0.0086	0.9060±0.0082	0.65
5.0	LMM	0.6645±0.3241	0.2731±0.0473	0.5958±0.0631	0.9049±0.1002	1.71
	ANN	0.7324±0.0663	0.2576±0.0343	0.6041±0.0155	0.9090±0.0215	0.01
	GA	0.6956±0.3325	0.2613±0.0545	0.5934±0.0631	0.9116±0.0937	29.82
	BAYESIAN	0.7356±0.0702	0.2578±0.0338	0.6011±0.0174	0.9060±0.0201	0.66

accurate for all optical thicknesses.

To examine the effectiveness the methods presented in this paper, three test cases are considered.

Case 1: Participating Medium with Type 1 Scattering Phase Function (Eq.* (13)*)

Table 2 shows the mean values of the estimated parameter and the standard deviation for the four methods along with computational time, with and without measurement errors. All the computations have been performed on a PC equipped with Intel-3 GHz, Pentium-4 processor, 4 GB of RAM and Compaq visual FORTRAN version 6.1 compiler. When there is no measurement error considered, the LMM predict the parameters exactly, but other methods retrieve with small error. When the measurement errors are increased, the percentage error in the retrieval is larger for LMM compared to other retrieval methods considered in the present work. Inverse analyses were performed by using simulated measurements containing random errors varying from 0.1% to 5%. The estimates obtained by using measurement errors of 10% or more were not so good, hence such results are not presented here. For each perturbation level, 40 different sets of random numbers are generated and each set is added to the measurement vectors to give 40 different sets of input data [30].

The process of convergence for the Levenberg-Marquardt method is shown graphically in Fig. 3. The curves represent the absorption, scattering coefficients of the participating medium and surface emissivities for the case where the measurement vectors are taken without any perturbation. The method worked well even with poor initial guesses, and with input data containing significant measurement errors. A starting value of the damping parameter 0.0001 worked well for all cases considered here, and it was reduced from iteration to iteration according to the approach originally proposed by Marquardt [17].

In order to perform the retrieval using GA, ANN, Bayesian algorithm, bounds on the variables, i.e., range of the parameters are considered. In the present analysis absorption, scattering coefficients varied from 0.001 to 2.0 m^{-1} and emissivities varied from 0.05 to 1.0. All the parameters involved in the current study are normalized with respect to their maximum possible values, thus ensuring that the range of all variables gets fixed between 0 and 1. Figure 4 shows the minimization of residual with the number of generations for GA. The present GA analysis uses the following combinations of input for best performance: Population size of 8, probability of mutation of 0.02, probability of cross over of 0.5, and maximum number of generations is equal to 400.

To estimate parameters using ANN, the forward problem is solved for randomly chosen parameters with in the given range, and results are stored in database. Approximately, 20,000 profiles were generated by varying the parameters randomly, within the range considered; out of these 15,000 profiles are used to train the ANN and the remaining 5000 are used for validation purposes.

Bayesian approach avoids the direct solution of the inverse problem; instead the forward problem is solved repeatedly for large sets of input parameters. Generation of database of parameters and corresponding observations is the key element in the Bayesian algorithm. The first step in generating the database is to

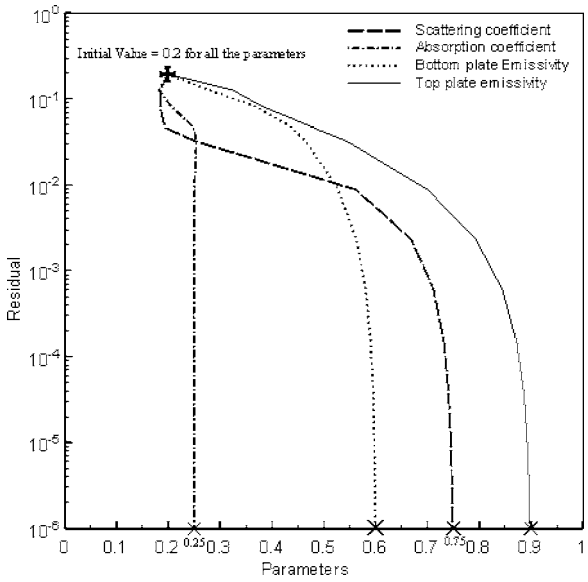

Fig. 3 Convergence of iteration procedure of Levenberg-Marquardt algorithm

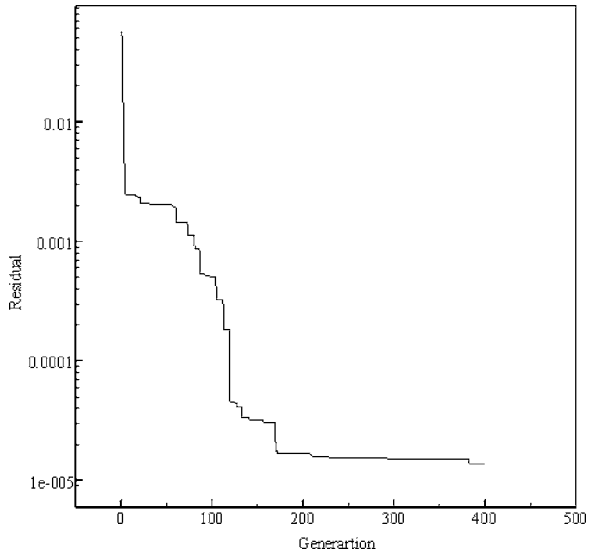

Fig. 4 Convergence history of GA for parameter retrieval in Mie scattering

create random profiles of absorption, scattering coefficient and emissivities. The distribution of these parameters is the prior information in the retrieval, so it is important that the profiles are realistic and completely cover the possible parameter range. In the present analysis 10^5 profiles are generated to form the database which takes a CPU time approximately of 4000 s. The Bayes theorem is used to combine a priori information about parameters with the forward model to select a physically likely profile that matches the observations.

Case 2: Participating Medium with Type 2 Scattering Phase Function (Eq. (14)***)***

Here, the problem remains the same as in the previous case, except that the type of scattering considered is different. Table 3 shows that, with no measurement error, the LMM predicts very accurately but the accuracy of the LMM decreases with the increase in the measurement error. It can be observed from the table that the genetic algorithm takes more time for convergence compared to other algorithms. Also, the genetic algorithm is not very accurate. When measurement errors increase, this method gives better estimates compared to the LMM. For a Raleigh type of scattering phase function, ANN requires 20,000 profiles for training and 5000 profiles for testing, which takes about 1200 s. Once the weights are converged, the ANN gives real time estimation of the parameters.

Case 3: Participating Medium with Type 3 Scattering Phase Function (Eq. (15)***)***

First of all, without measurement errors, the performances of all methods are investigated. It can be observed that for isotropic scattering phase function, all the methods failed to retrieve the absorption and scattering coefficients separately, but it is possible to retrieve the extinction coefficient which is the sum of absorption and scattering coefficients. Table 4 shows the effect of the measurement error on the estimated extinction coefficient and surface emissivities obtained from surface temperatures and heat fluxes. It is possible to demonstrate that the Bayesian retrieval algorithm gives a very good estimation of parameters, even for higher measurement errors compared to GA and LMM. The ANN gives the real time estimation of parameters with good accuracy but it requires time consuming data base creation and training.

Conclusions

An inverse method is presented for simultaneous estimation of absorption and scattering coefficient and surface emissivities for a participating medium between two parallel, diffuse, isothermal, infinitely large plates from the knowledge of temperatures and heat fluxes at the boundaries. The inverse problem is solved by using the four methods: The Levenberg-Marquardt algorithm, genetic algorithm, artificial neural network, and Bayesian algorithm. Noisy input data have been used to test the performance of the proposed methods. The results show that the parameters can be estimated with good accuracy using measured temperatures and heat fluxes only at the boundaries. Also, it is found that the increase in the error in the measurement reduces the accuracy in the retrieval of the Levenberg-Marquardt algorithm, and in order to reduce the errors of the inverse estimation, the measurement errors must be confined to an appropriate limit. Genetic algorithms are not efficient and time consuming but are quite robust, i.e., the optimization procedure will yield a near-global optimal solution. It is suggested that genetic algorithms be used when the traditional

Table 3 Results for the case of single layer of the participating medium using mode 2 type of scattering (Mean ± standard deviation)

η [%]	Actual value	σ_a, m^{-1} 0.75	σ_s, m^{-1} 0.25	ϵ_b 0.6	ϵ_t 0.9	CPU Time, s
0	LMM	0.7500	0.2500	0.6000	0.9000	7.81
	ANN	0.7491	0.2502	0.6025	0.9015	0.01
	GA	0.7450	0.2553	0.6010	0.8951	33.25
	BAYESIAN	0.7518	0.2511	0.6001	0.8997	1.62
0.1	LMM	0.7488 ± 0.0064	0.2500 ± 0.0014	0.5995 ± 0.0019	0.9003 ± 0.0021	7.58
	ANN	0.7487 ± 0.0018	0.2508 ± 0.0013	0.6065 ± 0.0004	0.9031 ± 0.0004	0.01
	GA	0.7415 ± 0.0171	0.2592 ± 0.0231	0.6012 ± 0.0005	0.8979 ± 0.0089	32.61
	BAYESIAN	0.7532 ± 0.0021	0.2524 ± 0.0016	0.6002 ± 0.0004	0.8987 ± 0.0005	1.57
1.0	LMM	0.7384 ± 0.0641	0.2503 ± 0.0142	0.5961 ± 0.0185	0.9037 ± 0.0212	7.52
	ANN	0.7467 ± 0.0180	0.2502 ± 0.0133	0.6060 ± 0.0042	0.9036 ± 0.0042	0.01
	GA	0.7328 ± 0.0532	0.2632 ± 0.0532	0.6032 ± 0.0012	0.9079 ± 0.0331	31.82
	BAYESIAN	0.7524 ± 0.0207	0.2506 ± 0.0160	0.5999 ± 0.0038	0.8992 ± 0.0046	1.52
2.0	LMM	0.7276 ± 0.1279	0.2507 ± 0.0287	0.5938 ± 0.0369	0.9080 ± 0.0425	7.56
	ANN	0.7446 ± 0.0358	0.2493 ± 0.0267	0.6054 ± 0.0084	0.9041 ± 0.0084	0.01
	GA	0.7289 ± 0.1251	0.2690 ± 0.0982	0.6049 ± 0.0089	0.9089 ± 0.0831	31.88
	BAYESIAN	0.7525 ± 0.0394	0.2476 ± 0.0311	0.5998 ± 0.0077	0.9000 ± 0.0093	1.56
5.0	LMM	0.7342 ± 0.3017	0.2135 ± 0.0939	0.6004 ± 0.0929	0.9090 ± 0.0913	7.01
	ANN	0.7392 ± 0.0882	0.2461 ± 0.0674	0.6034 ± 0.0208	0.9054 ± 0.0209	0.01
	GA	0.7198 ± 0.3256	0.2748 ± 0.1023	0.6070 ± 0.0103	0.9098 ± 0.0991	32.32
	BAYESIAN	0.7448 ± 0.0869	0.2440 ± 0.0681	0.5984 ± 0.0203	0.9034 ± 0.0227	1.51

Table 4 Results for the case of single layer of the participating medium using mode 3 type of scattering (Mean ± standard deviation)

η [%]		σ_e, m^{-1}	ϵ_b	ϵ_t	CPU Time, s
	Actual value	1.0	0.6	0.9	
0	LMM	1.0000	0.6000	0.9000	1.80
	ANN	0.9906	0.6019	0.8991	0.01
	GA	0.9897	0.6010	0.8979	25.90
	BAYESIAN	1.0023	0.6003	0.9011	1.18
0.1	LMM	0.9988±0.0063	0.5996±0.0017	0.9004±0.0021	1.09
	ANN	0.9831±0.0004	0.6051±0.0004	0.8979±0.0003	0.01
	GA	0.9861±0.0023	0.6011±0.0043	0.8967±0.0098	25.06
	BAYESIAN	1.0041±0.0010	0.6008±0.0003	0.9025±0.0003	1.06
1.0	LMM	0.9887±0.0631	0.5964±0.0164	0.9039±0.0213	1.14
	ANN	0.9818±0.0040	0.6046±0.0037	0.8985±0.0026	0.01
	GA	0.9812±0.0082	0.5919±0.0196	0.9075±0.0266	24.97
	BAYESIAN	1.0017±0.0105	0.6003±0.0031	0.9030±0.0028	1.03
2.0	LMM	0.9783±0.1257	0.5940±0.0328	0.9086±0.0427	1.16
	ANN	0.9798±0.0085	0.6040±0.0075	0.8992±0.0052	0.01
	GA	0.9725±0.0126	0.5897±0.0226	0.9139±0.0535	25.60
	BAYESIAN	0.9989±0.1138	0.5998±0.0063	0.9035±0.0057	1.10
5.0	LMM	0.9444±0.3089	0.5923±0.0846	0.9107±0.0876	1.11
	ANN	0.9696±0.0254	0.6024±0.0186	0.9012±0.0130	0.01
	GA	0.9702±0.0725	0.5914±0.0643	0.9126±0.0938	24.82
	BAYESIAN	0.9898±0.0562	0.5980±0.0165	0.9052±0.0145	1.05

optimization methods fail, or are difficult to apply. It can be observed that the Bayesian retrieval algorithm and artificial neural network are robust and yield accurate parameter estimation even when noise is present in the observations. The Bayesian algorithm combines prior information about properties with radiative transfer simulations to retrieve parameters. The retrieved parameter vector is the mean of the posterior probability density function. A large precalculated database of randomly chosen properties and corresponding simulated surface temperatures and heat flux is input to the algorithm. The technique efficiently integrates over only those database points that are close to the observed temperatures and heat fluxes, resulting in fast retrievals that are also accurate. The present inverse problem can be extended to multilayer radiative problems involved in the retrieval of atmospheric parameters simultaneously from satellite data.

Nomenclature

A = elements of the Jacobian matrix A
B = elements of the vector B
I = radiation intensity, W/m^2
L = length of the domain, m
M = half order of the Gauss quadrature
N = number of control volumes
q = heat flux, W/m^2
R = sum of square of residuals
T = temperature, K
w = weights for Gauss quadrature
x = vector of unknowns
y = measurement vector
Z = simulated results
z = Cartesian coordinate

Greek Symbols

β = scattering angle from the forward direction ($\pi - 2\times$polar angle), rad
Δz = control volume thickness, m
δ_{ij} = Dirac delta function
ϵ = emissivity of the surface
ϵ_c = tolerance for the stopping criteria
ζ = identity matrix
η = measurement error
λ = damping parameter
ξ = normally distributed random number
μ = direction cosine
σ = Stefan-Boltzmann constant, 5.67×10^{-8} W m^{-2} K^{-4}
σ_a = absorption coefficient, m^{-1}
σ_e = extinction coefficient, m^{-1}
σ_s = scattering coefficient, m^{-1}
τ = optical depth
Φ = scattering phase function
$\tilde{\omega}$ = single scattering albedo
Ω = solid angle, steradian

Subscripts

o = coordinate origin
B = blackbody
b = bottom plate
L = length of the plane parallel medium
ret = retrieved
st = standard deviation
t = top plate

Superscripts

$*$ = nondimensional

References

[1] Chandrasekhar, S., 1950, *Radiative Transfer*, Oxford University Press, London.
[2] Fiveland, W. A., 1987, "Discrete Ordinate Methods for Radiative Heat Transfer in Isotropically and Anisotropically Scattering Media," ASME J. Heat Transfer, **109**, pp. 809–812.
[3] Stamnes, K., Tsay, S. C., Wiscombe, W., and Jawaweera, K., 1988, "Numerically Stable Algorithm for Discrete-Ordinate-Method Radiative Transfer in Multiple Scattering and Emitting Layered Media," Appl. Opt., **27**, pp. 2502–2509.
[4] Kumar, S., Majumdar, A., and Tien, C. L., 1990, "The Differential-Discrete-Ordinate Method for Solutions of the Equation of Radiative Transfer," ASME J. Heat Transfer, **112**, pp. 424–429.
[5] Qin, Y., Jupp, D. L. B., and Box, M. A., 2002, "Extension of the Discrete-Ordinate Algorithm and Efficient Radiative Transfer Calculation," J. Quant. Spectrosc. Radiat. Transf., **74**, pp. 767–781.
[6] Li, H. Y., and Ozisik, M. N., 1992, "Identification of the Temperature Profile in an Absorbing, Emitting, and Isotropically Scattering Medium by Inverse Analysis," ASME J. Heat Transfer, **116**, pp. 1060–1063.
[7] Zhou, H. C., Yuan, P., Sheng, F., and Zheng, C. G., 2000, "Simultaneous

Estimation of the Profiles of the Temperature and the Scattering Albedo in an Absorbing, Emitting, and Isotropically Scattering Medium by Inverse Analysis," Int. J. Heat Mass Transfer, **43**, pp. 4361–4364.
[8] Liu, L. H., Tan, H. P., and Yu, Q. Z., 2001, "Inverse Radiation Problem of Sources and Emissivities in One-Dimensional Semitransparent Media," Int. J. Heat Mass Transfer, **44**, pp. 63–72.
[9] Silva Neto, A. J., and Ozisik, M. N., 1995, "An Inverse Problem of Simultaneous Estimation of Radiation Phase Function, Albedo and Optical Thickness," J. Quant. Spectrosc. Radiat. Transf., **53**, pp. 397–409.
[10] Hendricks, T. J., and Howell, J. R., 1996, "Absorption, Scattering Coefficients and Scattering Phase Functions in Reticulated Porous Ceramics," ASME J. Heat Transfer, **118**, pp. 79–87.
[11] Li, H. Y., and Yang, C. Y., 1997, "A Genetic Algorithm for Inverse Radiation Problems," Int. J. Heat Mass Transfer, **80**, pp. 1547–1549.
[12] Liu, L. H., Tan, H. P., and Yu, Q. Z., 1999, "Simultaneous Identification of Temperature Profile and Wall Emissivities in One-Dimensional Semitransparent Medium by Inverse Radiation Analysis," Numer. Heat Transfer, Part A, **36**, pp. 511–525.
[13] Park, H. M., and Yoon, T. Y., 2000, "Solution of the Inverse Radiation Problem Using a Conjugate Gradient Method," Int. J. Heat Mass Transfer, **43**, pp. 1767–1776.
[14] Franca, F., Morales, J. C., Oguma, M., and Howell, J. R., 1998, "Inverse Design of Thermal Systems with Radiation," *Proc. 11th International Heat Transfer Conf.*, Kyongju, Korea, 1, pp. 213–221.
[15] McCormick, N. J., 1992, "Inverse Radiative Transfer Problems: a Review," Nucl. Sci. Eng., **112**, pp. 185–198.
[16] Levenberg, K. A., 1944, "Method for the Solution of Certain Non-Linear Problems in Least Squares," Q. Appl. Math., **2**, pp. 164–168.
[17] Marquardt, D. W., 1963, "An Algorithm for Least-Squares Estimation of Nonlinear Parameters," J. Soc. Ind. Appl. Math., **11**, pp. 431–441.
[18] Hanke, M. A., 1997, "Regularizing Levenberg-Marquardt Scheme, with Applications to Inverse Groundwater Iteration Problems," Inverse Probl., **13**, pp. 79–95.
[19] Holland, J. H., 1962, "Outline for a Logical Theory of Adaptive Systems," J. Assoc. Comput. Mach., **3**, pp. 297–314.
[20] Goldberg, D. E., and Deb, K., 1991, "A comparative analysis of selection schemes used in genetic algorithms," in *Foundations of Genetic Algorithms*, G. J. E. Rawlins, (eds.), Morgan Kaufmann, San Mateo, CA, pp. 69–93.
[21] Tsintikidis, D., Haferman, J. L., Anagnostou, E. N., Krajewski, W. F., and Smith, T. F., 1997, "A Neural Network Approach to Estimating Rainfall from Spaceborne Microwave Data," IEEE Trans. Geosci. Remote Sens., **35**, pp. 1079–1092.
[22] Peterson, C., Rognvaldsson, T., and Lonnblad, L., 1994, "JETNET 3.0-a Versatile Artificial Neural Network Package," Comput. Phys. Commun., **81**, pp. 185–220.
[23] McFarlane, S. A., Evans, K. F., and Ackerman, A. S., 2002, "A Bayesian Algorithm for the Retrieval of Liquid Water Cloud Properties from Microwave Radiometer and Millimeter Radar Data," J. Geophys. Res., **107**, Article no. 4317.
[24] Sivia, D. S., 1996, *Data Analysis: A Bayesian Tutorial*, Clarendon, Oxford, England.
[25] Bernardo, J. M., and Smith, A. F. M., 1994, *Bayesian Theory*, Wiley, New York.
[26] Pereyra, Victor, 1978, "PASVA3: An adaptive finite-difference FORTRAN program for first order nonlinear boundary value problems," in *Lecture Notes in Computer Science*, Springer-Verlag, Berlin, Vol. 76, pp. 67–88.
[27] Siegel, R., and Howell, J. R., 2001, *Thermal Radiation Heat Transfer*, 4th ed., Taylor and Francis-Hemisphere, Washington.
[28] Carroll, D. L., 1996, *Genetic Algorithms and Optimizing Chemical Oxygen-Iodine Lasers, Developments in Theoretical and Applied Mechanics*, Wilson, H. B., Batra, R. C., Bert, C. W., Davis, A. M. J., Schapery, R. A., Stewart, D. S., and Swinson, F. F., eds., School of Engineering, The University of Alabama, Vol. 18, pp. 411–424.
[29] Heaslet, M. A., and Warming, R. F., 1965, "Radiative Transport and Wall Temperature Slip in an Absorbing Planar Medium," Int. J. Heat Mass Transfer, **8**, pp. 979–994.
[30] Swaminathan, V., Balaji, C., and Venkateshan, S. P., 2004, "Parameter Estimation in a Two-Layer Planar Gray Participating Medium," J. Thermophys. Heat Transfer, **18**, pp. 187–192.

Journal of Heat Transfer

Technical Briefs

Heat Transfer and Bubble Movement of Two-Side and One-Side Heating Subcooled Flow Boiling in Vertical Narrow Channels

Liang-Ming Pan
Institute of Engineering Thermophysics of Chongqing University,
Chongqing 400044, China

Tien-Chien Jen
Mechanical Engineering Department,
University of Wisconsin at Milwaukee,
Milwaukee, WI 53211
e-mail: jent@uwm.edu

Chuan He

Ming-dao Xin

Institute of Engineering Thermophysics of Chongqing University,
Chongqing 400044, China

Qing-hua Chen
Mechanical Engineering Department,
University of Wisconsin at Milwaukee,
Milwaukee, WI 53211

This paper investigates the bubble behavior of different heating methods of narrow rectangular channels. Comparisons were made on the onset of nucleate boiling (ONB) point and bubble behavior with various flow patterns. Results reveal that the wall superheat of two-side heating is lower than that in one-side heating at the same heat flux. This difference becomes obvious at a higher heat flux. Under the same subcooling condition, the required heat flux to start nucleate boiling for the one-side heating channel is higher than that for the two-side one. With similar bubbles behaviors, the cross-sectional subcooling tends to be higher for the two-side heating method. [DOI: 10.1115/1.2227040]

Contributed by the Heat Transfer Division of ASME for publication in the JOURNAL OF HEAT TRANSFER. Manuscript received June 9, 2005; final manuscript received March 8, 2006. Review conducted by Sathish G. Kandlikar.

Keywords: subcooled flow boiling, bubble behavior, two-side heating, one-side heating, narrow channels

1 Introduction

The channels employing hydraulic diameters between 200 μm and 3 mm are referred to as minichannels [1]. Compared with conventional channels from the view of the heat transfer, narrow and microchannels have significant heat transfer enhancement characteristics [2,3]. With a smooth internal surface and scouring by flowing fluid, the dirt formed on the surface of the channel wall can be easily removed and the fouling problem is not as serious as the deformed channels. Moreover, heat transfer elements can be easily assembled to compact devices. Since the innovative work of Ishibashi et al. [2], narrow channels have been adopted extensively in engineering applications, e.g., microelectronic cooling [4,5], advanced nuclear reactor [6,7], cryogenic, aviation, and space technology. Because the bubble size has approached the dimension of the channel, the size of the flow channel plays a critical role on the flow boiling heat transfer. This results in that the bubble in the narrow channel acts very differently from those in the non-narrow channel.

Yoshida et al. [8,9] studied the heat transfer performance of working media in a single-tube and double-tube thermosyphon, and investigated the effects of subcooling and inclination. They found that the performances of thermosyphon in single-tube and double-tube are quite different in the heat transfer rate and flow pattern. The effects of the heating methods on the parallel channel should be similar to the situation of a thermosyphon. However, there is no direct evidence about the comparison of bubble behavior dynamics of flow boiling in narrow channels between the one-side and the two-side heating situation.

During long historical practices of narrow channel investigation, a large number of experimental data and analytical results about one-side heating have been accumulated [10–12]. There are essentially no sufficient data available in the literature regarding the two-side heating for narrow channels. It will be very convenient if these one-side heating narrow channel data can be used to correlate and predict the two-side heating narrow channel transport phenomena and two-phase heat transfer performances.

For this reason, understanding the difference and similarity between these two heating methods (one-side heating and two-side heating) of the narrow channels are an essential task to develop the correlations. The feasibility of correlating the bubble behavior characteristics and boiling heat transfer features of one-side heating to two-side heating in narrow channels provides a convenient way to understand the inherent mechanism of heat transfer enhancement of narrow channels.

In the present work, we have experimentally compared the bubble behavior under the condition of one-side heating with that of two-side heating. Experimental studies are performed separately for a single plate heater system and a double plate heater system. A high-speed camera was used to compare the character-

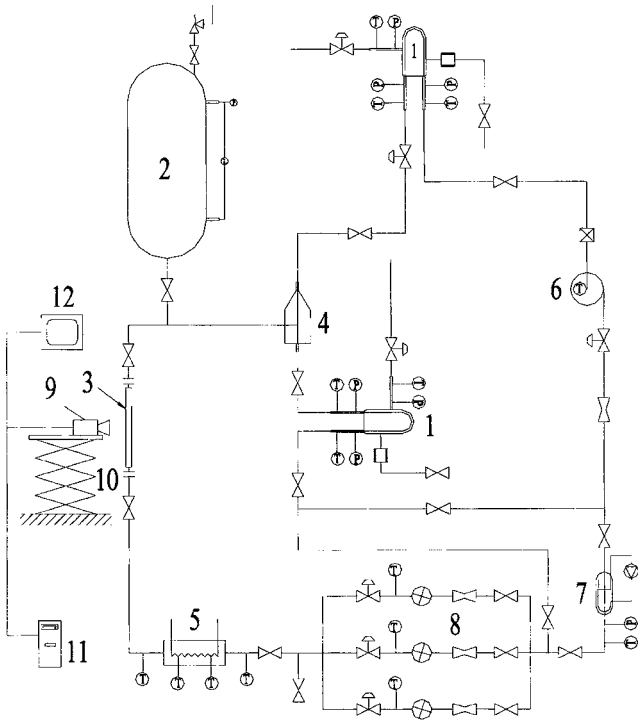

1.main heat exchanger; 2.pressurizer; 3.test-section 4.mixing condenser; 5.pre-heater; 6.pump; 7.refrigerating unit; 8.flowmeter unit; 9.high-speed camera; 10.lifter; 11.computer; 12.moniter

Fig. 1 Schematic diagram of test loop of R12

istics of bubble behavior. The onset of nucleate boiling (ONB) point and characteristics of the heat transfer of the narrow channel are also discussed.

2 Experimental Set-up and Data Treatment

2.1 Testing Apparatus for R12. Figure 1 is the schematic diagram of the complete experimental setup for the test loops and flow visualization. The test loop consists of a main test loop, water-cooling loop, power supply, control system, and other auxiliary systems. The test-loop unit consists of a main circulating pump, refrigerating unit, preheater, test section, condenser, heat exchanger, pressurizer, and flowmeter. Working fluid comes from pump 6 and then enters refrigerating unit 7, where it is refrigerated to the desired temperature if necessary. The flow rate is measured by the flowmeter with three different ranges of flow rates, and then working fluid enters the preheater to adjust the temperature to a designated temperature. After that, liquid is heated in test section 3 (details can be seen in Fig. 2). Then the two-phase flow enters condenser 4 to mix with the liquid directly coming from the pump. After cooling, the liquid flows back to the pump. The inlet temperature of the test section is controlled by a preheater and a refrigeration unit. The accuracy of the direct current power supply is ±0.8%. The mass flow rate is measured by a venturimeter with an accuracy of ±1% of the whole measuring range of 50–500 kg/h. Pressure and pressure difference are measured by the pressure transmitter with a FOUNDATION™ fieldbus model STG960 (accuracy of ±30 kPa) and pressure difference transmitter model ST3000 (Honeywell, accuracy of ±3500 Pa). The temperature is measured from a T-type sheathed thermocouple. Every sheathed thermocouple is calibrated individually and the temperature measurement error of all the thermocouples is less than 0.45°C. The error distribution of the whole measuring range was accounted for in the data acquisition system. And all the thermocouples are located at a distance of at least of 100 mm from the inlet header tank. To avoid the inlet effect, the ONB points can

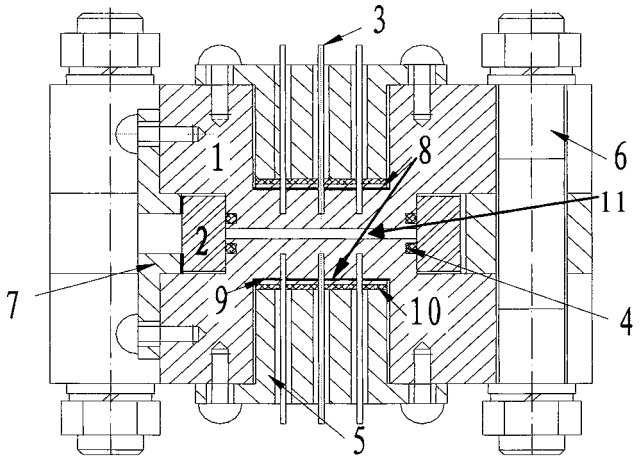

1. Channel plate; 2.glass; 3. sheathed thermocouple; 4. O-ring; 5. heater compacter; 6. bolt; 7. glass compacter; 8. heater; 9. mica; 10. insulation; 11. channel of 35x2 mm^2

Fig. 2 Cross-sectional view of test section

often be adjusted to more than 160 mm downstream. The IMP distributed data acquisition system is used to obtain various signals from the test loop and test section at the accuracy of 0.03%. Besides, with good insulation outside the test section, the heat loss is only up to 1%. With careful heat loss calibration before every formal experiment at the single-phase flow state, the heat loss is taken into account in the final data processing. The calibration process based on the conservation of thermal energy is used to compare the outlet enthalpy with the combination of the inlet enthalpy plus the power input to the liquid.

2.2 Data Treatment and Parameters' Range. Since a flat heating element is used, numerical simulation is first performed to confirm that the heat flux distribution is uniform along the heating side. As shown in Fig. 2, three thermocouples are installed at the same height in one channel plate. Comparisons between the measured temperatures of distributed location and the simulation data confirm the uniformity of the heat flux distribution. The channel plates are made of brass (70Cu-30Zn) which has a thermal conductivity of 115 W/mK at room temperature. Since it is subcooled boiling, with the assumption of quasi-equilibrium within every cross section, the mean temperature of the flow can be evaluated from a simple energy balance on a differential length. The wall temperature can then be evaluated as follows

$$T_W = T_i - \frac{q\Delta x}{k} \tag{1}$$

in which, Δx is the distance from the measuring point to the channel wall, which is due to the fact that the inserting location is inside the wall (not right on the surface). T_i is the measured temperature, T_w is the calculated channel wall temperature. k is the thermal conductivity of the brass channel plates, in which the effect of the temperature dependence is taken into consideration. q is the heat flux with which the heat loss has been accounted for.

The experimental setting of the present work is: the heating length of the test section is 400 mm, the cross section of the channel is 35 mm in width and 2 mm in gap size, the mass flux varies between 700 and 1500 kg/(m^2 s), the heat flux and the pressure are ranging from 25 to 70 kW/m^2 and 1.3 to 2.0 MPa, respectively. Note that the heat flux is defined as the heat transfer rate per unit heating area. The subcooled boiling condition is maintained by limiting the power input of the test section according to the inlet enthalpy. There is no extra measure used to preserve the subcooled flow. The pressure is defined as the average

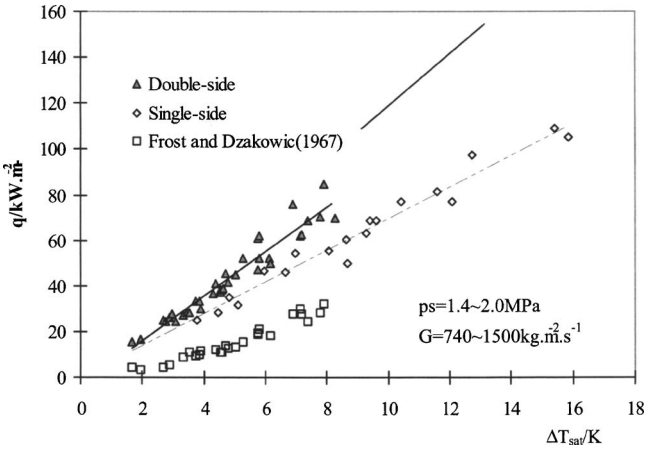

Fig. 3 Wall superheat versus the ONB point of one-side and two-side heating as well as the prediction of Frost and Dzakowic (see Ref. [18])

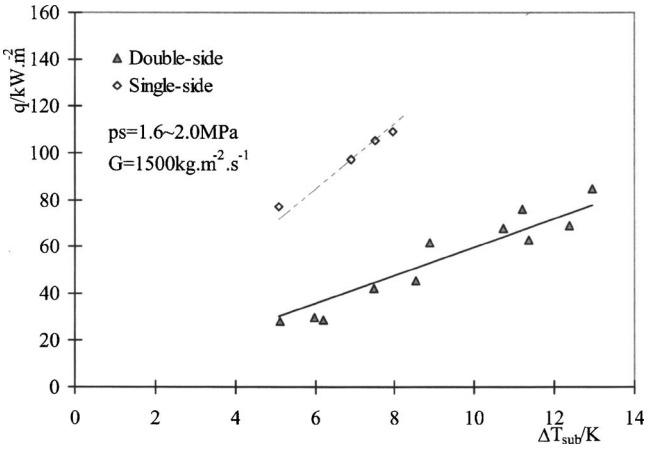

Fig. 4 Subcooling of liquid versus the ONB point of one-side and two-side heating

absolute pressure of the inlet and the outlet. The pressure is used as a reference to calculate the saturated temperature and other physical properties according to the computer code of NIST REFPROP (1992 Version, new version can be found at http://www.nist.gov). There are a total of 48 thermocouples used in the experiment to measure the temperatures of the test section with 24 thermocouples on each of the heating walls.

3 Experimental Procedures and Results Discussion

3.1 Experimental Method. Before the start of the experiment, careful calibration is performed to ensure the test equipment is ready. The pressurizer in the test loop is first started to increase the pressure to the desired value, then the main loop and the R-12 preheating equipment are used to adjust the flow rate and the inlet temperature to the desired value. The heating power supplied to the test section is increased gradually until the outlet temperature reaches the saturated boiling point, and then waits for a couple of minutes until all the parameters of every measuring point have no change within the accuracy of the measuring instruments. Then the temperature of all points of the test section is measured and the location of the ONB point of subcooled boiling is recorded. Meanwhile, a high-speed video camera is started to take images. After the two-side heating experimental data are recorded, one of the two heaters in Fig. 2 is cutoff to perform the one-side heating experiment with the same system parameters. Since two-phase flows are inherently unsteady, 50 samples per channel are obtained over a period of 0.5 s and averaged to achieve repeatable measurements. Under various operating conditions, 97 runs of two-side and one-side heating experiments are performed, and a large number of high-speed video images are recorded as well.

3.2 Effect of Heating Method on the ONB Point. The ONB point is a key transition point for the boiling heat transfer, and a critical point to adopt different correlations for the rate of the heat transfer.

The ONB points are determined by using high-speed video. According to the temperature of the heating wall as well as system parameters, the relationship between the subcooled ONB point and the wall superheat for one-side and two-side heating is shown in Fig. 3 with a system pressure $p_s = 1.4-2.0$ MPa and mass flux $G = 740-1500$ kg/m^2 s. The average subcooling of the ONB point in one-side and two-side heating is shown in Fig. 4 with a constant mass flux at $G = 1500$ kg/m^2 s. In these figures, the average subcooling is defined as the difference between the current cross-sectional temperature (calculated through thermal energy balance) and the saturated temperature at the present pressure. The heat flux is defined as the following

$$q = \frac{P}{A_{ha}} \tag{2}$$

in which P is the electric power input into the heating plate(s), (kW) and A_{ha} is the total heating area (m^2).

In Fig. 3, it can be seen that the different heating methods (one-side heating or two-side heating) have apparent effects on the subcooled ONB point and the wall superheat. With the same heat

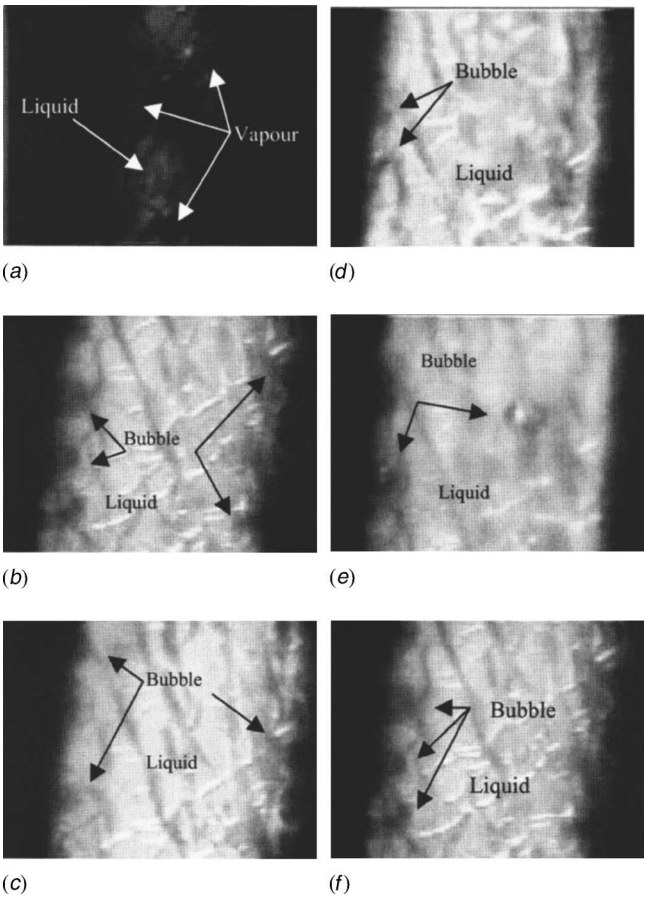

Fig. 5 Bubble morphology in different heating conditions: (*a*) two-side heating, (*b*) one-side heating, (*c*) two-side heating, (*d*) one-side heating, (*e*) two-side heating, and (*f*) one-side heating

Table 1 Experimental conditions of Fig. 5

No.	p/MPa	G/kg m^{-2} s^{-1}	q/kW m^{-2}	v/m s^{-1}	x_{out}	ΔT_{sub} K	Bubble description
5(*a*)	2.03	648.5	27.8	0.8	0.064	3.22	Liquid bridge was formed, bubbles filled half channel
5(*b*)	2.01	678.0	24.8	0.312	−0.018	6.44	Big bubbles coalesced small bubbles, which size increased
5(*c*)	1.81	812.7	28.0	0.291	0.036	6.18	Have big bubbles, in discrete moving
5(*d*)	1.81	800.7	28.2	0.278	−0.019	7.06	Moving discrete bubbles
5(*e*)	1.83	1059.4	38.7	0.3	0.022	8.21	Rolling moving, bigger bubbles move faster and coalesced small bubbles on rolling away
5(*f*)	1.82	1170.4	34.7	0.86	−0.026	4.01	Bubbles are very big, and the amount is few

flux input, the wall superheat of the subcooled ONB point in the two-side heating channel is less than that in one-side heating. This effect is more pronounced when the heat flux is further increased.

The reason of the increasing difference in the wall superheat phenomenon could be explained as follows: under the condition of two-side heating, the disturbances of the bubble were largely enhanced between both heating walls, which resulted in decreasing the wall superheat. This is similar to the heat transfer enhancement in narrow channels [2,13]. Comparing the two groups of the present experimental data with the correlation of Frost and Dzakowic [14] (which was extended from Davis and Anderson's [15] analytical solution to cover liquids other than high pressure water flows) at the same system parameter of two-side heating shows that the ΔT_{sup} is much higher in Frost and Dzakowic [14] than the experimental data for the two heating methods in the present study. This result also suggests that two-side heating has a lower superheat than the one-side heating case.

Comparing to the one-side and two-side heating cases, it can be seen from Fig. 4 that the heat flux for the onset of boiling is quite different under the same condition of subcooling. The heat flux required by the onset of boiling in the two-side heating channel is much less than that in one-side heating. With decreasing subcooling of the cross section, these two curves tend to approach each other. The reason for a different ONB heat flux between the two cases is due to the development of the two thermal boundary layers of both sides under the condition of two-side heating, which makes the ONB point shift to up-stream. With increasing heat flux, the disturbance between the two thermal boundary layers is enhanced, and the ONB point will shift further up-stream.

As described above, one-side and two-side heating have strong effects on the ONB point. Under the same operating conditions, the ONB is quite different when a different heating method is used. When the ONB point is considered, the two-side heating of subcooled flow boiling cannot be simply simulated under the one-side heating condition.

3.3 Bubble Morphology in Different Heating Conditions. For bubble morphology, it will be shown that the one-side heating method is quite different from the two-side heating method. As shown in Fig. 5, under approximately the same pressure, mass flow rate, heat flux, and average subcooling of cross-sectional conditions (see Table 1 for the operation conditions for Fig. 5), the bubble behavior displays many differences between the two heating methods.

Figures 5(*a*) and 5(*b*) illustrate the photoimages of the cases for two-side heating and one-side heating, respectively, under almost identical conditions (see Table 1). It can be seen from Fig. 5(*a*) that the channel was filled with a large amount of bubbles and the liquid only existed as a liquid bridge. On the contrary, as shown in Fig. 5(*b*), in one-side heating, only a few isolated bubbles scattered on the heating surface.

Similarly, Figs. 5(*c*) and 5(*d*) depict the photoimages for two-side heating and one-side heating, respectively, with a larger mass and heat flux, and slightly lower system pressure (see Table 1). Comparing Fig. 5(*c*) to Fig. 5(*d*), it can be observed that with two-side heating (Fig. 5(*c*)), the number of bubbles on the heating surface is larger than that of one-side heating (Fig. 5(*d*)).

Figures 5(*e*) and 5(*f*) show the images of the cases for two-side heating and one-side heating at a higher mass flux and wall heat flux (see Table 1), respectively. The difference of the working condition between them is mainly the subcooled temperature of the cross section, which are the 8.21 K for two-side heating and 4.01 K for the one-side heating. It is observed that the bubble morphology is very similar; both cases have big bubbles, and the bubbles are all rolling downstream. This implies that the two different heating methods have resulted in the same bubble morphology at a different subcooled temperature. When we do not consider the operational conditions other than flow patterns, the difference of the bubbles behavior between the two heating methods is not easy to be distinguished. Thus the results of the different heating methods are dominantly reflected on the subcooling of the cross-sectional liquid and wall superheat. This indicates that the differences of the behaviors of the bubbles are unapparent if we do not consider the relevant conditions.

From the working parameters of the photoimages, it can be seen that when the bubble morphology is similar, the subcooling of the section is higher for the two-side heating method. Meanwhile, under the situation of similar bubble morphology, bubbles will move at a higher speed for the one-side heating method than those at the two-side heating method. This mechanism can be explained as follows: under the condition of subcooled boiling, fluid near the nonheating wall of the one-side heating is a single-phase liquid, the friction is less than the one that has bubbles moving on the opposite heating wall.

4 Conclusion

(1) The heating methods of the narrow channels of two-side and one-side heating have strong effects on the wall superheat of the subcooled ONB point. At the same heat flux, the wall superheat under the condition of two-side heating is lower than that in one-side heating. When the heat flux is increased, the difference in the wall superheat between both cases is also increased.

(2) At the ONB point, under the same cross-sectional subcooling, the required heat flux to initiate nucleate boiling for the one-side heating narrow channel is higher than that for the two-side heating channel. By decreasing the cross-sectional subcooling, the difference narrows.

(3) When the operating conditions are nearly identical, the bubbles behavior in one-side and two-side heating is quite different as observed from the photoimages. Note that with similar bubbles behaviors, the cross-sectional subcooling tends to be higher for two-side heating cases.

Acknowledgment

The authors are grateful for the support of the National Science Foundation of China (No. 50406012) and the support of the National Key Laboratory of Bubble Physics and Natural Circulation, Nuclear Power Institute of China (No. 51482020103JW2001). Dr. Tien-Chien Jen and Qinghua Chen would also like to acknowledge the partial support from NSF (US) DMII GOALI 9908324.

Nomenclature

A_{ha} = heating area, m^2
k = thermal conductivity of materials, $W\,m^{-1}\,K^{-1}$
p = pressure, MPa
P = electric power input into the heating plate(s), kW,
G = mass flux of R-12, $kg\,m^{-2}\,s^{-1}$
q = heat flux, $kW\,m^{-2}$
T_i = temperature of the measuring point, K
T_w = temperature of channel wall, K
x_{out} = mass dryness fraction of outlet, $(H_{out}-H_{sat})/H_{sat}$
Δx = distance from measuring point to channel wall, m
ΔT_{sub} = subcooled temperature of R-12, $\Delta T_{sub}=T_{sat}$-T, K
ΔT_{sup} = superheated temperature of heating wall, $\Delta T_{sup}=T_W$-T_{sat}, K
v = velocity of bubbles, $m\,s^{-1}$

References

[1] Kandlikar, S. G., 2002, "Fundamental Issues Related to Flow Boiling in Minichannels and Microchannels," Exp. Therm. Fluid Sci., **26**, pp. 389–407.
[2] Ishibashi, E., and Nishikawa, K., 1969, "Saturated Boiling Heat Transfer in Narrow Spaces," Int. J. Heat Mass Transfer, **12**, pp. 863–894.
[3] Yao, S. C., and Chang, Y., 1983, "Pool Boiling Heat Transfer in a Confined Space," Int. J. Heat Mass Transfer, **26**(6), pp. 841–848.
[4] Mukherjee, S., and Mudawar, I., 2003, "Smart Pumpless Loop for Micro-Channel Electronic Cooling Using Flat and Enhanced Surfaces," IEEE Trans. Compon. Packag. Technol., **26**(1), pp. 99–109.
[5] Misale, M., and Bergles, A. E., 1997, "Influence of Channel Width on Natural Convection and Boiling Heat Transfer From Simulated Microelectronic Components," Exp. Therm. Fluid Sci., **14**(2), pp. 187–193.
[6] Larson, T. K., Oh, C. H., and Chapman, J. C., 1994, "Flooding in a Thin Rectangular Slit Geometry Representative of ATR Fuel Assembly Side-Plate Flow Channels," Nucl. Eng. Des., **152**(2), pp. 277–285.
[7] Ruggles, A. E., 1990, "Countercurrent Flow in Systems of Parallel Narrow Rectangular Channels," *Proc. of Advances in Gas-Liquid Flows, ASME Winter Annual Meeting*, pp. 243–250.
[8] Yoshida, M., Imura, H., and Ippohshi, S., 1993, "Flow and Heat Transfer in Two-Phase Double-Tube Thermosyphons (the Effect of Subcooling)," Heat Transfer-Jpn. Res., **22**(8), pp. 812–827.
[9] Imura, H., and Yoshida, M., 1991, "Heat-Transfer Characteristics in Two-Phase Double-Tube Thermosyphons," Heat Transfer-Jpn. Res., **20**(8), pp. 723–733.
[10] Boscary, J., Fabre, J., and Schlosser, J., 1999, "Critical Heat Flux of Water Subcooled Flow in One-Side Heated Swirl Tubes," Int. J. Heat Mass Transfer, **42**(2), pp. 287–301.
[11] Boscary, J., Araki, M., and Schlosser, J., 1998, "Dimensional Analysis of Critical Heat Flux in Subcooled Water Flow Under One-Side Heating Conditions for Fusion Application," Fusion Eng. Des., **43**(2), pp. 147–171.
[12] Boyd, R. D., Sr., and Penrose, C., 2002, "Conjugate Heat Transfer Measurements in a Nonuniformly Heated Circular Flow Channel Under Flow Boiling Conditions," Int. J. Heat Mass Transfer, **45**(8), pp. 1605–1613.
[13] Bowers, M. B., and Mudawar, I., 1994, "High Flux Boiling in Low Flow Rate, Low Pressure Drop Mini-Channel and Micro-Channel Heat Sinks," Int. J. Heat Mass Transfer, **37**, pp. 321–332.
[14] Frost, W., and Dzakowic, G. S., 1967, "An Extension of the Method of Predicting Incipient Boiling on Commercially Finished Surfaces," *ASME AIChE Heat Transfer Conference* Paper 67-HT-61, Seattle; http://wins.engr.wisc.edu/teaching/mpfBook/node35.html.
[15] Tong, L. S., and Tang, Y. S., 1997, *Boiling Heat Transfer and Two-Phase Flow*, Taylor & Francis, Washington, D.C., p. 251; Davis, E. J., and Anderson, G. H., 1966, "The Incipience of Nucleate Boiling in Forced Convection Flow," AIChE J. **12**, pp. 774–780.

A Theoretical Investigation Into the Optimal Longitudinal Profile of a Horizontal Pin Fin of Least Material Under the Influence of Pure Forced and Pure Natural Convection With a Diameter-Variable Convective Heat Transfer Coefficient

C. J. Kobus
Department of Mechanical Engineering,
Oakland University,
Rochester, MI 48309
e-mail: cjkobus@oakland.edu

R. B. Cavanaugh
Vehicle Thermal Systems Engineer,
GM North American Vehicle Engineering,
Warren, MI 48090

The increased importance of heat sinks in electronic cooling applications has resulted in a revived interest in extended surfaces, or fins. Also, space and cost constraints provide impetus for optimizing thermal performance for a given, or least, amount of material. The current research focuses on a pin fin design of least material, where the diameter of the pin fin varies axially to maintain the axial heat flux constant; thus all fin material is utilized equally. Although such fins have been studied in the past, the convective heat transfer coefficient was assumed to be constant, which is not entirely true since it is known to be a function of diameter for cylindrical bodies. The current research shows that an optimal fin based on a variable convective heat transfer coefficient yields a true optimal profile, and utilizes material better; that is, it uses a lower volume of material to achieve the same heat dissipation rate. This improvement in material utilization is show to be anywhere from approximately 3% to 14%.
[DOI: 10.1115/1.2227041]

Keywords: extended surface, optimization, heat transfer

Introduction

In a book devoted to extended surfaces, Kern and Kraus [1] describe and model various types of fins: longitudinal, radial and pin fins, and Kraus [2] summarized advances that have been made in extended surface technology since the optimal parabolic profile first proposed by Schmidt [4]. Also, the influence of fin profile on thermal performance has been investigated by a number of researchers [1–7].

The focus of this paper is on a particular type of pin fin. Sonn and Bar-Cohen [8] investigated the optimum diameter for a cylindrical pin fin having a specified fin volume. Their theoretical study assumed a constant material thermal conductivity, *k*, a uniform diameter, *D*, and a constant convective heat transfer coefficient, *h*. Li [9], recognizing that the convective heat transfer coefficient would, in general, be dependent on fin diameter, *D*, reformulated the above problem using empirical correlations found in the archival literature [3,10]. Li's solution, however, was a transcendental equation that had to be solved numerically. In any case, the work of Li [9] was for an optimal constant cross-sectional area fin, not a least material fin being investigated in the current paper.

A pin fin with a concave parabolic profile, similar to that shown in Fig. 1 is generally considered to be the classic optimum shaped fin; optimum shape being defined as the shape having a minimum amount of material for a given heat transfer rate [1,3,5]. This optimization is based on the implicit assumption of equal material utilization. That is, where the heat flux is constant at every cross section axially along the fin. The concave parabolic profile also assumed the convective heat transfer coefficient to be uniform along the length of the fin, even though the diameter of the fin changes. In general, this assumption cannot be valid, because of the known dependency of the heat transfer coefficient on diameter. To the best knowledge of the authors, this problem has not been fully addressed in the archival literature for forced convection in cross-flow or pure natural convection. (Various variable convective heat transfer coefficients based not on *D*, but on functions of either (or both) the coordinates along the major fin axis, *x*, and the fluid to fin temperature difference, θ, are reviewed in detail in Ref. [2].) Such is the specific focus of the present paper; modeling the optimum profile, or shape, of a pin fin when the convective heat transfer coefficient depends on diameter and, in the case of natural convection, the surface temperature.

Formulation of Theoretical Model

Applying the conservation of energy principle to a finite volume extending from some axial point between the base and tip of the fin, *x*, and an incremental distance from that point, $x+\Delta x$, as shown in Fig. 1, then taking the limit as $\Delta x \to 0$, the differential equation governing the temperature distribution in a pin fin is expressed as

$$\frac{d}{dx}\left(\frac{k}{4}D^2\frac{d\theta}{dx}\right) - h\,D\theta\left[1+\frac{1}{4}\left(\frac{dD}{dx}\right)^2\right]^{1/2} = 0 \tag{1}$$

where:

$$\theta = \theta(x) = T(x) - T_f \tag{2}$$

In the above equation, *k* is the thermal conductivity of the fin material, *D* is the variable diameter, and *h* is the convective heat transfer coefficient. The square root term in the above equation is what is usually termed the "length of arc" in the archival literature and is often simplified for cases where $(D_b/L) \leqslant 0.1$ [6], as will be discussed later. As mentioned earlier, the optimum shaped fin (the fin of least material) would ideally have a uniform heat flux over the length of the fin. The temperature distribution therefore must be linear and given by

$$\theta(x) = (T_b - T_f)\frac{x}{L} \tag{3}$$

where T_b and T_f are the base and fluid temperatures, respectively. (This assumes the tip of the pin fin approaches a point. The one-dimensional validity of pin fins and others was shown in Ref. [12] to be good where the Biot number, $\mathrm{Bi} \leqslant 0.3$ ($\mathrm{Bi} = hD/k$).) Substituting Eq. (3) into equation (1), assuming a constant material thermal conductivity, k, and neglecting the square of the convective surface slope term, $(dD/dx)^2/4$, due to its small order of magnitude, yields the following differential equation governing the diameter (profile) of the pin fin, $D(x)$.

$$\frac{dD(x)}{dx} = \left(\frac{2h}{k}\right)x \tag{4}$$

Neglecting the surface slope can be shown to be an excellent assumption by using Eq. (4) and recognizing that $dD/dx \leqslant (2hL/k)$. This is also studied in Ref. [6] for various pin fin

Contributed by the Heat Transfer Division of ASME for publication in the JOURNAL OF HEAT TRANSFER. Manuscript received July 27, 2005; final manuscript received February 21, 2006. Review conducted by Yogendra Joshi. Paper presented at the 2005 ASME Heat Transfer Summer Conference (HT2005), July 15–22, 2005, San Francisco, California, USA.

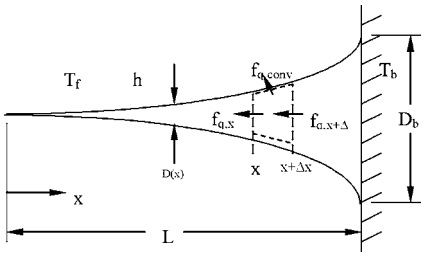

Fig. 1 Pin fin with concave axial profile

profiles and has been shown to be quite reasonable for cases where $(D_b/L) \leqslant 0.1$. Recent researchers [11] have included this "length of arc" into the formulation of an optimal shape, but assuming the convective heat transfer coefficient to be a constant.

The solution to Eq. (4), if the convective heat transfer coefficient, h, is assumed to be uniform over the entire length of the fin, is the classic concave parabolic profile.

$$D(x) = \left(\frac{h}{k}\right)x^2 \tag{5}$$

In this research, however, the above assumption will not be made as the convective heat transfer coefficient, h, will be allowed to be a variable based on the diameter. This variability will be unique to the mode of heat transfer (forced, natural, etc.) and will thus be handled separately.

Pure Forced Convection. If the convective heat transfer coefficient, h, is not assumed uniform over the length, but is instead dependent upon diameter, as it would be for forced convection in cross-flow, the profile will be different than that of the parabolic prediction. For forced convection cross-flow over cylinders, the Nusselt number, Nu_D, has been empirically determined [3,10] and can be expressed as:

$$\mathrm{Nu}_D = C\,\mathrm{Pr}^{1/3}\,\mathrm{Re}_D^n \tag{6}$$

The values of "C" and "n" depend on the particular domain of the Reynolds number, Re_D. The Prantdl number, Pr, involves the viscosity, μ, and the specific heat, c_p, as well as the thermal conductivity of the fluid, k_f. It should be noted that the optimal-shaped pin fin would be expected to be very slender; that is, the longitudinal diameter changes very gradually, both because of the low convective heat transfer coefficient (where fins would be used) and the relatively high thermal conductivity of the fin itself. Therefore, if one were to observe just a longitudinal portion (or subdomain) of the fin under most practical applications of an extended surface in a gas, it would appear to look very close to a cylinder. If the convective heat transfer were to be sufficiently high, the current approximation would have less merit, but in this case, the fin would probably not be one dimensional any longer as the Biot number would probably surpass accepted limits anyway. It should also be pointed out that the experimental uncertainty in obtaining dimensionless correlations is in many cases ±20 percent or more, likely compensating for use in very similar but not exactly identical geometries. Thus, the correlation for flow over a cylinder is used in the current research. (It is interesting that Aziz [7] used the same methodology, without justification, to attempt to get at an optimal profile with a variable heat transfer coefficient for pure forced convection only, but ended up with a transcendental equation that was solved numerically. No profile information, which is the objective of the current research, was obtained in the former.) Rearranging Eq. (6),

Table 1 Parameters related to optimum fin profile [10]

Re_D	C	n	$2/(2-n)$	ϕ/ϕ_c
0.4–4.0	0.989	0.330	1.198	1.134
4–4.0	0.911	0.385	1.238	1.123
40–4000	0.683	0.466	1.304	1.107
4000–40,000	0.193	0.618	1.447	1.076
40,000–4000,000	0.266	0.804	1.672	1.039

$$h = \frac{k_f}{D}C\,\mathrm{Pr}^{1/3}\,\mathrm{Re}_D^n = k_f C\,\mathrm{Pr}^{1/3}\left(\frac{\rho v_f}{\mu}\right)^n D^{n-1} = \beta D^{n-1} \tag{7}$$

Substituting (7) into (4) and solving yields the following, more general, optimum pin fin profile:

$$D(x) = \left(\frac{(2-n)}{k}\beta\right)^{1/(2-n)} x^{2/(2-n)} \tag{8}$$

where:

$$\beta = k_f C\,\mathrm{Pr}^{1/3}\left(\frac{\rho v_f}{\mu}\right)^n \tag{9}$$

It can be seen from Eq. (8) that a concave parabolic profile would only exist if $n=1$. However, for the empirical data for cross-flow forced convection [3,10], $n<1$. The optimum profile for a pin fin of the least material will depend on the particular domain of the Reynolds number in this case. The exponent, $2/(2-n)$, for the power function profile, represented in Eq. (8), is given in Table 1 for the various Reynolds number domains.

For conservative results, the Reynolds number domain should be determined using the base diameter of the fin, D_b, to compute the Reynolds number, $\mathrm{Re}_{Db}=(\rho_f v_f D_b/\mu_f)$. From Eq. (8), the relationship between the base diameter and fin length, L, is given by

$$D_b = \left(\frac{(2-n)}{k}\beta\right)^{1/(2-n)} L^{2/(2-n)} \tag{10}$$

If the base diameter, D_b, is known, the parameters "C" and "n" can be obtained from Table 1. The parameter β can then be computed from Eq. (9), and then the fin length, L, determined from Eq. (10). If the fin length, L, is known, the base diameter, D_b, can be iterated from Eq. (10) by initially guessing at a Reynolds number domain in Table 1.

As can be seen from Table 1, the optimum profile approaches a linear profile for small values of the Reynolds numbers. It is interesting that if the trends are consistent, it would appear that the optimum profile would approach a parabolic profile for large enough Reynolds numbers. All of these profiles may exist for different portions of the same fin.

Pure Natural Convection. If the convective heat transfer coefficient, h, is not assumed uniform over the length, but is instead dependent upon diameter, as it would also be for natural convection, the profile will again be different than parabolic. For natural convection from horizontal cylinders, the Nusselt number, Nu_D has been empirically determined [3,10] and can be expressed as:

$$\mathrm{Nu}_D = C(\mathrm{Pr}\,\mathrm{Gr}_D)^n \tag{11}$$

The values of "C" and "n" depend on the particular domain of the Grashof number, Gr_D. Also, the temperature difference in the Grashof number is already known from Eq. (3). Thus,

$$h = kC\,\mathrm{Pr}^n\left(\frac{\rho^2 g\beta\theta_w}{\mu^2}\right)^n\left(\frac{x}{L}\right)^n D^{3n-1} \tag{12}$$

Substituting (12) into (4) and solving yields the following, more general, optimum pin fin profile:

Table 2 Parameters related to optimum fin profile [10]

Gr_D	C	n	$(n+2)/(2-3n)$
$0-10^{-5}$ [13]	0.4	0	1.000
$10^{-10}-10^{-2}$ [14]	0.675	0.058	1.127
$10^{-2}-10^{2}$ [14]	1.020	0.148	1.380
$10^{2}-10^{4}$ [14]	0.850	0.188	1.524
$10^{4}-10^{7}$ [14]	0.480	0.250	1.800
$10^{7}-10^{12}$ [13,14]	0.125	0.333	2.331

$$D(x) = \left(\frac{(2-3n)}{(n+2)}\gamma\right)^{1/(2-3n)} x^{(n+2)/(2-3n)} \tag{13}$$

where:

$$\gamma = 2C\,\mathrm{Pr}^n\left(\frac{\rho^2 g\beta\theta_w}{\mu^2}\right)^n L^{-n} \tag{14}$$

It can be seen from Eq. (13) that a concave parabolic profile would only exist if $n=(2/7)$ exactly. However, for the empirical data for natural convection [10], $n<1$ in general and varies with the Grashof number. The optimum profile for a pin fin of the least material will thus depend upon the particular domain of the Grashof number. The exponent, $(n+2)/(2-3n)$, for the power function profile, represented by Eq. (13), is given in Table 2 for the various Grashof number domains.

For conservative results, the Grashof number domain should be determined using the base diameter of the fin, D_b, to compute the Grashof number, Gr_{Db}. From Eq. (13), the relationship between the base diameter and fin length, L, is given by

$$D_b = \left(\frac{(2-3n)}{(n+2)}\gamma\right)^{1/(2-3n)} L^{(n+2)/(2-3n)} \tag{15}$$

If the base diameter, D_b, is known, the parameters "C" and "n" can be obtained from Table 2. The parameter γ can then be computed from Eq. (14), and then the fin length, L, determined from Eq. (15). If the fin length, L, is known, the base diameter, D_b, can be iterated from Eq. (15) by initially guessing at a Grashof number domain in Table 2.

As can be seen from Table 2, the optimum profile approaches a linear profile for very small values of the Grashof number. It is interesting that it approaches a parabolic profile for a large enough Grashof number and even exceeds the parabolic profile in the largest domain, $10^7<\mathrm{Gr}_D<10^{12}$.

Comparison. It would be useful to compare the material savings utilizing the current variable convective heat transfer model with the prior model, assuming the heat transfer coefficient to be constant. In the instance of pure forced convection, the volume can be calculated by integrating the cross-sectional area, which involves the square of the diameter, given by either Eq. (5) or (8) for fixed and variable convective heat transfer coefficients, respectively. The ratio of these volumes, variable to fixed, can then be put into mathematical form, assuming the same base diameters, where

$$\frac{V}{V_c} = 5\frac{(2-n)^{1/2}}{(6-n)}\left(\frac{D_b}{d}\right)^{(1-n)/2} \tag{16}$$

In the above equation, d represents the diameter that is utilized to evaluate the constant convective heat transfer coefficient, h, for the case of the parabolic profile, Eq. (5) [12–14]. The problem here is that there is no archival literature available that quantifies how best to pick this diameter and thus evaluate a "correct" convective heat transfer coefficient. There are several possibilities however: the diameter, d, can be the base diameter (D_b), the arithmetic mean of the diameter ($D_b/2$), the mean value of the diameter ($D_b/3$), the surface area mean diameter ($3D_b/5$), and the volume (or mass) mean diameter ($5D_b/7$). For simplicity, it is assumed for the purpose here that the Reynolds stays in a single domain according to Table 1. In this case, the volume ratio shown in Eq. (16) for the five different possibilities above are all above unity. As surprising as this is at first (more material is used for the variable heat transfer coefficient fin), it should be noted that this is not the entire account. The implication here is that locking the profile into a classic parabolic will not yield a linear temperature profile in the case where the convective heat transfer coefficient varies over the surface. Therefore, it is almost certain that the model of Eq. (5) is simply not an optimal profile, and although it appears that less material is utilized, the heat transfer dissipation is less than what is predicted by the former model. Thus, instead of comparing volumes, it would be of more value to compare the actual heat dissipation rate *per unit volume*, or what will be termed a "material utilization factor." Such a parameter has been suggested recently by Kobus [15] to be that which best quantifies material utilization. A solution can be obtained here for comparative purposes by substituting Eq. (5) back into (1), thus demanding a parabolic profile, and then solving for the temperature distribution with a variable convective heat transfer coefficient. After some rearrangement, the equation governing the temperature distribution in a parabolic spline with a variable convective heat transfer coefficient is

$$x^2\frac{d^2\theta}{dx^2} + 4x\frac{d\theta}{dx} - M^2\theta = 0 \tag{17}$$

where

$$M = L\left(\frac{8L^2\overrightarrow{h}}{D_b}\right) = 2\left(\frac{D_b^{(1-n)}d^{(n-1)}}{(2-n)}\right)^{1/2} \tag{18}$$

Recognizing Eq. (17) as the general form of the Euler or Cauchy equation, a solution to this variable coefficient differential equation can be obtained by changing independent variables utilizing appropriate mapping transformations, effectively first transforming the variable coefficient differential equation to one with constant coefficients, then solving. The solution to the temperature distribution is:

$$\theta(x) = (T_b - T_f)\frac{x^\alpha}{L_c} \tag{19}$$

where

$$\alpha = \frac{1}{2}[(9+4M)^{1/2} - 3] \tag{20}$$

Referring to Eq. (19), where L_c is the length of the constant heat transfer coefficient parabolic fin, it is seen that an optimum temperature profile will only be obtained for $\alpha=1$. However, no combination of exponents, n, in Table 1, in combination with any of the averaging methods mentioned above will yield such a value. In any case, for $\alpha=1$, which is the optimum case, derivatives of Eqs. (3) and (19) can be taken, where the quotient of the heat dissipation rates of the variable heat transfer to the constant heat transfer coefficient can be obtained; thus

$$\frac{\dot{Q}}{\dot{Q}_c} = \left((2-n)\frac{D_b^{1-n}}{d^{1-n}}\right)^{1/2} \tag{21}$$

As was done with the volume ratio earlier, it becomes clear when calculations are performed utilizing the exponents in Table 1 that the heat dissipation ratio in Eq. (21) is greater than unity for all of the possible mean diameter values in combination with any exponent in any of the Reynolds number domains. Dividing Eq. (21) by (16) yields a ratio of material utilization factors between the variable convective heat transfer coefficient fin in the current research and the constant heat transfer coefficient parabolic fin of former research; thus,

$$\frac{\phi}{\phi_c} = \frac{(6-n)}{5} \tag{22}$$

Equation (22) illustrates the results of the material utilization factor comparison between the two fins. It is clearly seen that the above equation is independent of the averaging methods in finding the constant heat transfer coefficient for the parabolic fin in any of the Reynolds number domains (where $n<1$ always), and consequently yields a net gain in material utilization for the current variable heat transfer coefficient fin. This material utilization improvement is anywhere between 4% and 13.4%, depending upon the Reynolds number domain (see the last column in Table 1 for this number for the various domains). More realistically, the fin in the current research may be in several Reynolds domains simultaneously at different locations along the fin. However, since the material utilization factor is improved here over that of the parabolic fin for any domain, it will be improved also for several piecewise domains. In essence, however, this is a classic apples-to-oranges comparison; that is, the former model assuming a constant convective heat transfer coefficient, Eq. (5), is missing important physics that locks the profile into a parabolic shape, which was shown in this paper not to be correct in keeping the temperature profile linear. The comparison is thus between a true optimal fin and one that is not, which will yield only one possible true result: the true optimum fin utilizes material better.

Conclusions

A theoretical model has been formulated in the current research for predicting the optimum profile of a pin fin of least material with a variable convective heat transfer coefficient, assuming only the classical one-dimensionality of pin fins for $\mathrm{Bi} \leqslant 0.3$ [9] and $(D_b/L) \leqslant 0.1$ [8]. If the convective heat transfer coefficient is assumed to be uniform over the length of the fin, the model predicts the optimum profile to be the classic parabolic profile [4]. More realistically, however, the convective heat transfer coefficient naturally depends on diameter for forced convection in cross-flow and natural convection from a horizontal cylinder, thus the optimum profile is a power function whose exponent is generally less than 2. As can be seen from Tables 1 and 2, the optimum profile approaches a linear profile for small values of the Reynolds and Grashof numbers while approaching a parabolic profile for large enough Reynolds and Grashof numbers. It would be interesting to see what the optimal profile would be when the "length of arc" assumption is not used [11] and the convective heat transfer coefficient is allowed to vary with diameter. This could be the focus of more continuing research in this area.

Also, the current research was done for a single fin, rather than an array of optimum fins for application to heat sinks. To understand pin fin arrays, however, it is essential to first understand the phenomena for just a single fin. This was the progression for constant cross-sectional area pin fins. The application of single-fin insight to fin array heat sinks, where thermal and hydrodynamic bundle effects interact with many single fins, has been done before by many researchers, most recently by Kobus and Oshio [16–18]. The application of the insight of the current research to arrays of optimal fins can also be the subject of future research.

References

[1] Kern, D. Q., and Kraus, A. D., 1972, *Extended Surface Heat Transfer*, McGraw-Hill, New York, Chap. 2.
[2] Kraus, A. D., 1988, "Sixty-Five Years of Extended Surface Technology," Appl. Mech. Rev., **41**, pp. 321–364.
[3] Eckert, E. R. G., and Drake, R. M., Jr., 1972, *Analyses of Heat and Mass Transfer*, McGraw-Hill, New York, Chaps. 3 and 9.
[4] Schmidt, E., 1926, "Die Warmeubertragung Durch Rippen," Z. Ver. Deut. Ingenieure, **70**, pp. 885–889; pp. 947–951.
[5] Snider, A. D., and Kraus, A. D., 1986, "The Quest for the Optimum Longitudinal Fin Profile," ASME HTD, **64**, pp. 43–48.
[6] Chung, B. T. F., Talbot, D. J., and Van Dyke, J. M., "A New Look at the Optimum Dimensions of Convective Splines," AIChE Heat Transfer, **84**, pp. 108–113 (1988).
[7] Aziz, A., 1992, "Optimal Dimensions of Extended Surfaces Operations in a Convective Environment," Appl. Mech. Rev., **45**, pp. 155–173.
[8] Sonn, A., and Bar-Cohen, A., 1981, "Optimum Cylindrical Pin Fin," ASME J. Heat Transfer, **103**, pp. 814–815.
[9] Li, C. H., 1983, "Optimum Cylindrical Pin Fin," AIChE J., **29**, pp. 1043–1044.
[10] Holman, J. P., 1981, *Heat Transfer*, 5th ed., McGraw-Hill, New York, Chap. 6.
[11] Hanin, L., and Campo, A., 2003, "A New Minimum Volume Straight Cooling Fin Taking Into Account the 'Length of Arc'," Int. J. Heat Mass Transfer, **46**, pp. 5145–5152.
[12] Chung, B. T. F., and Iyer, J. R., 1993, "Optimum Design of Longitudinal Rectangular Fins and Cylindrical Spines With Variable Heat Transfer Coefficient," Heat Transfer Eng., **14**, pp. 31–42.
[13] McAdams, W. H., 1954, *Heat Transmission*, 3rd ed., McGraw-Hill, New York.
[14] Morgan, V. T., 1975, "The Overall Convective Heat Transfer From Smooth Circular Cylinder," *Advances in Heat Transfer*, T. F. Irvine and J. P. Hartnett, eds., Academic Press, New York, Vol. 11.
[15] Kobus, C. J., 2005, "A Material Utilization Factor for Quantifying the Performance of Optimal Shape Extended Surfaces of Minimum Volume," *Proceeding of the 2005 ASME International Mechanical Engineering Congress and R&D Expo (IMECE)*, Orlando, FL, November 5–11.
[16] Kobus, C. J., and Oshio, T., 2005, "Development of a Theoretical Model for Predicting the Thermal Performance Characteristics of a Vertical Pin-Fin Array Heat Sink under Combined Forced and Natural Convection With Impinging Flow," Int. J. Heat Mass Transfer, **48**, pp. 1053—1063.
[17] Kobus, C. J., and Oshio, T., 2005, "Predicting the Thermal Performance Characteristics of Staggered Vertical Pin-Fin Array Heat Sinks Under Combined Mode Radiation and Mixed Convection With Impinging Flow," Int. J. Heat Mass Transfer, **48**(13), pp. 2684–2696.
[18] Kobus, C. J., and Oshio, T., 2006, "Thermal Performance Characteristics of a Staggered Vertical Pin Fin Array Heat Sink With Assisting Mixed Convection in External and In-Duct Flow Configurations," Exp. Heat Transfer **19**(2), pp. 129–148.

Dryout Heat Flux During Penetration of Water Into Solidifying Rock

Michael Epstein
Fauske & Associates,
LLC, 16W070 West 83rd Street,
Burr Ridge, IL 60527

A model for the dryout heat flux during penetration of water into solidifying rock is developed by combining steady-state one-dimensional phase change theory with available semiempirical equations for (i) the dryout heat flux in a porous medium and (ii) the permeability of hot rock cooled by water. The model is in good agreement with measurements made during the pouring of water onto molten magma. The implication of the model with respect to stabilizing molten-nuclear-reactor-core material by flooding from above is discussed. [DOI: 10.1115/1.2227042]

Keywords: porous media, water ingression, solidifying rock, dryout heat flux

Introduction

The rate of solidification of magma (molten rock) during the injection of water into overlying rock has been reported to be considerably higher than would occur by conduction alone [1]. The process has been viewed as one in which cracks develop in the frozen roof of the magma chamber, owing to thermal contraction, which are wide enough to allow water to penetrate. In this manner the water acts to thin the crust barrier and enhance the solidification rate. This so-called water ingression process has been invoked as a potential mechanism for the rapid quenching of molten nuclear reactor core material by water flooding from above [2].

Lister [3] published a comprehensive one-dimensional model of water penetration into hot but initially solid rock under the high pressure conditions that prevail within the oceanic crust. In this paper, Lister's equations for the bulk permeability of cracked rock are exploited to deal with water penetration into an initially molten, heat-generating rock-like material at low pressure, which is a problem directly related to the question of the effectiveness of water in rendering molten-nuclear-reactor-core material permanently coolable.

Physical Model and Equations

The one-dimensional water penetration model is illustrated in Fig. 1. The figure shows the cracking and concomitant penetration of saturated water into a brittle crust. The cracks do not traverse the entire thickness of the crust. There is an intact layer of crust between a downward moving solidification front at temperature T_{mp} and a cracking front at temperature T_{cr}. Of course rock does not have a fixed melting point but a melting temperature range over which the heat of solidification is liberated. Nevertheless the sharp solidification front approximation employed here is permissible since the melting range is small compared with the total temperature decrease $T_{mp}-T_{bp}$. The cracking temperature T_{cr} is assumed to be a known quantity. As shown in Fig. 1, the water does not penetrate all the way to the cracking front. At some location $z=\delta$, where z is measured upward from the solidification front, the upward heat flux from the melt pool equals the maximum heat transfer capacity of the boiling descending water. This maximum or "dryout" heat flux is denoted by the symbol q. Thus, just above the solidifying boundary there is a dry region $0<z<\delta$ through which the heat flux from the melt layer is transmitted predominantly by conduction. The dry zone is capped by a two-phase steam-water zone, where water boils within the cracks caused by the contraction of the crust. The temperature of the two-phase zone is assumed to be spatially uniform and equal to the saturation temperature T_{bp} of water.

Since heat is being removed from the melt layer at the steady-state rate q, the solidification rate will achieve a constant value. Thus, the problem may be regarded as one belonging to the class of problems on the conduction of heat in moving solids [4]. The crust/melt-layer interface is assumed to be stationary and solid material passes through the interface with velocity u equal to the pool solidification velocity (see Fig. 1). In the dry conduction zone $0<z<\delta$, we have the following equation for the temperature distribution $T(z)$:

$$u\frac{dT}{dz}=\alpha\frac{d^2T}{dz^2} \tag{1}$$

At the crust/melt-layer interface the temperature equals the melting point of the material, T_{mp}, and the conduction heat flux is equal to the sum of the heat supplied by the latent heat of fusion and the heat supplied by the underlying, heat-generating molten layer. In mathematical terms, these boundary conditions are:

$$T(0)=T_{mp} \tag{2}$$

$$-k\left(\frac{dT}{dz}\right)_{z=0}=h_{fs}\rho u+q_{up} \tag{3}$$

where q_{up} is the upward convective heat flux from the melt layer to the underside of the crust (see Fig. 1) whose value may be estimated from available correlations on free convection heat transfer to the upper and lower boundaries of liquid layers with volumetric energy generation (see, e.g., [5]). At $z=\delta$ the temperature is fixed by the water saturation temperature, T_{bp}, and the temperature gradient is proportional to the dryout heat flux; so that,

$$T(\delta)=T_{bp} \tag{4}$$

$$-k\left(\frac{dT}{dz}\right)_{z=\delta}=q \tag{5}$$

The solution of Eq. (1) subject to the boundary conditions given by Eqs. (2) and (4) results in the temperature distribution

$$T=T_{mp}-(T_{mp}-T_{bp})\left(\frac{\exp\left(\frac{uz}{\alpha}\right)-1}{\exp\left(\frac{u\delta}{\alpha}\right)-1}\right) \tag{6}$$

The following explicit forms for the solidification velocity and the thickness of the conduction zone are then obtained from Eqs. (3), (5), and (6):

$$u=\frac{q-q_{up}}{\rho[h_{fs}+c(T_{mp}-T_{bp})]} \tag{7}$$

$$\delta=\frac{\alpha\rho[h_{fs}+c(T_{mp}-T_{bp})]}{q-q_{up}}\cdot\ln\frac{h_{fs}+c(T_{mp}-T_{bp})}{h_{fs}+(q_{up}/q)c(T_{mp}-T_{bp})} \tag{8}$$

Note from Eq. (7) that the melt layer solidification rate is proportional to the difference between the heat flux carried away by the upward percolation of steam and the heat flux transmitted to the freeze boundary from the melt layer. If the melt layer is very deep such that $q\leqslant q_{up}$, a situation is reached in which water ingression becomes ineffective in terms of solidifying the melt. The solidification front is prevented from propagating because the con-

Contributed by the Heat Transfer Division of ASME for publication in the JOURNAL OF HEAT TRANSFER. Manuscript received August 17, 2005; final manuscript received February 28, 2006. Review conducted by Chang Oh.

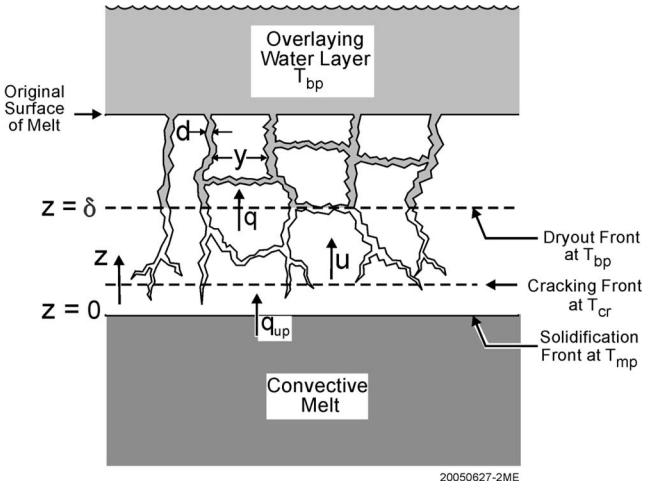

Fig. 1 An Illustration of the water ingression problem. The moving dry conduction zone lies between $z=0$ and $z=\delta$.

vective heat flux q_{up} impinging on the front thins the overlying conduction layer to a greater degree than can be accomplished through the counterflow percolation of water and steam.

A number of theoretical and semiempirical correlations for the dryout heat flux q in porous media of low permeability ($\kappa \lesssim 5 \times 10^{-9}$ m^2) have been derived from Darcy's law [6–8]. For water at one atmosphere pressure they all essentially agree with one another and are well represented by

$$q \approx \frac{h_{fg}\kappa(\rho_f - \rho_g)g}{2\nu_g} \tag{9}$$

The theory as it presently stands is not predictive because the permeability of the fractured crust is unknown. Fortunately Lister [3] has provided a semiempirical model that allows one to relate the permeability of hot-cracked-porous-rock penetrated by water to the temperature gradient in the conduction boundary layer evaluated at the cracking front. By algebraically combining the key equations in his paper one arrives at (see later)

$$\kappa = \frac{\sqrt{2}}{12}[\alpha_T(T_{cr} - T_{bp})]^3\left(-\frac{32\alpha N\phi}{u(dT/dz)_{T_{cr}}}\right)^{4/5} \tag{10}$$

Equation (10) is based on the propagation of a polygonal crack system and implicitly includes a crack edge stress intensity factor, an estimate of the lateral temperature difference required to cause sufficient tensile stress to induce cracking, and a detailed creep analysis that relates this temperature difference to the lateral distance y between cracks (see Fig. 1). Lister's analysis relied heavily on experimental data on crack propagation in quartz [9] and on high temperature creep of dunite and peridolite [10]. He used the data reported in [10] to show that the rock cracking temperature T_{cr} is in the range 800–1000 K.

The parameter N in Eq. (10) is a constant of numerical value $N=0.1$ K m$^{1/2}$ when all the other parameters are expressed in meters and degrees Kelvin; it is introduced here simply to convert Lister's equations, which are expressed in units of centimeters, to units of meters. The parameter ϕ corrects the crack edge stress intensity factor for departures from one-dimensional heat conduction in the vicinity of the crack edge and for the difference in cracking behavior between quartz and rock and is of order 2.0. The number 32 in Eq. (10) replaces the number 16 that would be derived directly from Lister's model equations. The motivation for his work was to examine the potential for water percolation in the oceanic crust at depths of about 7.0 km and corresponding pressures of about 10^3 atm. His calculations revealed a correlating coefficient of unity in the creep equation that relates the lateral (radial) temperature difference ΔT_r for crack propagation to the product $\phi y^{-1/2}$ (i.e., $\Delta T_r \cong N\phi y^{-1/2}$). As part of the present effort Lister's calculational procedure was repeated for atmospheric pressure conditions and the results showed a correlation coefficient of roughly 2.0; so that,

$$\Delta T_r \cong 2.0N\phi y^{-1/2} \tag{11}$$

Once κ is calculated from Eq. (10), the spacing y between cracks and the crack diameter d may be estimated from [3]

$$y^2 = \frac{12\kappa}{\sqrt{2}[\alpha_T(T_{cr} - T_{bp})]^3} \tag{12}$$

and

$$d^3 = \frac{12\kappa y}{\sqrt{2}} \tag{13}$$

(Lister also wrote an energy balance at the cracking front that led to the relation $-16k\,\Delta T_r = \rho c u (dT/dz)_{T_{cr}} y^2$. The equation for κ (Eq. (10)) can be found by combining this energy balance with Eqs. (11) and (12).)

The temperature gradient $(dT/dz)_{T_{cr}}$ in Eq. (10) is obtained from the solution of the purely one-dimensional conduction equation, which for the problem treated here is given by Eq. (6). Differentiating Eq. (6) with respect to vertical distance z and evaluating the result at $T=T_{cr}$ gives (see also Eqs. (7) and (8))

$$\left(\frac{dT}{dz}\right)_{T_{cr}} = -\frac{u}{\alpha}\left(T_{mp} - T_{cr} + \frac{h_{fs}}{c}\beta\right) \tag{14}$$

where β is defined as

$$\beta = \frac{1 + \dfrac{q_{up}}{q}\dfrac{c(T_{mp} - T_{bp})}{h_{fs}}}{1 - \dfrac{q_{up}}{q}} \tag{15}$$

Inserting Eq. (14) into Eq. (10) gives the permeability of the cracked crust

$$\kappa = \frac{\sqrt{2}}{12}[\alpha_T(T_{cr} - T_{bp})]^3\left(\frac{32\alpha^2 N\phi}{u^2(T_{mp} - T_{cr} + \beta h_{fs}/c)}\right)^{4/5} \tag{16}$$

Setting $\beta=0$ yields the permeability expression for Lister's problem of water penetration into a semi-infinite region of hot rock. In the present problem of a surface crust permeated by water above a melt layer the conduction boundary layer is finite and this gives rise to the β term.

Equation (16) gives κ in terms of the as yet unknown dryout heat flux q (via β) and unknown melt solidification velocity u. A relationship between u and q has already been derived (Eq. (7)) and the dryout heat flux formula, Eq. (9), provides a relationship between q and κ. Combining these equations in a manner that eliminates κ and u leads to the following nonlinear algebraic equation for q:

$$q = \frac{h_{fg}(\rho_f - \rho_g)g}{\sqrt{2}(12)\nu_g}[\alpha_T(T_{cr} - T_{bp})]^3\left(\frac{32\alpha^2 N\phi\rho^2[h_{fs} + c(T_{mp} - T_{bp})]^2}{(q - q_{up})^2(T_{mp} - T_{cr} + \beta h_{fs}/c)}\right)^{4/5} \tag{17}$$

where β is the function of q given by Eq. (14). If convection heat transfer from the interior of the melt layer to the melt front is negligible $q_{up}=0$ and $\beta=1.0$, and Eq. (16) can be solved explicitly for q:

$$q_0 = \left(\frac{h_{fg}(\rho_f - \rho_g)g}{\sqrt{2}(12)\nu_g}\right)^{5/13} [\alpha_T(T_{cr} - T_{bp})]^{15/13}\left(\frac{32\alpha^2 N\phi\rho^2[h_{fs} + c(T_{mp} - T_{bp})]^2}{T_{mp} - T_{cr} + h_{fs}/c}\right)^{4/13} \quad (18)$$

where q_0 denotes the dryout heat flux in the absence of melt layer convection ($q_{up}=0$).

Results and Concluding Remarks

It is of interest to make use of Eq. (18) to estimate the heat transfer from the lava during the Heimaey eruption in Iceland in 1973 [1]. Water was poured onto the molten lava to prevent it from reaching the town. The physical properties of rock are given in the nomenclature list. Upon inserting these properties into Eq. (18), one gets $q_0=34.9$ kW m^{-2} for the choice $T_{cr}=1000$ K. If the lower end of the cracking temperature range is selected, namely $T_{cr}=800$ K, $q_0=20.4$ kW m^{-2} is predicted. The flow of 100 kg s^{-1} of water, applied in one place, spread over about 7×10^3 m^2 of lava. From this observation an upward heat flux of roughly 40 kW m^{-2} was inferred [1]. Considering the complexity of the problem the agreement between either theoretical value and the measured value of q_0 is regarded as good. The remaining calculations for water penetration into lava are performed with $T_{cr}=1000$ K.

Drill holes showed that after two weeks of watering the lava solidification front reached a depth of approximately 12 m. Thus, the solidification front velocity was roughly 0.01 mm s^{-1}. The predicted front velocity is, from Eq. (7) with $q_{up}=0$, u$=9.14\times10^{-3}$ mm s^{-1}. Temperature probes inserted into the drill holes indicated that the conduction zone, where the temperature increased from 373 to 1400 K, was only a fraction of a meter thick. This is consistent with the estimated thickness $\delta=0.21$ m obtained from Eq. (8). The predicted properties of the crack matrix within the water-cooled rock are permeability $\kappa=6.81\times10^{-11}$ m^2, crack separation distance $y=2.63$ cm, and crack diameter $d=0.25$ mm, as predicted from Eqs. (16), (12), and (13), respectively. The predicted intensely fractured rock is in agreement with observations [1]. Lister [3] opined that his treatment of the cracking front may be to rudimentary to make useful predictions. The application of his model for κ to the problem of water penetration into solidifying rock suggests otherwise.

In the nuclear reactor safety application there is a significant upward convective heat flux q_{up} from the melt layer to the underside of the crust. Using known thermophysical property values for reactor core melts, which are not very different from those of rock, except for a higher melting point $T_{mp}\cong2200$ K and higher assumed cracking temperature $T_{cr}\cong2000$ K, Eq. (17) was solved for q_{up} values from 10^{-2} to 100 kW m^{-2}. The results for q were substituted into Eq. (7) to obtain the corresponding values of u. The predicted u vs q_{up} and q vs q_{up} trends are plotted in Fig. 2. An examination of the figure reveals that, while the dryout heat flux q ultimately increases with increasing q_{up}, q asymptotically approaches q_{up} after q_{up} exceeds q_0, the dryout heat flux in the absence of melt layer convection. Accordingly, the solidification rate decreases dramatically with increasing q_{up} once q_{up} exceeds q_0 (see Eq. (7) as $q\rightarrow q_{up}$). If it is permissible to extrapolate Lister's cracking model, which is based on the data for rocks, to solidified reactor core material, one must conclude from Fig. 2 that sustained cracking and water ingression due to crust-cooling shrinkage is not possible under the strong convection conditions that prevail within molten reactor core layers ($q_{up}\cong200$ kW m^{-2}). However, the values of the parameters in the cracking theory upon which Eq. (10) is based vary from one material to another and those for reactor core material may be significantly different from those for rock. Thus, with regard to the case for water penetration into solidifying reactor core material, well-controlled laboratory experiments must be the ultimate arbiter. Such experiments are presently being conducted and the model presented here is being used to rationalize the dryout heat flux measurements [11].

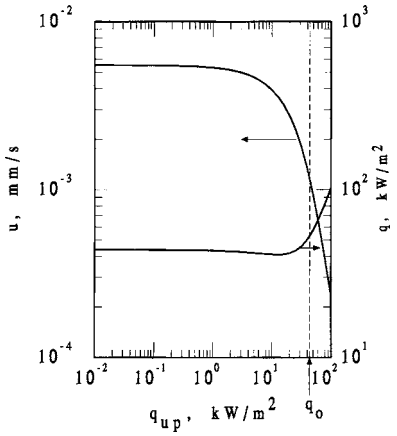

Fig. 2 Solidification front velocity and dryout heat flux versus melt layer convective heat flux for molten reactor core thermophysical properties but rock material creep behavior

Nomenclature

- c = specific heat of crust material (rock), 10^3 J kg^{-1} K^{-1}
- d = crack diameter
- g = gravitational acceleration
- h_{fg} = latent heat of evaporation of water, 2.26×10^6 J kg^{-1}
- h_{fs} = latent heat of fusion of melt layer material (rock), 1.4×10^5 J kg^{-1}
- k = thermal conductivity of crust (rock), 2.9 W m^{-1} K^{-1}
- N = numerical constant in Eq. (10), 0.1 K m$^{1/2}$
- q = dryout heat flux
- q_{up} = upward convective flux from melt layer
- q_0 = dryout heat flux when convection in the melt layer is negligible
- T = temperature (local) in crust conduction layer
- T_{bp} = boiling point of water, 373 K
- T_{cr} = cracking temperature for rock, 800–1000 K
- T_{mp} = solidification temperature of melt layer material (rock), 1425 K
- u = solidification front or cracking front velocity
- y = spacing between cracks
- z = vertical distance measured into crust from solidification front

Greek Letters

- α = thermal diffusivity of crust material (rock), 9.0×10^{-7} m^2 s^{-1}
- α_T = coefficient of linear expansion of crust material (rock), 1.5×10^{-5} K^{-1}
- β = parameter defined by Eq. (15)
- δ = thickness of conduction boundary layer or location of dryout front
- ΔT_r = lateral temperature rise between cracks
- κ = permeability (bulk) of cracked crust
- ν_g = kinematic viscosity of steam, 2.02×10^{-5} m^2 s^{-1}
- ρ = density of crust material (rock), 3200 kg m^{-3}
- ρ_f = density of water (liquid), 960 kg m^{-3}
- ρ_g = density of steam, 0.6 kg m^{-3}

ϕ = empirical factor in Lister's crack propagation analysis for rock, 2.0

References

[1] Bjornsson, H., Bjornsson, S., and Sigurgeirsson, Th., 1982, "Penetration of Water Into Hot Rock Boundaries of Magma at Crimsvotn," Nature, **295**, pp. 580–581.

[2] Farmer, M. T., Schneider, J. P., Bonomo, B., Theofanous, T. G., and Spencer, B. W., 1992, "Modeling and Database for Melt-Water Interfacial Heat Transfer," *Proc. 2nd OECD (NEA) CSNI Specialist Meeting on Molten Core Debris-Concrete Interactions*, Karlsruhe, Germany, April 1–3, Report kfk 5108, pp. 403–418.

[3] Lister, C. R. B., 1974, "On the Penetration of Water Into Hot Rock," Geophys. J. R. Astron. Soc., **39**, pp. 465–509.

[4] Carslaw, H. S., and Jaeger, J. L., 1959, *Conduction of Heat in Solids*, 2nd ed., Oxford University Press, Oxford.

[5] Kulacki, F. A., and Goldstein, R. J., 1972, "Thermal Convection in a Horizontal Fluid Layer With Uniform Volumetric Energy Sources," J. Fluid Mech., **55**, pp. 271–287.

[6] Dhir, V., and Catton, I., 1977, "Dryout Heat Fluxes for Inductively Heated Particulate Beds," ASME J. Heat Transfer, **99**, pp. 250–256.

[7] Hardee, H. C., and Nilson, R. H., 1977, "Natural Convection in Porous Media With Heat Generation," Nucl. Sci. Eng., **63**, pp. 119–132.

[8] Lipinski, R. J., 1980, "A Particle-Bed Dryout Model With Upward and Downward Boiling," Trans. Am. Nucl. Soc., **35**, pp. 358–360.

[9] Martin, R. J., 1972, "Time-Dependent Crack Growth in Quartz and its Application to the Creep of Rocks," J. Geophys. Res., **77**, pp. 1406–1420.

[10] Carter, N. J., and Ave'Lallement, H. G., 1970, "High Temperature Flow of Dunite and Peridotite," Geol. Soc. Am. Bull., **81**, pp. 2181–2197.

[11] Farmer, M. T., Lomperski, S., and Basu, S., 2005, "Status of the Melt Coolability and Concrete Interaction (MCCI) Program at Argonne National Laboratory," *Proc. of ICAPP'05, Seoul, Korea*, May 15–19, Paper 5644.

Fin Efficiency of an Annular Fin Composed of a Substrate Metallic Fin and a Coating Layer

Ping Tu

Hideo Inaba
e-mail: inaba@mech.okayama-u.ac.jp

Akihiko Horibe

Zhongmin Li

Naoto Haruki

Department of Mechanical Engineering,
Faculty of Engineering,
Okayama University,
Tsushimanaka 3-1-1,
Okayama 700-8530, Japan

An analytical solution to a composite annular fin made of a substrate metallic fin and a coating layer has been carried out. Useful expressions for calculating temperature distribution and fin efficiency have been derived. Comparing the analytical results to those of numerical calculation, the premise for the expressions is also explored. Theoretical analyzing results show that fin efficiency of a coated fin decreases with an increase of the coating layer thickness if the thermal conductivity of coating layer is much less than that of the substrate metallic fin. Whereas, the reverse influence of the coating layer thickness on the fin efficiency appears if the thermal conductivity of the coating layer is beyond the above range. [DOI: 10.1115/1.2227043]

Keywords: fin efficiency, composite annular fin, effect of coating layer thickness

1 Introduction

Being extended surfaces, fins are commonly attached to solid surfaces for the purpose of increasing heat transfer between solid surfaces and ambient fluids. From the viewpoint of heat transfer enhancement, fins are especially advantageous for surface heat-exchange with gases [1]. Consequently there are a number of uses for extended surfaces in practical applications such as HVAC equipment, electronic cooling apparatus, and internal-combustion engines. Usually conventional fins are made from metals or alloys to take advantage of their high thermal conductivity. Recently, the fin surface is treated specially and different kinds of composite fin are manufactured to satisfy some special requirements. Here, a composite fin is defined as a fin composed of a primary fin of metallic material (substrate) and a layer of another material coated on the substrate fin surface. In dehumidifying heat exchangers, a multilayer coating is employed, for which the bottom layer is an anti-corrosion treatment and the upper layer is a hydrophilic coating to reduce the airside pressure drop in wetting condition [2]. Composite fins can also be found in a galvanized steel heat exchanger whose finned tube is made from carbon steel and is coated with zinc to intensify its heat transfer performance [3]. Adsorbent plays an important role in adsorption heat pump systems and dehumidifying devices. As all the commercial adsorbent material such as silica gel, activated carbon, and zeolite have a very low thermal conductivity that is not more than 0.5 W/mK, the global heat transfer coefficient of such devices is limited severely. In order to accelerate the adsorption process that is a combination of heat and mass transfer process, a novel type of heat exchanger whose fins and tubes are coated by adsorbent and binder mixtures is being developed. Such kinds of heat exchanger are reported in the literature [4,5].

Fin efficiency is an index evaluating the effect of extended surfaces on heat transfer performance. Concerning its calculation for composite fins, various studies have been carried out. Most of them are about longitudinal fins of rectangular profile for their relatively simple geometric shape. Only two articles concerning composite annular fins are available in the literature so far [3,6]. In Ref. [3], the authors established an analytical solution to the fin efficiency of annular fins made of two materials. It was found that a zinc coating layer could considerably increase the efficiency of a galvanized fin. However, there is no mention about the premise of the analysis process [3]. Basing on statistical theory, Campo [6] proposed a simple quasi-one-dimensional model for annular fins and demonstrated that his result based on the arithmetic spatial mean of the thermal conductivities coincided perfectly with the result in Ref. [3]. However, the reported results were confined to the coating material with relatively high thermal conductivity.

Basing on the above, the existed formula for calculating temperature distribution and fin efficiency of coated annular fin is limited. This work is motivated by a desire to develop a general formula. Meanwhile, clarifying quantitatively the effect of the coating layer thickness is our central goal.

2 Theoretical Analyzing

The basic geometry of an annular fin considered in this paper is a circular fin of rectangular profile and shown in Fig. 1. The composite fin consists of two layers of different materials, which have different thermal physical properties according to detailed applications as mentioned above. In the y-direction along the fin thickness, the coating layer with a thermal conductivity of k_2 and a thickness of δ is above the substrate metallic fin whose thermal conductivity is k_1 and thickness is t_f. Both of them have the same geometric parameter in the r-direction along the fin length that are inner radius r_b on the fin base and radius r_e on the fin tip. The ratio of r_e to r_b is designated as radius ratio ξ. The normal geometric parameters for a bare annular fin proper to heat exchanger environments are shown below. Radius r_b takes values from $r_b=5$ to 15 mm. Radius ratio ξ is from 1.5 to 3.0. Fin thickness t_f varies from 0.1 to 1 mm. The heat transfer coefficient between the fin surface and the ambient fluid h is usually constrained from 20 to 100 W/m^2 K. The transverse thermal resistance of the bare metallic fin in the y-direction is expressed as t/k_1, and as it is so small that the temperature gradient occurs in the radial direction predominantly for the above parametric spectrum [7]. Then the composite annular fin can be simplified as a two-dimensional coating layer on a one-dimensional metallic annular fin. The present approach is constrained according to *Murray-Gardner assumptions* [8] and the thermal contact resistance between the coating layer and the metallic fin is neglected. Therefore, the steady heat conduction energy equations of substrate metallic fin and that of coating layer are described as Eqs. (1) and (2)

$$k_1 t\left(\frac{d^2\theta_1}{dr^2}+\frac{1}{r}\frac{d\theta_1}{dr}\right)+\left.k_2\frac{\partial\theta_2}{\partial y}\right|_{y=0}=0 \tag{1}$$

$$\frac{\partial^2\theta_2}{\partial y^2}+\frac{\partial^2\theta_2}{\partial r^2}+\frac{1}{r}\frac{\partial\theta_2}{\partial r}=0 \tag{2}$$

where θ is dimensionless temperature defined as $\theta=(T-T_g)/(T_b-T_g)$. The dimensionless temperature of the substrate fin is θ_1 and its independent variable is r. While, that for the coating layer is θ_2

Contributed by the Heat Transfer Division of ASME for publication in the JOURNAL OF HEAT TRANSFER. Manuscript received August 29, 2005; final manuscript received February 21, 2006. Review conducted by John H. Lienhard V.

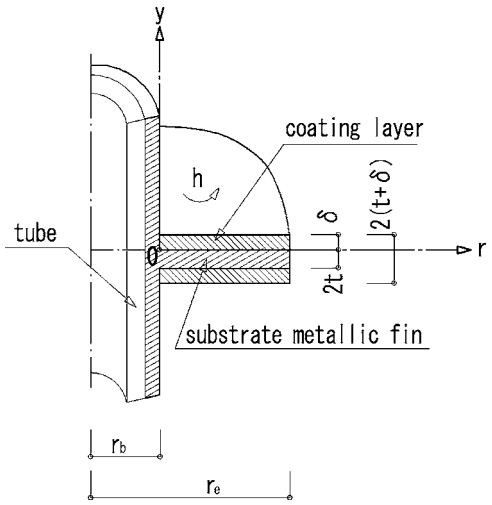

Fig. 1 Schematic view of a composite annular fin

and it has two independent variables that are r and y.

Equations (1) and (2) are subject to the following boundary conditions at such locations as the fin base, the fin tip, the interface between two materials, and the composite fin surface, described in Eqs. (3)–(6), respectively

$$r = r_b \quad \theta_1 = 1 \quad \theta_2(r_b, y) = 1 \tag{3}$$

$$r = r_e \quad \frac{d\theta_1}{dr} = 0 \quad \frac{\partial \theta_2}{\partial r} = 0 \tag{4}$$

$$y = 0 \quad \theta_1(r) = \theta_2(r, 0) \tag{5}$$

$$y = \delta \quad \frac{\partial \theta_2}{\partial y} = -\frac{h}{k_2}\theta_2 \tag{6}$$

Setting $\theta_2(r,y) = R(r)Y(y)$ and utilizing the usual method of separation of variables $R(r)$ and $Y(y)$, we can obtain Eqs. (7) and (8). Here m is the fin parameter

$$\frac{d^2Y(y)}{dy^2} + m^2 Y(y) = 0 \tag{7}$$

$$\frac{d^2R(r)}{dr^2} + \frac{1}{r}\frac{dR(r)}{dr} - m^2 R(r) = 0 \tag{8}$$

Then we are able to give the general solutions to the above equations as follows

$$R(r) = c_1 I_0(mr) + c_2 K_0(mr) \tag{9}$$

$$Y(y) = c_3 \cos(my) + c_4 \sin(my) \tag{10}$$

$$\theta_2(r,y) = [c_1 I_0(mr) + c_2 K_0(mr)][c_3 \cos(my) + c_4 \sin(my)] \tag{11}$$

Here, $c_1 - c_4$ are integration variables; I_0 and K_0 are the modified Bessel functions of the first and second kind with order 0. According to boundary condition Eq. (5), substituting $\theta_1(r)$ with $\theta_2(r,y)$ in Eq. (1) and separating the variables, Eq. (12) is introduced for $y = 0$

$$Y(y)\left[\frac{d^2R(r)}{dr^2} + \frac{1}{r}\frac{dR(r)}{dr}\right] + \frac{k_2}{k_1 t}R(r)\frac{dY(y)}{dy} = 0 \quad \text{for } y = 0 \tag{12}$$

Inserting Eq. (8) into Eq. (12), we can get the following expression

$$\frac{dY(y)}{dy} + \frac{m^2 k_1 t}{k_2} Y(y) = 0 \quad \text{for } y = 0 \tag{13}$$

The relation between c_4 and c_3 described in Eq. (14) is achieved by combining Eq. (10) with Eq. (13)

$$c_4 = \frac{-mk_1 t}{k_2} c_3 \tag{14}$$

Together with Eq. (9), boundary condition of Eq. (4) for $\theta_2(r,y)$ gives

$$c_2 = \frac{I_1(mr_e)}{K_1(mr_e)} c_1 \tag{15}$$

Inserting Eqs. (14) and (15) into Eq. (11) and replacing $c_3 c_4 / K_1(mr_e)$ with coefficient c, the temperature distribution in the coating layer can be given below

$$\theta_2(r,y) = c[I_0(mr)K_1(mr_e) + K_0(mr)I_1(mr_e)]\left[\cos(my) - \frac{mk_1 t}{k_2}\sin(my)\right] \tag{16}$$

Coefficient c can be obtained utilizing the boundary condition Eq. (3) for $\theta_2(r,y)$ with the consideration that $Y(y)$ is unity at the fin base

$$c = \frac{1}{I_0(mr_b)K_1(mr_e) + K_0(mr_b)I_1(mr_e)} \tag{17}$$

Finally, we are able to give the expression calculating the coating layer temperature

$$\theta_2(r,y) = \left[\cos(my) - \frac{mk_1 t}{k_2}\sin(my)\right] \times \frac{I_0(mr)K_1(mr_e) + K_0(mr)I_1(mr_e)}{I_0(mr_b)K_1(mr_e) + K_0(mr_b)I_1(mr_e)} \tag{18}$$

Here it is not difficult to solve the deviation equation (1) with combination of its boundary conditions Eqs. (3) and (4) for $\theta_1(r)$

$$\theta_1(r) = \frac{I_0(mr)K_1(mr_e) + K_0(mr)I_1(mr_e)}{I_0(mr_b)K_1(mr_e) + K_0(mr_b)I_1(mr_e)} \tag{19}$$

Then the relationship between $\theta_2(r,y)$ and $\theta_1(r)$ can be expressed as next

$$\theta_2(r,y) = \left[\cos(my) - \frac{mk_1 t}{k_2}\sin(my)\right]\theta_1(r) \tag{20}$$

Applying Eq. (6) the boundary condition at the composite fin surface, the implicit expression Eq. (21) in $m\delta$ is obtained. Expanding $\tan(m\delta)$ into series and reserving the terms that are not higher than order 3, we can get the expression for fin parameter m

$$\tan(m\delta) = \frac{hk_2 - m^2 k_1 k_2 t}{mk_2^2 + hmk_1 t} \tag{21}$$

$$m \approx \sqrt{\frac{hk_2}{\delta k_2^2 + \delta h k_1 t + k_1 k_2 t}} \tag{22}$$

Shown in Eq. (23), fin efficiency is defined as the ratio of the total heat dissipated by the fin to that which would be dissipated if the entire fin surface were at the fin base temperature T_b [1]

$$\eta = \frac{\int_{r_b}^{r_e} 2\pi r \theta_2(r,\delta) h dr}{\pi(r_e^2 - r_b^2)h} \tag{23}$$

Integrating temperature $\theta_2(r,\delta)$ along radial direction finally give us the expression calculating the fin efficiency of a composite annular fin

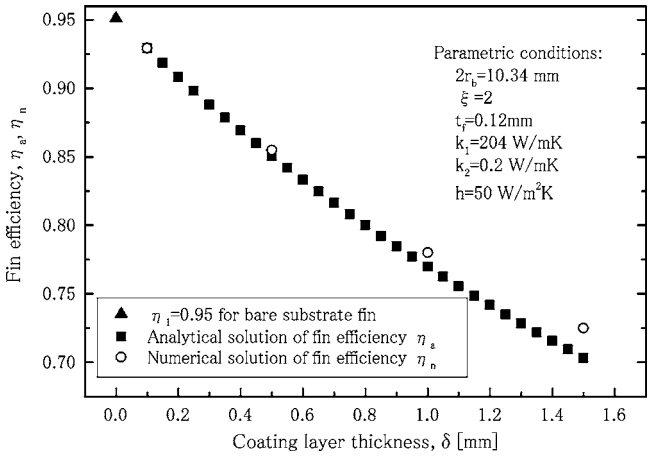

Fig. 2 Comparison of analytical solutions to numerical calculation results

$$\eta = \left[\cos(m\delta) - \frac{mk_1 t}{k_2}\sin(m\delta)\right] \times \frac{2r_b}{m(r_e^2 - r_b^2)} \frac{I_1(mr_e)K_1(mr_b) - I_1(mr_b)K_1(mr_e)}{I_1(mr_e)K_0(mr_b) + I_0(mr_b)K_1(mr_e)} \tag{24}$$

It is noteworthy that for the uncoated fin, $\delta = 0$ makes Eqs. (22) and (24) be reduced to the well-known fin parameter $m_1 = \sqrt{h/k_1 t}$ and the formula of fin efficiency for single annular fin [1].

3 Numerical Calculation

In order to evaluate the accuracy of the above analysis solution, we also accomplished the numerical calculation. The steady heat conduction energy equation of a composite annular fin and the boundary conditions are as follows

$$\frac{\partial^2\theta}{\partial y^2} + \frac{\partial^2\theta}{\partial r^2} + \frac{1}{r}\frac{\partial\theta}{\partial r} = 0 \tag{25}$$

$$r = r_b \quad \theta = 1; \quad r = r_e \quad \frac{\partial\theta}{\partial r} = 0$$

$$y = 0 \quad \frac{\partial\theta}{\partial y} = 0; \quad y = t + \delta \quad \frac{\partial\theta}{\partial y} = -\frac{h}{k_2}\theta \tag{26}$$

Here the temperature of both the metallic substrate fin and the coating layer are designed as θ and considered two dimensionally. Note that the original point of coordinate y starts from the symmetry of the substrate fin in the y-direction that differs from the analytical model shown in Fig. 1. The traditional control-volume method [9] was adopted and the calculation was continued until the relative variation of temperature was less than 10^{-7}.

The comparison between the analytical solutions to the numerical calculation results is illustrated in Fig. 2. It is the graph of the fin efficiency plotted against the coating layer thickness for the given parametric conditions, among them k_2 equals to 0.2 W/mK that is much less than $k_1 = 204$ W/mK. Here η_a stands for the fin efficiency from the analytical solution, η_n stands for that from the numerical solution, and η_1 stands for the uncoated bare substrate fin. As shown in Fig. 2, if the coating layer is relatively thin, the analytical results agree very well with those of the numerical calculation. However, deviation between η_n and η_a is observed for a relatively thick coating layer. This is caused by the approximation of the analytical solution. Furthermore, we studied numerous cases and found that the relative deviation is not more than 5% if the Bi number [10] is less than 1.0, i.e.

$$\mathrm{Bi} = \frac{h\delta}{k_2}\left(1 + \frac{t/k_1}{\delta/k_2}\right) \tag{27}$$

$$\frac{|\eta_a - \eta_n|}{\eta_n} \leqslant 5\% \quad \text{if } Bi \leqslant 1.0 \tag{28}$$

4 Effect of the Coating Layer Thickness

Zinc and frost whose thermal conductivity are quite different from each other may show a reverse trend concerning the influence of the coating layer thickness on fin efficiency and this intuition drove us to be particularly interested in revealing it in more detail. Comparing Eq. (24) with the formula of fin efficiency for a single annular fin gives

$$\eta = \left[\cos(m\delta) - \frac{mk_1 t}{k_2}\sin(m\delta)\right]\eta_m \tag{29}$$

Here η_m is the fin efficiency analogized to a single fin and its expression is the following

$$\eta_m = \frac{2r_b}{m(r_e^2 - r_b^2)} \frac{I_1(mr_e)K_1(mr_b) - I_1(mr_b)K_1(mr_e)}{I_1(mr_e)K_0(mr_b) + I_0(mr_b)K_1(mr_e)} \tag{30}$$

Notice that the above fin parameter keeps the same meaning as that of composite fin defined in Eq. (22). Combining with Eq. (22) and expanding $\cos(m\delta) - (mk_1 t/k_2)\sin(m\delta)$ into series in terms of δ, then neglecting the terms whose order are higher than 2, we can get the following approximation

$$\cos(m\delta) - \frac{mk_1 t}{k_2}\sin(m\delta) \approx 1 - \frac{h}{k_2}\delta \tag{31}$$

Then we are able to introduce another kind of expression for fin efficiency

$$\eta \approx \left[1 - \frac{h}{k_2}\delta\right]\eta_m \tag{32}$$

Consequently the expression of temperature Eq. (20) can be simplified

$$\theta_2(r,y) \approx \left(1 - \frac{h}{k_2}y\right)\theta_1(r) \tag{33}$$

It demonstrates that the fin efficiency of the composite fin is smaller than that of the analogized single fin in the case that they have the same fin parameter m. If the fin is an uncoated single fin, it is well known that an increase in the fin thickness contributes to a higher fin efficiency [1]. Hence, we can draw the same conclusion for the analogized single fin. That is fin efficiency η_m increases if the coating layer thickness δ rises up. While, fin efficiency η is decided by the combination of k_2, δ, h, and η_m according to Eq. (32), and the relationship among them is quite complex.

4.1 If k_2 is Much Less Than k_1. A hydrophilic coating evaporator, a frosted or fouled heat exchanger, and an adsorber with adsorbent coated on a metal surface all employ this kind of composite fin whose k_2 is much less than k_1. According to Eqs. (32) and (33), the following relations are derived

$$\eta < \eta_m$$

$$\theta_2(r,y) < \theta_1(r) \tag{34}$$

Due to the transverse thermal resistance represented by y/k_2, the temperature descends along the transverse direction in the coating layer. As a result, the temperature of the coating layer surface is much less than that of the substrate fin for a relatively thick coating. The above temperature profile probably yields a smaller fin efficiency of the composite fin. If the coating layer thickness increases, the item $1 - (h/k_2)\delta$ decreases abruptly for a very small

k_2. While, as mentioned above, the fin efficiency η_m increases gradually. Because variation gradient of η_m with δ is smaller than that of $1-(h/k_2)\delta$, their combining effects cause the composite fin efficiency decrease as shown in Fig. 2. As can be seen, the thicker the coating, the less efficient the composite fin.

4.2 In the Case That k_2 is Near to k_1 or k_2 is Greater Than k_1. A galvanized steel fin is a good example of the case that k_2 is greater than k_1. We can rewrite the expression of fin parameter according to Eq. (22)

$$m=\sqrt{\frac{h}{k_1 t+\delta\left(k_2+\frac{htk_1}{k_2}\right)}} \tag{35}$$

In the practical parametric range proper to heat exchanger, the term htk_1/k_2 is much less than that of k_2, and it can be neglected

$$m\approx\sqrt{\frac{h}{k_1 t+k_2\delta}} \tag{36}$$

Then we can rearrange the above denominator as follows

$$k_1 t+k_2\delta=\left(\frac{k_1 t}{t+\delta}+\frac{k_2\delta}{t+\delta}\right)(t+\delta)=\overline{k}(t+\delta) \tag{37}$$

Here $\overline{k}$ is defined as the equivalent thermal conductivity and it is the arithmetic spatial mean of k_1 and k_2 [6]. Then fin parameter can be expressed basing on $\overline{k}$

$$\overline{m}=\sqrt{\frac{h}{\overline{k}(t+\delta)}} \tag{38}$$

Meanwhile, as the term $(h/k_2)\delta$ is almost equal to zero for a big k_2, the expressions concerning temperature distribution and fin efficiency can be simplified

$$\theta_2(r,y)\approx\theta_1(r) \tag{39}$$

$$\eta\approx\frac{2r_b}{\overline{m}(r_e^2-r_b^2)}\frac{I_1(\overline{m}r_e)K_1(\overline{m}r_b)-I_1(\overline{m}r_b)K_1(\overline{m}r_e)}{I_1(\overline{m}r_e)K_0(\overline{m}r_b)+I_0(\overline{m}r_b)K_1(\overline{m}r_e)} \tag{40}$$

The above expressions indicate that the temperature distribution of the coating layer has almost no variation in the y-direction and it is similar to that of the substrate fin. This relation indicates that the transverse thermal resistance of the coating layer is so small that it can be neglected. Moreover, the composite fin that consists of different materials can be considered as a single fin with a equivalent thermal conductivity $\overline{k}$ and a thickness $t+\delta$. Therefore, a thicker coating layer introduces a smaller fin parameter and leads to a more uniform temperature distribution in the r-direction. Then higher fin efficiency can be gained. Hence, in this case, the coating treatment on the fin surface enhances heat transfer from the fin.

5 Conclusions

We analyzed the temperature profile and fin efficiency of a composite annular fin made of a substrate metallic fin and a coating layer. Our work provides general applicability and leads to the following conclusions.

(1) If Bi is less than 1.0, the analytical solution with the assumption that a composite fin is considered as a two-dimensional coating layer on a one-dimensional substrate metallic fin is effective enough. The expressions concerning temperature distribution and fin efficiency have been derived.
(2) Fin efficiency decreases with an increase of the coating layer thickness if the thermal conductivity of the coating layer is much less than that of the substrate metallic fin. On the contrary, the heat transfer performance will be intensified with the coating treatment on the substrate metallic fin surface if the thermal conductivity of the coating layer is beyond the above range.

Nomenclature

Bi = Biot number, as defined in Eq. (27)
c = coefficient defined in Eq. (16)
c_1, c_2, c_3, c_4 = integration variable
h = convective heat transfer coefficient (W/m^2K)
I_n = modified Bessel function of the first kind and of order n
K_n = modified Bessel function of the second kind and of order n
k = thermal conductivity (W/mK)
$\overline{k}$ = equivalent thermal conductivity (W/mK), $\overline{k}=k_1 t/(t+\delta)+k_2\delta/(t+\delta)$
m = fin parameter (m^{-1})
$\overline{m}$ = fin parameter based on equivalent thermal conductivity (m^{-1})
r = radial distance (m)
R = function of r
t = semi-thickness of substrate metallic fin (m)
t_f = substrate metallic fin thickness (m)
T = temperature (K)
T_g = ambient fluid temperature (K)
y = axial distance (m)
Y = function of y

Greek Symbols

δ = coating layer thickness (m)
η = fin efficiency
η_m = fin efficiency analogized to a single fin, as defined in Eq. (30)
θ = dimensionless temperature, $\theta=(T-T_g)/(T_b-T_g)$
ξ = radius ratio, $\xi=r_e/r_b$

Subscripts

1 = substrate metallic fin
2 = coating layer
a = result of analytical solution
b = base of the fin
e = extremity of the fin
n = result of numerical solution

References

[1] Schneider, P. J., 1974, *Conduction Heat Transfer*, 6th ed., Addison-Wesley, London, pp. 67–96.
[2] Wang, C. C., and Chang, C. T., 1998, "Heat and Mass Transfer for Plate Fin-and-Tube Heat Exchangers, With and Without Hydrophilic Coating," Int. J. Heat Mass Transfer, **41**, pp. 3109–3120.
[3] Lalot, S., Tournier, C., and Jensen, M., 1999, "Fin Efficiency of Annular Fins Made of Two Materials," Int. J. Heat Mass Transfer, **42**, pp. 3461–3467.
[4] Restuccia, G., Freni, A., and Maggio, G., 2002, "A Zeolite-Coated Bed for Air Conditioning Adsorption Systems: Parametric Study of Heat and Mass Transfer by Dynamic Simulation," Appl. Therm. Eng., **22**, pp. 619–630.
[5] Waszkiewicz, S., Jenkins, S., Saidani-Scott, H., and Tierney, M., 2003, "Analysis of a Finned Heat Exchanger Working in an Adsorption Refrigeration System Using Zeolite and Methanol," Heat Transfer Eng., **22**, pp. 71–78.
[6] Campo, A., 2002, "Statistical Heat Transfer From Uniform Annular Fins With High Thermal Conductivity Coating," Int. J. Thermophys., **15**, pp. 242–245.
[7] Lau, W., and Tan, C. W., 1973, "Errors in One-Dimensional Heat Transfer Analysis in Straight and Annular Fins," ASME J. Heat Transfer, **95**, pp. 549–551.
[8] Kraus, A. D., Aziz, A., and Welty, J., 2001, *Extended Surface Heat Transfer*, Wiley-Interscience, New York, p. 11.
[9] Patankar, S. V., 1980, *Numerical Heat Transfer and Fluid Flow*, Hemisphere, New York.
[10] Xia, Y., and Jacobi, A. M., 2004, "An Exact Solution to Steady Heat Conduction in a Two-Dimensional Slab on a One-Dimensional Fin: Application to Frosted Heat Exchanger," Int. J. Heat Mass Transfer **47**, pp. 3317–3326.

Journal of Heat Transfer

Discussion

Discussion: "Effect of Tip Clearance on the Thermal and Hydrodynamic Performance of a Shrouded Pin Fin Array" (Moores, K. A., and Joshi, Y. K., 2003, ASME J. Heat Transfer, 125, pp. 999–1006)

P. Razelos
Professor Emeritus
College of Staten Island,
CUNY, Staten Island, NY 10314
and
2 Kanigos St.,
Athens 10677, Greece
e-mail: razel@ath.forthnet.gr

[DOI: 10.1115/1.2227054]

In this paper the authors present the experimental results of the effects of tip clearance on the thermal and hydrodynamic performance of a shrouded pin fin array. The authors have employed the most modern experimental techniques to obtain their results. This is indeed an excellent experimental work. The authors refer to two cases of existing similar experimental work, where pin fins have been used for cooling purposes: (a) cooling of turbine's blades in aircraft engines and (b) cooling of electronic equipment. A comprehensive discussion with regard of turbines' experiments, it can be found in the recent book by Han et al. [1]. On the other hand, the authors' work can be useful to manufacturers that produce ready made electronic coolers found in the market as CF-512, BF-02, etc.

Experimental endeavors are costly and time consuming, while analytical solutions of extended surface heat transfer requires only mathematical skills. Most of the analytical results have been obtained, assuming the surface heat transfer coefficient constant. In this respect the heat transfer community is indebted to experimentalists for providing valuable information that can be used to obtain more realistic mathematical results. However, experimentalists often, as in the present case, have to use analytically obtained results. For example, the authors employed mathematical results obtained previously by Kraus and Bar-Cohen, authors' Ref. [20].[1] It is also apparent that rudimentary theoretical background of fin analysis is a prerequisite for any experimental endeavor, for designing an experiment. Therefore, there is a blend between experiment and analysis.

In the following, discussion we offer some suggestions that might help the authors, and for the sake of the readers, to improve the representation of their results. These comments refer: to the authors' mathematical expressions (Eqs. (9)–(12)), and to evaluation of the pin fins' performance (fin efficiency).

It is of vital importance in any fin analysis to define the parameters that characterize the problem. For a single spine, there are three parameters, having definite physical significance, similar to those commonly used dimensionless numbers in other fields, e.g., Reynolds, Nusselt, Sherwood, etc. These dimensionless numbers are usually formed from the geometry and other given physical quantities. In the present case we have: the thermal conductivity k of the fin's material, and heat transfer coefficient h. Note, that since the purpose of authors' experiments is to determine experimentally h, one can use either $\overline{h}$ or the authors' h_{100}, but for the moment we will simply call it h. The fins geometry is characterized by its height H, and the base and tip's diameters D_{ew} and D_T. The first parameter introduced is the ratio λ, which is equal to the ratio of the two diameters $\lambda = D_T/D_{ew} = r_T/r_{ew}$. The other two are

$$u^2 = (H/r_{ew})^2(hr_{ew}D_{ew}/k) = (H/r_{ew})\mathrm{Bi} \tag{1}$$

$$\mathrm{Bi} = hD_{ew}/k \tag{2}$$

The parameter $u^2 = hH/(kr_{ew}/H)$ represents the ratio of *convection/conduction energy*, and the second is the well known Biot Number, that represents the ratio of the internal to the external thermal resistances. It has been shown [2–5] that in any pin fin analysis, the parameters u and $\mathrm{Bi}^{1/2}$ should represent the dimensional height and base semithickness of the pin fin, respectively. It is worth noticing that using u as dimensionless height of a fin is nothing new. For example, Gardner's [6] efficiency graphs, appearing in all the textbooks and handbooks, are plotted versus u. Also, as shown in Ref. 2, the pin's dimensionless heat dissipation it is also plotted versus u. Also, the Biot number, Bi, (actually it should have been $\mathrm{Bi}^{1/2}$), has been extensively used, either to derive the criteria, which will guarantee the fin will not introduce any insulating effect, Schneider [7,2], Kraus et al. [8], or to derive the criteria for the validity of the one-dimensional approach by Irey [9], (cylindrical pin fins), [2], and Lau and Tan [10]. Irey, Law and Tan, and all the authors on fin analysis found in the heat transfer literature, instead of u are using the ratio H/D, or H/w, where w is the base thickness.

For some technical reasons the authors use trapezoidal instead of cylindrical profile pins, which introduces the additional parameter λ. In fact, the authors pin fins are nearly cylindrical, because the values of λ are: $\lambda = 0.9175$, 0.8750, 0.8325, and their average values are: $\lambda_{ave} = 0.9583$, 0.9375, and 0.9183. I believe that with these values λ their calculated results would have not been any different, if the authors had employed instead the pertinent equations for the cylindrical spines, given below. In addition, on the author's page 1003, there is no reference for the definition of

[1] In the following I will refer to the author's Ref. [20] as K-B.

Contributed by the Heat Transfer Division of ASME for publication in the JOURNAL OF HEAT TRANSFER. Manuscript received February 15, 2005; final manuscript received June 18, 2005. Review conducted by Vijay Dhir.

efficiency, which is different from the one defined by Gardner [6], while from their Eq. (10) one can see that by definition

$$\eta = \frac{\overline{\Theta}}{\Theta_{ew}} \tag{3}$$

where, in the foregoing equation, the numerator is the space average dimensionless temperature.

Let us now discuss Eqs. (11), (12a), (12b) that were derived by K-B. In spines and longitudinal fins analysis it is advantageous to locate the origin of the coordinate, $x=0$, at the tip of the fin. However, symbol *b*, in their nomenclature, that represents the distance between the tip and the base of the fin, is not correct. As is shown in the Fig. 3.10 of K-B, *b* symbolizes the distance between a fictitious tip, (determined by λ), and the base of the fin, while the symbol *a*, (that does not appear in the author's nomenclature but only in the pertinent equations), represents the distance from the fictitious tip to the tip of pin. Therefore, the distance *b* depends on the parameter λ, while $a=b-H$. Thus, the extremely complicated expression for the dimensionless temperature, Eq. (3.73) in K-B, involves the distances the *b* and *a*, instead of the given parameters *H* and λ. All of this enormously complicated formulation by K-B could have been circumvented if one selects the real tip to be the origin of coordinates, $(0 \leqslant x \leqslant H)$. For this particular case, the pertinent equations, given below, are taken from Ref. 4.

The profile of the fin and the dimensionless temperature are as follows

$$z = \lambda + (1-\lambda)\varphi \quad \phi = x/H \tag{4}$$

The dimensionless temperature, defined as $\theta = T/\overline{T}_{fl}$, where $\overline{T}_{fl}$ is the average fluid temperature both measured above thee ambient temperature, is equal to

$$\theta = \left(\frac{1}{z}\right)^{1/2} [C_1 I_1(2pz^{1/2}) + C_2 K_1(2pz^{1/2}\,]\quad p = u/(1-\lambda) \tag{5}$$

The foregoing equations show that the dimensionless temperature $\theta = \theta(\varphi, u, \lambda)$, while for a given *u* is a function of φ and λ, with $z(0)=\lambda$, and $z(1)=1$. Note that integrating Eq. (4) from 0 to 1, we obtain the average fin diameter, $D_{\text{ave}}=D_{\text{end}}\ (1+\lambda)/2$, thus $0.9163 \leqslant z_{\text{ave}} \leqslant 1$. In order to obtain the dimensionless temperature, Θ_x, the authors use Eqs. (11), (12a), (12b), (Eq. (3.73) in K-B). However, the K-B dimensionless temperature has been obtained using constant *h*, and initial conditions (I think they mean boundary conditions) of $Q(x=b)=Q_{pf}$, and $\Theta(x=b)=\Theta_{ew}$. However, the temperature is not specified at $x=b$. I believe that a more reasonable boundary condition would have been to consider an adiabatic tip, $Q(x=b)=0$. For example, when the authors' parameter $C=0$, the top plate is adiabatic, while the authors also never considered the heat transfer from the tip, their Eq. (10). This new boundary condition would have simplified the equations considerably, especially the expression for the heat dissipation (see Ref. 5). Now, the boundary conditions that accompany (5) are $Q(u)=Q_{pf}$, and $(d\theta/dx)_{x=0}=0$. We may now observe that, because the values of λ, are nearly one, which result in very large values of the parameter $p=u/(1-\lambda)$, it would have been be justified to use for their calculations the following much simpler expression for cylindrical spines

$$\theta = B\frac{\cosh(\xi)}{\cosh(u)}, \quad \xi = u \times (x/H) \tag{6}$$

In the foregoing equation the symbol *B* is equal to $B = (k^2 Q_{pf}/\pi h\ \text{Bi}^{3/2}\theta_{en})$.

Finally, it is necessary for those who are in involved in any fin analysis or experiment endeavor, at the end they should always compare the heat transferred by the fin, to the heat that would have been transferred from the fin's base area in the absence of the fin. This ratio was introduced by Gardner [6], as fin effectiveness. The later could be calculated using the average heat transfer coefficient determined experimentally, and the results will be on the conservative side, because in the bare surface, where the heat transfer coefficient can be easily determined from known formulas, would be larger. It has been also shown in Refs. 2 and 3 that, for straight fins and spines the effectiveness is equal to $1/\sqrt{\text{Bi}}$, which poses restrictions on the values of Bi, that was neglected by the authors.

I may suggest further, that the authors extend their experimental work to the following two other important problems. The first one is the case where fins are used in heat exchangers, and the second the in arrays of fins. Notice that the boundary conditions in the first are constant temperature and insulated tip, and in the second the temperatures are specified. With regard of the second problem that authors should consult [11].

I hope these comments will help the authors to improve the presentation and to design their new experiments.

References

[1] Han, J.-C., Dutta, S., and Ekkand, S. V., 2000, *Gas Turbine and Cooling Technology*, Taylor and Francis, New York.

[2] Razelos, P., 2003, "A Critical Review of Extended Surface Heat Transfer," Heat Transfer Eng., **24**(6), pp. 11–28.

[3] Razelos, P., and Georgiou, E., 1992, "Two-Dimensional Effects and Design Criteria for Convective Extended Surfaces," Heat Transfer Eng., **38**(3), pp. 38–48.

[4] Das, S., and Razelos, P., 1997, "Optimization of Convective Trapezoidal Profile Circular Pin Fins," Int. Commun. Heat Mass Transfer, **24**(4), pp. 533–541.

[5] Razelos, P., 1983, "The Optimum Dimensions of Convective Pin Fins," ASME J. Heat Transfer, **105**, pp. 411–413.

[6] Gardner, K. A., 1945, "Efficiency of Extended Heat Transfer," Trans. ASME, **67**, pp. 621–631.

[7] Schneider, P. J., 1955, *Conduction Heat Transfer*, Addison-Wesley, New York, p. 69.

[8] Kraus, A. D., Aziz, A., and Welty, J., 2000, *Extended Surface Heat Transfer*, Wiely, New York.

[9] Irey, R. K., 1968, "Errors of the One-Dimensional Fin Solution," ASME J. Heat Transfer, **90**, pp. 175–176.

[10] Law, W., and Tan, C. W., 1973, "Errors in One-Dimensional Heat Transfer Analysis in Straight and Annular Fins," ASME J. Heat Transfer, **95**, pp. 549–551.

[11] Razelos, P., 1980, "An Efficient Algorithm for Evaluating Arrays of Extended Surfaces," ASME J. Heat Transfer, **102**, pp. 185–186.

Closure to "Discussion of 'Effect of Tip Clearance on the Thermal and Hydrodynamic Performance of a Shrouded Pin Fin Array' " (2006, ASME J. Heat Transfer, 128, pp. 855–856)

Kevin A. Moores
CALCE Electronics Products and Systems Center,
Mechanical Engineering Dept.,
University of Maryland,
College Park, MD 20742

Yogendra K. Joshi
George W. Woodruff School of Mechanical Engineering,
Georgia Institute of Technology,
Atlanta, GA 30332-0405

[DOI: 10.1115/1.2227055]

The authors would like to express their appreciation to Dr. Razelos for his interest and thoughtful comments regarding their work. The arguments that he presents in Ref. [2] for the use of dimensionless parameters u and $\mathrm{Bi}^{1/2}$ to represent the dimensional geometry of the pins are compelling and will be closely considered in future studies. However, the authors believe that the form of their experimental results as originally presented is reasonable, given that their intent was to investigate the little considered effect of tip clearance and to put those results into the context of other pin fin array studies. As noted by Dr. Razelos, the use of H/D in the authors' work is consistent with that used in a preponderance of fin array analysis and characterization studies in the literature.

The contention that a simpler model of the pin efficiency and temperature profile may have sufficed is well taken. While more rigorous, the treatment of Kraus and Bar-Cohen [20] most likely did not produce a substantially different result compared with that, which would have been obtained using the simpler expressions of cylindrical fins and assuming averaged dimensions. While the coordinate system of Ref. [20] was applied correctly in our work, the authors regret that the definition of the variable b, as Dr. Razelos properly points out, is misleading as defined in the nomenclature, particularly if the reader is not acquainted with the coordinate system employed by Kraus and Bar-Cohen. In future work, the authors will revisit the use of simpler treatments as well as that for tapered fins described in Ref. [4] with the intent of putting the results into a more accessible form.

With respect to the comments concerning the equations used to define fin efficiency and thermal profile, Eq. (10) is equivalent to a one-dimensional form defined by Gardener [6] in which the surface area of the fin is replaced with its height. As a result, heat transfer from the tip of the pins was not explicitly considered in the calculation of fin efficiency. It may be possible to include this in the form of a modified height.

Equations (11), (12*a*), and (12*b*), as correctly noted, were derived assuming a specified pin base heat flow ($Q_{x=b}$) and dimensionless base temperature ($\theta_{x=b}$). However, contrary to the assertion that $\theta_{x=b}$ is not specified, it was in fact considered to be known based on the use of average endwall temperature measurements, which were taken to represent an effective value for the entire array, just as $Q_{x=b}$ and h were assumed to be uniform across the plate. The authors would also dispute the recommendation that the more customary adiabatic tip condition be adopted in the formation of the dimensionless temperature profile. Since heat transfer from the tips of the pins was present in all but the case of $C=0$, and its very presence was the primary point of interest in this study, such an assumption would seem counterproductive. Equations (11), (12*a*), and (12*b*) on the other hand, do not preclude heat transfer from the tip. Finally, while the authors did not explicitly state the range of Biot number considered, for the full range of H/D and Re reported, $0.31 \leqslant \sqrt{\mathrm{Bi}} \leqslant 0.97$, where $\mathrm{Bi} = (h_{Aw})(D_{ew})/k_{\mathrm{fin}}$. The authors would again like to thank Dr. Razelos for his constructive remarks and suggestions.

Note: Equation E1 in Dr. Razelos' discussion appears to be in error as the middle term is not dimensionless.

Contributed by the Heat Transfer Division of ASME for publication in the JOURNAL OF HEAT TRANSFER. Manuscript received May 27, 2005; final manuscript received December 29, 2005.

Journal of Heat Transfer

Erratum

Erratum: "Thermal Resistance of Nanowire-Plane Interfaces" [Journal of Heat Transfer, 2005, 127(6), pp. 664–668]

V. Bahadur, J. Xu, Y. Liu, and T. S. Fisher

(1) Page 665: The line above Eq. (10) should read "Here, E_m is the inverse of the effective modulus and is defined as."

(2) Page 667: In the Nomenclature list for the fourth symbol, i.e., E_m, the text explaining the symbol should read "Inverse of effective modulus of elasticity for nanowire substrate combination, m^2/N."

